



HAL
open science

The Role of AGN Feedback in Galaxy Formation

Rebekka Bieri

► **To cite this version:**

Rebekka Bieri. The Role of AGN Feedback in Galaxy Formation. Astrophysics [astro-ph]. Université Pierre et Marie Curie - Paris VI, 2016. English. NNT : 2016PA066292 . tel-01496864

HAL Id: tel-01496864

<https://theses.hal.science/tel-01496864>

Submitted on 28 Mar 2017

HAL is a multi-disciplinary open access archive for the deposit and dissemination of scientific research documents, whether they are published or not. The documents may come from teaching and research institutions in France or abroad, or from public or private research centers.

L'archive ouverte pluridisciplinaire **HAL**, est destinée au dépôt et à la diffusion de documents scientifiques de niveau recherche, publiés ou non, émanant des établissements d'enseignement et de recherche français ou étrangers, des laboratoires publics ou privés.

THÈSE DE DOCTORAT
DE L'UNIVERSITÉ PIERRE ET MARIE CURIE
École Doctorale d'Astronomie & Astrophysique d'Île-de-France
Institut d'Astrophysique de Paris

THE ROLE OF AGN FEEDBACK IN
GALAXY FORMATION

Présentée par

REBEKKA BIERI

Institute Lagrange de Paris Fellow

Thèse dirigée par :

Prof. Dr. Joseph Silk
Dr. Gary A. Mamon
Dr. Yohan Dubois

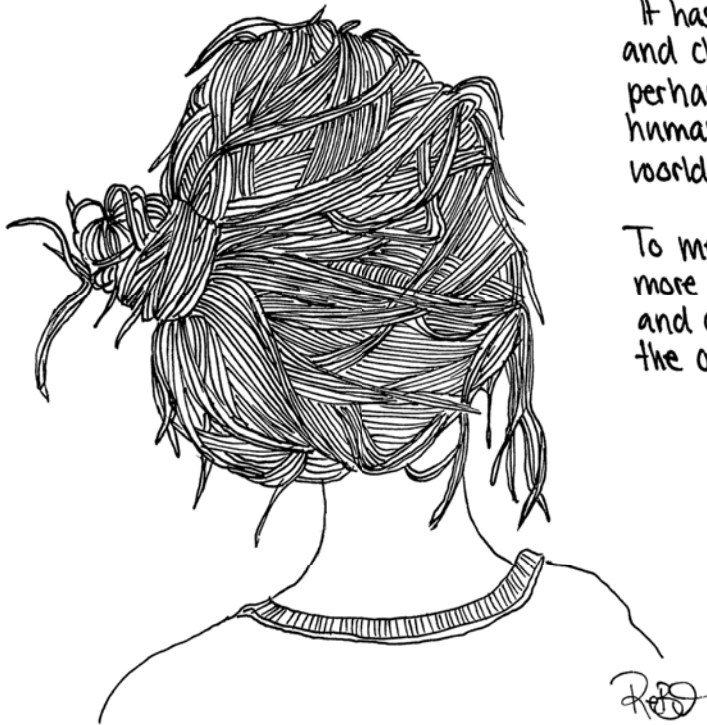
Et soutenue septembre 2016 devant un Jury composé de :

Prof. Dr. Lars Hernquist	Rapporteur
Prof. Dr. Tiziana di Matteo	Rapporteur
Prof. Dr. Benoit Semelin	Président du Jury
Dr. Thorsten Naab	Examineur
Prof. Dr. Romain Teyssier	Examineur
Prof. Dr. Joseph Silk	Directeur de thèse
Dr. Yohan Dubois	Directeur de thèse

Paris 2016

Our Earth is a very small stage in a vast cosmic area. Our posturings, our imagined self-importance, the delusion that we have some privileged position in the Universe, are challenged by the knowledge that our planet is a lonely speck in the great enveloping cosmic dark. In our obscurity, in all this vastness, there is no hint that help will come from elsewhere to save us from ourselves.

The Earth is the only world known so far to harbor life. There is nowhere else, at least in the near future, to which our species could migrate. Visit, yes. Settle, not yet. Like it or not, for the moment the Earth is where we make our stand.



It has been said that astronomy is a humbling and character-building experience. There is perhaps no better demonstration of the folly of human conceits than a distant image of our tiny world within the great cosmos.

To me, it underscores our responsibility to deal more kindly with one another, and to preserve and cherish the pale blue dot that is our Earth, the only home we have ever known.

- Carl Sagan

Abstract

Supermassive black holes (SMBHs) are known to reside in the centres of most large galaxies. The masses of these SMBHs are known to correlate with large-scale properties of the host galaxy suggesting that the growth of the BHs and large-scale structures are tightly linked. A natural explanation for the observed correlation is to invoke a self-regulated mechanism involving feedback from Active Galactic Nuclei (AGN).

The focus of this thesis is on the interactions between AGN outflows and the ISM and how the feedback impacts the host galaxy. In particular, it focuses on the two possible mechanism of outflows, namely, outflows related to AGN jets and outflows produced by AGN radiation.

High resolution, galaxy scale hydrodynamical simulations of jet-driven feedback have shown that AGN activity can over-pressurise dense star-formation regions of galaxies and thus enhance star formation, leading to a positive feedback effect. I propose, that such AGN-induced pressure-regulated star formation may also be a possible explanation of the high star formation rates recently found in the high-redshift Universe.

In order to study in more detail the effects of over-pressurisation of the galaxy, I have performed a large set of isolated disc simulations with varying gas-richness in the galaxy. I found that even moderate levels of over-pressurisation of the galaxy boosts the global star formation rate by an order of magnitude. Additionally, stable discs turn unstable which leads to significant fragmentation of the gas content of the galaxy, similar to what is observed in high-redshift galaxies. The observed increase in the star formation rate of the galaxy is in line with theoretical predictions.

I have also studied in detail how radiation emitted from a thin accretion disc surrounding the BH effectively couples to the surrounding ISM and drives a large scale wind. Quasar activity is typically triggered by extreme episodes of gas accretion onto the SMBH, in particular in high-redshift galaxies. The photons emitted by a quasar eventually couple to the gas and drive large scale winds. In most hydrodynamical simulations, quasar feedback is approximated as a local thermal energy deposit within a few resolution elements, where the efficiency of the coupling between radiation of the gas is represented by a single parameter tuned to match global observations.

In reality, this parameter conceals various physical processes that are not yet fully understood as they rely on a number of assumptions about, for instance, the absorption of photons, mean free paths, optical depths, and shielding. To study the coupling between the photons and the gas I simulated the photon propagation using radiation-hydrodynamical equations (RHD), which describe the emission, absorption and propagation of photons with the gas and dust. Such an approach is critical for a better understanding of the coupling between the radiation and gas and how hydrodynamical sub-grid models can be improved in light of these results.

The simulations show that high luminosity quasars are indeed capable of driving large-scale high-velocity winds. Infrared radiation is necessary to efficiently transfer momentum to the gas via multi-scattering on dust in dense clouds. The typical number of multi-scatterings is only about a quarter of the mean optical depth around the BH and declines quickly as the central gas cloud expands and breaks up, allowing the radiation to escape through low density channels.

Keywords: galaxies: formation — galaxies: evolution — galaxies: high-redshift — galaxies: ISM — galaxies: active — methods: numerical

Résumé

L'objectif de ma thèse porte sur les interactions entre les noyaux actifs de galaxies et le milieu interstellaire des galaxies. En particulier, je mets l'accent sur les deux mécanismes possibles responsables de la production des vents par les trous noirs : les jets et les vents produits par le rayonnement de ces trous noirs.

Les simulations hydrodynamiques de haute résolution des galaxies comprenant la rétroaction d'un jet ont montré que l'activité des noyaux actifs peut conduire à une pression excessive sur les régions denses de formation stellaire dans les galaxies, et donc à augmenter la formation d'étoiles, conduisant à un effet positif de rétroaction. Je montre que ces noyaux actifs induits par pression régulée et formation d'étoiles peuvent aussi être une explication possible des taux de formation stellaire élevés observés dans l'Univers à haut décalage spectral.

De plus, j'ai également étudié en détails comment le rayonnement émis à partir d'un disque d'accrétion autour du trou noir agit efficacement avec le milieu interstellaire et entraîne un fort vent galactique, en simulant la propagation des photons à partir des équations hydrodynamiques du rayonnement.

Les simulations montrent que la grande luminosité d'un quasar est en effet capable de conduire des vents à grande échelle et à grande vitesse. Le rayonnement infrarouge est nécessaire pour transférer efficacement le gaz par multi-diffusion sur la poussière dans les nuages denses. Le nombre typique de multi-diffusion diminue rapidement quand le nuage central de gaz central se dilate et se rompt, ce qui permet au rayonnement de s'échapper à travers les canaux à faible densité.

Mots clés: galaxies: formation — galaxies: évolution — galaxies: haut décalage spectral — galaxies: milieu interstellaire — galaxies: actives — méthodes: numériques

Contents

Contents	vi
List of Figures	ix
List of Tables	xii
1 Introduction	1
2 The Formation of Galaxies	7
2.1 Dark Matter Statistics	9
2.1.1 Spherical Top-Hat Collapse Model	9
2.1.2 The Halo Mass Function	10
2.2 N-body Simulations	12
2.2.1 Comparing N -body Simulations with Observations	15
2.3 Including the Baryons into the Picture	16
2.3.1 Physics of the Interstellar Medium	18
2.3.1.1 Radiative Cooling and Heating	18
2.3.1.2 Star Formation	20
2.3.2 Feedback Processes	21
2.3.3 Comparing Hydrodynamical Simulations with Observations	24
2.4 Active Galactic Nuclei	29
2.4.1 Classification of AGN	31
2.4.2 Correlating the AGN power to the Accretion Rate and AGN mode	34
2.4.3 Radio Galaxies and Jets	38
2.4.4 Quasars	41
2.4.5 Positive or Negative Feedback	43
2.4.5.1 Observations	43
2.4.5.2 Theoretical Work	46
3 Numerical Modeling of Galaxies	49
3.1 Collisionless N -body systems	50
3.1.1 Particle-Mesh Method	51
3.2 Collisional Systems	53
3.2.1 Deriving the Fluid Equations	53
3.2.2 Different Approaches to solve the Fluid Equations	55
3.2.3 Discretising the Fluid to solve it on a Grid	56
3.3 RAMSES: A numerical N -body and HD code using adaptive mesh refinement (AMR)	60
3.3.1 Adaptive Mesh Refinement structure	60
3.3.2 Time-stepping Scheme	62
3.4 Sub-grid physics to study galaxy formation and evolution	63
3.4.1 Radiative Cooling and Heating	63
3.4.2 Polytropic Equation of State	65
3.4.3 Star Formation	66
3.4.4 Supernova Feedback	67
3.4.5 Black Hole Feedback	70
3.5 Radiation-Hydrodynamics (RHD)	72

3.5.1	The Radiation-Hydrodynamics equations	72
3.5.2	Moments of the RT equation	74
3.5.3	The RHD equations	75
3.5.4	Closing the Moment Equations	76
3.6	RAMSES-RT: An RHD extension to RAMSES to model propagation of photons	77
4	External pressure-triggering of star formation	81
4.1	Jet Propagation	83
4.2	Playing with Positive Feedback: External Pressure-triggering of a Star-forming Disk Galaxy	85
4.2.1	Introduction	85
4.2.2	Simulation Set-up	86
4.2.3	Results	88
4.2.3.1	Disc fragmentation and star formation history	88
4.2.3.2	Mass Flow Rate	91
4.2.4	Conclusions	91
4.3	External pressure-triggering of star formation in a disc galaxy: a template for positive feedback	93
4.3.1	Introduction	93
4.3.2	Simulation Set-up	95
4.3.2.1	Basic simulation scheme	95
4.3.2.2	Application of external pressure	97
4.3.3	Results	101
4.3.3.1	Qualitative differences	101
4.3.3.2	Disc fragmentation	103
4.3.3.3	Star formation history	104
4.3.3.4	Clump properties	106
4.3.3.5	The galaxy's mass budget	109
4.3.3.6	The star formation rate	112
4.3.3.7	The Kennicutt-Schmidt relation	114
4.3.4	Conclusions	116
4.3.5	Appendix	117
4.3.5.1	Bipolar pressure increase	117
4.3.5.2	Effects of supernova feedback	117
4.3.5.3	Convergence Studies	118
5	Feedback from Radiatively-driven AGN Winds	123
5.1	Setting up the initial two-phase density distribution	124
5.2	Outflows Driven by Quasars in High-Redshift Galaxies with Radiation Hydrodynamics	126
5.2.1	Introduction	126
5.2.2	Methods	129
5.2.2.1	Initial Gas Density Distribution	129
5.2.3	Radiation Hydrodynamics	131
5.2.3.1	Modeling the Quasar	132
5.2.4	Results	134
5.2.4.1	Effects of Different Cloud Sizes	136
5.2.4.2	Qualitative Effects of Cloud Sizes	136
5.2.4.3	Effects of Different Photon Groups on the Cloud Evolution	144

CONTENTS

5.2.4.4	Efficiency of the Photon-Gas Coupling	147
5.2.5	Evolution of the Optical Depth	148
5.2.5.1	Effects of the Quasar Position	152
5.2.5.2	Comparison between Different Luminosities	153
5.2.6	Discussion	156
5.2.7	Conclusions	157
5.2.8	Appendix	159
6	Conclusions and Perspectives	161
6.1	Conclusions	161
6.2	Future Prospects	163
	Acknowledgements	167
	Bibliography	171

List of Figures

2.1	Evolution and formation of the Cosmic web from Millenium simulation	13
2.2	Comparison between Bolshoi simulation and SDSS survey	14
2.3	Comparison of galaxy luminosity function with halo mass function	16
2.4	Comparison of the predicted stellar mass function from Horizon-AGN simulation to observational data	26
2.5	Comparison of the predicted stellar mass function to observational data from the EAGLE and Illustris simulation.	27
2.6	Comparison of the predicted stellar mass function of different large scale hydrodynamical simulations	28
2.7	Stellar-halo mass relation at different redshifts	29
2.8	BH mass as a function of spheroid velocity dispersion	30
2.9	The AGN paradigm according to the unified model	32
2.10	Quasar Luminosity Function for different bands	33
2.11	Mean accretion rate scaled by Eddington rate, plotted against cavity power and the radiative power, scaled by the Eddington luminosity	36
2.12	Schematic view of the relationship between accretion rate and released power .	37
2.13	Number density of quasars as a function of redshift	38
2.14	Schematic representation of an FR 2 jet	40
2.15	Redshift distribution of the $z \geq 5.7$ quasars	42
3.1	Schematic representation of the ‘Cloud-in-Cell’ method	52
3.2	Riemann Problem in 2D	57
3.3	Reconstruction of the initial function	58
3.4	Illustration of the Total Variation Dimishing method	59
3.5	2D representation of the oct-tree structure of RAMSES	61
3.6	Cooling rates as a function of temperature.	63
3.7	Heating/cooling rate colored by the net-cooling time used in RAMSES assuming zero metallicity	64
3.8	Energy spectrum of an average quasar adopted by Sazonov et al. (2004)	73
4.1	Stellar massstar formation rate relation at $1.5 < z < 2.5$	82
4.2	Pressure slices through $z = 0$ at $t = 13$ Myr, showing $\log p$ normalised to the ambient pressure	83
4.3	Gas density maps for the low gas fraction simulations	88
4.4	Gas density maps for the high gas fraction simulations	89
4.5	SFR as a function of time	89
4.6	Time evolution of the net mass flow rate and cumulative net mass flow	90
4.7	Mean pressure versus radius at different times	98
4.8	Schematic representation of the hydrodynamics of a disc galaxy with AGN jets	99
4.9	Gas density maps of two of the <i>gasLow_fb</i> simulations without enhancement of the external pressure and with enhancement of the external pressure	101
4.10	Gas density map for a selection of the <i>gasHigh_fb</i> and <i>gasHigh_d_fb</i> simulations	102
4.11	Time evolution of the number of clumps for a selection of simulations with supernova feedback	103
4.12	Local Toomre parameter for the relaxed disc at $t = 0$ for the <i>gasLow</i> and <i>gasHigh</i> simulations	105
4.13	SFR for a selection of the simulations with supernova feedback	105

LIST OF FIGURES

4.14	Average clump mass for the <i>gasLow_fb</i> , <i>gasHigh_fb</i> , and <i>gasHigh_d_fb</i> simulations	107
4.15	Density PDF at different times for a selection of the <i>gasLow_fb</i> , <i>gasHigh_fb</i> and <i>gasHigh_d_fb</i> simulations	108
4.16	Time evolution of the mass flow rate for selected runs from the <i>gasLow_fb</i> , <i>gasHigh_fb</i> and <i>gasHigh_d_fb</i> simulations	110
4.17	Time evolution of the mass in newly formed stars plus dense gas, newly formed stars, and dense gas relative to the initial gas mass for a selection of the simulations with SN feedback	111
4.18	Time evolution of the star formation rate for all the <i>gasLow_fb</i> , <i>gasHigh_fb</i> , and <i>gasHigh_d_fb</i> simulations	113
4.19	Kennicutt-Schmidt (KS) relation for selected runs from the <i>gasLow_fb</i> , <i>gasHigh_fb</i> and <i>gasHigh_d_fb</i> simulations at 16 different times in color	114
4.20	Star formation rate (SFR) as a function of time	118
4.21	Gas density maps of the <i>gasHigh</i> non-feedback and feedback simulations without enhancement of the external pressure	119
4.22	Gas density maps of the <i>gasHigh</i> non-feedback and feedback simulations with pressure enhancement	119
4.23	Time evolution of the number of clumps for a selection of the <i>gasLow</i> , <i>gasHigh</i> , and <i>gasHigh_d</i> simulations	120
4.24	Time evolution of SFR for a selection of the <i>gasLow</i> , <i>gasHigh</i> , and <i>gasHigh_d</i> simulations	120
4.25	Time evolution of the number of clumps and SFR for the low resolution and high resolution <i>gasHigh_fb</i> simulations	121
5.1	Visualisation of density scalar field and statistical distribution of the fractal cube	125
5.2	Broad-band spectrum of a typical quasar (adopted from Sazonov et al., 2004) .	132
5.3	Slices of the gas density for the <i>L46_smallC</i> simulations, <i>L46_medC</i> simulations, and for the <i>L46_bigC</i> simulations	135
5.4	Evolution of the mean density, temperature, and H II fraction (bottom) of the clouds as a function of time for the <i>L46_smallC</i> , <i>L46_medC</i> , and <i>L46_bigC</i> simulations	137
5.5	Slices of the gas density, temperature, ionisation fraction, and velocity field for a slice of a zoomed region in the <i>L46_bigC</i> simulation	139
5.6	Slices of the IR and optical + UV radiation flux (over all directions) as a function of time for the <i>L46_bigC</i> simulation	140
5.7	Mass-weighted velocity versus density for the <i>L46_medC</i> simulation and mass-weighted velocity versus temperature for the <i>L46_medC</i> simulation.	141
5.8	Mass outflow rate as a function of radius for three different times 1, 3 and 7 Myr from top to bottom for the <i>L46</i> simulations	143
5.9	Zoomed-in slices of a cloud region in the <i>L46_medC</i> simulation at 5 Myr, showing, from left to right, maps of density, temperature, H II fraction, and velocity	145
5.10	Evolution of the total momentum for simulations where the contribution of different photon groups are included	146
5.11	Evolution of the mechanical advantage (momentum input rate \dot{p} over L/c , where L is bolometric luminosity) as a function of time for the <i>L46</i> simulations	148

LIST OF FIGURES

5.12	Evolution of the optical depth τ_{IR} as a function of time for the <i>L46_smallC</i> , <i>L46_medC</i> , and <i>L46_bigC</i> simulations and fraction of solid angle over the sphere covered by an optical depth greater than a threshold optical depth τ_{thres}	149
5.13	Evolution of the reduction factor η , providing a measure of the coupling efficiency of IR photons as a function of time for the <i>L46</i> simulations	151
5.14	Initial density distribution of the different environments for the quasar with <i>L46_bigC_min</i> ρ_{Q} , <i>L46_bigC_med</i> ρ_{Q} , and <i>L46_bigC_max</i> ρ_{Q}	152
5.15	Evolution of the mechanical advantage for the <i>L46_bigC</i> simulations, where the position of the quasar within the density field has been varied; Evolution of the mean galaxy optical depth τ_{IR} with the one $\pm\sigma$ standard deviation (shaded areas); Fractions of solid angle over the sphere covered with τ_{IR} larger than a threshold optical depth τ_{thres}	154
5.16	Evolution of the mechanical advantage for low and high quasar luminosities, respectively $L = 10^{43} \text{ erg s}^{-1}$ (<i>L43</i>) and $L = 10^{46} \text{ erg s}^{-1}$ (<i>L46</i>), and two different local gas densities; Evolution of the mean IR optical depth with the $\pm 1 \sigma$ standard deviation; Evolution of the reduction factor η	155
5.17	Convergence test of the mechanical advantage for the lower resolution <i>L46_medC_med</i> ρ_{Q} simulation using different values for the reduced speed of light c_{red}	160

List of Tables

1.1	The six Λ CDM cosmological parameters as recently measured by Planck (Planck Collaboration et al., 2015a). The errors correspond to 68% confidence limits.	3
4.1	Galaxy parameters for the induced Pressure Simulations	96
4.2	Physical parameters of runs for the induced pressure simulations	100
5.1	Properties of the photon groups used in the simulations	133
5.2	Simulation parameters for the radiative feedback simulations	136

Introduction

Our Earth is a very small dot within the great cosmos, a lonely planet orbiting an average star situated on the outskirts of a spiral galaxy that contains about 400 billion other stars. The Galaxy does not stand alone in the Universe but is one of about 100 billion other observable galaxies. These galaxies are organised within galaxy groups and clusters altogether creating a web-like structure called the *cosmic-web*. The cosmic-web spans enormous ranges extending up to about 30 Gpc in diameter within the ‘observable universe’. The filaments are itself surrounded by vast empty spaces, that contain almost no galaxies called *voids*. Typical voids have a diameter of about 10 to 100 Mpc¹. But even the galaxies themselves are surrounded by large empty space. For instance, our closest, largest galactic neighbour, the Andromeda galaxy, is about 1 Mpc away. The theory of galaxy formation is set within the evolution of these larger scales.

This picture of our Universe has not been known for a long time. The scientific recognition that even our own Galaxy is just one amongst many others only dates back to the beginning of the 20th century. The first observation of the Andromeda galaxy was first described in 964 as a small cloud, then referred to as *nebulae*. The first to relate the structure of our own galaxy with the observed nebulae was the German philosopher Immanuel Kant who suggested in 1755 that the observed nebulae were not individual stellar objects but huge unresolved congeries of stars of the same type and structure as our galaxy: island worlds floating in an immense sea of empty space.

Much of our theoretical understanding of the Universe began with the theory of general relativity (Einstein, 1916) that relates the geometry of space to the energy density of space. The theory of general relativity has met with great success. Not only, could it explain the necessary corrections to the precession of Mercury’s orbit, but it was also tested in its predictive power first by Sir Arthur Eddington and his team (Eddington, 1919; Dyson et al., 1920) that measured ‘precisely’ the predicted amount of deflection of light around the Sun.

At the time, the equations of general relativity presented a problem because they allowed for the Universe to expand or contract. It was thought that the Universe was finite and unchanging, and so a new term Λ was added to the field equations that exactly cancelled out the expansion.

In 1922, Alexander Friedmann (Friedmann, 1922) (and later Georges Lemaître (Lemaître, 1927)) found an exact solution to Einstein’s field equations that describes the evolution of the Universe and that naturally includes an expansion factor. The solution stands on the assumption of the *cosmological principle*, which states that on scales larger than 100 h^{-1} Mpc the Universe is homogeneous and isotropic, meaning that there is no preferred location or direction in the Universe.

Two years later, in 1929, Edwin Hubble (Hubble, 1929) showed that distant galaxies are in fact moving away from us with their velocity directly proportional to their distance. With the assumption of the cosmological principle, this implies that the Universe is indeed expanding isotropically everywhere.

Together with the metric of a flat, homogeneous, and isotropic Universe, proven by Howard Robertson and Arthur Walker (Robertson, 1935, 1936a,b; Walker, 1935) to be one out of three possibilities consistent with the cosmological principle, one can derive from

¹ Galactic distances are usually measured in parsecs (pc): $\text{pc} \sim 3 \times 10^{16}$ km.

the Einstein equations the following pair of equations

$$\begin{aligned}\dot{\rho} &= -3\frac{\dot{a}}{a}\left(\rho + \frac{p}{c^2}\right) \quad , \\ \frac{\ddot{a}}{a} &= -\frac{4\pi G}{3}\left(\rho + \frac{3p}{c^2}\right) + \frac{\Lambda c^2}{3} \quad ,\end{aligned}\tag{1.1}$$

with ρ being the density, a the expansion, p the pressure of the Universe, c the speed of light, G the gravitational constant, and Λ the cosmological constant. While little is understood about Λ , it is attributed to the presence of a *dark energy* with an equation of state leading to a negative pressure of the Universe.

These equations form the base of our understanding of the Universe and successfully describes the average expansion of the Universe on large scales. The first equation is a version of the law of energy conservation, assuming that the expansion of the Universe is an adiabatic process on large scales, which is a consequence of the cosmological principle. The second equation, on the other hand, states that both the energy density and the pressure cause the expansion rate of the Universe \dot{a} to decrease as a consequence of the gravitational force. The cosmological constant causes an acceleration in the expansion of the Universe.

In addition, the Friedmann (Eq. 1.1) equations can be written in terms of various density parameters, Ω , for different species. Scaled to the present-day density of the Universe, the various density parameters add up to unity by construction. Further, the *Hubble parameter* can be defined as $H \equiv \dot{a}/a$, where H_0 is referred to as the present day expansion rate.

Assuming a minimal 6-parameter model, also referred to as the Λ CDM model (Riess et al., 1998), which assumes the existence of a cosmological constant Λ , cold dark matter (CDM), and zero curvature of the Universe, the Friedmann equations can be simplified to

$$H(a) = H_0\sqrt{\Omega_m a^{-3} + \Omega_{\text{rad}} a^{-4} + \Omega_\Lambda} \quad ,\tag{1.2}$$

where Ω_m is the matter density parameter, Ω_{rad} the radiation density parameter, and Ω_Λ the density parameter associated with the dark energy ($\Omega_\Lambda = 1 - \Omega_m - \Omega_{\text{rad}}$).

Relatively recent observation programs have placed different constraints on the density composition of our Universe as well the additional free parameters of this model. Particularly strong constraints come from observations of the cosmic microwave background (CMB). When the Universe was very young, shortly after the Big Bang, the density was too high to allow photons to freely stream. The CMB was created at the point where the density dropped low enough due to the expansion that photons stopped interacting with electrons and the opaque Universe became transparent to radiation, also called the time of *recombination*. This event is imprinted in the Universe on the last scattering surface, and is the closest we can get to an image of the Universe after its formation about 13.7 Gyr years ago. Hence, the CMB is the afterglow radiation left over from the hot Big Bang and this glow is strongest today in the microwave region of the radio spectrum.

Space missions observing the CMB such as NASA's WMAP (e.g., Komatsu et al., 2011) and ESA's Planck (e.g., Planck Collaboration et al., 2014, 2015a) have enabled the determination of the parameters that led to the emergence of a Λ CDM cosmology with a minimum of 6 parameters. It is successful in describing the evolution of the Universe from a hot, dense initial state dominated by radiation to the cool, low density state dominated by non-relativistic matter and the cosmological constant at the present day. The parameters are listed in Table 1.1.

The origin and behaviour of the dark energy have yet to be fully understood but observations have shown that the mass and energy content of the Universe is composed by more

Table 1.1: The six Λ CDM cosmological parameters as recently measured by Planck (Planck Collaboration et al., 2015a). The errors correspond to 68% confidence limits.

H_0	$67.74 \pm 0.46 \text{ km s}^{-1}\text{Mpc}^{-1}$	Hubble parameter
t_0	$13.799 \pm 0.021 \text{ Gyr}$	Age of the Universe
$\Omega_{\Lambda,0}$	0.6911 ± 0.0061	Dark energy density parameter
$\Omega_{m,0}$	0.3089 ± 0.0062	Total matter density parameter
$\Omega_{b,0}$	0.0486 ± 0.0003	Baryon density parameter
$\Omega_{\text{cdm},0}$	0.259 ± 0.002	Cold dark matter density parameter

than two thirds of this dark energy, one quarter of CDM, and only about 5% of ordinary luminous matter (Planck Collaboration et al., 2015a). The luminous matter is generally referred to as baryonic matter (as leptons provide a negligible contribution to the total mass). It is thought that only the baryons participate in electro-magnetic interactions, and are, thus, the only matter we are able to see.

Since the assumption of homogeneity is incorrect on small scales, due to the presence of stars and galaxies in our Universe, there must be small inhomogeneities present at a certain time in history of our Universe. Observations of the CMB greatly support this idea. The photons which were released during recombination could travel relatively undisturbed through space to us at the present time and cooled down through the expansion of the Universe to give a homogeneous blackbody radiation field with a mean temperature of $T_{\text{CMB}} = 2.75 \text{ K}$. However, Planck and WMAP revealed small temperature deviations of the order of 10^{-5} K in the temperature field. These fluctuations, that possibly have quantum mechanical origins, are coupled via the Boltzmann equation $\rho \approx T^4$ to perturbations in the matter field.

While Λ CDM has been successful in describing observations on large scales, it is not the end of the story. Some questions are still left un-answered, most importantly regarding the nature of both dark energy and DM, as well as the origin of the primordial fluctuations that are thought to seed structure formation (for an overview see Liddle & Lyth, 2000; Liddle, 2002).

Since DM comprises about 84% of the matter content of the Universe, it is gravitationally dominant on large scales, and is, therefore, crucial to understanding structure formation. To describe and understand the evolution of the DM density field at early times, a perturbative approach is usually used. This approach takes the assumption that DM can be described as a collisionless, self-gravitating matter, often modeled as a pressureless fluid, that strongly affects the gravitational evolution of the Universe. The primordial fluctuations grow under their own gravity. At some point the non-linearity of the density evolution becomes evident, making a fully analytical description of structure formation much more difficult.

In general, numerical simulations are necessary to model the non-linear phase of structure growth as, in the regime of non-linearity the different perturbations, or modes in Fourier space, do not grow independently. So called mode-mode coupling modifies both the shape and amplitude of the power spectrum of the density perturbations over the range of wavenumbers that have become non-linear.

Empirical models (e.g., White & Rees, 1978; Blumenthal et al., 1984; Fall & Efstathiou, 1980) together with pure DM simulations (e.g., Springel et al., 2005b; Diemand et al., 2008; Klypin et al., 2011, also see Section 3.1) have shown that in the CDM scenario, the

perturbations expand to larger scales by rapid expansion of the Universe and later collapse under their own gravity to form sheets (pancakes) and filaments that, in turn feed the formation and growth of bound, collapsed, and virialised objects, the DM halos, forming together the *cosmic web*. The DM halos evolve hierarchically within the cosmic web, where small halos merge to form larger halos, which later merge with more massive halos to form even more massive ones, and so on.

Since visible matter and DM are coupled via gravity, the luminous matter composed of baryons (i.e., gas and stars) follows the DM into the halos, where they form gaseous halos. Collisions between the gas particles allows them to radiate energy away and cool, forming cold, dense gas disks at the centre of these halos. Hence, the entire luminous content of galaxies results from the cooling and fragmentation of residual gas within the potential well provided by the DM. Further cooling and fragmentation leads to the formation of dense molecular clouds, the birthplace of stars.

Assuming, now, that each DM halo hosts a galaxy of proportional mass, one finds, by comparing the mass function of DM halos provided by theoretical models, and the luminosity function of galaxies given by observations, insufficient galaxy luminosity at both the low and high mass end of the luminosity function. Some mechanism that regulates the way baryons collapse, cool, and form stars within these halos is required. This mechanism is likely to be “feedback”, operating either within the halos (i.e., stellar feedback and black hole feedback) themselves or in their surrounding gas (i.e., UV heating). For the faint end galaxies, Supernova (SN) feedback and stellar winds are traditionally assumed to be the main driver of these low mass galaxies (Dekel & Silk, 1986). At the high-mass end, an effective interaction is provided by active galactic nuclei (AGN) feedback from supermassive black holes (SMBH) which are thought to be ubiquitous at the center of local galaxies (e.g., Magorrian et al., 1998; Hu, 2008; Kormendy et al., 2011). Rapid gas accretion onto black holes leads to energy release capable of driving outflows that regulate star formation and the baryonic content of galaxies (Silk & Rees, 1998) and, thus, their own growth (via self-regulation) and that of the surrounding galaxy (Kormendy & Ho, 2013).

AGN can exert either *negative* or *positive* feedback on their surroundings. The former describes cases where the AGN inhibits star formation by heating and dispersing the gas in the galaxy, while the latter describes the possibility that an AGN may trigger star formation. AGN feedback can operate in *quasar-mode* from radiation at high accretion rates, or *radio-mode* from AGN jets at predominantly low accretion rates (Churazov et al., 2005; Russell et al., 2013a). It is still unclear how efficiently AGN feedback delivers energy (through heating, e.g., Silk & Rees, 1998) and momentum (through physical pushing, King, 2003) to the galaxy’s gas and what mode of feedback dominates.

Both semi-analytical models (e.g., Croton et al., 2006; Bower et al., 2006) and hydrodynamical cosmological simulations (e.g., Di Matteo et al., 2005, 2008; Sijacki et al., 2007; Booth & Schaye, 2009; Dubois et al., 2010a) argue that negative feedback from AGN is an important ingredient in the formation and evolution of massive galaxies and is, in particular, capable of suppressing star formation in order to reproduce the observed high-end tail of the galaxy luminosity function, and the low SFRs in massive galaxies. Moreover, observations show that cooling flows in the hot circumgalactic and intracluster media can be suppressed by the energy transferred by AGN jets (Birzan et al., 2004; Dunn et al., 2005), again negatively impacting star formation. Exactly how the outflows couple to the galaxy’s gas is, however, still not fully understood and conceals complex physics that may influence the evolution of galaxies.

This negative AGN feedback is mitigated by evidence of the positive impact of AGN on star formation. It has been argued that a jet that propagates through an inhomogeneous

interstellar medium (ISM) may also trigger or enhance star formation in a galaxy (i.e., positive feedback). Begelman & Cioffi (1989) and Rees (1989) proposed that the radio jet activity triggers star formation and might serve as an explanation for the alignment of radio and optical structures in high-redshift radio galaxies. Radio jet-induced star formation has also been considered as a source powering luminous starbursts (Silk, 2005, 2013; Bieri et al., 2015, 2016b). Ishibashi & Fabian (2012) provide a theoretical framework linking AGN feedback triggering of star formation in the host galaxy to the oversized evolution of massive galaxies over cosmic time. Negative and positive feedback are not necessarily contradictory as AGN activity may both quench and induce star formation in different parts of the host galaxy and on different timescales (Silk, 2013; Zubovas et al., 2013a; Zinn et al., 2013; Cresci et al., 2015b).

Even though it is understood that photons emitted from the thin gaseous accretion disc surrounding the black hole (BH) (Shakura & Sunyaev, 1973) effectively couple to the encompassing ISM and eventually drive a large scale wind, exactly how efficient radiation couples to the gas via the dust is not yet fully understood. Detailed radiation hydrodynamics simulations are needed to improve the general understanding in how the quasar radiation couples to the gas, in particular via the infrared coupling with the dust, and how they eventually drive powerful quasar winds (Bieri et al., 2016a). Such an approach relies on fewer assumptions and is physically correct and will, eventually, provide more accurate sub-grid models for large-scale cosmological simulations.

The research of this thesis focuses on, precisely, the interactions between AGN outflows and the ISM and how the feedback impacts the host galaxy. In particular it focuses on the two possible mechanism of outflows (I) related to AGN jets and (II) related to outflows produced by the radiation of AGN. I investigated

1. Under which conditions AGN jet feedback induces or suppresses star formation and whether jet-induced star-formation is a possible explanation for the starburst galaxies found at high-redshift
2. How radiation emitted from a thin accretion disc surrounding the BH effectively couples to the surrounding ISM and drives a large-scale wind.

Chapter 2 will explain in more detail the relevant theories that lead to the comparison between the halo mass function and the galaxy luminosity function, which motivates the need for feedback processes as a regulator for the mass content in galaxies. It focusses on AGN feedback and review observational evidence and predictions from simulations for both negative and positive feedback from AGN.

Chapter 3 describes the numerical techniques used for the simulations presented in this thesis. It will mostly focus on the techniques employed in the adaptive mesh refinement code RAMSES and the radiative hydrodynamics (RHD) extension RAMSES-RT used for the results presented later on.

Chapter 4 will then focus on the investigation of AGN-induced, pressure triggered, star formation and examine under which conditions it induces star formation. It mainly focuses on the two papers from (Bieri et al., 2015) and (Bieri et al., 2016b).

Chapter 5 describes the detailed investigation of how the radiation emitted from the thin accretion disc surrounding the SMBH effectively couples to the ISM by means of radiation-hydrodynamics. This Chapter is extracted from Bieri et al. (2016a).

The Formation of Galaxies

Galaxy formation and evolution is a highly non-linear process and poses significant challenges to our current understanding of the Universe. The current paradigm of galaxy formation in a cosmological context is that galaxies form inside DM halos in a cold DM (CDM) Universe (White & Rees, 1978; Blumenthal et al., 1984) with a cosmological constant leading to a Λ CDM model (Riess et al., 1998). DM comprises about 84% of the matter content of the Universe, is gravitationally dominant on large scales, and is, therefore, crucial to the understanding of structure formation. The realisation that we live in a DM dominated Universe led to the development of the first comprehensive theory of galaxy formation (e.g., White & Rees, 1978; Fall & Efstathiou, 1980). These analytical models embedded simple gas physics within the hierarchical growth of structure formation, whereby the DM halos evolve within the cosmic web and merged over time forming successively more massive halos (White & Rees, 1978).

Within these models the luminous matter composed of baryons (i.e., gas and stars) follows the DM into the halos, where they form gaseous halos and eventually cool to form cold, dense gas discs at their centre. Further cooling and fragmentation leads to the formation of dense molecular clouds and stars within.

The understanding of structure formation is, therefore, tightly connected with the formation and evolution of DM halos. Relevant for the theory of galaxy formation within a hierarchical cosmological growth are (i) the halo mass function of DM halos at a given time and (ii) the formation history of DM halos.

There are two ways to generate information about the abundance and evolution of DM halos: through Monte Carlo trees making use of the Press-Schechter (1974) theory and its extension to give progenitor distributions (Bond et al., 1991; White & Frenk, 1991; Lacey et al., 1993; Cole et al., 2000a; Parkinson et al., 2008) or through N -body simulations (Springel et al., 2005b; Diemand et al., 2008). The later has the advantage to track the non-linear collapse of structures. It has been shown that even with the simple underlying assumptions made in the Press-Schechter approach, their predictions agree remarkably well with N -body simulations (see Section 2.1.2 for more detail).

Despite the successes of the N -body simulations in understanding the scale of observed galaxy masses, it was soon realised that there were a number of problems. One particular issue is between the mass function of DM halos, provided by the N -body simulations, and the luminosity function of galaxies given by observations. By assuming that stellar mass follows halo mass we are left with a theoretical prediction that leads to too many small galaxies, too many big galaxies in the nearby Universe, and too many baryons within the galaxy halos.

To alleviate the problem of the excess baryons to form stars within galaxies, efficient outflows and feedback were introduced. Feedback both heats the gas in the halo, preventing it from cooling, and ejects gas from the galaxy and the halo, lowering the total gas content available to form stars.

While in low-mass galaxies, supernovae (SNe) and stellar winds can deplete cold-gas reservoirs and regulate star formation (e.g., Dekel & Silk, 1986), they are ineffective in the deeper gravitational potential well of massive galaxies. A more effective interaction for the high-mass galaxies may be provided by active galactic nuclei (AGN) feedback from supermassive black holes (SMBH) which are thought to be ubiquitous at the center of local galaxies (e.g., Magorrian et al., 1998; Hu, 2008; Kormendy et al., 2011). Rapid gas accretion onto BHs lead to energy release capable of driving high-velocity outflows (see e.g., Blandford & Payne, 1982; Begelman, 1985; Silk, 2005; Tortora et al., 2009), that are

thought to have a high impact on the host galaxy by expelling and/or heating gas, and with this regulating the baryonic content and star formation of the galaxies (Silk & Rees, 1998).

Probably the strongest evidence supporting the existence of AGN feedback is provided by observations of X-ray lobes and radio cavities in galaxy groups and clusters (e.g., McNamara & Nulsen, 2007, 2012). These have been interpreted as buoyantly rising bubbles of higher entropy material injected by an AGN. The inclusion of AGN feedback in numerical hydrodynamical simulations, but also semi-analytical models, lead, furthermore, to a better reproduction of the high-end tail of the galaxy mass function (e.g., Di Matteo et al., 2005; Croton et al., 2006; Bower et al., 2006; Sijacki et al., 2007; Di Matteo et al., 2008; Booth & Schaye, 2009; Dubois et al., 2010a), that additionally motivated the inclusion of AGN feedback in the galaxy formation theory.

However, we do not yet fully understand the physical mechanisms of the coupling between the AGN and the interstellar medium (ISM) of the host galaxy. The lack of understanding about the communication of the AGN feedback and the galaxy is partly due to the inability to capture the extremely wide dynamical range of the AGN cycle: from sub-pc scales where accretion discs form to galactic-size lobes of radio galaxies. Another complication arises because, to date, most of these studies have treated the ISM with relatively simple ‘sub-grid’ prescriptions that ignore the additional complications introduced by the multi-phase small-scale structure.

Interestingly, galaxy scale simulations show that properties of the ISM even determine whether AGN feedback is capable of driving out a large amount of gas out of the galaxy or whether it may actually foster star formation (e.g., Gaibler et al., 2012; Wagner & Bicknell, 2011; Wagner et al., 2012). The findings that AGN feedback may not only result in suppressed star formation but also may trigger the formation of stars (positive feedback) is also supported by recent observations (Cresci et al., 2015b,a; Salomé et al., 2015; Zinn et al., 2013).

This all motivates a deeper investigation of the precise interactions between AGN outflows and the ISM, how feedback impacts the host galaxy, and the communication mechanism of the AGN with the galaxy’s gas.

This Chapter will explain in more detail the relevant theories that lead to the comparison between the halo mass function and the galaxy luminosity function, which motivates the need for feedback processes as a regulator for the mass content in low and high mass galaxies. It will focus on AGN feedback and review observational evidence and numerical predictions for both negative and positive feedback from AGN.

Section 2.1 describes how the abundance of DM halos can be calculated using Press-Schechter theory. Section 2.2 explains the findings of N -body simulations. Section 2.3 discusses the inclusion of baryonic physics in the models, with Section 2.3.1 focusing on the physics of cooling and star formation within the ISM and Section 2.3.2 explaining the effect of feedback on the baryonic content of the galaxies. Section 2.3.3 discusses comparisons of hydrodynamical simulations with observations, mainly focusing on the stellar mass function. Finally, Section 2.4 focuses in more detail on AGN feedback and whether it only negatively or positively impacts the SFR within the galaxy.

2.1 Dark Matter Statistics

The abundance of DM halos is an important factor for theories of structure formation. To first order, the abundance of a halo of mass M is a function of mass only. The Press-Schechter theory (Press & Schechter, 1974), which uses the spherical top-hat collapse model and linear growth theory, gives an intuitive and useful analytic description of this mass function. This section will briefly review the spherical top-hat collapse model and explain the halo mass function that later will become important when comparing theoretical predictions with observations. It will summarise how the Press-Schechter theory can be extended to get some information about the evolution of the DM halos.

2.1.1 Spherical Top-Hat Collapse Model

The spherical top-hat collapse model is a simple way to develop an understanding of the formation of structures from the evolution of non-linear perturbations within the density field. It assumes a spherical symmetric region with radius R with a uniform overdensity δ at initial time t in an Einstein de Sitter Universe with $\Lambda = 0$ (see Chapter 1). It does not make any assumption on the dynamics of the system.

Spherical gravitational systems have the great advantage that they are easily described by the gravitational force inside a sphere and, hence, only depends on the matter inside, also known as *Birkhoff's theorem*. Assuming that the overdensities are spherically symmetric, they can be treated as a separate system where their radius is a function of time evolving with Friedman's equation (Equation 1.1 from the Introduction), that has a parametric solution as a function of $\theta \in [0, 2\pi)$ with $\theta = H_0\eta(\Omega_m - 1)^{1/2}$, and the conformal time η^1

$$r(\theta) = A(1 - \cos \theta) \quad , \quad (2.1)$$

$$t(\theta) = B(\theta - \sin \theta) \quad . \quad (2.2)$$

Here, H_0 is the Hubble constant at present time ($H_0 = 100h\text{km s}^{-1}\text{Mpc}^{-1}$, $h \sim 0.7$), Ω_m is the matter (DM plus baryonic matter) density today ($\Omega_m = 0.3156 \pm 0.0091$ see Planck Collaboration et al., 2015b). Further, $A = r_0\Omega_m/(2(\Omega_m - 1))$ and $B = H_0^{-1}\Omega_m/(2(\Omega_m - 1)^{3/2})$, where r_0 is the size of the Universe at the current time.

For early times, when θ is small, one can expand the function to first order and obtain a linear theory for the development of the overdense region

$$r_{\text{lin}}(t) = \frac{A}{2} \left(\frac{6t}{B}\right)^{2/3} \left[1 - \frac{1}{20} \left(\frac{6t}{B}\right)^{2/3}\right] \quad . \quad (2.3)$$

The first term on the right hand side corresponds to the background expansion of the critical density of the Universe and scales as $r \propto a \propto t^{2/3}$, whereas the second term stands for the expansion of the perturbations. The density ρ_m becomes

$$\rho_m = \frac{M}{4/3\pi r^3} \quad , \quad (2.4)$$

$$= \frac{1}{6\pi t^2 G} \left[1 + \frac{3}{20} \left(\frac{6t}{B}\right)^{2/3}\right] \quad , \quad (2.5)$$

¹The conformal time at a certain time t is given by $\eta = \int_0^t dt'/a(t')$, with $a(t)$ the scale factor of the FLRW metric, and $t = 0$ is at the Big Bang.

and for the density perturbation δ

$$\delta \equiv \frac{\rho_m - \bar{\rho}_m}{\bar{\rho}_m} \quad , \quad (2.6)$$

$$\approx \frac{3}{20} \left(\frac{6t}{B} \right)^{2/3} \quad . \quad (2.7)$$

Substituting the scale factor dependence for $t = \frac{2}{3H_0\Omega^{1/2}}a^{3/2}$ and A and B into equation 2.7 yields the equation

$$a = \left(\frac{3}{4} \right)^{2/3} \left(\frac{3 a_{init}}{5 \delta_{init}} \right) (\theta - \sin \theta)^{2/3} \quad . \quad (2.8)$$

Using the equations above, especially equation 2.8, a few key events in the history of the density perturbations can be quantified. At the beginning, overdense regions grow with the Hubble expansion. At a specific time, this expansion stops under its own self-gravity, reaching a maximum expansion at $\theta = \pi$. Substituting this solution into equation 2.8 reveals that this turnaround occurs when the linear density contrast is $\delta_{\text{turnaround}} \approx 1.06$. Hence, shortly after a perturbation's overdensity exceeds unity, it turns around and begins to contract. The final collapse occurs when $\theta = 2\pi$. The overdensity at this point is $\delta_{\text{collapse}} \approx 1.69$.

It is at the turnaround point where the linear spherical collapse model starts to become invalid. Clearly, the assumption of a perfectly spherically symmetric, pressureless overdensity is ideal and the collapse is not expected to continue to a singularity. In fact, the overdense regions virialise rather than collapse to a point. Because of the collisionless nature of dark matter, it cannot dissipate its energy and the collapse of the DM halts. The DM particles obtain virial equilibrium through dynamical friction which results in a pressure-supported virialised collapsed structure, the dark matter halo.

The average density within the virialised object is usually estimated by assuming a virialised radius of half of the turnaround radius. The density of the spherical region will, therefore, increase by a factor of eight until virialisation whereas the density of the non virialised region increases only by a factor of four. This occurs when the density reaches

$$\delta_{\text{vir}} = 18\pi^2 \approx 178 \quad . \quad (2.9)$$

This number is important for defining a bound object in N -body simulations. Typically an overdensity of $\delta_{\text{vir}} = 200$ is assumed.

2.1.2 The Halo Mass Function

The so-called Press-Schechter (Press & Schechter, 1974) theory provides an analytic formalism for the process of structure formation once the overdensities have collapsed into a halo. It relies entirely on the linear theory and provides insight into the evolution of the halo mass function, discussed below, and succeeds in describing the hierarchical clustering seen in N -body simulations discussed in Section 3.1.

The idea of the Press-Schechter theory is that a halo forms at peaks of matter density fluctuations in the early Universe. Those fluctuations are described by spheres of mass M and the initial density distribution is assumed to be Gaussian. It therefore makes the assumption that the probability distribution function of relative overdensity σ can be described by a Gaussian function with zero mean

$$p(\delta) = \frac{1}{\sqrt{2\sigma(M)}} \exp\left(-\frac{\delta^2}{2\sigma^2(M)}\right) \quad , \quad (2.10)$$

where δ is defined as in equation 2.6 and is the overdensity associated with M . Finally, $\sigma(M)$ is the standard deviation.

Further, it assumes that σ within a sphere of radius R is monotonically decreasing as a function of mass. Large scales, therefore, correspond to a smaller standard deviation and hence are smaller in amplitude than those on small scales. This results in a *bottom up* picture of structure formation as small structures are believed to form before large structures.

The Press-Schechter theory assumes the linear theory of the spherical collapse model (described above in Section 2.1.1) to be valid until the density reaches the threshold of δ_c and collapses immediately afterwards, where δ_c is derived above

$$\delta_{\text{collapse}} \equiv \delta_c \approx 1.69 \quad . \quad (2.11)$$

It is assumed that at any given time, all regions that have a density over δ_c collapse and form halos. This approximation can somehow be justified by the fact that gravitational instability operates very quickly.

The fraction of a sphere of radius R that exceeds a threshold at a given time t is given by

$$f(\delta > \delta_c) = \frac{1}{2} \operatorname{erfc} \left(\frac{\delta_c}{\sqrt{2}\sigma(R)} \right) \quad , \quad (2.12)$$

with $\operatorname{erfc}(x)$ being the complementary error function that describes the probability that the error of a measurement drawn from a standard Gaussian distribution lies outside the region $-\delta_c$ and δ_c . It is defined as the integral of the Gaussian function

$$\operatorname{erfc}(x) = \frac{2}{\sqrt{\pi}} \int_x^\infty \exp(-x^2) dx \quad . \quad (2.13)$$

By, mistakenly, assuming that this fraction can be identified with the fraction of particles which are part of collapsed lumps with masses greater than M we run into a problem. For small masses M , the mean square function goes to infinity and, therefore, the fraction of points, f , converges to 1/2. Hence, the formula above predicts that only half of the particles are part of lumps of any mass. In other words, the negative part of the Gaussian distribution has been left out as it corresponds to underdense regions. The so-called ‘swindle’ in the Press-Schechter approach is to multiply the mass fraction by an arbitrary factor of 2.

Generally, the fraction of mass that is in halos between mass M and $M + dM$ is given by then differentiating the function (Eq. 2.12) with respect to M . To get the *number density* of collapsed objects, the fraction of mass in halos in the range $M \rightarrow M + dM$ is multiplied by the number density of all halos ρ_m/M assuming that all of the mass is composed of such halos. The number density then becomes

$$\begin{aligned} \frac{dn(M, t)}{d \ln M} &= \frac{\rho_m}{M} \frac{\partial f}{\partial R} \frac{dR}{d \ln M} \quad , \\ &= \sqrt{\frac{2}{\pi}} \frac{\rho_m}{M} \frac{\partial \sigma}{\partial R} \frac{dR}{d \ln M} \cdot \frac{\delta_c(t)}{\sigma^2} \exp \left(-\frac{\delta_c^2(t)}{2\sigma^2} \right) \quad , \end{aligned} \quad (2.14)$$

where $\delta_c(t) = \delta_c/D(t)$ is the critical overdensity linearly extrapolated to the present time. Note that, here, equation 2.12 is here multiplied by a factor of 2 as discussed above.

The normal procedure to find the number density is by calculating σ and its derivative from the linear theory matter power spectrum.

Despite the simple underlying assumptions made above, the Press-Schechter formula for $dn/d\ln M$ agrees remarkably well with N -body simulations. The formula is known to deviate in detail at both high and low mass ends as it tends to systematically under-predict large-mass halos and overestimates the abundance of small-mass halos in comparison with simulations (see Hu & Kravtsov, 2003 for a study of the relative contributions of each source of error as a function of halo mass).

Refinements to this theory have since been made. In particular, a better fit to the mass function in N -body simulations has been proposed by assuming that the halos are elliptical instead of spherical (e.g., Lee & Shandarin, 1998; Sheth et al., 2001). Sheth et al. (2001) were able to show that this replacement plausibly leads to a mass function almost identical to that which Sheth & Tormen (1999) had earlier fitted to a subset of numerical data. Similar results have been found by Jenkins et al. (2001).

The Press-Schechter theory can be extended to allow predictions for merger histories and merger rates of DM halos (e.g., Bower, 1991). Bond et al. (1991) proposed an alternative to the Press-Schechter theory based on excursion sets to statistically estimate how many small halos would be subsumed into larger ones. This approach reduced the number of low-mass halos compared to the Press-Schechter theory and increased the number of large-mass halos and is therefore in better agreement with simulations.

2.2 N-body Simulations

The evolution of cosmic structures beyond the linear regime can only be addressed in limiting cases, notably the large-scale limit, with a simple extension of the linear theory to higher order and under a prohibitive amount of simplifying assumptions.

To better understand the non-linear evolution of the DM density field on a long timescale, as well as to get an understanding of the distribution of the DM halos within the Universe, the help of numerical simulations is needed. Numerical simulations are extremely important in the study of structure formation in a cosmological context as they provide accurate numerical predictions to be tested against theories and observations.

Gravity is the dominant force that drives structure formation. Unless an accurate description of the very early Universe, or the behaviour of objects near a massive black hole is needed, gravity can be well described by the Newtonian theory. DM is thought to be made of collisionless particles that interact only through gravity and can be well represented by a set of point particles, N -bodies (see Section 3.1 for a more detailed discussion).

N -body simulations follow the evolution of the DM component from the very early stages, where small density fluctuations perturb an otherwise homogeneous distribution, to the current time with its highly non-linear structures. Hence, the features introduced by the specific cosmological model are imprinted on the initial conditions of the simulation, i.e. on the primordial perturbation field. Usually, the initial conditions are derived analytically and start a certain time after the Big Bang (e.g., Zaldarriaga & Seljak, 2000; Lewis & Bridle, 2002; Lewis, 2013). This can be done because about the first ~ 100 million years (Myr) of the evolution of the Universe after the Big Bang are still within the quasi-linear regime and, hence, can be derived analytically.

Including a statistical distribution of initial positions and velocities of the particles, the system is evolved forward in time according to the gravitational forces acting on the DM density field within an expanding Universe. At the end of the simulation, after approximately 13.7 Gyr, the simulation provides a prediction for the large-scale distribution of the

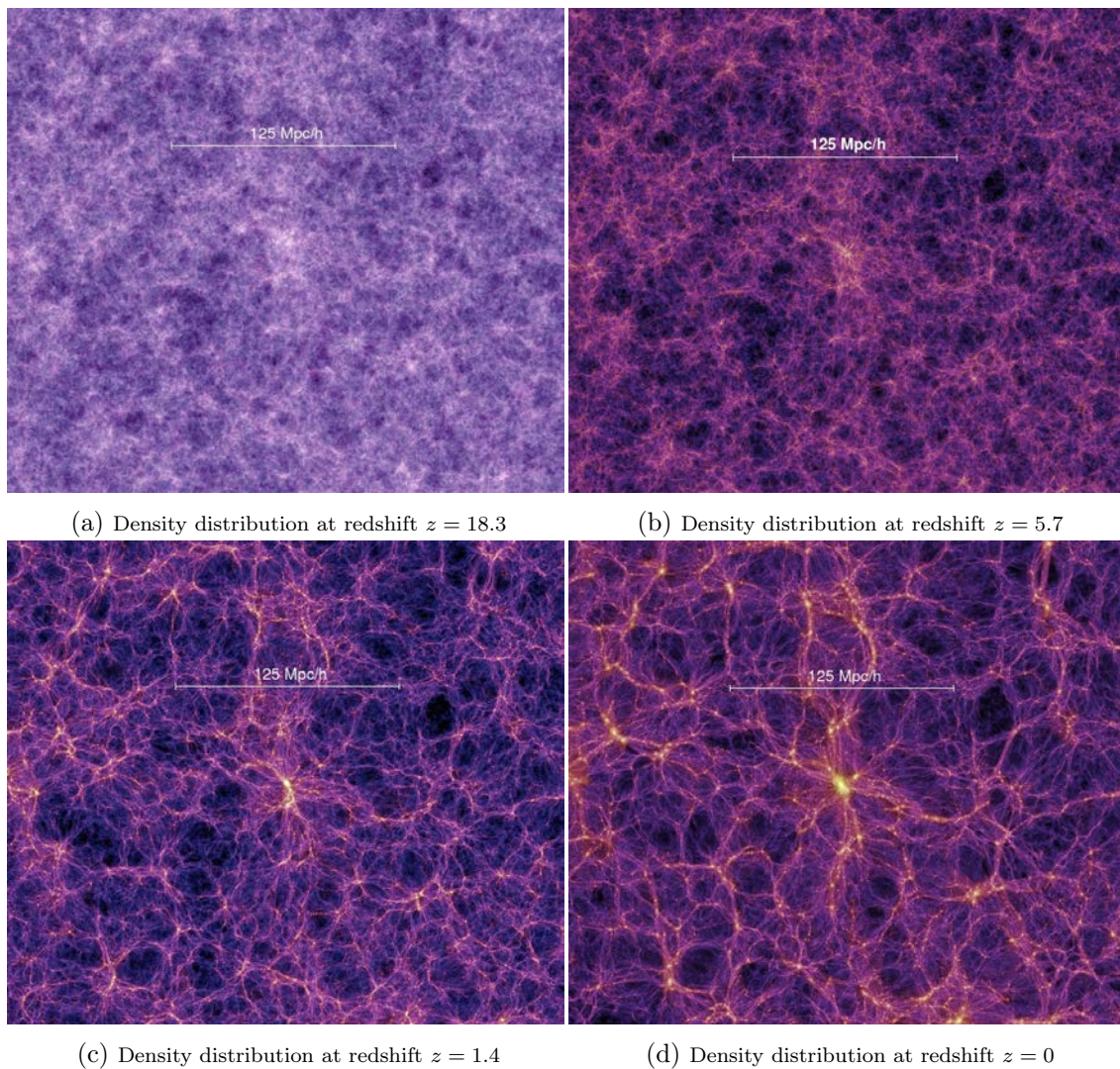


Figure 2.1: Slices through the density field that are all 15 Mpc/h thick and a size of 375 Mpc/h wide, for four different redshifts (times). As the simulation proceeds the DM distribution evolves from a homogeneous state to a more pronounced structured distribution consisting of large walls, filaments, and haloes (densest structures). At the end of the simulation the Universe is filled in large portions by underdense structures, so called voids, that are surrounded by the cosmic web. Credit: Springel et al. (2005b).

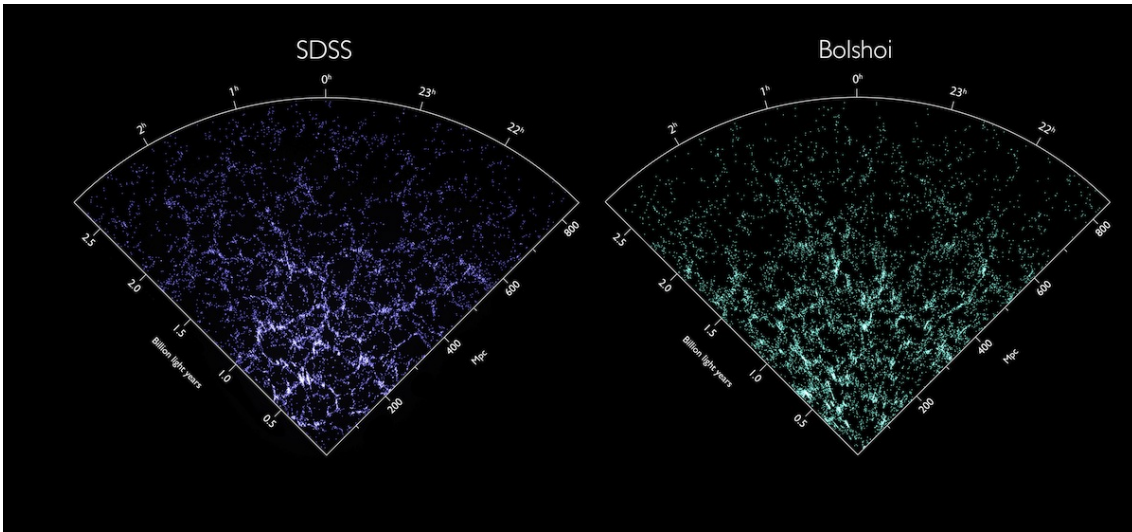


Figure 2.2: Map of the galaxy distribution in the nearby universe observed by the Sloan Digital Sky Survey (left) and predicted by the Bolshoi Simulation (right). Comparison between the luminous web structure of the galaxy distribution within the Universe with the DM structure of the simulations shows close agreement. This indicates that the DM simulations manage to well represent the large scale structure of the Universe. Credit: Nina McCurdy and Joel Primack/University of California, Santa Cruz; Ralf Kaehler and Risa Wechsler/Stanford University; Sloan Digital Sky Survey; Michael Busha/University of Zurich.

matter within the assumed cosmological model. Since the simulation represents a random region of the Universe, comparisons with observations must be statistical.

Such N -body simulations of large-scale structures have met great success. There are various simulations (e.g., Springel et al., 2005b; Diemand et al., 2008; Klypin et al., 2011) that successfully simulated the evolution of the DM content of the Universe and reproduce the observed luminous cosmic web (de Lapparent et al., 1986). They all reveal a picture where over the course of time the DM collapses into large walls, filaments, and haloes building up the cosmic web structure that is surrounded by immense voids, with densities as low as one tenth of the cosmological mean.

A visual representation of an evolution of such a cosmological simulation (here the *Milennium* simulation performed by Springel et al., 2005b) is shown in Figure 2.1, where it visualises that as the simulation proceeds, the matter distribution evolves from a state of homogeneity to a more and more pronounced filamentary structure. A comparison of the N -body simulations with the observations such as the Sloan Digital Sky Survey (SDSS) reveals that the general structure of the cosmic web matches the cosmic structure revealed by deep galaxy studies, shown in Figure 2.2, where the galaxy distribution predicted by the N -body (*Bolshoi*) simulation of Klypin et al. (2011) is shown in comparison of the galaxy structure observed by SDSS.

Such a close match between the predictions of the N -body simulations and the observations, provides evidence that the underlying theoretical assumptions of structure formation, coming from the standard Λ CDM model, provide, at least on large scales, a fairly accurate picture of how the Universe actually evolved. However, while the simulations appear to agree broadly with observations, the details in the highly non-linear regime exhibit important differences.

2.2.1 Comparing N -body Simulations with Observations

First of all, in order to compare the statistical properties of the N -body simulations with observations, the number of galaxies have to be counted within the simulation. By assuming that each DM halo hosts a galaxy of proportional mass, the problem is reduced to finding the number of halos within the N -body simulations. The essence of finding the halos is to convert a discrete representation of a continuous density field into a countable set of 'objects', the halos. In general, this conversion is affected both by the degree of discreteness in the realisation (i.e., the particle mass within the simulation) as well as by the detailed characteristics of the object definition algorithm. Additionally, high resolution simulations, such as e.g., Springel et al., 2005b; Diemand et al., 2008; Klypin et al., 2011, reveal that within the virialised region of a large halo there can also be various smaller, bound 'sub-halos'. The distinction between the larger halo and its substructures complicates comparisons between theory, simulation, and observation. It is beyond the subject of this thesis to go into detail of the different ways halos can be defined and the reader may be referred to Hoffmann et al., 2014; Lee et al., 2014; Behroozi et al., 2015 for a detailed discussion.

Having found the number of DM halos, and by assuming a constant DM mass-to-light ratio, the theoretical predictions can be compared with observations. Such comparisons are however not without complications. For instance, attempts to reproduce the observed number of Milky-Way satellites using N -body simulations, and by assuming that each simulated DM satellite halo contains a galaxy, overproduced the number of low mass satellites by several orders of magnitude (Moore et al., 1999). Additionally, Moore et al. (1999) found that simulations with cold DM fails to reproduce the rotation curves of DM dominated galaxies, one of the key problems that it was designed to resolve. While it is almost certain that the existing sample of Milky-Way satellite galaxies is incomplete (Koposov et al., 2008; Tollerud et al., 2008) and new satellite galaxies are still discovered (e.g., Belokurov et al., 2009, 2010), it appears unlikely that new observations will uncover as many galaxies as DM simulations predict to exist around the Milky-Way.

For another comparison, one can compare the mass function of DM halos with the luminosity function of galaxies obtained from wide redshift surveys. The galaxy luminosity function is then fitted by a Schechter (1976) function

$$\phi(L)dL = \frac{\phi^*}{L^*} \left(\frac{L}{L^*} \right)^\alpha \exp(-L/L^*)dL \quad , \quad (2.15)$$

where L is the luminosity, L^* a characteristic galaxy luminosity where the power-law form of the function cuts off, the parameter ϕ^* has units of number density and provides the normalization, and α is the curvature of the function. Yang et al. (2003) use $L^* = 9.64 \times 10^9 h^{-1}L_\odot$, $\alpha = -1.21$ and $\phi^* = 1.61 \times 10^{-2} h^3 \text{Mpc}^{-3}$.

To compare the theoretical prediction with the galaxy luminosity function from observations, one firstly assumes that each DM halo hosts exactly one galaxy, and that each galaxy has exactly the same DM-mass-to-light ratio M/L . This makes it possible to convert the halo mass function to a theoretical prediction of the galaxy luminosity function. The DM-mass-to-light ratio is chosen, such that the theoretical prediction overlaps at one point with the observations. Figure 5.1, taken from Yang et al. (2003), shows a comparison of the halo mass function (using $M/L = 100hM_\odot/L_\odot$) and the galaxy luminosity function of the 2dFGRS galaxy survey (Norberg et al., 2002). Compared to the theoretical prediction, the pure DM model over-predicts the galaxy luminosity function at both the low and high mass end. This suggests that the DM-mass-to-light ratio decreases (increases) in reality with the mass at the low (high) mass end and is thus not constant.

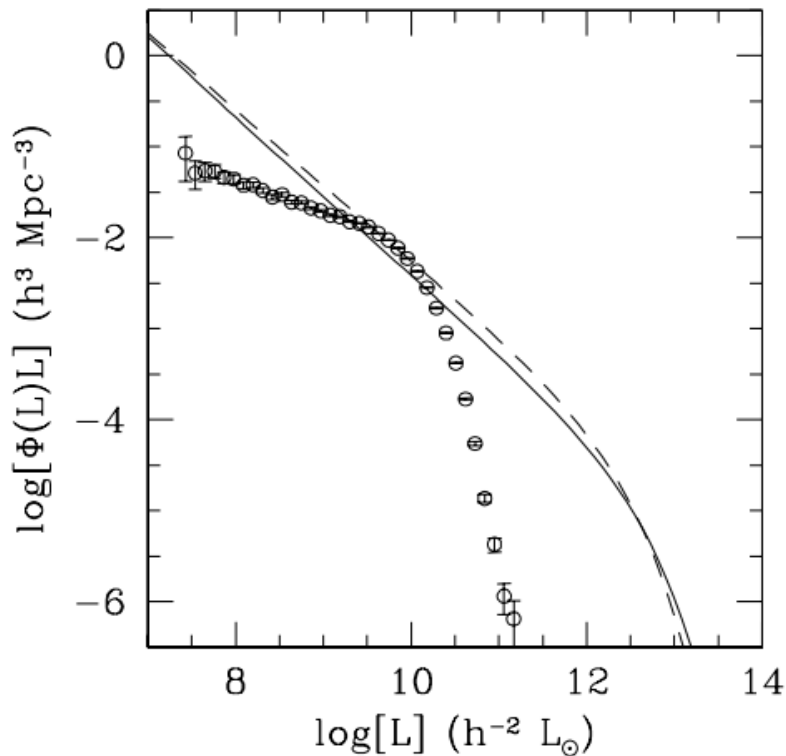


Figure 2.3: A comparison of the galaxy luminosity function with the halo mass function. Open circles with error bars correspond to the 2dFGRS (Norberg et al., 2002) luminosity function. Solid (dashed) lines correspond to the luminosity function that one would obtain from the Seth & Tormen (Press-Schechter) halo mass function under the assumption that each halo hosts exactly one galaxy with a mass-to-light ratio of $M/L = 100hM/L_{\odot}$. Note that the DM only prediction expects both too many faint and bright galaxies. This suggests that in reality the mass-to-light ratio decreases (increases) with mass at the low (high) mass end.

As a result of these various problems, different authors have attempted to explain these discrepancies by invoking physical mechanisms that produce or prevent star formation in the majority of the smaller and bigger halos, which, in turn, makes the DM substructures fainter or completely dark in the process. It has also been suggested that there is a problem with the Λ CDM model and that, some alternative cosmologies, such as warm dark matter, prevent the formation of the smallest haloes (e.g., Sommer-Larsen & Dolgov, 2001; Anderhalden et al., 2013).

The following Section will solely focus on the additional baryonic processes and the effects that they can have on the galaxies.

2.3 Including the Baryons into the Picture

DM is thought to only interact gravitationally with luminous matter (or at most very weakly electromagnetically). Therefore, it does on its own not provide a complete description of the Universe, especially at galaxy scales. The luminous matter is referred to as baryonic matter since leptons provide a negligible contribution to the total mass. As discussed in the Introduction a combination of experimental measures merge a picture in

which the matter content of the Universe is shared between DM ($\sim 84\%$) and the baryonic matter ($\sim 16\%$).

Including baryons into the theory of galaxy formation is very challenging because of the collisional nature of the baryonic matter as well as the complexity of the physics involved in the processes, that includes gas cooling and heating, star formation, feedback from stars and from the black hole, radiation, cosmic rays, to name a few (see Section 2.3.2 for more detail).

Numerical simulations have shown that the growth of a galaxy is coupled to the development of large scale structure, where the baryons are dragged along by the gravitationally dominant DM and eventually concentrate towards the deep potential wells of the DM halos forming a hot gaseous halo. While the collapse of DM halts as it reaches virial equilibrium in haloes, baryons can radiate away their binding energy, which allows them to collapse further and fragment into smaller structures, such as galaxies and stars. These galaxies then grow through mergers and gas accretion.

Gas falling towards a galaxy gains kinetic energy until it reaches the hydrostatic halo. If the infall velocity is supersonic, an accretion shock forms near the virial radius of the galaxy² and the incoming gas is heated up to the virial temperature of the halo. According to the simplest picture of spherical collapse onto the galaxy, all the gas in the DM halo is heated to the virial temperature of that halo and reaches a quasi-static equilibrium that is supported by the pressure of the hot gas before it is able to radiatively cool down and settle into a rotationally supported disc, where it can form stars (e.g., Rees & Ostriker, 1977; Fall & Efstathiou, 1980; Birnboim et al., 2007) This form of gas accretion onto the galaxy is also called *hot accretion* (Katz et al., 2003; Kereš et al., 2005).

Within some radius, the so called cooling radius, the cooling time of the gas is, however, shorter than the age of the Universe (see Section 3.4.1 for more detail).

Whether or not hot accretion is the dominant mode depends on the so-called cooling radius, where it lies with respect to the halo, and hence depends on the mass and redshift of the halo. For high mass halos, for instance, the cooling radius lies well inside the halo, which allows a quasi-static equilibrium to form and accretion on to the galaxy is regulated by the cooling function. For lower mass halos, on the other hand, the cooling radius is larger than the virial radius because of which no hot halo will form and the gas will not go through an accretion shock at the virial radius. Because gas accreted in this manner is never heated to high virial temperature, this mode is also referred to as *cold accretion* (Rees & Ostriker, 1977; Katz et al., 2003; Kereš et al., 2005). The accretion rate onto the central galaxy depends in this case on the infall rate, but not on the cooling rate (White & Frenk, 1991; Katz & Gunn, 1991).

Numerical simulations reveal a more complicated picture than just spherical accretion often assumed by analytic and semi-analytic studies of galaxy formation (e.g., Binney, 1977; White & Frenk, 1991; Birnboim & Dekel, 2003). As already discussed above, the DM collapses to form the cosmic web, a network of sheets and filaments, where the galaxies form within the densest regions, the haloes. These filamentary structures can have an important effect on gas accretion where galaxies can be fed by gas coming along the filaments. Because the average density of the accreting gas is higher in the filaments the cooling time will also be smaller and it will thus be easier to radiate away the gravitational binding energy. Filaments therefore feed galaxies preferentially through cold accretion. Both modes can however coexist. It has been shown, that especially at high redshift cold streams penetrate

²The virial radius is defined as the radius within which virial equilibrium holds, i.e., within which the potential energy of the system is equal to twice its kinetic energy in absolute value.

the hot virialised haloes of massive galaxies (Kereš et al., 2005; Dekel & Birnboim, 2006; Ocvirk et al., 2008; Kereš et al., 2009; Dekel et al., 2009).

Simulations have shown that cold mode accretion can be very efficient (e.g., Dekel & Birnboim, 2006; Behroozi et al., 2013) that in turn leads to galaxies with unrealistic high baryon fractions. However, accretion flows can be moderated or stopped by introducing very efficient outflows and feedback recipes (e.g., Dubois et al., 2010b; van de Voort et al., 2011; Dubois et al., 2013; Nelson et al., 2015; Hopkins et al., 2016). Also, some of the studies of cold streams are affected by numerical problems (see (e.g., Nelson et al., 2013)).

Section 2.3.1 will further explain how gas can radiatively cool and eventually form stars. Section 2.3.2 explains different feedback mechanisms as a possible solution to alleviate the problem of the excess baryons in the galaxies. And Section 2.3.3 will then compare hydrodynamical simulations employing such feedback recipes with observations. Finally, Section 2.4 will further focus on the feedback from SMBHs, the focus during this PhD thesis.

2.3.1 Physics of the Interstellar Medium

The entire luminous content of galaxies results from the cooling and fragmentation of gas within the potential wells of the DM haloes. Additionally, both observations and simulations of galaxies show that galaxy evolution is highly affected by how stars form, evolve, and die within the galaxy. The latter likely being the most important. In order to form stars, gas has to first lose its pressure support and collapse into dense molecular clouds where stars are formed.

Hence, the process of gas cooling (and heating) is a necessary and fundamental ingredient for stars to form and for the evolution of galaxies.

This Section will first revise how gas can cool (Section 2.3.1.1) before explaining how stars can be formed within the galaxy (Section 2.3.1.2).

2.3.1.1 Radiative Cooling and Heating

The baryons are coupled to the evolution of the large scale structure and finally concentrate towards the deep potential wells of the DM halos forming a hot gaseous halo. Unlike DM, baryons can radiate away their binding energy, allowing them to collapse further and fragment into smaller structures, such as galaxies and molecular clouds.

After virialisation, the gas can be in one of three regimes summarised below, with τ_{netcool} being the characteristic cooling time (fully defined in Section 3.4.1), $\tau_{\text{Hubble}} \equiv 14$ Gyr the Hubble time-scale, and τ_{dyn} the dynamical time of the system (the rotation time for a disc galaxy or free-fall time for a giant molecular cloud):

1. $\tau_{\text{netcool}} > \tau_{\text{Hubble}}$
The gas cannot cool, even on cosmological timescales and therefore not collapse. This regime is a good approximation to conditions inside massive haloes.
2. $\tau_{\text{Hubble}} > \tau_{\text{netcool}} > \tau_{\text{dyn}}$
With the cooling time being bigger than the dynamical time of the system the underlying gas distribution changes faster than the temperature of the gas. The gas cools

quasi-adiabatically meaning that at each time, the gas can return to a dynamic equilibrium and will maintain a constant Jeans length λ_J or Jeans mass M_J^3 , thus, the gas pressure forces and gravitational forces are in balance. With $M_J \propto \rho \lambda_J^3 \propto c_s \rho^{-1/2}$ (see Binney & Tremaine, 2008), where c_s is the sound speed of the gas and proportional to the temperature T we obtain $\rho \propto T^3$.

3. $\tau_{\text{Hubble}} > \tau_{\text{dyn}} > \tau_{\text{netcool}}$

Cooling occurs on a faster timescale than the system dynamically changes, and, hence, the temperature will change faster than the density, and the system can become unstable. For $\tau_{\text{dyn}} \gg \tau_{\text{netcool}}$, the cloud has no time to collapse and its mass eventually exceeds the Jeans mass. The system will fragment until the mass of the fragments is of the same order of the Jeans mass, where it is able to return to the previous, quasi-adiabatic state. This regime is important because the fragmentation of the gas is a necessary process to form stars.

There are different processes that cause astrophysical particles to radiate energy and with this the gas to cool. The main process that causes radiative cooling involves a combination of collisions between either electrons and ions, or electrons and photons. In the former case, the cooling rate is proportional to the density squared, since it describes the collision between two particles. In the latter case, the cooling rate is proportional to the gas density, since the number of particles that a photon may interact with increases linearly with density. In detail the different *cooling processes* are:

- *Collisional ionisation cooling*: Radiative losses from collisions between electrons and ions/atoms causing ionisation. Involved species are H, He, HeII, He (2^3 S).
- *Recombination cooling*: Radiative losses from collisions between electrons and ions recombining to form neutral/less ionised particles. Involved species are HII, HeII, and HeIII.
- *Dielectronic recombination (DR) cooling (He)*: Electrons are captured by ions (atom), and this capture is accompanied by excitation of an initially bound electron. Involved specie is HeII.
- *Collisional excitation cooling*: Radiative losses caused by electrons in atoms/ions radiating energy from excitation by collisions. Involved species are H (all n), HeII ($n = 2$), HeI ($n = 2, 3, 4$ triplets).
- *Bremsstrahlung cooling of all ions*: Radiation emitted by an electron being decelerated via electromagnetic interaction as it passes an ion. Involved species HII, HeII, and HeIII.
- *Compton cooling*: Low-energy cosmic microwave background photons remove energy from electrons via Compton-scattering.

On the other hand *heating processes* are:

- *Photoionisation*: External photons exciting and removing electrons from atoms/ions

³The Jeans mass is defined as the mass for which the internal gas pressure is not strong enough to prevent gravitational collapse of a region filled with matter. Structures above this mass are expected to collapse.

- *Compton heating*: Heating from background radiation if the gas temperature is lower than the CMB temperature (i.e., inverse Compton scattering for cooling process).

Both lists are adapted from Cen (1992), that also gives a detailed description of the construction of such a cooling model, in which the change in thermal energy and number density of electrons, helium, hydrogen, as well as ions due to various cooling processes is considered.

2.3.1.2 Star Formation

Star formation occurs in dense molecular clouds in regions where the density is about hundred particles per cubic centimetre and whose temperatures is around 10 K (Blitz, 1993; Williams et al., 2000). Hence, the overall star formation rate (SFR) of a galaxy is closely related to its ability to form such dense molecular clouds in the ISM. Observations show that the gas distribution is highly clumpy, where most of the gas is distributed over giant molecular clouds (GMCs), which have masses between $10^5 - 10^7 M_\odot$ and sizes over a few tens of parsecs. The GMCs have an approximated lifetime of around 10^7 yr (e.g., Leisawitz et al., 1989; Fukui et al., 1999). Compared to the lifetime of a galaxy such a time-scale is short and therefore if GMCs were only supported against gravitational collapse by thermal pressure, they would collapse and form stars in a free fall time

$$t_{\text{ff}} \propto \frac{1}{\sqrt{G\rho}} \simeq 3.6 \times 10^6 \text{yr} \left(\frac{n_{\text{H}}}{100 \text{cm}^{-3}} \right) \quad (2.16)$$

where ρ is their mean density and n_{H} is their number density.

The Jeans mass for a self-gravitating, homogeneous, isothermal sphere of gas is defined as

$$M_{\text{J}} = c_{\text{s}}^3 \sqrt{\frac{\pi^3}{G^3 \rho}} \simeq 40 M_\odot \left(\frac{c_{\text{s}}}{0.2 \text{km s}^{-1}} \right)^3 \left(\frac{n_{\text{H}}}{100 \text{cm}^{-3}} \right) \quad (2.17)$$

with c_{s} being the sound speed, and indicates that structures with masses above this mass are not pressure supported against gravitational collapse, and hence should collapse in a free-fall time. General GMCs have number densities of above 100cm^{-3} , that is several orders of magnitude bigger than their Jeans mass and are thus expected to collapse faster than the inferred lifetimes of GMCs.

Since turbulence and magnetic fields provide additional pressure support, they help stabilising the GMCs against gravitational collapse and, thus, are expected to play a significant role in star formation.

Therefore, star formation is deeply connected with the underlying density structure and the ability to form dense molecular clouds in the ISM. From observations we know that it is possible to relate the amount of newly formed stars to the amount of local gas, also known as *Kennicutt relation* (Kennicutt, 1998a)

$$\Sigma_* = 2.5 \times 10^{-4} \frac{\Sigma_{\text{g}}^{1.4}}{1 M_\odot \text{pc}^{-2}} M_\odot \text{kpc}^{-2} \text{yr}^{-1} \quad , \quad (2.18)$$

where Σ_* is the surface density of star formation and Σ_{g} the gas surface density. The Kennicutt (1998) star formation relation is generically fit by

$$\Sigma_* = \epsilon \frac{\Sigma_{\text{g}}}{t_{\text{dyn}}} \quad , \quad (2.19)$$

for theoretical and observational reasons (Elmegreen, 1997; Silk, 1997; Genzel et al., 2010b). In equation (2.19), ϵ is a dimensionless normalisation constant, and t_{dyn} is the dynamical time (the rotation time for a disc galaxy or free-fall time for a giant molecular cloud). This simple relation fits surprisingly well observations over several orders of magnitude in both quantities (Krumholz et al., 2012, and references therein), and with the same normalisation for global galaxies (including high redshift ones, Genzel et al., 2010b) to molecular clouds (Heiderman et al., 2010; Lada et al., 2010) as well as in the nearby M51 galaxy (Kennicutt et al., 2007).

The normalisation ϵ is a measure of the star formation efficiency, often defined as the fraction of gas turned into stars per dynamical time and is usually of order a few percent ($\epsilon \sim 0.01 - 0.02$; Krumholz & Tan, 2007).

2.3.2 Feedback Processes

With the assumption that light traces mass, the galaxy luminosity function obtained from observations can be compared with the theoretical prediction of the halo mass function. The comparison shows that theory over-predicts both the low and high mass end of the luminosity function. Therefore, the models predict too many small and big galaxies in the nearby Universe. Additionally, they predict too few massive galaxies at high redshift, and too many baryons within the galaxy halos. Furthermore, there are also structural problems, where for example the cuspleness of DM is found to be excessive in dwarf and barred galaxies (e.g., Moore, 1994; Navarro et al., 1997) or galaxies have too massive bulges, and/or are not extended enough. The latter has to do with the fact that stars are forming too efficiently early in the process of galaxy formation (Brook et al., 2011). The early formation of stars, especially near the centres of the host halos, ensures that a large amount of mass is locked up in low angular momentum material that in turn prevents the formation of an extended thin, Milky-Way like galaxy. The same can be said for elliptical galaxies where observations of distant galaxies revealed that these massive galaxies were more compact in the past (e.g., Daddi et al., 2005; Trujillo et al., 2006). Here, late dry minor mergers are thought to be the important mechanism for growing the galaxy sizes as fast as found in the observations (e.g., Naab et al., 2009; Dubois et al., 2013, 2016; Oser et al., 2010, 2012).

A solution to all these difficulties likely lies in feedback, that slows down the collapse of gas into galaxies, dense substructures, and eventually stars. There is a vast range of different feedback mechanisms from various physical processes such as reionisation at very high redshift, supernova (SN) explosions from massive stars, radiation from young stars, tidal and ram pressure stripping, cosmic rays, and the effect of the energy release from the accretion discs of supermassive black holes, also called active galactic nuclei (AGN) feedback:

- *The UV background*, which reionised the Universe at $z > 6$, heats the intergalactic gas and is argued to be effective at halting or preventing star formation, mostly in low mass galaxies, using analytical arguments, observations, N -body simulations, and semi-analytic models (e.g., Benson et al., 2002; Somerville, 2002; Benson et al., 2003; Kravtsov et al., 2004; Moore et al., 2006; Madau et al., 2008; Muñoz et al., 2009; Macciò et al., 2010; Busha et al., 2010). The gas in these halos is photo-evaporated after reionisation. The effect of the UV background on the evolution of galaxies and whether or not reionisation is effective in suppressing star formation in low-mass halos is still subject to debate (e.g., Scannapieco et al., 2011; Wadepuhl &

Springel, 2011; and references therein). To further complicate the picture, the extent of the epoch of reionisation itself is also poorly constrained, with only a lower limit of ($z > 6$) on its completion provided by observations (e.g., Cen et al., 2009; Mesinger & Furlanetto, 2009).

- *Stellar feedback* from massive stars are found to significantly affect the ISM by regulating star formation (Mac Low & Klessen, 2004; McKee & Ostriker, 2007; and references therein), driving turbulence (Kim et al., 2001; de Avillez & Breitschwerdt, 2004; Joung & Mac Low, 2006; Agertz et al., 2009; Tamburro et al., 2009), and generating galactic outflows (Martin, 1999; Oppenheimer & Davé, 2006). The galactic winds driven by stellar feedback have been proposed by Dekel & Silk (1986) to be responsible for the suppression of star formation by removing the gas from the galaxies and hence reducing the amount of baryons available to form stars (see also Efstathiou, 2000). Over the last few years there has been an intense effort in incorporating and model these processes in cosmological simulations (e.g., Dubois & Teyssier, 2008b; Scannapieco et al., 2008; Agertz et al., 2009; Joung et al., 2009; Governato et al., 2010; Teyssier et al., 2013; Kimm et al., 2015). However, SN feedback has not only proven to be challenging to model but the results are generally mixed. The contradictions between the different studies find their origin in the different numerical recipes, spatial and/or mass resolution adopted in the models, along with the variety of galaxy masses and merger histories (see Scannapieco et al., 2011 for more detail). It is, therefore, still unclear to what extent SNe impact the star formation in low-mass (but also high mass) galaxies.

Additionally, *Cosmic Rays* (CRs) are thought to originate from SNe, that are thought to strongly interact with the magnetic field and exchange energy until equilibrium is reached. In the galactic disc there is rough equipartition of the magnetic and CR energy density (e.g., Beck & Krause, 2005). This indicates that CRs plays a role in the dynamics of the ISM. Although the energy injection rate of CRs is small compared to other sources of energy as for instance from stars, the rate at which they inject momentum is not. Theoretical models of dynamical halos in which CRs diffuse and are advected out in a galactic wind predict steady, supersonic galaxy-scale outflows driven by a combination of CRs and thermal pressure (e.g., Breitschwerdt et al., 1991; Everett et al., 2008). Socrates et al. (2008) show that the luminosity of a star-forming galaxy can be significantly reduced by the production and subsequent expulsion of cosmic rays from its ISM. On similar lines Booth et al. (2013); Salem et al. (2014); Girichidis et al. (2014); Salem et al. (2016) additionally show that CRs are able to drive winds and that by including CR feedback they are able to better reproduce observations.

- Along with SN feedback, *radiation* from young massive stars is also found to have an impact on the evolution of star-forming regions, both in low and high mass galaxies (see Roškar et al., 2014; Hopkins et al., 2011, 2015). There are mainly three radiative feedback processes from stars: (I) photoionisation heating of gas, (II) direct pressure from ionising photons, and (III) indirect pressure from reprocessed, multi-scattering, infrared (IR) photons. Generally, the winds generated by radiation from stars are thought to have an impact on the evolution of the star-forming regions. Because the massive stars only live for a few Myrs, they travel less far from their birthplace, hence emit the radiation closest to where they were formed, and thus directly af-

fect the ability of these regions to form more stars. Murray et al. (2010) argued that the UV radiation, converted into far infrared radiation by scattering on dust, can provide enough momentum to the surrounding gas to dissolve giant molecular clouds (GMCs) on even significant shorter timescales than required by SN feedback alone. Further, they argued that the radiation pressure can form cold gas outflows at the escape velocity of the host halo (Murray et al., 2011). Roškar et al. (2014) found, that while radiative feedback appears as a viable mechanism to regulate the stellar mass fraction in massive galaxies, it also prevents the formation of discs with reasonable morphologies (thin discs). However, simulations by Rosdahl et al. (2015) using radiative hydrodynamics suggest that radiation feedback is more gentle and less effective than assumed in subgrid prescriptions. As the other descriptions above, the exact effect of radiation from young stars on the evolution of galaxies is still part of active research.

- *Ram-pressure stripping* happens as a satellite passes through the hot halo gas. While doing so the incident gas pressure becomes stronger than the gravitational force of the satellite, and gas is removed in the process. *Tidal stripping* occurs when a satellite halo hosting a galaxy orbits close to a larger host galaxy and the tidal forces become sufficiently strong to remove material. Unlike other feedback mechanisms, this is the only one that can also remove DM and stars, besides gas from the subhalo. Cooper et al. (2010) argue that in order to match the observed surface brightness and velocity dispersion profiles the satellite galaxy suffered from substantial tidal stripping and Klimentowski et al. (2010) found that tidal stripping determines a subhalo baryon content and final morphology. Fattahi et al. (2016) argue along similar lines. Mayer et al. (2006) pointed out the importance of a simultaneous interplay between ram pressure and tidal stripping. In their simulations, tidal forces excite star formation and thus stellar feedback, as well as reshaped the gas distribution so that it can be more easily stripped due to ram pressure. They argued that, together with stellar feedback, ram pressure stripping is needed to entirely remove the gas component within the satellite halo. A similar conclusion was found by Nickerson et al. (2011).
- While the above explained feedback mechanism are most efficient in low-mass, dwarf galaxies, active galactic nuclei (AGN) feedback from supermassive black holes (SMBHs) is advocated to provide an effective feedback mechanism for high-mass galaxies. SMBHs are thought to be ubiquitous at the center of local galaxies (e.g., Magorrian et al., 1998; Hu, 2008; Kormendy & Ho, 2013) and rapid gas accretion onto the black holes (BHs) lead to energy release capable of driving outflows that regulate star formation and the baryonic content of galaxies (Silk & Rees, 1998) and thus their own growth and that of the surrounding galaxy (Kormendy & Ho, 2013). AGN feedback can operate in *quasar-mode* from radiation at high accretion rates, or *radio-mode* from AGN jets at predominantly low accretion rates (Churazov et al., 2005; Russell et al., 2013a). The photons emitted by a quasar eventually couple to the gas and drive large-scale winds.

Both semi-analytical models (e.g., Croton et al., 2006; Bower, 1991) and hydrodynamical simulations (e.g., Di Matteo et al., 2005, 2008; Sijacki et al., 2007; Dubois et al., 2012a) argued that AGN feedback is an important ingredient in the formation and evolution of massive galaxies and is, in particular, capable of suppressing star formation in order to reproduce the observed high-end tail of the galaxy luminosity

function. Although the general picture of BHs exerting strong feedback on their host galaxies is very attractive, the details remain vague, primarily because the coupling mechanism between the AGN and the ISM of the host galaxy is unknown.

Over the last three years, my research focused on the interactions between the AGN outflows and the ISM, how the feedback impacts the host galaxy, and the communication mechanism of the AGN with the galaxy's gas. Because of this, Section 2.4 will focus in more detail on AGN feedback.

2.3.3 Comparing Hydrodynamical Simulations with Observations

As discussed above, one particular issue of a galaxy formation theory employing only DM is that they overproduce the stellar content of the low and high mass galaxies (see Section 2.2.1). This has motivated the community to advocate feedback processes, such as those from SNe and AGN.

Indeed, simulations have shown that feedback from both SNe and BHs, acting as a general heating mechanism, can prevent the formation of too many stars and regulates the assembly of a galaxy. Such feedback mechanisms have, thus, emerged as a crucial ingredient of any successful galaxy formation simulation (e.g., Di Matteo et al., 2003, 2005; Springel et al., 2005a; Governato et al., 2007; Scannapieco et al., 2008; Jubelgas et al., 2008; Dubois & Teyssier, 2008b; Scannapieco et al., 2009; Ceverino & Klypin, 2009; Joung et al., 2009; Booth & Schaye, 2009; Colín et al., 2010; Sales et al., 2010; Stinson et al., 2010; Fabjan et al., 2010; Wadepuhl & Springel, 2011; Dubois et al., 2012a).

Despite this progress, there are still some remaining difficulties. For example, simulations including subgrid feedback models have still too many stars forming in the galaxies (e.g., Guo et al., 2010), or the produced mass function had the wrong shape and normalisation, and the galaxies were too massive and too compact. In addition, stars form too early and the stellar disc is often too concentrated, with steeply declining rotation curves that did not agree with observations (e.g., Abadi et al., 2003a,b; Stinson et al., 2010). Furthermore, the models were not able to simultaneously reproduce the stellar masses and the thermodynamical properties of the gas in groups and clusters (e.g. Scannapieco et al., 2012 and references therein for a detailed discussion).

Such difficulties have led to little consensus on what determines the morphology of a galaxy, what the main feedback mechanisms are, and what their roles on different mass scales and at different times are. An ongoing debate is whether the difficulties in reproducing realistic discs are predominantly a consequence of insufficient numerical resolution (see Governato et al., 2004), or inappropriate modelling of the relevant physics (e.g., Mayer et al., 2008; Piontek & Steinmetz, 2011), or actually a failure of the cosmological model (e.g., Sommer-Larsen & Dolgov, 2001).

Because of this, semi-analytical models (e.g., White & Rees, 1978; White & Frenk, 1991; Kauffmann et al., 1993; Hatton et al., 2003; Baugh, 2006; Benson, 2012) have for a long time become the method of choice to compare observations and theory (see Cooray & Sheth, 2002; Baugh, 2006 for reviews). They have been successful in reproducing many properties of galaxies over some fraction of the age of the Universe. Thanks to the inclusion of more detailed numerical simulations, and empirical calibrations from data, the semi-analytical approach offers a flexible and relatively computationally inexpensive way to probe the phenomenology of galaxy formation as well as the theoretical analysis and interpretation of large surveys (e.g., Cole et al., 2000b; Hatton et al., 2003; Bower et al., 2006; Somerville et al., 2012).

However, hydrodynamical simulations have a number of important advantages over the semi-analytical approaches. While they are computationally more demanding than the semi-analytical approach, these simulations evolve DM and baryons self-consistently, and hence include automatically the back-reaction of the baryons on the collisionless matter, both inside and outside of haloes. Furthermore, the higher resolution description of the baryonic component in hydrodynamical simulations allow for predictions of the baryonic distribution within galaxies and a more detailed discussion and comparison with observations.

Because of these advantages, new large-scale hydrodynamical simulations have attempted to employ strong feedback subgrid models and better resolution than previous studies. The idea is that, with a better reproduction of the observations, the simulations can be used as a self-consistent study of galaxy formation and evolution, as well as making predictions for the next generation of galaxy surveys. The use of large-scale cosmological hydrodynamical simulations is to model not only the galaxies but also their surroundings, the intergalactic medium (IGM), at the same time. This is important, because the inclusion of the environment of a galaxy might be critical for a better understanding of the different feedback cycles. Additionally, the box sizes of the current generation of cosmological simulations (~ 100 Mpc) offers detailed survey-scale predictions that can be compared to galaxy surveys across a large fraction of cosmic time. These recent state-of-the-art hydrodynamical simulations include Horizon-AGN (Dubois et al., 2014), Illustris (Vogelsberger et al., 2014), MassiveBlack-II (Khandai et al., 2015a), and Eagle (Schaye et al., 2015), and all employ stellar and AGN feedback, where the exact implementation varies.

The different simulations were compared to galaxy properties in order to establish whether they provide a reliable framework for interpreting current and future observational datasets. Most notably, the stellar mass functions have been compared with observations at both high and low redshift. Figure 2.4 shows a comparison of the predicted stellar mass function of the Horizon-AGN simulation (Dubois et al., 2014) to observational data in the redshift range $0 < z < 6$ (Kaviraj et al., 2016). Across the redshift range shown, the Horizon-AGN produces good agreement with the observations, indicating that model galaxies within the simulation broadly reproduces the cosmic star formation history in the real Universe. Note that, in this simulation only the BH feedback parameters were tuned to reproduce the local $M_{\text{BH}}-\sigma$ relation. Apart from this, none of the other feedback parameters were calibrated. However, there remains two points of tension worth noting. First, the model tends to overproduce low mass galaxies at all epochs, which may be because the stellar feedback prescriptions used do not succeed in a quenching of star formation in the small halos. And secondly, at high redshift the simulation predicts too low galaxy stellar masses, across the mass range shown.

Left panel of Figure 2.5 shows a comparison of stellar mass function of the EAGLE reference simulation (Schaye et al., 2015) with observations from the Galaxy And Mass Assembly (GAMA) survey (Baldry et al., 2012; open circles) and from SDSS (Li & White, 2009; filled circles). Since the observables of the galaxy luminosity function were used for the calibration of the subgrid models for the feedback in the EAGLE simulation, their simulation data manages to fit, by design, the observed stellar mass functions.

The right panel shows a comparison of the stellar mass function from the Illustris simulation (Vogelsberger et al., 2014) with current observations (Moustakas et al., 2013; Bernardi et al., 2013) based on data from SDSS, and the PRISM Multi-object Survey (PRIMUS) (Coil et al., 2011; Cool et al., 2013). Similar to the Horizon-AGN simulation, only the BH feedback parameters were tuned to reproduce the local $M_{\text{BH}}-\sigma$ relation and apart from this, none of the other feedback parameters were calibrated.

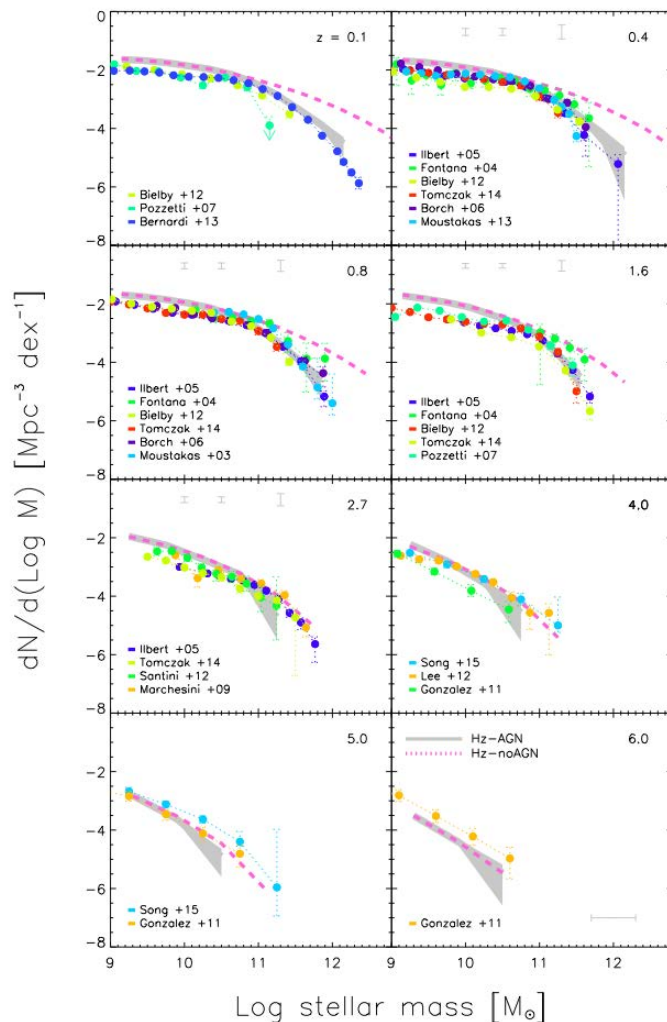


Figure 2.4: Comparison of the predicted stellar mass function from the Horizon-AGN simulation (grey shaded region; Dubois et al., 2014) to observational data (indicated in the legend) in the redshift range $0 < z < 6$. The pink dashed lines indicate predictions from the Horizon-noAGN simulation, a simulation with the same initial condition but without BHs. The observational uncertainties due to cosmic variance is indicated with vertical error bars. The horizontal error bar (0.3 dex) indicates typical observational uncertainties in stellar masses derived from SED fitting. Across the redshift range shown, the Horizon-AGN simulation produces good agreement with observations, indicating that the model galaxies within the simulation broadly reproduce the cosmic star formation history in the real Universe. The picture is taken from Kaviraj et al. (2016).

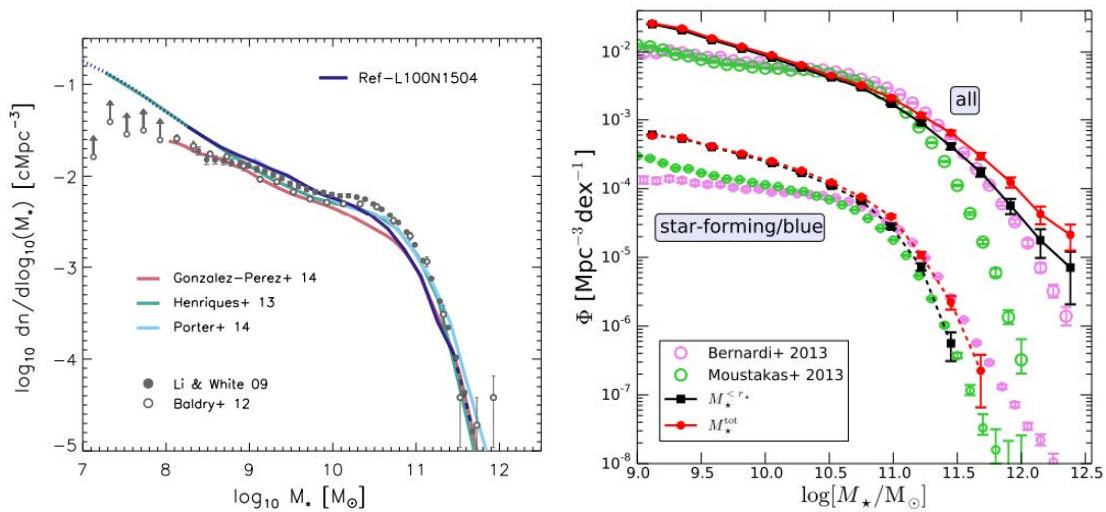


Figure 2.5: *Left*: Comparison of the predicted stellar mass function from the EAGLE simulation (dark blue line; Schaye et al., 2015) to observational data of the GAMA survey (open circles; $z < 0.06$; Baldry et al., 2012) and SDSS (filled circles; $z \sim 0.07$; Li & White, 2009) at redshift $z = 0.1$ and semi-analytic models (indicated in the Legend). The agreement with data is relatively good for both EAGLE and the semi-analytic models. The picture is taken from Schaye et al. (2015). Note, however, that the feedback recipes in the EAGLE simulation are also tuned to match exactly the galaxy luminosity function. *Right*: Comparison of the galaxy stellar mass function from the Illustris simulation (solid black and red line; Vogelsberger et al., 2014) compared to observationally derived values (Moustakas et al., 2013; Bernardi et al., 2013). The stellar mass function is shown using two measurements of stellar mass: total stellar mass excluding satellite contributions (red line) and the central stellar mass (black line) to compare with observations which are uncertain to the massive end. The Illustris simulation manages to well reproduce the galaxy luminosity function for the mid to high mass galaxies. There are still some discrepancies in the low mass region related to the stellar content of the low mass galaxies and some slight discrepancies for the massive galaxies. However, similar to the Horizon-AGN simulation, ‘only’ the efficiency parameter of the BH feedback is tuned to match global observations.

It is apparent that the three large-scale cosmological simulations all succeed in reproducing the shape and normalisation of the observed stellar mass functions. For the Illustris simulations there are still some discrepancies related to the stellar content of the low mass galaxies and some slight discrepancies for the massive galaxies, that requires further investigation.

Finally, the left panel of Figure 2.6 shows a comparison of the different stellar mass functions from different large cosmological hydrodynamical simulations EAGLE (Schaye et al., 2015), Oppenheimer et al. (2010), Puchwein & Springel (2013), the Illustris simulation (Vogelsberger et al., 2014, data taken from Genel et al., 2014), and the MassiveBlack-II simulation (Khandai et al., 2015b) with the GAMA and SDSS observations (picture taken from Schaye et al., 2015). The differences between the models stem from the implementations of the feedback recipes, number of tuned parameters, choices of what the parameters were tuned to, slightly different resolutions, as well as numerical techniques to model the hydrodynamics. A detailed discussion is however beyond the scope of this thesis.

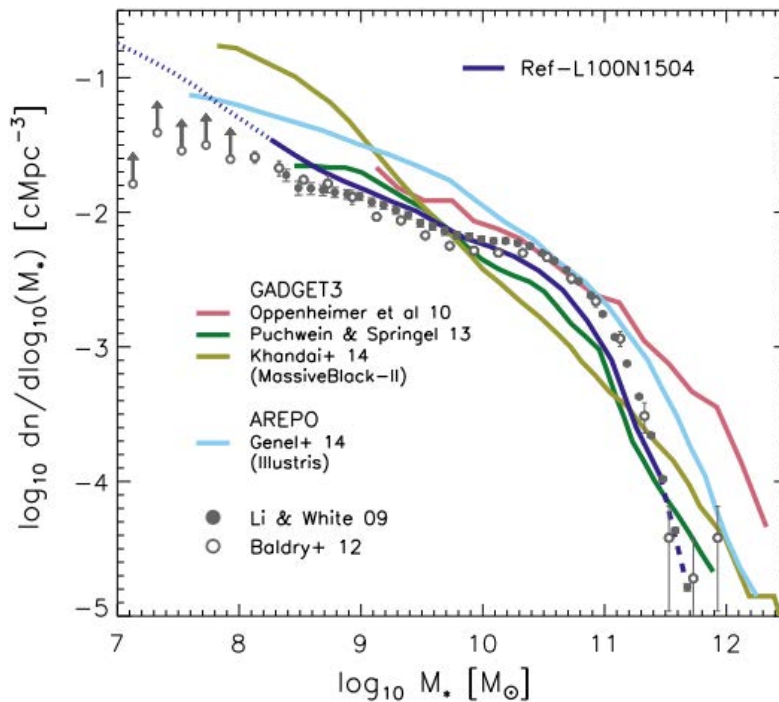


Figure 2.6: Comparison of the predicted stellar mass function of different large scale hydrodynamical simulations noted in the legend. In the left panel they are also shown in comparison with observations. Except for Oppenheimer et al. (2010), all simulations include AGN feedback. Apart from MassiveBlack-II, all models were calibrated to the data, albeit the number of tuned parameters differs between different models (see text for more detail). The comparison shows that differences arise due to different implementations of feedback recipes, different number of tuned parameters, as well as different numerical techniques to model the hydrodynamics.

Because these state-of-the-art large-scale hydrodynamical simulations have now progressed to a state where they approximately reproduce the observed stellar mass functions from high to low redshifts along with a number of other key observations such as, star formation histories and star formation main sequence, they, now, allow for a self-consistent study of galaxy evolution over cosmic time. In addition, they also allow predictions for the next generation of galaxy surveys. With this motivation, various observations have been compared with the large-scale cosmological simulations mentioned above. Such as, the morphologies of the galaxies (e.g., Snyder et al., 2015; Dubois et al., 2016) or the stellar mass assembly (e.g., Rodriguez-Gomez et al., 2016; Kaviraj et al., 2016; Lagos et al., 2016). Additionally, the simulations now allow to better understand observations and their limitations. For example, the contamination to weak gravitational lensing from intrinsic alignments (e.g., Chisari et al., 2015; Tenneti et al., 2015b,a; Velliscig et al., 2015; Chisari et al., 2016; Hilbert et al., 2016), or the effect of baryons on redshift space distortions and cosmic density (e.g., Hellwing et al., 2016). Furthermore, they also provide the necessary accuracy to revisit theoretical models of, for example, reionisation (e.g., Bauer et al., 2015; Sharma et al., 2016b,a), and the evolution of black holes over the cosmic time (e.g., Sijacki et al., 2015; Volonteri et al., 2016; Rosas-Guevara et al., 2016). However, a detailed discussion is beyond the topic of this thesis and the reader is referred to the corresponding publications.

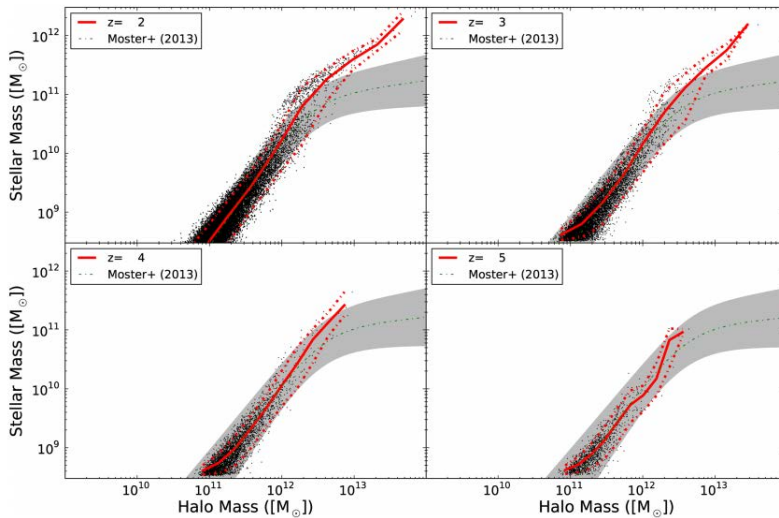


Figure 2.7: Stellar-halo mass relation at different redshifts. The green line is the expected relation between the total (gas + stars + DM) halo mass and the stellar mass, obtained by abundance matching techniques by Moster et al., (2010), with the scatter (grey shaded area) derived for the relation. The black points are simulated galaxies from a cosmological volume simulation by Kannan et al., 2014. The red lines trace the mean of the distribution and the red dotted lines indicate the 10 and 90 percentile limits of the distribution. The simulated galaxies, using a subgrid recipe for SN feedback, match the relation below $M_h < 10^{12} M_\odot$, but star formation is too efficient in the high-mass haloes because of the lack of AGN feedback.

2.4 Active Galactic Nuclei

Feedback processes, such as UV heating, SN feedback, and radiation from young stars, discussed above, have only a small impact on the formation of massive galaxies, mostly because of the deeper potential wells of the massive galaxies that do not let the gas escape. For instance, feedback from SN explosions fails to stop the flowing of cold gas towards the centre of the galaxies (Powell et al., 2011). The gas that is pushed away due to the SNe tends to only modestly interact with the cold infalling gas, hence, SN feedback is unable to prevent the formation of too many stars within the massive galaxies. This is exemplified in Figure 2.7 comparing the relation between the stellar mass (from galaxy luminosity) and total halo mass (M_h). The simulated galaxy data by Kannan et al., 2014, obtained with a cosmological hydrodynamical simulation including a subgrid recipe for SN feedback but no BH feedback, is compared with the expected relation derived by Moster et al. (2010). The expected relation is obtained by *abundance matching* techniques, i.e., by ranking BH halo masses, from cosmological simulations, and luminosities, from observations, and pairing them in the same order. It shows that for high mass galaxies (e.g., galaxies with a DM halo mass above $10^{12} M_\odot$) SN feedback is unable to prevent the formation of stars and star formation is too efficient.

A clue towards a solution to these problems comes from supermassive black holes (SMBHs) that are found at the centres of most, if not all, massive galaxies (e.g., Magorrian et al., 1998; Hu, 2008; Kormendy et al., 2011). Scaling relations over several orders of magnitude have been identified between the BH masses and the large-scale properties of the host galaxy, such as the relation of the SMBH mass to bulge mass, luminosity, and velocity dis-

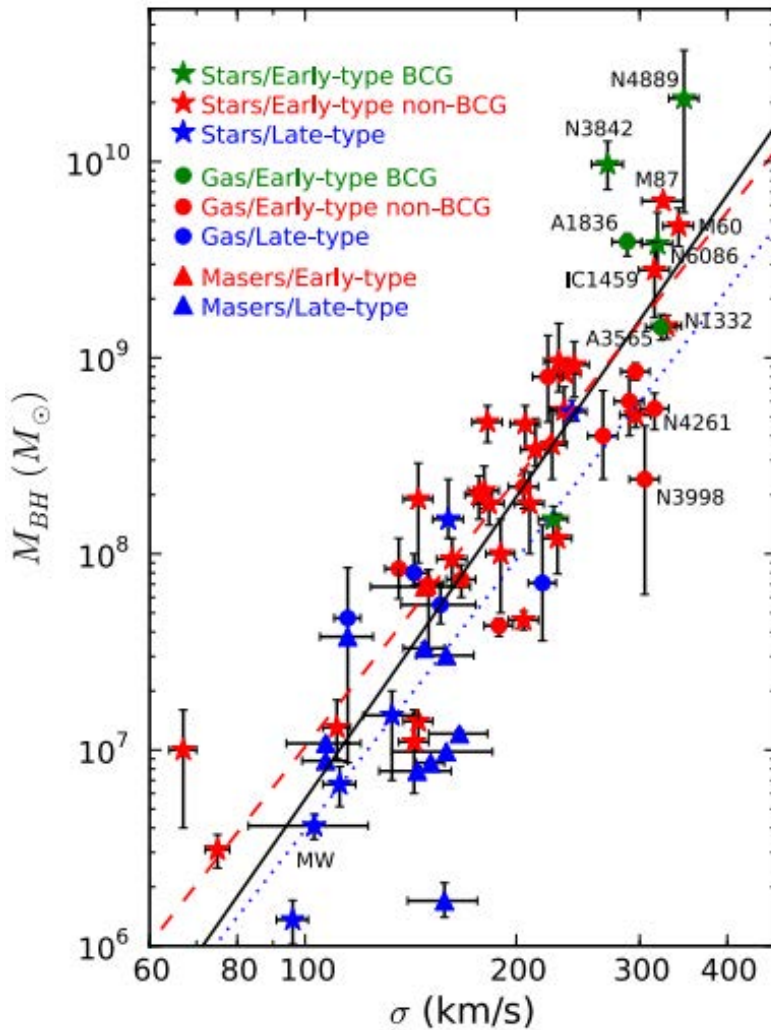


Figure 2.8: BH mass as a function of spheroid velocity dispersion (luminosity-weighted within one effective radius). The small scatter in this correlation, over several orders of magnitude, point towards a co-evolution between the BHs and their host galaxies. Figure taken from McConnell et al. (2011).

persion (Magorrian et al., 1998; Ferrarese & Merritt, 2000; Gebhardt et al., 2000; Aller & Richstone, 2007; Hopkins et al., 2007; Feoli & Mancini, 2009; Kormendy et al., 2011; for a review see Kormendy & Ho, 2013). An illustration of the BH mass and velocity dispersion is shown in Figure 2.8. The small scatter in these correlations (relative to other galaxy properties; Hopkins et al., 2009; Kormendy & Ho, 2013) point towards a co-evolution between the BHs and their host galaxies (see Heckman & Kauffmann, 2011 for a review) and suggest that the growth of BHs and large-scale structures are tightly linked.

Active Galactic Nuclei (AGN), that are powered by accreting BHs and release a fraction of the rest-mass accreted energy back into the galactic gas are thought to play the role of regulating the BH growth itself, but also the baryonic mass content of the massive galaxies (Silk & Rees, 1998, and Silk, 2011 for a review). It has been suggested (Binney & Tabor, 1995) that the energy release from the BH regulates accretion from the ambient gas onto the BH, leading to an oscillation-type feedback cycle (Novak et al., 2012a): Rapid gas

accretion onto the BH, triggered by some process, fuels BH growth and leads to the release of part of its binding energy into the surrounding gas. Due to a variety of physical processes including, radiation pressure on dust and lines, magnetic processes, and Compton heating (see e.g., Blandford & Znajek, 1977; Blandford & Payne, 1982; Begelman, 1985; Chang et al., 1987; Murray & Chiang, 1995; Murray et al., 2005; Silk, 2005; Tortora et al., 2009; McKinney et al., 2012), a high velocity outflow driven from the gaseous accretion disc develops. Having pushed out a fraction of its fuel supply, the energy fades and allows the BH to again accrete more gas.

Both semi-analytical models and numerical simulations (e.g., Croton et al., 2006; Bower et al., 2006; Di Matteo et al., 2005, 2008; Dubois et al., 2010b) have shown that negative AGN feedback is an important ingredient in the formation and evolution of massive galaxies, in particular in shaping the observed high-end tail of the galaxy mass function, and the low SFRs in massive galaxies. Moreover, observations show that cooling flows in the hot circumgalactic and intracluster media can be suppressed by the energy transferred by AGN jets (Bîrzan et al., 2004; Dunn et al., 2005), again negatively impacting star formation. Other potential roles of AGN feedback include the morphological transformation between spirals and ellipticals (e.g., Dubois et al., 2013, 2016; Welker et al., 2015), where AGN feedback leads to regulation of the thermodynamical properties of the intercluster medium (e.g., Sijacki et al., 2007; Puchwein et al., 2008; McCarthy et al., 2010; Gaspari et al., 2011; Teyssier et al., 2011; Martizzi et al., 2012; Planelles et al., 2014).

Because of the close connection between the massive galaxy and the BH, reconstructing the growth of the BH through the history of accretion onto the BH, as well as establishing the effect of AGN feedback onto the gas distribution within the galaxy, is of key importance to massive galaxy evolution. However, both processes are still not fully understood. For instance, it is still unclear how exactly the photons couple to the gas and drive a large scale wind. Mainly because this coupling conceals complex physics about optical depth of the gas, amount of dust, and self-shielding.

Section 2.4.1 discusses the observational features and nature of AGN and Section 2.4.5 will discuss in which situations AGN feedback is expected to exert *negative* or *positive* feedback on their surroundings. The former describes cases where AGN inhibits star formation by heating and dispersing the gas in the galaxy, while the latter describes the possibility that AGN may trigger star formation. Chapter 4 discusses how this positive feedback effect, triggered by AGN outflows (e.g., Silk, 2005; Zubovas et al., 2013a), has been proposed as a possible explanation of the remarkably high star formation rates in the high-redshift Universe (e.g., Drouart et al., 2014; Piconcelli et al., 2015; Rodighiero et al., 2015).

2.4.1 Classification of AGN

In AGN the central black hole accretes matter, giving rise to a number of phenomena which historically resulted in different AGN classes that will be revised in this Section.

The two largest groups of active galaxies are *Seyfert galaxies* and *quasars*. Seyfert galaxies show a bright point-like nucleus in the optical with a luminosity comparable with the host galaxy. Their even more luminous counterparts are the quasars, where the active nucleus outshines the galaxy making them appear star-like at large distances (hence the name quasar from quasi star). Both show an unusually blue continuum with a strong broad and narrow line emission, referred to as ‘type I’, or only a narrow emission lines, referred to as ‘type II’. Another class was added when Baade & Minkowski (1954) identified the bright radio source Cygnus A that shows one of the strongest radio sources in the sky,

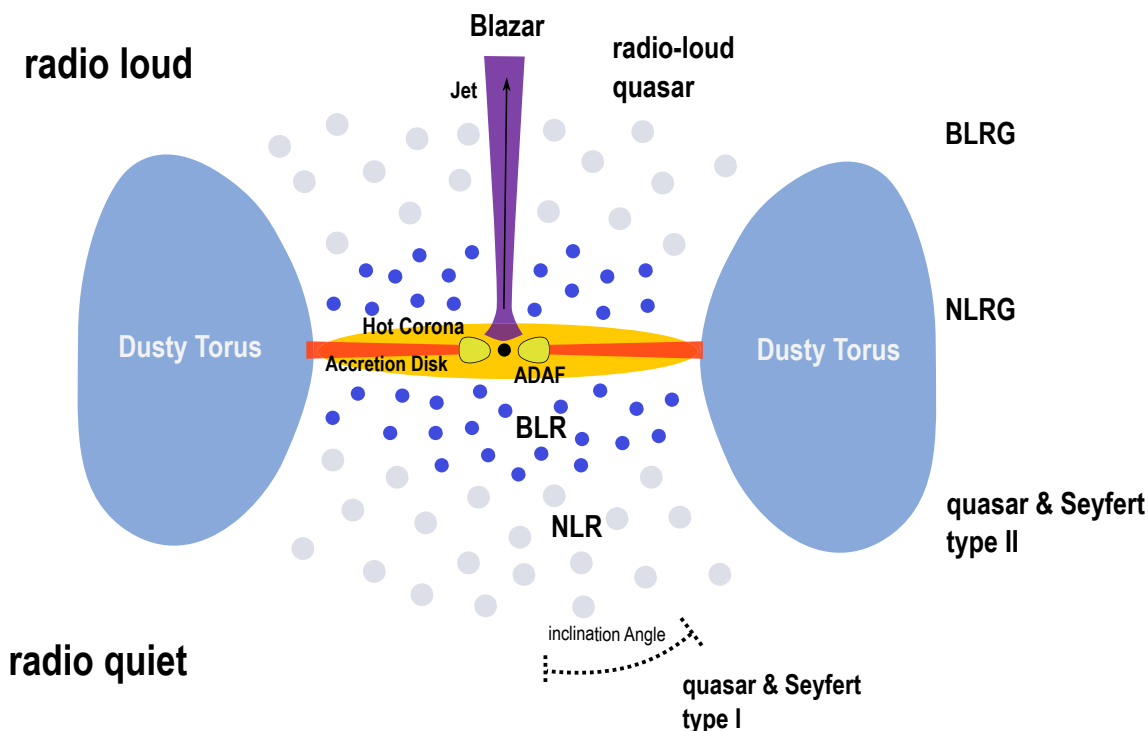


Figure 2.9: The AGN paradigm according to the unified model. The central BH is surrounded by a thick accretion torus (ADAF) and a thin standard accretion disc. A dusty torus emitting at infrared wavelengths is located further out. The emitting clouds of the narrow-line region (NLR) are visible at all inclination angles, whereas the broad-line region (BLR) is obscured by the dusty torus for larger inclinations. The lower half describes radio-quiet AGN, whereas the upper half corresponds to radio-loud AGNs. Note that if a jet is present, it would extend in *both* directions. The Figure is not drawn to scale. Figure is adapted from PhD Thesis of Volker Gaibler.

hence, also referred to as *radio galaxies*. The strong radio emission in these galaxies, can be separated into two strong radio-emitting regions around the galaxy as well as a compact core in the centre of the galaxy in high resolution data.

However, the detection of broad emission lines in the polarised light of type II Seyfert galaxies (Antonucci & Miller, 1985) indicated that the two types are not distinct classes but may rather result from different viewing angles on the exact same objects, if the polarised light is interpreted as scattered light. This ultimately led to the development of the *unified model* (Barthel, 1989; Antonucci, 1993; Urry & Padovani, 1995), which explains most of the different AGN classes due to different viewing angles. Additionally, they include *radio-loud* and *radio-quiet* objects, depending on whether a prominent (radio-emitting) jet is present. Figure 2.9 shows a sketch of the basic constituents of an AGN according to the unified scheme.

At the center of the galaxy resides the BH with a Schwarzschild radius

$$r_S \approx 10^{-4} \text{pc} \left(\frac{M_{\text{BH}}}{10^9 M_{\odot}} \right) . \quad (2.20)$$

Surrounding the BH is a rotating disc of gas called the *accretion disc*. Rapid accretion of this gas onto the BH leads to an optically thick but geometrically thin standard accretion disc (Shakura & Sunyaev, 1973), which extends out to $\sim 100 r_S$. For low accretion rates

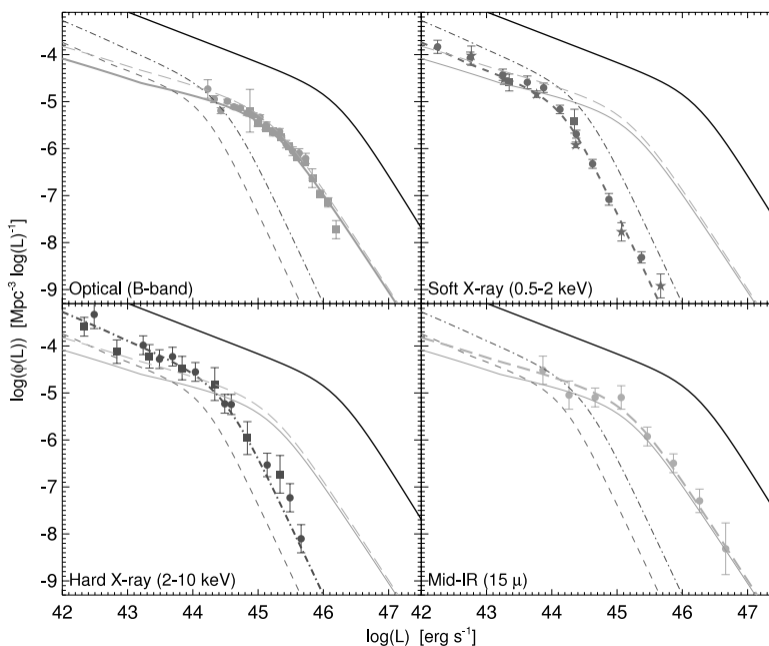


Figure 2.10: Quasar Luminosity Function (QLF) at $z \sim 1$ (black lines), with the resulting observed QLF in several bands: optical, soft X-ray, hard X-ray, and infrared (IR). The Figure demonstrates the range and probability of different quasar luminosities. The observations at each band are consistently produced from a single bolometric QLF and together provide strong constraints on the QLF shape. The Figure is taken from Hopkins et al., 2007.

this evolves into an optically thin and geometrically thick advection dominated accretion flow (ADAF, originally mentioned by Narayan & Yi, 1995) and a truncated accretion disc (see below for a more detailed discussion). The accretion disc produces a strong optical/UV continuum due to its high temperatures (multicolor black body), while the ADAF and a hot corona enclosing the accretion disc, produce hard X-ray radiation by inverse-Compton scattering. A thick dusty torus is surrounding the accretion disc, that expands to scales of several pc and contains molecular gas and dust. The torus is heated by the intense radiation from the central components where the radiation is absorbed by the dust and re-emitted in the infrared (IR). The inner part of the AGN additionally contains a broad-line region (BLR), consisting of dense and fast-moving clouds that are ionised by the intense disc radiation and shocks. The inner BLR is responsible for the broad permitted emission lines (with full width at half maximum of around $1\,000 - 10\,000 \text{ km s}^{-1}$)⁴. Even further outwards lies the narrow-line region (NLR) that can extend beyond the dusty torus and consists of lower density ionised clouds that move at lower velocities and show both forbidden⁵ and

⁴For any possible transition between two atomic states of an atomic nuclei, atom, or molecules there exist a number of rules (see Bunker & Jensen, 1998). If these rules are respected the transition is called *permitted*. They are emitted by atoms undergoing radiative transitions. Recaptures occur to excited levels, and the excited atoms then decay to lower and lower levels by radiative transitions and eventually end in the ground level.

⁵*Forbidden* spectral lines are associated with absorption or emission of light by an atomic nuclei, atom, or molecules, that undergoes a transition that is not allowed by a particular set of rules (see Bunker & Jensen, 1998) but is allowed if the approximation associated with this particular rule is not made. They can be thought of collisionally excited lines, which arise from levels close to the ground level and which therefore can be excited by collisions with thermal electrons. Usually forbidden spectral lines are associated

permitted emission lines of several 100 km s^{-1} wide.

While, historically, quasars have been discovered as radio sources with star-like counterparts at optical wavelengths, most of them ($\sim 90\%$) are actually radio-quiet. The lower half of Figure 2.9 corresponds to the radio-quiet sources such as radio-loud quasars and Seyfert galaxies. The upper half, on the other hand, corresponds to radio-loud sources such as radio-loud quasars and radio galaxies, which form two highly directed plasma streams, so called *jets*, that are usually directed opposite to each other along the angular momentum axis of the accretion disc. The class of *blazars* is generally defined by having one of the two jets pointing directly to the observer, where relativistic effects such as Doppler effect and beaming⁶ result in a high variability of luminosity on short time scales as well as a flat spectra.

With a *small inclination angle* between the observer and the disc/torus axis both the BLR and NLR are visible and the AGN is observed as type I with broad emission lines. On the other hand, for larger inclination angles, only the NLR is visible since the BLR is obscured by the dusty torus. In this case, the AGN appears as type II with only narrow emission lines. This is not only valid for Seyfert galaxies and quasars, but also for radio galaxies. Different studies (e.g., Osterbrock & Shaw, 1988; Barthel, 1989; Mullin et al., 2008) find that obscuration by the torus generally corresponds to inclinations of more than $\sim 45^\circ$.

2.4.2 Correlating the AGN power to the Accretion Rate and AGN mode

The radiation power associated with AGN are amongst the greatest in the Universe. The luminosity of typical Seyfert I galaxies is $\sim 10^{44} \text{ erg s}^{-1}$, and for quasars they can even exceed $10^{46} \text{ erg s}^{-1}$. Figure 2.10 shows the bolometric quasar luminosity function at redshift $z \sim 1$ to demonstrate the range and probability of different quasar luminosities⁷.

It is assumed that a significant fraction of the accreted rest-mass energy is radiated away close to the event horizon of the BH, leading to an accretion bolometric luminosity given by

$$L = \eta \dot{M}_{\text{BH}} c^2 \quad , \quad (2.21)$$

where \dot{M}_{BH} is the BH accretion rate, c the speed of light in vacuum, and η is the radiative efficiency of the BH. If the accreted matter emits all of its potential energy beyond the innermost stable circular orbit of the BH, then $\eta = 0.06$ for a non-rotating Schwarzschild BH, and $\eta \approx 0.42$ for a maximally rotating Kerr BH⁸. Studies comparing observed AGN luminosities and the inferred BH mass density suggest that, on average, $\eta = 0.1 - 0.2$ (Soltan, 1982; Fabian & Iwasawa, 1999; Tremaine et al., 2002), a value consistent with moderately spinning black holes.

with low density gas.

⁶*Relativistic beaming* is the process by which relativistic effects modify the apparent luminosity of emitting matter, where the matter is moving at speeds close to the speed of light.

⁷ For a comparison, the luminosity of our Sun is $\sim 3.8 \times 10^{33} \text{ erg s}^{-1}$ and of the giant elliptical galaxy M87 it is $2 \times 10^{44} \text{ erg s}^{-1}$. *Gamma-Ray Bursts*, that are believed to be caused due to violent merging of a binary neutron star, have the highest peak luminosity of a few $10^{51} \text{ erg s}^{-1}$, but they are powered by extremely short-lived explosive events that take a mere of a second. The lifetime of a typical quasar, on the other hand, is of order 10^7 yrs and hence AGNs manage to emit the most energy throughout their lifespan of all the known astrophysical sources.

⁸The efficiency of energy extraction for a rotating BH is higher than for a non-rotating Schwarzschild BH because the last stable orbit is at a smaller radius.

The power of an AGN, measured with their bolometric luminosity L_{bol} is generally compared with the *Eddington luminosity* given by

$$L_{\text{Edd}} = \frac{4\pi GM_{\text{BH}}c}{\kappa} = 1.26 \times 10^{47} \text{ erg s}^{-1} \left(\frac{M_{\text{BH}}}{10^9 M_{\odot}} \right), \quad (2.22)$$

where κ represents the opacity, M_{BH} the mass of the accreting BH, and G the gravitational constant. The Eddington luminosity gives the limiting luminosity of a spherically symmetric object, assuming that the radiation pressure on accreting matter, acting outward, equals the gravitational force, acting inward. If the luminosity is higher, the accretion onto the central BH cannot be sustained anymore. Because of the assumption of spherical symmetry the Eddington luminosity gives only a soft limit (see slim discs, e.g., Abramowicz et al., 1988 for more information), but gives an idea of the maximum power radiated away by a quasar. The ratio between the bolometric luminosity and Eddington luminosity $\lambda \equiv L_{\text{bol}}/L_{\text{Edd}}$ is referred to as *Eddington ratio*.

With $\dot{M}_{\text{Edd}} = L_{\text{Edd}}/(\eta c^2)$ the maximum accretion rate is given by

$$\dot{M}_{\text{Edd}} = \frac{4\pi GM_{\text{BH}}}{\kappa \eta c} = 22 M_{\odot} \text{yr}^{-1} \left(\frac{M_{\text{BH}}}{10^9 M_{\odot}} \right) \left(\frac{0.1}{\eta} \right), \quad (2.23)$$

For AGN there are at least three spectral states (Merloni & Heinz, 2008):

1. *low/hard state*: Emission is dominated by a hard X-ray power law with an exponential cut-off. Radio emission is always detected in this state (see Fender 2006 for more detail) and usually with flat or inverted spectrum. This is commonly interpreted as due to a compact, persistent, and self-absorbed jet of low intrinsic power.
2. *high/soft state*: Emission is dominated by a thermal component that likely originated from a standard accretion disc (Shakura & Sunyaev, 1973). The model assumes that the disc is in local thermal equilibrium, and can radiate its heat very efficiently.
3. *intermediate (or very high) state*: Associated with transitions between hard and soft states, and are often occurring at a source's highest flux level where both the thermal and steep power-law component substantially contributes to the spectrum.

With these different spectral states come also a number of interesting observations (see also Figure 2.11 taken from Russell et al., 2013b):

- Detailed multi-wavelength observations of nearby galaxies have shown a clear trend for the low/hard state to be low-luminosity AGNs. Additionally, the lower luminosity AGN have shown a tendency to be more radio loud as the Eddington-scaled accretion rate decreases (see Ho, 2002 and references therein; Nagar et al., 2005) and hence have a *low radiative efficiency*. This state is sometimes also referred to as *low kinetic (LK) mode* and is associated with a radio jet.
→ *Low accretion rates are associated with radio jets.*
- The most luminous sources are most likely accreting at a high rate close to the Eddington limit (McLure & Dunlop, 2004; Kollmeier et al., 2006). They are usually referred to as the *high radiative (HR) mode* (or the *quasar mode* used mostly in cosmology). They also can be accompanied with bright radio loud quasars, characterised by both radiatively efficient accretion flows and powerful jets, referred to as *high kinetic (HK) mode*.
→ *Fast accretion rates are associated with quasars (sometimes accompanied by jets)*

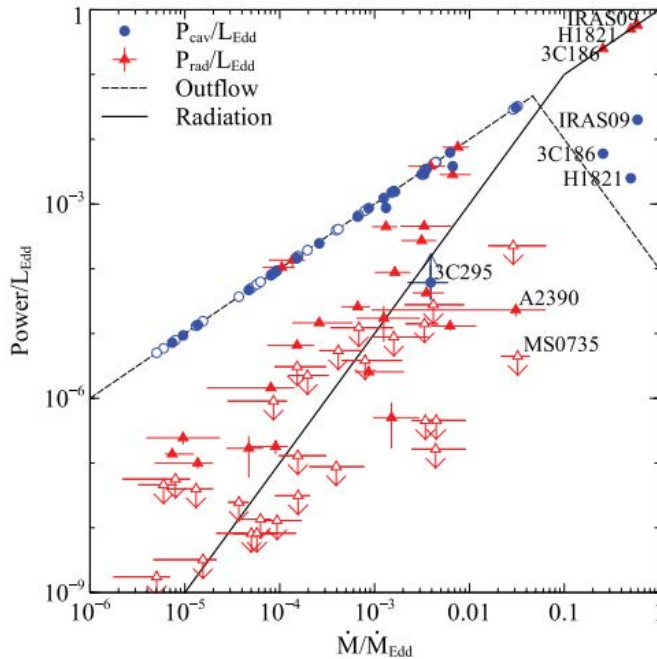


Figure 2.11: The mean accretion rate scaled by the Eddington rate, plotted against the cavity power (blue circles) and the radiative power (red triangles), scaled by the Eddington luminosity. For each point there are two points. Solid symbols denote detected nuclear X-ray point sources, whereas the upper limits are shown by the open symbols. The different quasar sources are labelled. To guide the eye, the radiation and outflow model lines are overplotted. They show a transition from outflow domination (kinetic mode) at low accretion rates to radiative domination at high accretion rates. Figure is taken from Russell et al. (2013b).

Thus, BHs accreting above a critical accretion rate (~ 0.03 Eddington) fall into two different states, one with (HK) and one without jets (HR). The reason for this dichotomy has been subject of debate (see for example Sikora et al., 2007; Blundell, 2008; Kaiser & Best, 2008 for some discussion), but BH spin and change in accretion mode are the most popular explanations.

Figure 2.12 shows a schematic view of the various modes discussed above as a function of accretion rate onto the BH. It also shows the three different regims: below the critical Eddington ratio, where only the LK mode is dominating, whereas above the line two different modes are possible; one where the kinetic and radiative power are comparable and high (HK), and one where kinetic power is quenched (HR).

Note that the radiative efficiency depends on both the accretion efficiency, representing the maximal amount of potential energy that can be extracted per unit rest mass energy from matter accreting onto the BH, and on the nature of the accretion flow itself that determines the luminosity of the source.

Accretion Discs

In the process of accreting matter gravitational energy is converted into thermal and/or kinetic energy. However, for accretion to be possible, the rotating matter around the BH has to lose its angular momentum, believed to be happening due to *turbulent viscosity* in

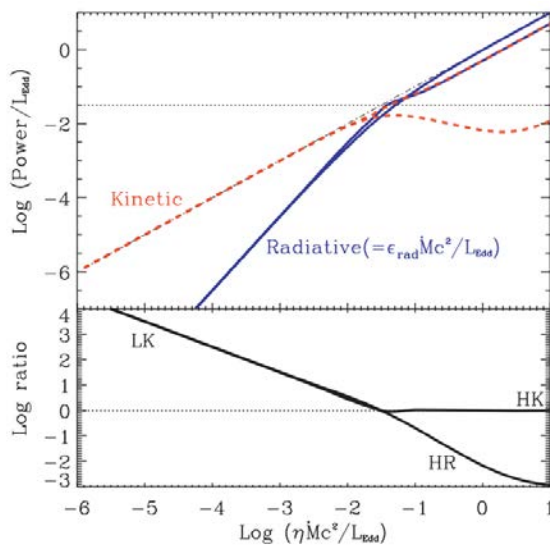


Figure 2.12: Schematic view of the relationship between accretion rate and released power, both in units of the Eddington luminosity. The blue solid lines show the radiated power, whereas the red dashed lines the released kinetic power. The black horizontal dotted line marks the critical Eddington ratio where a change of accretion mode is assumed to occur. Below this rate, the LK mode is dominating, where most of the power emerges in kinetic form, whereas above the line, two different modes are possible: one where kinetic and radiative power are comparable and high (HK), and one where kinetic power is quenched (HR). The lower panel shows the corresponding ratios between kinetic and radiative power as a function of accretion rate. Figure taken from Merloni & Heinz, 2008.

the accretion disc that transports the angular momentum and mass inwards. Balbus & Hawley (1991) identified that the magneto-rotational instability (MRI), which is effective in weakly magnetised, differentially rotating discs, is the driving force for the viscosity. The magnetic stresses provide the needed angular momentum transport on the dynamical timescale of the disc that causes the turbulence responsible for the turbulent viscosity.

As mentioned above, the standard accretion disc (Shakura & Sunyaev, 1973) is formed when the accretion onto the BH is close to the Eddington rate (although below/sub Eddington) and the opacity of the disc is very high. The model assumes that the disc is in local thermal equilibrium, and can radiate its heat very efficiently, giving rise to a quasar.

The launching of jets, on the other hand, is found for AGN with lower accretion rates of the percent level of the Eddington accretion rate. Observations of micro-quasars (accreting stellar mass black holes) indicates that the launching of a radio jet is linked with a truncation of the accretion disc and the formation of an inner hot flow (ADAF in Figure 2.9; Narayan & Yi, 1995; Fender et al., 2004; Done et al., 2007). ADAFs are considered radiatively inefficient, geometrically extended, similar in shape to a corona rather than a disc, and very hot. Because of their low efficiency, ADAFs are assumed to be much less luminous than the standard accretion discs. For actual jet formation, there are mainly two models considered. In the first model, the acceleration and collimation of matter from the ADAF is launched due to the magnetic fields of the rotating disc (Blandford & Payne, 1982) and the energy originates from the accretion power. In the second scenario, a jet is launched by magnetic field lines that are dragged with the BH rotation in the ergosphere (Blandford & Znajek, 1977). The energy for the second model is extracted from a conversion of the

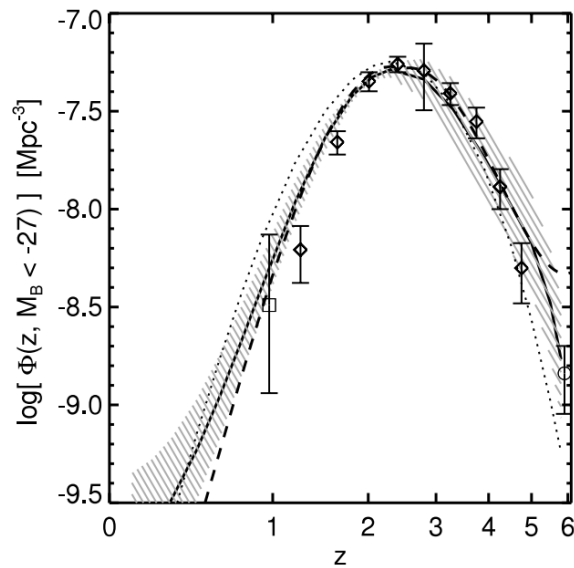


Figure 2.13: Number density of quasars with magnitude below -27 as a function of redshift. Symbols show the best-fit values to data in each redshift, dotted lines the best-fit model, and solid lines the best-fit full model (shaded range showing the 1σ uncertainty). This Figure demonstrates that quasars are much more common at redshift $z \sim 2 - 3$ and then declines again for higher redshift. The Figure is taken from Hopkins et al., 2007.

rotational energy of a spinning BH in the magnetic field, anchored in the accretion disc, into electromagnetic energy. A feature of powering jets by the BH spin is that a huge reservoir of energy can be tapped, also in episodes of low accretion that are typical for strong jet formation and, additionally, it could even be ‘refilled’ by a subsequent stronger accretion phase. Variations of ADAFs include convection-dominated accretion flows (CDAFs; see e.g., Di Matteo et al., 2000; Quataert & Gruzinov, 2000, for more details), advection-dominated inflow-outflow solutions (ADIOSs; Narayan & Yi, 1995; Blandford & Begelman, 1999; Begelman, 2012 for more information), magnetically arrested disc (MAD; Narayan et al., 2003), and magnetically choked accretion flows (MCAF; McKinney et al., 2012).

In summary, the luminosity of the BH, as well as mode of AGN, depends on the accretion onto the BH and the subsequent flow properties of the accretion disc, as well as the spin and mass of the BH. A full model embedded within the unified model of AGN including the evolutionary effects of the accretion disc around the BH has to be made in the future. Additionally, AGN luminosities vary considerably with cosmic evolution. Observations indicate that quasars were brighter and much more common at redshifts of around $z \sim 2 - 3$ (e.g., Croom et al., 2004; Richards et al., 2006), and decline again for higher redshift (see Figure 2.13 for an illustration). The fraction of radio-loud AGN, on the other hand, increases with galaxy mass, reaching $> 30\%$ for the most massive galaxies (Best et al., 2005). Thus, galactic evolution, the matter reservoir available for accretion, BH growth due to accretion, as well as feedback of the AGN onto the environment all influence the evolution and properties of these objects.

2.4.3 Radio Galaxies and Jets

Jet activity is accompanied by synchrotron emission from relativistic electrons in the magnetised plasma, that is most prominently observable at radio frequencies and, thus, is the

reason why AGN associated with jet activity are usually called *radio galaxies* or *radio-loud quasars*.

Radio interferometers allowed for the observation and study of these objects in more detail. The subsequent physical model for the double radio sources (Blandford & Rees, 1974; Scheuer, 1974) interpreted the sources as being powered by an AGN via collimated powerful beams (*jets*).

Morphology Following Fanaroff & Riley (1974) double radio sources are divided into two distinct classes: FR 1 are brightest in the center, i.e. when the separation between the brightest regions on opposite sides of the central galaxy is less than half the total extent of the source. They typically show a bright jet in the center which then decollimates and forms *plumes* at larger distances. The second class, the FR 2 sources, are brightest at the outer edges, i.e. the separation between the brightest regions is larger than half the total extent. They show dim jets but extended lobes with a bright hotspot at the outer edges.

These morphological properties are correlated with the radio power of the sources, with the FR 1 sources being lower power ($\leq 10^{25}$ W Hz $^{-1}$ at 1.4 GHz; Bridle & Perley, 1984) and the FR 2 showing high radio power ($\geq 10^{25}$ W Hz $^{-1}$). The FR 2 are believed to be able to transfer their power with beams to large distances without dramatic energy losses, while this is not the case for the FR 1 class.

The origin of the dichotomy is still unclear. Possible explanations could depend on the central source, how the jet is formed, or the environment where the jet propagates through. Both jet classes are believed to have relativistic jets in the inner regions. While the FR 2 class are thought to remain also relativistic on large scales, the FR 1 class seems to entrain a significant amount of ambient matter, that slows down the jet on scales larger than a few kpc and cause decollimation.

Figure 2.14 shows a schematic representation of an FR 2 source. The bipolar jet is formed in the accretion disc of the active nucleus, that is in radio images visible as a *core*. While the jet propagates, internal shocks are excited in the beam and the jet plasma passes through regions of rarefaction and compression. Interactions with the ambient gas leads to the formation of a terminal shock and a post-shock *hotspot*. The shocked plasma leaves the region of very high pressure sideways and forms a backflow that inflates the cocoon. Generated vortices are advected with the flow and inflate the cocoon. Since the ambient gas is much denser than the jet plasma, the jet head propagates much slower than the beam speed which leads to a fast corresponding backflow. The cocoon is over-pressured with respect to the environment and drives a bow shock into the ambient medium, leading to the formation of a thick shell of shocked ambient gas. Because the cocoon pressure is generally higher in the region around the jet head, the axial propagation is faster than the lateral propagation, leading to the bow shock to be elongated. The strong shearing at the contact discontinuity between the jet plasma and the ambient gas causes Kelvin-Helmholtz and Rayleigh-Taylor instabilities. These instabilities grow and form fingers that are entrained with the backflow and lead towards the disc and eventually mix with the cocoon gas. *Lobes* are visible in the radio frequencies in the outer regions of the cocoon, where the synchrotron-emitting electrons are still very energetic.

Jet parameters Jet speed, density, and power are the three most important jet parameters governing its behaviour, and the discussion will be especially relevant in Chapter 4.

- *Jet speed*: It is generally assumed that jets move at relativistic speeds on the pc up to kpc scale. Evidence for this can be found in several observations (e.g., Zensus,

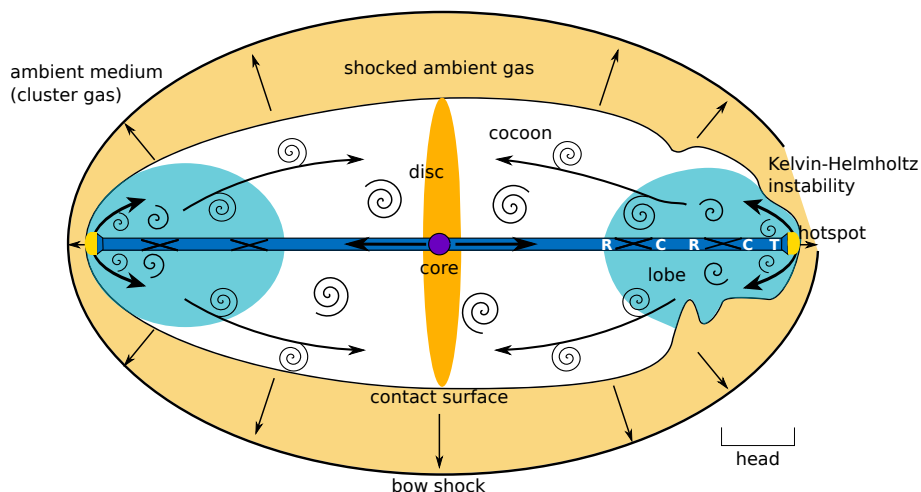


Figure 2.14: Schematic representation of an FR 2 jet. The beam (dark blue) emerges from the accretion disc around the BH and the plasma passes through regions of rarefaction (R) and compression (C) at internal shocks until it is decelerated at the terminal shock (T). Once shocked, the plasma streams out of the high-pressure region of the hotspot (yellow) and forms a backflow. Vortices that are generated are advected with the flow and inflate the cocoon (inner white region and light blue region). Lobes are visible at the outer parts of the cocoon, where the radio-emitting electrons did not yet cool down. The over-pressured cocoon drives a bow shock outwards into the ambient medium that forms a thick shell of shocked ambient gas. The strong shearing between the backflow and the shocked ambient gas causes Kelvin-Helmholtz instabilities to form that lead to *fingers* of ambient gas reaching into the cocoon. Figure taken from Bieri et al. (2016b).

1997; Wardle & Aaron, 1997; Hardcastle et al., 1999). These observations suggest that jets are moving at relativistic speeds between $0.5 c$ and $0.7 c$.

- *Jet power:* Observations of X-ray cavities reveal jet powers between $1.5 \times 10^{44} \text{ erg s}^{-1}$ (for Perseus A; Rafferty et al., 2006) as a relatively low-power system, to $1.6 \times 10^{46} \text{ erg s}^{-1}$ (for Hercules A; Nulsen et al., 2005), and up to $1.7 \times 10^{46} \text{ erg s}^{-1}$ for MS0735.6+7421 system (McNamara et al., 2005).
- *Jet density:* Density is the hardest to constrain, since the non-thermal synchrotron emission carries no information about this, and since the observed radio-emitting particles are an unknown fraction of the total jet matter. There are, however, four ways to indirectly estimate the jet density:
 - The kinetic jet power L_j of a bipolar jet can be related with the jet speed v , the density ρ , and the jet beam radius r_j by $L_j = \pi r_j^2 \rho v^3$. Assuming a typical beam radius of $r_j = 1 \text{ kpc}$, the particle density is less than 10^{-4} cm^{-3} for a powerful jet with $10^{46} \text{ erg s}^{-1}$ and even less for weaker ones. In comparison, the ambient intergalactic gas generally has densities of two to three orders of magnitude higher.
 - Considering, for an upper limit, that a BH accretes at 10% of its Eddington limit and transfers all matter to the jet, then, $0.1 \dot{M}_{\text{Edd}} = 2\pi r_j^2 \rho v$. For a powerful source with a $10^9 M_\odot$ BH, this corresponds to a density of, again, 10^{-4} particles

per cm^3 . Note, that this is an upper limit and for more realistic scenarios, the mass flux in the jet will be much smaller than this.

- A third way to estimate the jet density is by using a simple one-dimensional model for the jet head propagation. The jet head moves with a speed v_h through the ambient gas with density ρ_a that is assumed to be at rest. Momentum balance in the jet head frame, and assuming the jet crossing as a working surface, gives

$$\rho_a v_h^2 = \rho_j (v_j - v_a)^2 \quad (2.24)$$

where the subscript a denotes the ambient gas, h the jet head, and j with the jet. Note, that this is only a simple estimate and any change in the working surface will yield somewhat different results. Scheuer (1995) found that the head advances with a speed of $\leq 0.1 c$, and Alexander et al. (1984) found a head advance speed of $\leq 0.05 c$ for Cygnus A. This supports the above estimate that the jet densities are $< 10^{-3}$ particles per cm^3 .

In conclusion, extragalactic jets have densities that are smaller than a factor of 10^{-2} with respect to the ambient density, but largely unconstrained otherwise.

2.4.4 Quasars

Extreme episodes of gas accretion onto BHs, in particular in high-redshift galaxies, are followed by quasar activity. Quasars are the most energetic and distant members of AGNs. The first quasar was located as a strong radio source by Maarten Schmidt (Schmidt, 1963). Because of its star-like appearance it was identified as a star. However, the very strong and broad emission lines detected (something only seen for the hottest stars), featuring the elements of Hydrogen, Helium, Carbon, and Magnesium, implied very large velocity width for the line emitting gas of several thousand km s^{-1} . Additionally, a very blue optical continuum was found that definitively distinguished the object from a star. Because of the similarity to the appearance of stars, these objects are also referred to as quasars (from quasi-stellar radio source) and QSO (quasi-stellar object). Although first observed in the radio, (Sandage, 1965) already found that several other celestial objects had similar characteristics to these quasars but without the radio emission.

Within a few years of their initial discovery in 1963, quasars with values of redshifts as high as $z \sim 2$ were being identified (e.g., Schmidt, 1965; Arp et al., 1967). The first quasar at $z > 5.5$ was discovered by Fan et al. (2000). Since then, considerable effort has been made to find more, because quasars trace the underlying BH population and, thus, can yield information on the BH growth and formation (e.g., Merloni, 2004; Marconi et al., 2004; Shankar et al., 2004; Hopkins et al., 2006; Merloni & Heinz, 2008; Draper & Ballantyne, 2012). The discovery and characterisation of a statistically significant sample of quasars at the high redshift range is also important to, for instance, better understand the formation and growth of the SMBHs, that is still unclear and debated (e.g., Volonteri, 2012; Dubois et al., 2012a; DeGraf et al., 2012; Volonteri & Bellovary, 2012; Becerra et al., 2015; Glover, 2015; Di Matteo et al., 2016).

Numerous studies, established a sample of more than 100 quasars in the high-redshift ($z > 5.5$) Universe⁹. Figure 2.15 shows the distribution of the high redshift quasars color-coded by their discovery surveys. The findings suggest that there are fundamental changes

⁹ Such surveys include Pan-STARRS1 (Panaromic Survey Telescope & Rapid Response System 1; Morganson et al., 2012), UKIDSS (UK Infrared Telescope; Venemans et al., 2007; Mortlock et al., 2009, 2011, FIRST/radio (Faint Images of the Radio Sky at Twenty cm; McGreer et al., 2006; Cool & Schaefer,

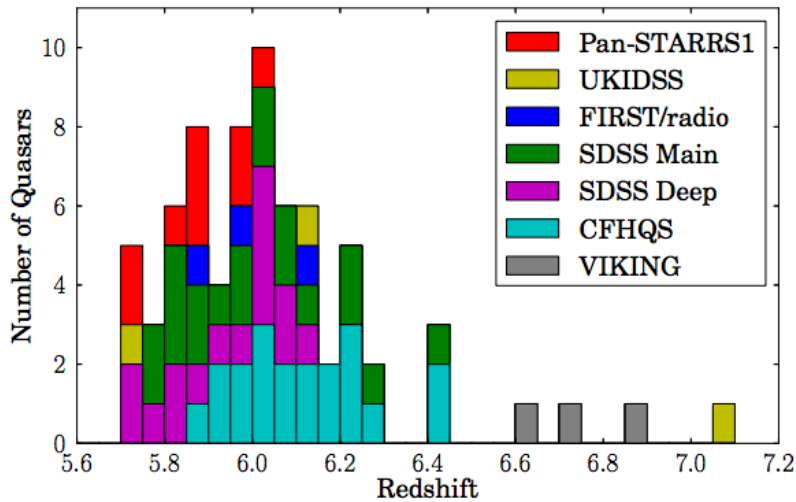


Figure 2.15: Redshift distribution of the $z \geq 5.7$ quasars published by Bañados et al., 2014. The surveys include: Pan-STARRS1, UKIDSS, FIRST/radio, SDSS Main, SDSS Deep, CFHQS, VIKING. The findings suggest that fundamental changes are happening in the inter galactic medium in the redshift range $6 \leq z \leq 7$, weakly constraining the epoch of reionisation.

happening in the inter galactic medium in the redshift range $6 < z < 7$, suggesting that the end of reionisation process occurs at redshift near $z \sim 6$. This again gives an idea of the formation time as well as growth of the first BHs (see e.g., Haiman et al., 2005 for more information). Figure 2.13 shows the number density of quasars as a function of redshift, which demonstrates that quasars are most common around redshift $z \sim 2 - 3$ compared to today and higher redshifts.

The main results of the study of the high-redshift quasars include (i) BHs are part of the evolution of cosmic structures, (ii) massive BHs ($> 10^8 M_{\odot}$) have formed less than a Gyr after the Big Bang (e.g., Willott et al., 2007; Kurk et al., 2009; Jiang et al., 2008; Mortlock et al., 2011); (iii) quasar host galaxies are massive and form stars intensively (up to $1000 M_{\odot} \text{ yr}^{-1}$; see e.g., Walter et al., 2009); and (iv) the neutral fraction of Hydrogen in the intergalactic medium increases rapidly above $z > 6$ which provides strong constraints on the end of reionisation (e.g., Fan et al., 2006).

Additionally to providing information about the underlying BH population, quasars are also thought to dramatically alter both the immediate environment of the BH, from which accretion is occurring, and the more distant ISM of the galaxy within which the BH resides. Photons, emitted by a quasar, couple to the gas and drive a large-scale wind. The aim of Chapter 5 investigates the detailed coupling between the gas and the radiation using radiation-hydrodynamical equations, that describe the emission, absorption, and propagation of photons with the gas and dust.

2002; Cool & Moellenbrock, 2003; Cool et al., 2005a,b, 2006, SDSS Deep (Sloan Digital Sky Survey; Mahabal et al., 2005; Goto, 2006; Jiang et al., 2008, 2009; De Rosa et al., 2011; Wang et al., 2013, CFHQS (Canada-France High-z Quasar Survey; Willott et al., 2007, 2009, 2010b,a, and VIKING (VISTA Kilo-degree Infrared Galaxy survey; Venemans et al., 2003).

2.4.5 Positive or Negative Feedback

As discussed above, AGN feedback is advocated to suppress star formation in massive galaxies in order to reproduce the observed high-end tail of the galaxy mass function. And, indeed, recent large-scale cosmological simulations (e.g., Dubois et al., 2014; Vogelsberger et al., 2014; Khandai et al., 2015a; Schaye et al., 2015), employing strong AGN and stellar feedback, produced good agreement with the observations. However, despite negative feedback from AGN being an important ingredient in the formation and evolution of massive galaxies, the details remain vague, primarily because the coupling mechanism between the AGN and the ISM of the host galaxy is still unknown.

From an observational point of view the impact of AGN feedback on star formation is still not fully understood, mostly because of the difficult nature of their observations, particularly at higher redshift. While there are several detailed observations available showing the interaction of the AGN with interstellar gas, both for jets and winds, it is still unclear what their actual importance on the evolution of the host galaxy is and how they affect the star formation within the galaxy.

Both recent observations (Zinn et al., 2013; Cresci et al., 2015b,a; Salomé et al., 2015) and simulations (Gaibler et al., 2012; Wagner et al., 2012) suggest that local interactions between jets and cold gas may not only result in suppressed star-formation but may also trigger star formation (positive feedback). Both modes can coexist in a single galaxy during different or overlapping phases.

This paints a more complicated picture that will be discussed in this Section along with observational evidence and theoretical models for both positive and negative feedback.

2.4.5.1 Observations

This Section will discuss the wealth of different, sometimes conflicting, observations that exemplifies the complex picture of the effect of AGN feedback on galactic scales.

There are many observations supporting the conclusion that AGN quench star formation in the host galaxy. For example, energetic outflows have been detected using emission and absorption line features from distant radio galaxies (e.g., Nesvadba et al., 2006; Morganti et al., 2005, 2007, 2013; Lehnert et al., 2011), quasars (e.g., de Kool et al., 2001; Chartas et al., 2007; Rupke & Veilleux, 2011; Dasyra et al., 2014; Cicone et al., 2014; Tadhunter et al., 2014; García-Burillo et al., 2015), and starburst galaxies (e.g., Heckman et al., 1990; Heckman & Lehnert, 2000; Martin, 2005; Alexander et al., 2010). These winds have been suggested to be responsible for sweeping galaxies of their gas and, thus, to negatively impact the star formation within the galaxy. McNamara & Nulsen (2007, 2012) discuss observations of X-ray lobes and radio cavities in galaxy groups and clusters that give strong evidence for metal-enriched outflows that leave the galaxy with little cold gas to form stars.

Fabian (2012) describes how both radio-loud and radio-quiet quasars drive winds and bubbles that expel gas that might otherwise form stars, and how they prevent accretion of new gas. They argue that evidence of AGN feedback can be seen when galactic outflows with high velocity (e.g. $> 500\text{km s}^{-1}$) components and an outflow power exceeding that predicted by a central starburst is observed. However, the details are not easy to disentangle, since there is no clear dividing line between star- and AGN-driven outflows. Nevertheless, the several observations listed by Fabian (2012) show evidence of AGN feedback with simultaneously high velocity outflows and outflow powers of around one percent of the bolometric luminosity of the AGN.

Bîrzan et al. (2004) and Dunn et al. (2005) show that cooling flows in the hot circumgalactic and intracluster medium can be suppressed by the energy transferred by AGN jets

and thus quenches star formation. Schwamb et al. (2016) argue that the sudden decline in molecular gas observed in their galaxy sample implies that the gas reservoirs are depleted on timescales much shorter than mere exhaustion by star formation. They argue that this drop in molecular gas is due to very efficient AGN feedback that negatively impacts star formation in the host galaxy through the expulsion of residual molecular gas.

It is expected that any gas dispersed, heated, or blown away through the interaction of the AGN with the galaxy is likely to suppress star formation (Morganti et al., 2005; Nesvadba et al., 2008). Morganti et al. (2015) (and references therein) argue that the presence of cold molecular gas with the outflows is a powerful way to quantify the characteristics and impact of AGN feedback on the cold gas. They show that a relativistic jet can drive a large amount of molecular gas, although not always fast enough to actually fully expel the gas from the galaxy.

On the other hand, recent observations, often using more resolved observations, indicate that the situation is more complicated and that AGNs may not always be able to quench star formation in the host galaxy. For instance, Karouzos et al. (2016) find evidence against the negative impact of AGN outflows even at small redshifts ($z < 0.1$) and for low luminosities ($L < 10^{42}$ erg s $^{-1}$). Using Gemini Multi-Object Spectrograph data on six low redshift, type II AGN, they find that while velocities up to 600 km s $^{-1}$ are large, the small size (< 2.1 kpc) of the outflows are too small to quench an entire galaxy. Similar conclusions were reached by Labiano et al. (2016) that examine two low-redshift radio-loud AGNs with outflows in different stages of the process. Their calculated kinematics, star formation efficiency, and star formation rates indicate that AGN feedback is not necessarily responsible for the low SFR in evolved AGN systems, but, instead, that perhaps the calculated SFRs are too low or that the estimated molecular gas content of these galaxies is too high.

Moreover, evidence in the high-redshift Universe for jet-induced star formation is also discussed, for instance, in Bicknell et al. (2000). Similarly, Dey et al. (1997) show observational evidence of a high-redshift galaxy where star formation may be triggered by the expansion of the radio source into the ambient medium. Rocca-Volmerange et al. (2013) find high levels of star formation in powerful radio galaxies and argue that either gas-rich mergers and/or jet-cloud interactions are the favoured triggering mechanism for the intense star formation necessary to explain the properties of the spectral energy distributions. Furthermore, more jet-induced star formation has also been invoked to explain recent star formation and the alignment of emission line regions in many young galaxies (Privon et al., 2008; Tadhunter et al., 2011).

There are other, more indirect, connections between AGN feedback and star formation, which suggest possible positive feedback from AGN. Klamer et al. (2004) discuss that CO emission observed in high-redshift galaxies is correlated with star formation triggered by relativistic jets. Other indirect links have been discussed by McCarthy et al. (1991) and McCarthy (1993), arguing that the jet lobe distance ratios are strongly correlated with the presence of thermal line-emitting gas (indicating star formation) and, the closer the lobe, the higher brightness of the line emission (and, hence, the higher the star formation). Along similar lines, Podigachoski et al. (2015) discuss that the star-forming properties of the AGN hosts are similar to those of the general population of equally massive non-AGN galaxies at comparable redshifts. They conclude that there is weak evidence of universal quenching of star formation within their observed sample.

Some observers also find evidence for AGN-triggered star formation on Giant Molecular Cloud (GMC) or smaller cloud scales. Tremblay (2016) present observations from ALMA showing that AGN the jet-driven bubbles are capable of blowing giant molecular clouds

away before gravity pulls them back again. Additionally, these observations suggest, that in the outer regions of the molecular clouds star formation is triggered by the expanding jet bubble.

Moreover, Croft et al. (2006); Inskip et al. (2008); Salomé et al. (2015); Mirabel et al. (2015) discuss different local observations that indicate that AGN jets are capable of locally inducing star formation, even if the ambient medium is only moderately dense. This suggests that jet-induced star formation may have been quite common in the early Universe where gas densities were much higher than today, and when AGN activity was much more prevalent.

Jet feedback is not the only AGN mode associated with triggers star formation. For instance, Rauch et al. (2013) discuss a possible high-redshift candidate where quasar feedback is thought to trigger external star formation. Cresci et al. (2015b) use the Measuring Active Galactic Nuclei Under MUSE Microscope (MAGNUM) survey and present evidence of a possible example of mixed feedback in a Seyfert-like, radio-quiet galaxy. They observe double-sided ionisation cones of high-velocity gas, interpreted as outflowing gas, surrounded by star forming knots in clumps exposed to the resulting outflow. They proposed that compression by the nuclear outflow is triggering the star formation in these clumps. In such cases, it is the relative efficiency of negative and positive feedback, and the timescale on which they operate, that determines the net effect on the star formation.

A similarly complicated interplay between quasar winds and star formation in the host galaxy has been investigated by Carniani et al. (2016) that studied two quasars with fast outflows and find an anti-correlation with star-formation in the host galaxy. They conclude that the most likely possibility is the simultaneous positive and negative feedback in the galaxy, in which the outflows remove gas that could form stars along the direction of its propagation, while compressing gas around the edges of the outflow, triggering star formation. They also postulate that several cycles of feedback could be necessary to totally quench star formation. Similarly, Cano-Díaz et al. (2012) presented evidence that star formation is suppressed in the region affected by fast outflows whereas in the other regions the galaxy is forming stars.

An explanation for the high star formation rate due to quasar feedback can be found in Cresci et al. (2015a) who propose that the triggering of star formation is through enhanced gas pressure in the ISM induced by AGN feedback. A similar explanation of enhanced star formation within molecular clouds due to high external hydrostatic pressure has been used by Swinbank et al. (2015).

Concerning the different modes of AGN feedback, observations indicate that radio-loud quasars are more likely to trigger star formation than their radio-quiet counterparts. Analysing almost 20,000 quasars from the SDSS, Kalfountzou et al. (2012) uses [OII] emission line to estimate SFRs in quasars with and without jets. After finding higher SFRs in the radio-loud AGN, they conclude that the jets trigger star formation. Zinn et al. (2013) combine far-infrared and radio data on several hundred AGN from the Chandra Deep Field South to examine differences in star formation because of AGN jets. Using the far-infrared data as a tracer for star formation, they find a correlation between enhanced SFRs and radio-loud quasars, even when compared to radio quiet quasars with similar luminosities. Their results indicate positive feedback from the mechanical energy of jets and negative feedback from the from the photo-dissociation and heating of molecular gas. They argue that both modes of AGN feedback can coexist in single galaxies during different or overlapping phases.

In summary, several observations point out a more complicated picture of the interaction

of AGNs and the ISM. It seems that the picture of AGN exerting negative feedback on the host galaxy is, while very attractive, also possibly too simplistic. Whether AGN feedback is positive or negative may likely depend on the detailed properties of the ISM. Additionally, different observations have shown that the two modes can also be found at the same time within a galaxy. Detailed models are needed in order to better understand the inner workings and the efficiency of AGN feedback. The next Section will discuss some attempts.

2.4.5.2 Theoretical Work

Early investigations into the interaction of quasar-driven outflows and the ISM focused on explaining the emission lines and kinematics of broad and narrow line regions (Blumenthal & Mathews, 1979; Weymann et al., 1982; Schiano, 1986). Most of the work focused on quasar winds and assumed that they are driven by radiation pressure (Mushotzky et al., 1972; Williams, 1972).

The possible importance of quasar winds in the evolution of galaxies comes from theories aiming to explain the tight correlations between BHs and their host galaxies (Silk & Rees, 1998; Umemura, 2001).

At this point, the role of radio jets in galaxy evolution was still unclear, although some observations (explained in more detail above) have shown cases in which outflows are driven by jets (Morganti et al., 1998). However, theoretical models mostly focused on explaining the existence of alignment effects, where observations have shown that star formation occurs along the jet axis. De Young (1981) proposed a model where the existence of young stars in two radio galaxies is explained by the entrainment of interstellar matter by the outflowing gas powered by the radio source. Later work by the same author (De Young, 1989) using numerical simulations of high-energy radio jets passing through a dense protogalactic gas confirmed the earlier model and showed that, due to the high-energy jet, stars are formed along the axis of the radio source, hence, exerting positive feedback on the gas.

A simple model by Begelman & Cioffi (1989) shows that the jet cocoons of shocked gas, which surround powerful double radio sources, can have significantly higher pressures than the surrounding IGM. Their model suggests that overpressured cocoons in high-redshift galaxies engulf and compress circumgalactic clouds, drive them over the Jeans limit, and trigger star formation.

Rees (1989) and Chambers et al. (1990) argued along similar lines, showing that, because of the AGN jet, clouds within the galaxies are squeezed by the higher pressure. They showed that this compression pushes many clouds over the threshold for gravitational instability, thereby, triggering a burst of star formation. Daly (1990) argued that the tunnelling of the jet through the ambient gas leads to two coupled shock systems. The driven shock wave propagates along the jet axis and the blast wave propagating perpendicular to the jet axis. The blast wave not only shock heats the ambient gas, but can also trigger star formation. Additionally, van Breugel & Dey (1993) and Bicknell et al. (2000) constructed a jet-cloud model to explain spectroscopic features indicated elevated star formation along the jet axis.

While early work on jet models mostly focused on jet-triggered star formation, the strongest link between radio jets and galaxy evolution came from the need to overcome catastrophic cooling in galaxy cluster halos that resulted in unrealistic entropy profiles (Babul et al., 2002; Mathews et al., 2003). Additionally, jet feedback was suggested to keep massive, early-type galaxies passively star-forming (Benson & Madau, 2003).

While the model that quasar feedback exerts strong negative feedback on the galaxy environment already existed, the idea that radio jets may affect the galaxy evolution in a similar manner is more recent. It has notably been motivated by observations indicating strong interactions between jet and ISM on kpc scales in compact radio sources (Holt et al., 2008; Morganti et al., 2005).

In more recent years, jet feedback, together with feedback from quasars, has been routinely employed in both semi-analytical models and numerical simulations (e.g., Croton et al., 2006; Bower et al., 2006; Di Matteo et al., 2005, 2008; Dubois et al., 2010b). These studies have shown that AGN feedback is an attractive mechanism to not only explain the observed co-evolution of BHs and their host galaxy, but also to shape the observed high-mass tail of the galaxy mass function and to resolve tensions between the hierarchical standard model of galaxy formation and observational constraints.

Using the same AGN feedback implementation as for cosmological simulations (Dubois et al., 2010b), Gabor & Bournaud (2014) performed high-resolution simulations of idealised $z \sim 2$ isolated disc galaxies. They found that, despite powerful bursts and high outflow rates, AGN feedback has little effect on the dense gas in the galaxy disc. They conclude that AGN-driven outflows do not cause rapid quenching of star formation, although they may remove significant amount of gas over long timescales. Such a long-term AGN-driven quenching of the in situ star formation in the host galaxy was found by Dubois et al. (2013).

The role of AGN feedback on galactic scales is, therefore, still not fully understood. The lack of understanding about AGN feedback and its effect on the interstellar gas is partly due to different complications in the numerical modelling of AGN feedback. One complication comes from the inability to capture the extremely wide dynamical range of the AGN cycle, from sub-pc scales of the accretion discs to galactic-size lobes of radio galaxies. Another complication comes from the inadequate treatment of the ISM, i.e. whether the ISM forms a continuous gas distribution or whether individual small-scale clouds are resolved, and interact with the propagating jet or radiation driven wind. In principle, the ISM must be treated as a multiphase inhomogeneous turbulent medium, that requires high-resolution three-dimensional simulations. These two reasons, the wide range of physical scales and the treatment of an inhomogeneous ISM, explain why a pc-to-kpc scale theory of AGN feedback has not yet been incorporated in larger scale simulations.

High resolution, galaxy scale hydrodynamical simulations of jet-driven feedback (e.g., Wagner et al., 2012; Gaibler et al., 2012), but also radiative feedback using radiation hydrodynamics including a clumpy ISM (e.g., Ciotti & Ostriker, 2007, 2012; Novak et al., 2012b; Bieri et al., 2016a) have only recently become feasible. These studies include an adequate treatment of the ISM necessary to investigate the dependence of AGN feedback on jet/radiation power and the properties of the ISM. Such galaxy scale simulations show that the ISM properties determine whether AGN feedback is negative or positive.

Wagner et al. (2012) perform three-dimensional relativistic hydrodynamic simulations and investigated the dependence of AGN feedback on the jet power and properties of the ISM. They found that for a given total mass and volume filling factor of dense clouds, negative feedback is more efficient the smaller the cloud sizes. Pressure-triggered star formation, on the other hand, is more important if clouds are sufficiently large for them to not be completely destroyed through ablation before having a chance to collapse gravitationally. Similar conclusions for strong negative feedback in spherical cloud distributions and positive feedback in disc galaxies were found for energy-driven AGN disc winds (Wagner et al., 2013). Additionally, Sutherland & Bicknell (2007) found, by performing similar simulations, that if an AGN jet propagates perpendicular to the gas-rich galactic disc and

its interaction depth is short (or order the disc height) negative feedback is comparatively weak.

These simulations suggest that conditions for positive AGN feedback from jets, and also for energy-driven¹⁰ AGN winds, may be optimal in galaxies with larger clouds, e.g. high-redshift and gas-rich galaxies. Gaibler et al. (2012) performed three-dimensional hydrodynamic simulations of jets propagating perpendicular to a thick disc. Their simulations showed, that after a brief phase in which the jet was confined while drilling through the disc, the jets emerged at different times into the halo, showing that the interaction of jets with a dense ISM can lead to asymmetries in the jet morphology. Once the jet propagates outside the disc, a ring of compressed gas, associated with enhanced star-formation, propagated cylindrically outward from the jet axis into the disc. The jets inflated cocoons and bubble eventually engulfed and pressurised the entire disc that led to galaxy-wide enhanced star formation. By the end of the simulation, the SFR was enhanced by a factor of three since jet injection and was still rising.

Wagner et al. (2016) reviews theoretical work on both positive and negative feedback from radio-loud and radio-quiet AGN. They conclude that it depends on the geometry and density of the ISM, whether the outflow from an AGN exerts negative or positive feedback (along the lines of Wagner et al., 2012). While spherically distributed clouds with lower densities cause negative feedback, disc configurations and higher density clouds are more conducive to positive feedback.

Ishibashi & Fabian (2012) also provide a theoretical framework for triggered star formation due to an AGN outflow and link it to the oversized evolution of massive galaxies over cosmic time. They argue that stars are formed at increasingly large distance from the center of the galaxy and, hence, predict an ‘inside out’ growth of star formation. This process has also been seen by Dugan et al. (2014), analysing the simulation of a radio-loud jet by Gaibler et al. (2012). Further, Zubovas & King (2012) argued that cooling in galaxy wide outflows leads to two-phase gas and subsequent star formation.

Moreover, jet-induced star formation has also been considered as a source for powering luminous starbursts (e.g. Drouart et al., 2014; Piconcelli et al., 2015; Rodighiero et al., 2015) that are increasingly found in the high-redshift Universe (Silk, 2005; Bieri et al., 2015, 2016b; see Chapter 4 for a detailed discussion).

Furthermore, there have also been studies of AGN feedback focusing on smaller scales, such as shocks from jets or winds striking clouds. Zubovas et al. (2014) find that over-pressured shocks striking gas clouds causes fragmentation and star formation and Dugan et al. (2016) defines a threshold ram pressure below which over-pressured, high-velocity shocks cause gas clouds to collapse and form stars, whereas above this pressure the gas cloud is completely destroyed.

However, it is not a priori clear whether the findings of idealised galaxy scale simulations will hold in a more realistic and violent cosmological environment where filamentary accretion affects the evolution of these galaxies, possibly in a way that is not predicted by isolated disc simulations. Further simulations, embedded in a realistic cosmological environment will help to better understand the conditions under which AGN induce star formation or exert negative feedback onto the galaxy.

¹⁰Strictly speaking, energy-driven (or energy-conserving) is when energy is conserved, therefore the momentum should just increase with time as more gas is swept up. Energy-conserving outflows lead to $\dot{p} \gg L/c$, with p being the momentum of the outflow, L the bolometric luminosity of the AGN, and c the speed of light, because of the work done by shock-heated gas.

Numerical Modeling of Galaxies

The formation and evolution of galaxies within the large-scale structure of the cosmic web is a highly non-linear and complex problem that cannot be entirely described by analytical techniques. An important requirement for any model is the ability to compare with observations to test whether it is able to reproduce observed properties of galaxies, such as spatial distribution, stellar properties and histories, and galaxy morphologies.

Importantly, another motivation for numerical methods, is that everything in the Universe happens on a very long timescale. Even when dynamical times are short (in astrophysical terms), like at the very centre of our galaxy, one can usually only hope to see stars move enough to measure their transverse velocity across the sky. Hence, the Universe, is in general, viewed as a (almost) static snapshot. With simulations we are able to directly access the evolution of a system, say a galaxy, for times longer than the human race has existed. Hence, with simulations we are able to find out more about the past of the system and where it will end up in the future.

Unlike other fields of physics, it is difficult to perform experiments that test astrophysical theories, mostly because of the enormous distances and timescales involved in astrophysics. While it is very important and necessary to compare our theoretical predictions with observations, numerical simulations allow us also to perform experiments in order to better understand the different physical processes which govern galaxy formation. While we might know through observations that we have to go from a starting point to an end point, numerical simulations allow us to test different scenarios and the interesting physical processes between the start and the end point provided by the observations.

There are two major numerical approaches that have been developed in order to understand the processes that govern galaxy formation. Hydrodynamical (HD) simulations attempt to directly solve the full non-linear equations involved in galaxy formation whereas semi-analytic models (SAMs) treat the physical processes associated with galaxy formation using approximate, analytical techniques. As with HD simulations, the degree of approximation varies with the complexity of the physics considered, ranging from precision-calibrated estimates using the evolution and merger rates of dark matter halos, to empirically motivated scaling relations with a larger parameter uncertainty.

It is important for the two approaches to work together as they both provide a control for the other. The two fields tend to intersect, especially, when processes below the resolution of the simulations are included and so the treatment of the physics is often at the ‘sub-grid’ level, and a semi-analytic approach is used to describe the underlying non-resolved physics. However, unlike in SAMs, using sub-grid models in HD simulations allows one to study the direct effect of the underlying model on the gas distribution and subsequent evolution of the system. Approaches to combine the advantages of HD simulations with SAMs have also been shown (Moster et al., 2011, 2012), where SAMs are used to define the initial conditions of a series of HD simulations, that are intended to mimic the galaxy evolution from a given redshift to the present day.

From the numerical point of view, large-scale structures and the study of halo formation are largely determined by the dynamics of cold dark matter which can be approximated by a set of point particles. Already the calculation of the gravitational forces of such N -body systems and subsequent motion of the bodies interacting is computationally challenging, but the Universe we observe is baryonic and hence dark matter alone is insufficient to fully describe galaxy formation. Baryonic processes must be included in the simulations in order to be able to compare the models with observations. This makes the problem much

more difficult since, at the very least, the movement of the baryonic fluid must be followed. In addition, a wide range of baryonic processes can be added to the simulation, such as cooling, and sub-grid physics.

Within recent years a considerable effort has been invested in developing ever more refined techniques and methods to solve the wide range of physical processes for galaxy formation such as hydrodynamical phenomena, magnetic fields, stellar and black hole feedback mechanisms, photons, and cosmic rays, to name a few. Hence, when the collisional component is included in the simulations the complexity of the problem increases as does the computational cost.

The principal components are concerned with in this thesis are dark matter, star, gas, and the black hole in the center of the galaxy. The first two can be thought of as collisionless fluids whose calculation we will discuss in Section 3.1. However, in order to create stars, we must simulate the gas surrounding them, i.e. interstellar gas, which experiences pressure and viscosity via inter-particle collisions, even at the densities ($0.2 - 20 \text{ atoms cm}^{-3}$) typically found in the inter-galactic medium (IGM). The calculation of such a collisional system is described in Section 3.2.

The descriptions of this Chapter will mostly focus on the techniques employed in the adaptive mesh refinement code RAMSES and the radiative hydrodynamics (RHD) extension RAMSES-RT, used for the results presented later on. Section 3.3 will summarise how the dark matter, stars, and gas is simulated within RAMSES. Section 3.4 describes the physics associated with the baryons such as the cooling and heating mechanism, feedback mechanisms, as well as unresolved turbulence within the interstellar medium. Further, Section 3.5 explains how radiation couples to the hydrodynamics and how the interaction of the photons with the gas can be modelled self-consistently. Finally, Section 3.6 describes RAMSES-RT and how the RHD equations are implemented within RAMSES, which is later used to study the coupling of the photons with the interstellar gas.

3.1 Collisionless N -body systems

Cold dark matter (CDM) comprises about 80% of the matter content of the Universe and is therefore important to the understanding of structure formation. CDM is thought to be collisionless particles that interact only through gravity. Stars, on the other hand are not collisionless, but their interaction cross-sections are small enough to rarely collide head-on. Hence, both dark matter and stars can be described as a fluid using the differentiable distribution function $f(\mathbf{x}, \dot{\mathbf{x}}, t)$, which obeys the collisionless Boltzmann equation:

$$\frac{df}{dt} = \frac{\partial f}{\partial t} + \dot{\mathbf{x}} \frac{\partial f}{\partial \mathbf{x}} - \nabla \phi \frac{\partial f}{\partial \mathbf{v}} = 0 \quad , \quad (3.1)$$

where \mathbf{v} is the velocity at the position \mathbf{x} of the distribution at time t and ϕ is the gravitational potential.

An approximate solution for the collisionless Boltzmann equation can be found by sampling the smooth distribution function f by a discrete set of N points that move according to the Hamiltonian equations of motion

$$\frac{d\mathbf{x}_i}{dt} = \mathbf{v}_i \quad , \quad (3.2)$$

$$m_i \frac{d\mathbf{v}_i}{dt} = \mathbf{F}_i \quad , \quad (3.3)$$

under their mutual gravitational attraction

$$\ddot{\mathbf{x}} = -\nabla \phi \quad , \quad (3.4)$$

where the gravitational potential ϕ is the solution to the Poisson equation

$$\nabla_x^2 \phi = 4\pi G \rho \quad . \quad (3.5)$$

The force on the i th N -body particle (i.e., the force at a given point in the gravitational field sampled by N massive particles) is given by

$$\mathbf{F}_i(\mathbf{x}_i) = \sum_{j=1; j \neq i}^N \frac{G m_i m_j (\mathbf{x}_i - \mathbf{x}_j)}{|\mathbf{x}_i - \mathbf{x}_j|^3} \quad , \quad (3.6)$$

where G is the gravitational constant, m_i is the mass of the i th particle, and \mathbf{x}_i is its position. Solving this equation requires the initial knowledge of the positions (\mathbf{x}_i) and velocities (\mathbf{v}_i).

The simplest way to solve for the force is with a brute force *direct* summation over all the particles. The direct summation method is computationally expensive as it scales as N^2 and usually not appropriate for large simulations. It has only been achieved for up to 2×10^6 number of (stellar) particles for a small number of simulations using special hardware chips operated in parallel (e.g., Harfst et al., 2007). Situations where it is beneficial to use the direct summation approach is where an accurate force computation is called for, such as close encounters or stellar clusters.

Because the direct summation method is too slow for most large simulations, it is wise to approximate the force calculation provided the force errors are random and small enough. Since the force field is often noisy, because it is made of discrete particles, small random errors will not significantly affect the system. Numerical techniques such as the *Particle-Mesh*, *Tree-Method*, and some *Hybrid methods* have been developed to solve the N -body problem with acceptable accuracy and reduce the N^2 problem to a more manageable form that scales as $\sim N \log N$, or N in the case of the fast multipole method (Ambrosiano et al., 1988).

In this Section we will only focus on the *Particle-Mesh* method as it is employed in RAMSES used for the simulations presented later on.

3.1.1 Particle-Mesh Method

The Particle-Mesh (PM) method typically consists of the following five main steps:

1. Map the mass density ρ on a regular mesh.
2. Solve the Poisson equation to find ϕ (Eq. 3.5).
3. Compute the particle acceleration at each grid point using the computed value of ϕ .
4. Update the particle velocity using the particle acceleration (Eq. (3.3)).
5. Update the particle positions using the particle velocity (Eq. (3.2)).

The simplicity of this method is one of the big advantages but using a fixed grid can bring problems regarding the force accuracy of the simulation, as the spacial resolution is limited by the grid size. Because of this problem *adaptive meshes*, with varying resolution where it is needed, are often employed rather than a fixed grid. The adaptive mesh method brings more subtleties and makes the implementation more complicated as cells of different sizes have to be evolved with different time-step lengths, and the grid structure cannot be represented by ordinary arrays as in the case of homogeneous grids.

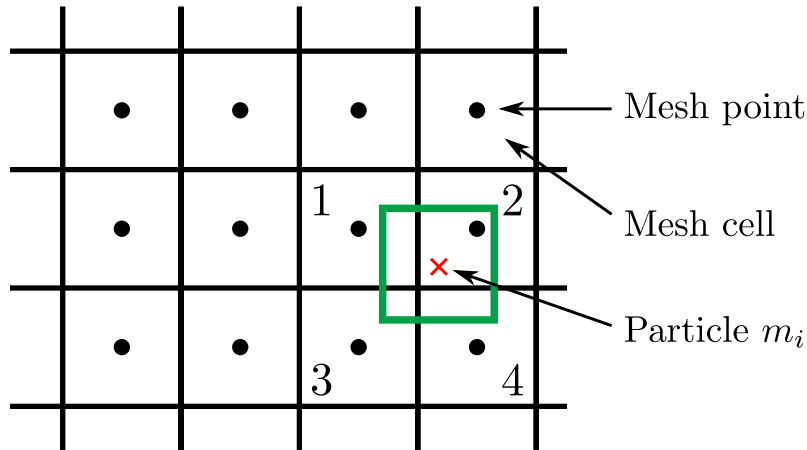


Figure 3.1: ‘Cloud-in-Cell’ method used to distribute the mass density of the particle situated at the red cross and with mass m_i between neighbouring grid cells (1,2,3,4) according to how much of the cube overlaps with each cell. The method is used in order to be able to calculate the gravitational potential.

The mapping of the particles onto the grid cells can be performed using a bi-linear interpolation, also called ‘cloud-in-cell’ (CIC) technique (Hockney & Eastwood, 1981). Higher order mapping techniques can be found in Peng et al. (2007). With the CIC technique, each particle is considered to be a cubic ‘cloud’ with the same physical size of its grid cell centered on the particle. The particle mass is then distributed between the neighbouring grid cells according to how much of the cube overlaps with each cell (see Figure 3.1 for an illustration).

Once the density is mapped onto the grid, the Poisson equation must be solved at every point. This can, for instance, be done with a *conjugate gradient* method that iteratively solves for the gravitational potential. Another possibility to solve for the potential would have been to use a *fast Fourier transform* (see Binney & Tremaine (2008) for a detailed description).

Having determined the gravitational potential, the acceleration of each particle feeling the force of the gravitational field can be calculated. To calculate the acceleration on the mesh a 7-point (in 3D, $2n+1$ points for n dimension) finite difference approximation of the gradient can be used. In two-dimensions the 5-point stencil is made up of the point itself and its four neighbours. With this approximation the first derivative of a two-dimensional function $\phi(x, y)$ is given by

$$\nabla\phi(x, y) = \frac{\partial\phi}{\partial x} + \frac{\partial\phi}{\partial y} \quad (3.7)$$

$$\approx \frac{\phi_{i+1,j} - \phi_{i-1,j}}{2\Delta x} + \frac{\phi_{i+1,j} - \phi_{i-1,j}}{2\Delta y} \quad (3.8)$$

with Δx and Δy being the width of the cell.

Using the calculated acceleration at the center of each grid cell we can determine with the inverse CIC method the acceleration of each individual particle where the total acceleration of each particle is the sum of the acceleration of each cell the ‘cloud’ of the particle overlaps.

Finally, the new velocity and position of each particle is calculated using a second-order integration technique. The leapfrog integrator solves exactly an approximated Hamiltonian and thus preserves certain conserved quantities exactly, such as angular momentum and

the phase-space volume. With this method the particle is first given a half *kick*, then the position of the particle is updated with the *drift* step, and finally another half *kick* is given to the particle:

$$\dot{\mathbf{x}}' = \dot{\mathbf{x}}_0 + \frac{1}{2}\mathbf{a}_0\Delta t \quad (3.9)$$

$$\mathbf{x}_1 = \mathbf{x}_0 + \dot{\mathbf{x}}'\Delta t \quad (3.10)$$

$$\dot{\mathbf{x}}_1 = \dot{\mathbf{x}}' + \frac{1}{2}\mathbf{a}_1\Delta t \quad (3.11)$$

where $\mathbf{a}_0 = -\nabla\phi(\mathbf{x}_0)$ and $\mathbf{a}_1 = -\nabla\phi(\mathbf{x}_1)$, while the intermediate velocity $\dot{\mathbf{x}}'$ serves only as an auxiliary quantity. For more information on the leap-frog method and other methods see Dehnen & Read (2011).

3.2 Collisional Systems

Although gravity is an important force in the Universe it is crucial to introduce the baryons for studying galaxy formation and evolution processes. The baryons introduce important properties such as feedback mechanisms, cooling, and heating, which are thought to influence the distribution of the baryons in galaxies. This Section reviews how baryons can be simulated and Section 3.4 describes how the physics associated with the baryons such as cooling and heating mechanisms and feedback mechanisms can be modelled.

3.2.1 Deriving the Fluid Equations

In contrast to dark matter, baryons are a highly collisional fluid. Here, the baryons are treated as an astrophysical inviscid fluid whose distribution function is the solution f to the *collisional Boltzmann equation*

$$\frac{df}{dt} = \frac{\partial f}{\partial t} + \dot{\mathbf{x}}\frac{\partial f}{\partial \mathbf{x}} - \nabla\phi\frac{\partial f}{\partial \mathbf{v}} = \left[\frac{\partial f}{\partial t}\right]_{\text{coll}} . \quad (3.12)$$

The left-hand side of the equation is exactly the same as already written in equation (3.1), where the right-hand side of the equation accounts for changes to f by collisions. The collisional term is zero for the collisionless particles such as dark matter and stars.

Observables are extracted from f by taking moments of the Boltzmann equation. The density ρ , bulk velocity v , and specific internal energy of the fluid e at a position \mathbf{x} and time t are given by

$$\begin{aligned} \rho(\mathbf{x}, t) &\equiv \int m f(\mathbf{x}, \mathbf{u}, t) d\mathbf{u} \quad , \\ \mathbf{v}(\mathbf{x}, t) &\equiv \frac{1}{\rho} \int \mathbf{u} m f(\mathbf{x}, \mathbf{u}, t) d\mathbf{u} \quad , \\ e(\mathbf{x}, t) &\equiv \frac{1}{\rho} \int m \tilde{u}^2 f(\mathbf{x}, \mathbf{u}, t) d\mathbf{u} \quad , \end{aligned} \quad (3.13)$$

where \tilde{u} is the velocity of a given particle with respect to the bulk velocity of the fluid and m is the mass of the particles sampling the distribution function.

Assuming the collisions to be elastic and the contributions from collisions involving more than two particles is negligible, the distribution is well represented by the Maxwellian

distribution

$$f(\mathbf{x}, \mathbf{u}, t) d\mathbf{u} = n(\mathbf{x}, t) \left[\frac{m}{2\pi k_B T(\mathbf{x}, t)} \right]^{3/2} \exp \left[-\frac{m(\mathbf{u} - \mathbf{v})^2}{2k_B T(\mathbf{x}, t)} \right] d\mathbf{u} \quad , \quad (3.14)$$

and we get the usual formula for the specific energy of a monoatomic gas $e = \frac{3}{2} \frac{k_B}{m} T$, at temperature T and where k_B is the Boltzmann constant¹.

With some mathematical juggling we can recover from the moment equations (Eq. 3.13) the *continuity equations*, which can be written in their conservative Lagrangian form as

$$\frac{\partial \rho}{\partial t} + \nabla \cdot (\rho \mathbf{u}) = s_1 \quad , \quad (3.15)$$

$$\frac{\partial}{\partial t}(\rho \mathbf{u}) + \nabla \cdot (\rho \mathbf{u} \otimes \mathbf{u}) + \nabla P = \mathbf{s}_2 \quad , \quad (3.16)$$

$$\frac{\partial E}{\partial t} + \nabla \cdot (E \mathbf{u} + P \mathbf{u}) = s_3 \quad , \quad (3.17)$$

where ρ , \mathbf{u} , P , and E are the mass density, velocity, pressure, total energy per unit volume of the flow, and \otimes is the outer product, respectively. The total energy E is given by the sum of the kinetic and internal energy of the fluid

$$E = \frac{1}{2} \rho \mathbf{u} \cdot \mathbf{u} + e \quad . \quad (3.18)$$

Each of the equations express different conservations laws, with the *mass conservation* in equation (Eq. 3.15), *momentum conservation* in equation (Eq. 3.16), and *energy conservation* (Eq. 3.17). Together this system forms the basic equations of fluid mechanics. The terms on the right-hand side are the sink and source terms reflecting the loss or gain of mass, momentum, and energy. In the absence of any sinks or sources, i.e. the source terms are zero, the system of the three equations build a hyperbolic system of conservations laws called the *Euler equations*.

This system is closed by the ideal gas equation of state which relates the pressure and energy:

$$P = (\gamma - 1) \rho e \quad , \quad (3.19)$$

where γ is the adiabatic index.

The Euler equations (i.e., no source or sinks) can be rewritten in their conservative form as

$$\frac{\partial \mathbf{U}}{\partial t} + \nabla \cdot \mathbf{F}(\mathbf{U}) = 0 \quad , \quad (3.20)$$

where \mathbf{U} consists of the conserved quantities

$$\mathbf{U} \equiv (\rho, \rho \mathbf{u}, E) \quad (3.21)$$

and

$$\mathbf{F}(\mathbf{U}) \equiv (\rho \mathbf{u}, \rho \mathbf{u} \otimes \mathbf{u} + P, E \mathbf{u} + P \mathbf{u}) \quad . \quad (3.22)$$

This parametrisation will become useful later on in Section 3.2.3 when discussing numerical solutions of the Euler equations.

To couple the baryons with the dark matter and stars, the gravitational potential is included in the momentum equation (Eq. 3.16) as a source term to build

$$\frac{\partial}{\partial t}(\rho \mathbf{u}) + \nabla \cdot (\rho \mathbf{u} \otimes \mathbf{u}) + \nabla P = -\rho \nabla \phi = \rho \mathbf{g} \quad , \quad (3.23)$$

¹ $k_B = 1.38064852 \times 10^{-23} \text{ m}^2 \text{ kg s}^{-2} \text{ K}^{-1}$.

where \mathbf{g} is the local gravitational acceleration.

Other terms accounting for additional physics can also be added to the Euler equations: viscosity (building the Navier-Stokes equations), radiative transfer, magnetic fields, and more. Additionally, new continuity equations can be derived to describe the flow of, for instance, chemicals or photon packets. Section 3.5 will later focus on the addition of photons to the fluid equations, used to study the coupling of photons with the interstellar medium.

3.2.2 Different Approaches to solve the Fluid Equations

There is a huge range of different numerical methods for HD simulations used within astrophysics. They can mostly be divided into three fundamental methods:

- *Grid-based (or Eulerian) Method*: The Euler equations (Eq. 3.20) are numerically evolved on a discrete spacial mesh, where the differential operator is calculated using a second-order finite difference approximation. The fluid quantities are then updated at each point of the grid. To capture the large density ranges often found in galaxy formation simulations or around shocks, an adaptive method is used which recursively refines high density cells (See Section 3.3 for more information). The main (cosmological) AMR codes today are *Art* (Kravtsov et al., 1997), *Orion* (Klein, 1999), *Flash* (Fryxell et al., 2000), *RAMSES* (Teyssier, 2002), and *Enzo* (O’Shea et al., 2004).
- *Smoothed Particle Hydrodynamics (SPH) (or Lagrangian) Method*: Traces the fluid elements, such as density and pressure, with particles. It is a Lagrangian scheme as the geometry of the flow is closely followed by the particles. An average of a particular quantity such as mass, energy, pressure, or density is calculated considering the local neighbourhood within a smoothing length of each particle. Mathematically this is done by a *kernel* function (see Dehnen (2001) for more information). The most widely used examples of SPH codes are *Gasoline* (Wadsley et al., 2004) and *Gadget* (Springel, 2005).
- *Moving-Mesh Method*: Replaces the smoothing kernel used in SPH codes with a grid computed via Voronoi tessellation. The method tries to retain the high accuracy of mesh-based HD methods for shocks while at the same time using the advantages of Galilean-invariance and geometric flexibility of the SPH codes. Hence the principal idea for achieving such a convergence is by allowing the mesh itself to move and deform (see (Springel, 2010) for further detail). This has been implemented into *Arepo* (Springel, 2011).

In theory all methods will give the same answer, provided they both solve the same underlying equations. In practice, since most treatments of numerical fluid dynamics are approximations that have different numerical error, each method has its own advantages and disadvantages.

There are many reasons why the SPH approach is attractive. One reason is that it closely related to N -body codes since both are particle based. The particles in an SPH code naturally trace the flow of mass in high density regions and no adaptive refinement is needed. In addition, the computational time is significantly reduced in low density regions which allows more computational time available for high density regions. Also by modelling gas flow with particles, one may track their evolution without specifically

adding tracer particles to follow the gas flow as one would have to do with a grid based code (and is implemented into RAMSES). Furthermore, grid based techniques experience numerical diffusion caused by numerical errors in tracing the motion of structures across the grid in bulk flows. AMR codes can also suffer from problems due to their inherent non-Galilean-invariance, which can be reduced at the cost of extra resolution.

A number of comparison tests between SPH and grid based codes have been performed in the last few years (e.g., Agertz et al., 2007; Khokhlov, 1998; Scannapieco, 2013). They demonstrated that the main problem of SPH is that it is poor at capturing instabilities. Agertz et al. (2007) demonstrate that for the situation where a dense flow moves past low-density flows the low-density flow tends to be under-sampled as a result of the smoothing kernel. This results in the inability to produce Kelvin-Helmholtz instabilities in such situations. On a similar note, a dense sphere moving through a low-density wind does not experience shredding from turbulence and survives much longer than expected from the Kelvin-Helmholtz timescale. While these were idealised test cases this is still worrying for various types of simulations such as for the study of accretion flows, outflows, ram pressure stripping and so on. Furthermore, Mitchell et al. (2009) demonstrate that SPH particles retain their entropy which causes artificial cusps to form in simulations of two gas clouds colliding (as in the merger of galaxy clusters).

It is important to note that since Agertz et al. (2007), improvements in the SPH methods have been made to address the problems pointed out in this paper (e.g., Price, 2008; Heß & Springel, 2010; Junk et al., 2010; Abel, 2011; Murante et al., 2011; Read & Hayfield, 2012), although issues with numerical convergence remain (Zhu et al., 2015).

If subgrid physics such as feedback mechanisms are involved, even more discrepancy can appear (Scannapieco et al., 2012). Subgrid physics, however, is an important topic itself where a lot of discussions and improvements still have to be made. Current effort is focused on implementing more realistic subgrid models (e.g., Agertz et al., 2013; Kimm et al., 2015; Hopkins et al., 2011). Additionally, future computing power will also help in resolving important physics used to calibrate and test the various subgrid models.

For the purpose of this thesis we will concentrate on Eulerian, grid-based techniques. The subgrid models used for the simulations will be discussed in 3.4.

3.2.3 Discretising the Fluid to solve it on a Grid

In order to be able to solve the fluid equation (Eq. 3.20) numerically we discretise the equations and with this the underlying fluid into individual chunks (grid cells) and compute the continuity equations at each grid point by computing the partial differential equations only with respect to the neighbouring grid cells. With \mathbf{U} in equation (3.20) consisting of conserved quantities such a problem is also called the *Riemann Problem* and naturally arises due to the discreteness of the grid where for each grid cell an individual Riemann Problem has to be solved.

More precisely, the Riemann problem for equation (3.20) is an initial value problem with *left* and *right* initial data at the discontinuity. The solution to this Riemann problem is made of three waves: *rarefaction* waves propagating towards the denser medium, a rapid *shock* wave propagating towards the less dense medium, and a slow *contact* wave to the least dense medium.

One can rewrite equation (3.20) into quasi-linear form as

$$\frac{\partial \mathbf{U}}{\partial t} + \mathbf{J} \nabla \cdot \mathbf{U} = 0 \quad (3.24)$$

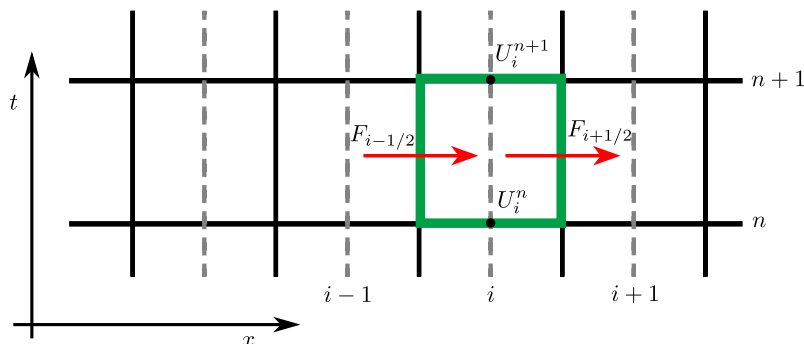


Figure 3.2: Control volume of dimensions Δx by Δt is computational cell i marked in green. New value \mathbf{U}_i^{n+1} is given in terms of old value \mathbf{U}_i^n and intercell fluxes $\mathbf{F}_{i-1/2}$ and $\mathbf{F}_{i+1/2}$.

where \mathbf{J} is the Jacobian matrix $\mathbf{J} \equiv \partial \mathbf{F} / \partial \mathbf{U}$ and the three eigenvalues are the characteristic speed of each of the waves propagating within the system.

To solve equation (3.20) in the discretised form it is evaluated in the computational cell i (marked in green in Figure 3.2 and at position x_i) of dimension Δx by Δt . In one-dimension this discretisation can be written as

$$\mathbf{U}_i^{n+1} = \mathbf{U}_i^n + \frac{\Delta t}{\Delta x} \left(\mathbf{F}_{i+1/2}^{n+1/2} - \mathbf{F}_{i-1/2}^{n+1/2} \right) \quad (3.25)$$

where n corresponds to time index ($n = t$ and $n + 1 = t + \Delta t$). The notation \mathbf{U}_i^n means the discrete value of \mathbf{U} in the center of cell i (at position x_i) at time t^n . $\mathbf{F}_{i+1/2}^{n+1/2}$ and $\mathbf{F}_{i-1/2}^{n+1/2}$ are intercell fluxes evaluated at the cell interfaces.

Equation (3.25) is an explicit² conservative formula that gives a time-centered marching scheme in terms of the data \mathbf{U}_i^n , and the grid dimensions Δx , Δt , and the intercell fluxes $\mathbf{F}_{i+1/2}$ and $\mathbf{F}_{i-1/2}$.

The procedure to find \mathbf{U}_i^{n+1} is as follows

1. First the most accurate left and right initial values (\mathbf{U}_i^n , \mathbf{U}_{i+1}^n) have to be found such that no spurious diffusion terms, or strongly oscillating solutions around the discontinuity is introduced.
2. Once the good left and right initial values (\mathbf{U}_i^n , \mathbf{U}_{i+1}^n) are found one is left with finding a solution for the flux across the cell. This can be done in a way such that the solution of the flux across the cell is completely defined by the fluxes at the interface $i - 1/2$ (on position $x_{i-1/2}$) and $i + 1/2$ (on position $x_{i+1/2}$).
3. Once the flux has been determined, all that is left to do is to put the solutions into equation (3.25) to determine \mathbf{U}_i^{n+1} .

These three steps will now be briefly explained.

² Note that in equation (3.25) the state of a system at later time is calculated from the state of the system at the current time. Such a method is also called *explicit* method. There also exists another approach to find a solution to the Riemann problem by solving an equation involving the current state of the system at time t and the later one at time $t + \Delta t$. Such an approach is called *implicit* method. Implicit methods require an extra computation and can be much harder to implement. On the other hand they do not diverge from an analytical solution regardless of the size of Δt (although a smaller value will give faster convergence), whereas explicit methods require Δt to be small enough to be stable (hence are *conditionally stable*.)

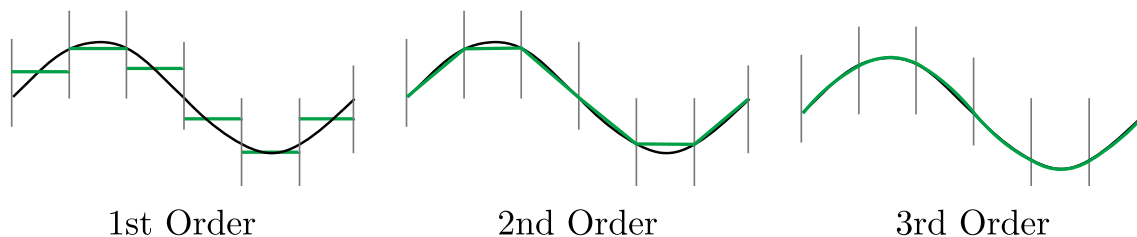


Figure 3.3: Reconstruction (green) of the initial function (black) with a first (left), second (middle), and third (right) order scheme.

(1) Finding good left and right values of \mathbf{U} at the discontinuity

Several methods exist to determine the most accurate left and right initial values.

The *first order* Godunov method (Godunov 1956) takes the most intuitive approach and uses only the left and right data ($\mathbf{U}_i^n, \mathbf{U}_{i+1}^n$), from which the intercell flux is determined. Because the Godunov method takes only the central value of the flux across the discontinuity it is also called *piecewise constant method* (PCM). Although stable, the Godunov method introduces a spurious diffusion term that prevents the method from producing discontinuities.

Higher order solutions rely on a better representation of the left and right values rather than only taking the central discretised values of \mathbf{U} within each cell (see Figure 3.3 for a representation). There are various ways to reconstruct the initial function from which the left and right values are reconstructed, but generally the second order solution approximates the initial function with a linear function, hence called the *piecewise linear method*, whereas the third order solutions approximates the initial function with a parabolic function (usually found via Spline-Interpolation), also called the *piecewise parabolic method* (PPM); see Figure 3.3 for an illustration.

One problem of the PLM method is that it is *non-monotoneous* (i.e., a maximum can become a minimum and vice versa) and this introduces solutions that oscillate around sharp discontinuities. A solution to this problem has been introduced by Harten et al. 1983 which is to limit the slope used for the interpolation between the left and right points in order to preserve the monotonicity of the solution, also called the *Total Variation Diminishing* (TVD) scheme. To do so, one defines

$$TV^n = \sum_i |\mathbf{U}_{i+1}^n - \mathbf{U}_i^n| \quad , \quad (3.26)$$

and ensures that the condition

$$TV^{n+1} \leq TV^n \quad (3.27)$$

is always verified. With $\Delta U_i = \min(\Delta U_L, \Delta U_R)$, the MinMod, used for the results presented later, in one-dimension is

$$U_{i+1/2,L}^n = U_i^n + \frac{\Delta U_i}{2} \quad , \quad (3.28)$$

$$U_{i-1/2,R}^n = U_i^n - \frac{\Delta U_i}{2} \quad (3.29)$$

and hence ensures that $U_{i+1/2,L}^n \leq U_{i+1/2,R}^n$. An illustration of the two slope limiters is shown in Figure 3.4.

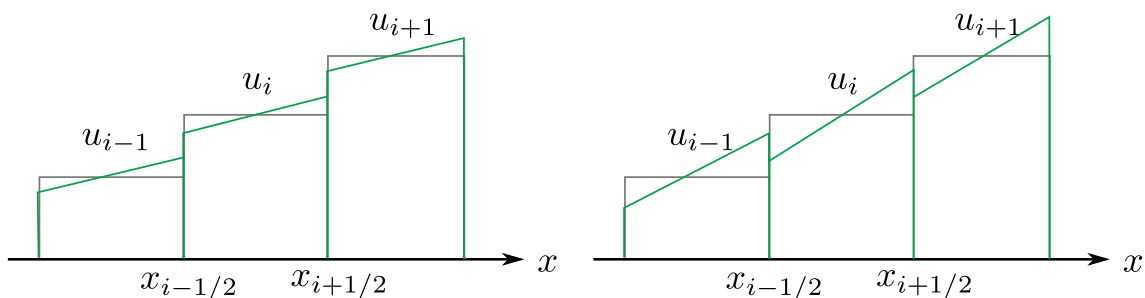


Figure 3.4: Illustration of the Total Variation Diminishing (TVD) method: *left* MinMod and *right* MonCen. The reconstruction is shown in green and the piecewise constant function is shown in black.

(2) Finding a solution for the flux across the cell

Having established the left and right initial values ($\mathbf{U}_i^n, \mathbf{U}_{i+1}^n$) at the discontinuity one is left with finding the flux $\mathbf{F}_{i+1/2}^{n+1/2} = \mathbf{F}(\text{RP}[\mathbf{U}_L^n, \mathbf{U}_R^n])$. Where \mathbf{U}_L and \mathbf{U}_R are the cell centred values in the left and right cell, respectively.

A simple type of approximation to find the flux for the Riemann problem was proposed by Harten et al. (1983), which makes a local linearisation of the Euler equation and calculates the flux using the possible wave patterns in the exact solution that are represented by a single wave pattern.

One such approximation is the *Harten-Lax-von Leer* (HLL) approximation that only takes the two (out of four) fastest waves into account. Another flux approximation function is the *Global Lax-Friedrich* (GLF) solver takes only the two fastest waves propagating in two opposite directions, and finally the *HLLC* (HLL Contact) solver (Toro et al., 1993), used for the results presented later on, that takes the same two waves as the HLL solver but also incorporate the contact discontinuity into the wave pattern:

$$(\mathbf{F}_{\text{HLL}})_{i+1/2}^{n+1/2} = \frac{\lambda^+ \mathbf{F}(\mathbf{U}_L) - \lambda^- \mathbf{F}(\mathbf{U}_R) + \lambda^+ \lambda^- (\mathbf{U}_R - \mathbf{U}_L)}{\lambda^+ - \lambda^-} \quad (3.30)$$

where \mathbf{U}_L and \mathbf{U}_R are the cell centred values in the left and right cell, respectively. Additionally, $\lambda^+ = \max(0, \lambda_i^{\max}, \lambda_{i+1}^{\max})$ and $\lambda^- = \min(0, \lambda_i^{\min}, \lambda_{i+1}^{\min})$ are the maximum and minimum eigenvalues of the Jacobian $\partial \mathbf{F} / \partial \mathbf{U}$ that, as already mentioned above, corresponds to the wave speeds of the waves propagating within the system.

The resulting HLLC solver is as accurate and robust as an exact Riemann solver, but it is simpler and computationally much more efficient than the latter.

(3) Determine \mathbf{U}_i^{n+1}

Once the flux has finally been determined all that is left to do is to put the solutions into equation (3.25) to determine \mathbf{U}_i^{n+1} . And the calculation is finished.

All the equations above have been presented in their one-dimensional form. The three-dimensional setup can, however, be reduced to three one-dimensional problems with the unsplit method.

3.3 RAMSES: A numerical N -body and HD code using adaptive mesh refinement (AMR)

RAMSES (**R**affinement **A**daptatif de Maille **S**ans **E**ffort **S**urhumain) is an N -body and HD code written by Teyssier (2002) and used for all the simulations presented in this thesis. It is written in Fortran 90, can be run in parallel across different computers using the Message-Passing Interface (MPI), and has been tested on various different super-computer architectures.

The code is able to simultaneously follow particles that are gravitationally coupled with an inviscid fluid, where they are coupled by considering the total density field when solving the Poisson equation to compute the gravitational potential and the force field. The code is an Eulerian code and, hence, uses a grid to calculate the hydrodynamics whereas the N -body solver is based on the PM-technique (see Section 3.1.1 and Section 3.2.3). In RAMSES, the Euler equations are solved in their conservative forms which has the advantage that energy is perfectly conserved and therefore the flow is not altered by some energy sinks. The HD solver is a second-order unsplit Godunov scheme made for perfect gases. It used the PLM method to reconstruct the initial function via linear interpolation between the left and right points whereas either the MinMod or MonCen TVD scheme can be chosen. Additionally, to find the intercell flux there exists the HLL, GLF, and HLLC solver (see Section 3.2.3 for more detail). For the results presented in this Thesis the HLLC solver and the MinMod scheme is used.

To have additional refinement at places with higher mass (or other criteria), the grid is recursively refined adaptively where the data structure is based on a tree. Additionally, an adaptive time-stepping scheme is implemented (see Section 3.3.2).

The RAMSES code has been tested for various physical problems (e.g., Booth et al., 2013; Roškar et al., 2014; Dubois et al., 2014; Agertz & Kravtsov, 2015; Rosdahl et al., 2015; Dubois et al., 2015a; Volonteri et al., 2016; Habouzit et al., 2016; Dubois et al., 2016). It has proven to be extremely suitable for studying problems related to galaxy formation and their dynamics as both dark matter, stars, and gas must be taken into account. Additionally, many other physical processes such as heating and cooling (Section 3.4.1), star formation (Section 3.4.3), stellar feedback mechanisms (Section 3.4.4), magneto-hydrodynamics ((Fromang et al., 2006; Teyssier et al., 2006)), black hole physics (Section 3.4.5), as well as radiative hydrodynamics (Section 3.6) have been implemented in the code.

From the wide range of stellar feedback mechanisms implemented into RAMSES over the last few years (e.g., Dubois & Teyssier, 2008b; Agertz et al., 2013; Teyssier et al., 2013) the one used for the simulations presented in this thesis will be summarised in Section 3.4.4.

3.3.1 Adaptive Mesh Refinement structure

The easiest way to solve the fluid equations on a grid is to use a uniform Eulerian grid. Having a uniform grid everywhere however results in poor resolution for regions of high density or is computationally too expensive because of high resolution everywhere. For example, in galaxy scale simulations, the density variation between giant molecular clouds (~ 100 pc) and the interstellar medium (~ 10 kpc) is several orders of magnitude. Hence, it is preferable to have a constant mass resolution to place better resolution in denser regions. As another example, simulations of supernovae, jets, or heat bubbles from black holes propagating through the ISM may wish to resolve the shock boundary more highly relative to the more uniform and un-shocked medium. Refining only in places of interest leads to adaptive mesh refinement (AMR).

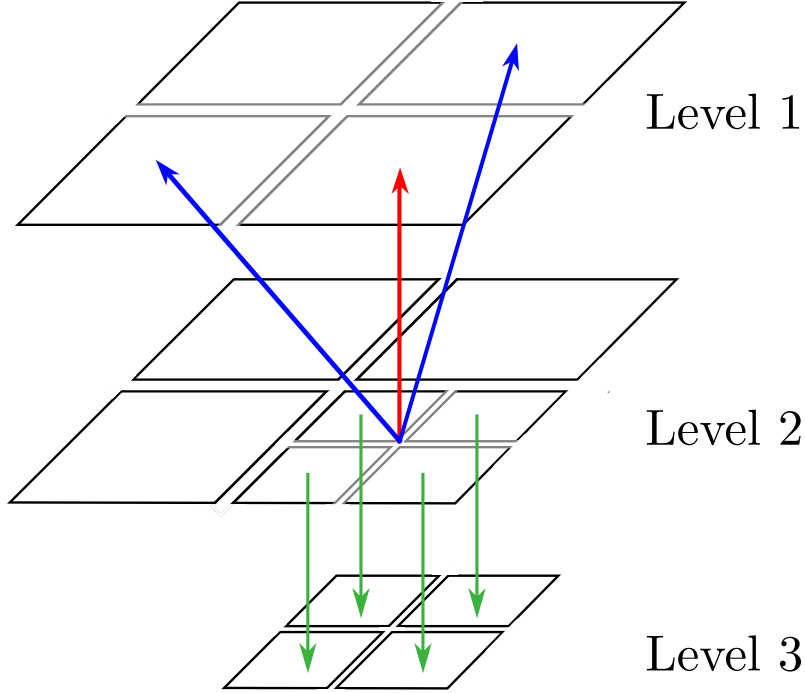


Figure 3.5: 2D representation of the oct-tree structure of RAMSES. Each oct (here on Level 2) points to its mother cell (red arrow) and the neighbouring mother cells (blue arrows), and to its children octs (green arrows).

The basic grid element in RAMSES is an oct, which is a grid composed of eight cells (in three dimensions, four cells in 2D, and two in 1D). Each cell stores the gas properties of density, momentum, internal energy and metallicity (plus any other passive scalar one may wish), and is also used for calculating and storing the gravitational force. The whole simulation box is one oct at Level 1 ($l = 1$), which is then homogeneously refined to a minimum refinement level l_{\min} . This uniform grid is called the *coarse* level and has a resolution given by $2^{-l_{\min}} \times \text{boxlen}$, with boxlen being the length of the entire simulation box. The grid is then allowed to refine by subdividing itself by a power-of-two where, at a given level l , the cell has a spatial resolution of $2^{-l} \times \text{boxlen}$. Eventually, the grid either exceeds the resolution that is required by the refinement criterion, or reaches a maximum refinement level l_{\max} , giving the box a maximum *effective* resolution of $2^{l_{\max}}$ cells widths per box width. If, on the other hand, a grid cell does not meet this refinement criterion then it will be destroyed and the next coarser level is considered.

In RAMSES, the octs are stored in a tree-like structure, which allows the calculation of the forces and the grid refinements level by level (see Figure 3.5 for a 2D representation of the data structure). Each oct points to its *mother* cell (red arrow in Figure 3.5) of one level lower, the neighbouring mother cells on each face of the oct (6 cells in 3D, and 2 cells in 2D; blue arrows in Figure 3.5), and, if refinement is done, to the *daughter* octs (up to 8 octs in 3D, 4 octs in 2D, and 2 octs in 1D). The calculation of the HD equations is only done on the *leaf* cells, which are the cells without daughters.

An important rule concerning the refinement is that RAMSES allows neighbouring cells to only differ by one level across cell boundaries, i.e., $l - 1 \leq l' \leq l + 1$, with l' being the level of the cell in question.

The criteria used to determine whether a particular grid cell should be refined depends on the different applications. As already alluded in this Section, simulations of strong shocks benefit from refinement based on pressure or density gradients, whereas for galaxy simulations, or cosmological simulations, a refinement on mass is perfectly suitable. It is also possible to refine on a passive scalar that traces certain flows of interest, for example a jet emerging from a black hole at the center of a galaxy.

A widely used technique in computationally expensive simulations, notably astrophysical numerical simulations, is to split a computational task across multiple processors, often with independent system memory. This is done using the *Message Passing Interface* (MPI) that splits the simulation volume into multiple *domains*, which is a volume of adjacent grid cells and particles, as well as *ghost* regions surrounding the domain. After each time-step, the code communicates changes in adjacent domains between processors. After a number of user-specified time-steps, the domain decomposition is reshuffled for better load-balancing. In RAMSES the location of these domains is determined using the Peano-Hilbert curve (Peano, 1890; Hilbert 1891). The curve is specifically designed to link cells such that each cell is adjacent to the next cell on the curve. The domains are split along this curve such that each processor is given an equal number of grid cells. This process is also known as *load-balancing*, whereas the ability of a code to optimally use multiple processors is known as *scaling*. Processes that require significant communication between CPU's typically reduce the quality of the scaling. RAMSES scales reasonably well for galaxy simulations, where there are multiple regions that only interact via gravity, whereas for problems with a single point source, for example a jet, or a supernovae event, the initial scaling can be poor.

3.3.2 Time-stepping Scheme

RAMSES uses the *Courant* condition to determine the minimum time-step within the simulation, which states that in a single time-step no information should move further than the length of one cell. Since the information speed is the sound crossing time, this translates to the constraint

$$\Delta t \leq \frac{\Delta x}{c_s} \quad (3.31)$$

where Δx is the cell width at a given level and c_s is the sound speed.

To determine the time-step for an adaptive mesh, where on each level the Courant conditions are satisfied, RAMSES proceeds as follows. First, a coarse time-step length $\Delta t_{l_{\min}}$ is estimated via (the minimum of) Courant conditions in all l_{\min} cells. Before the coarse step is executed, the timestep of the higher levels are determined recursively: The next finer level is told to execute the same time-step in two sub-steps and additionally has to satisfy the Courant conditions for all the cells. It then asks its next finer level to execute two timesteps with additionally satisfying the Courant condition. This continues until the highest available level l_{\max} , which contains no daughter octs. On this level, the two substeps are finally executed, with step lengths $\Delta t_{l_{\max}} \leq \Delta t_{l_{\min}}/2^{l_{\max}-l_{\min}}$. Once the two sub-steps are executed, the $l_{\max} - 1$ time-step is re-evaluated to be no longer than the sum of the two sub-steps just executed at l_{\max} , and then one $l_{\max} - 1$ step is executed. Then it goes back to l_{\max} to execute two steps, and so on. The sub-stepping continues further in this fashion across the level hierarchy and ends with one time-step for the coarsest level cells.

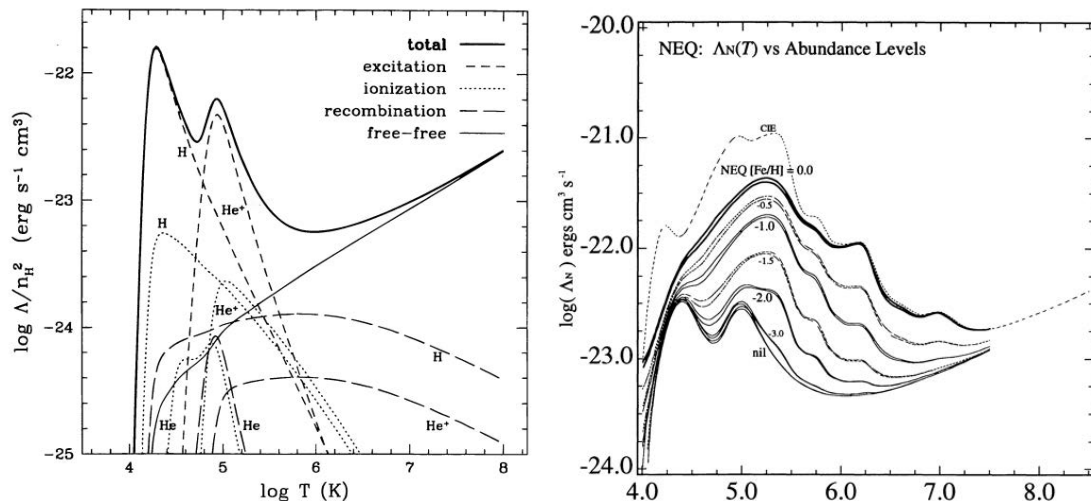


Figure 3.6: Cooling rates as a function of temperature. *Left*: Contribution of the different species in the primordial gas (Katz et al., 1996). At high temperatures the cooling process is dominated by Bremsstrahlung. Different collisional processes contribute towards the net cooling effect at intermediate temperatures. Below 10^4 K the gas can still cool with the help of metal line and molecular cooling. *Right*: Effect of metal-line cooling on the cooling function (Sutherland & Dopita, 1993). The metals can increase the cooling efficiency. At certain temperatures a metallicity of only 10% increases the cooling efficiency by an order of magnitude.

3.4 Sub-grid physics to study galaxy formation and evolution

3.4.1 Radiative Cooling and Heating

The process of gas cooling and heating is a necessary and fundamental ingredient in galaxy formation. As discussed above, gas falls into the potential wells of the dark matter halos forming a hot gaseous halo. In order to form stars inside galaxies, the gas is required to cool and to collapse into molecular clouds where the gas loses its pressure support via *radiative cooling*.

With cooling and heating, the energy equation (Eq. 3.17) can be written as

$$\frac{\partial E}{\partial t} + \nabla \cdot (E\mathbf{u} + P\mathbf{u}) = \underbrace{\frac{\rho}{m_P} \Gamma}_{\text{heating rate}} - \underbrace{\left(\frac{\rho}{m_P}\right)^2 \Lambda(\rho, T)}_{\text{cooling rate}} \quad (3.32)$$

with the first term of the right hand side being the *heating rate* and the second term being the *cooling rate* both in energy emitted per unit volume per unit time. Both terms depend only on the gas density, temperature, and ionisation state. However, collisional ionisation equilibrium (CIE) is usually assumed, which allows the ionisation state to be calculated as functions of temperature and density only, and thus the ionisation state does not need to be tracked in the code.

The left side (taken from Katz et al., 1996) of Figure 3.6 shows $\Lambda(T)$ for a gas consisting only of hydrogen and helium and in absence of the UV radiation. It shows that at high temperatures ($T > 10^6$ K), typically the temperature of a hot gas halo, the cooling process

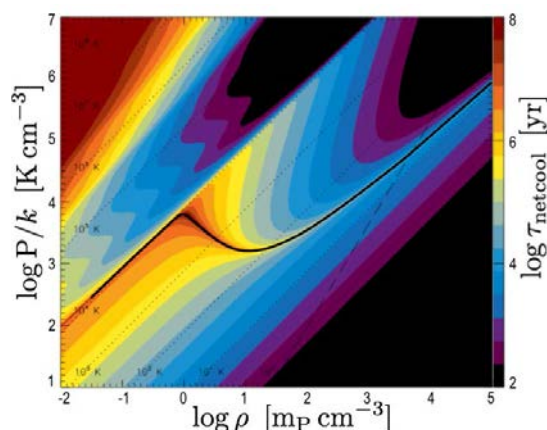


Figure 3.7: Heating/cooling rate colored by the net-cooling time used in RAMSES assuming zero metallicity. Values below the solid correspond to cooling, whereas above the black line, the gas is cooled.

is dominated by Bremsstrahlung (written free-free in Figure 3.6). At intermediate temperatures ($T = 10^4 - 10^6$ K), different collisional processes contribute towards the net cooling effect down to the temperature of $T = 10^4$ K. Below 10^4 K the gas can still cool with help of metal line and molecular cooling that takes place in very dense molecular clouds, and are, thus, very important for the formation of stars. Since metals and molecules have more emission lines than hydrogen and helium, metal-enriched gas as well as molecular gas provides a more efficient cooling than gas with a low metallicity. Dalgarno & McCray (1972), Rosen & Bregman (1995) as well as Sutherland & Dopita (1993), also discuss the effect of metal-line cooling on the cooling function. The right side of Figure 3.6 (taken from Sutherland & Dopita, 1993), shows how the metals can increase the cooling efficiency and that at certain temperatures a metallicity of only 10% increases the cooling efficiency by an order of magnitude.

Assuming that the number density of each ion is roughly in equilibrium at each value of total gas density ρ , temperature T , and metallicity Z , tabulated values of $\Lambda(\rho, T, Z)$ can be constructed where for a given (ρ, T, Z) the value of the cooling function can be found by interpolating across the table. Such an approach is taken by RAMSES since it does not require memory-intensive tracking of the chemistry of the gas. Various cooling models are implemented into RAMSES but the one used in the simulations presented in this thesis use the standard H and He cooling from Katz et al. (1996), with an additional contribution from metals based on the Sutherland & Dopita (1993) model above 10^4 K. Below 10^4 K RAMSES uses the rates of Rosen & Bregman (1995). The functions implemented cover a wide grid of temperatures and metallicities using published atomic data and processes. The UV background is included as a separate parameter in Λ where RAMSES employs the model provided by Haardt & Madau (1996). Figure 3.7 shows such a cooling function employed in RAMSES, where zero metallicity is assumed, and where the solid black line is the pressure of the equilibrium gas, i.e., when

$$\frac{\rho}{m_P} \Gamma - \left(\frac{\rho}{m_P} \right)^2 \Lambda(T_{eq}) \stackrel{!}{=} 0 \quad . \quad (3.33)$$

Hence, below the solid black line, the gas is heated, whereas, above the black line, the gas is cooled.

For a better understanding about the time it takes the gas to cool, one defines the ‘net cooling time’ τ_{netcool}

$$\tau_{\text{netcool}} \equiv \frac{\epsilon}{\dot{\epsilon}} = \frac{\epsilon}{\Lambda(\rho, T)} \propto \frac{\rho T}{\Lambda(\rho, T)} \quad , \quad (3.34)$$

where the temperature of the gas is given by

$$T = \epsilon \frac{(\gamma - 1) m_H}{\rho k_B} \mu \quad , \quad (3.35)$$

with γ the ratio of specific heat ($\gamma = 5/3$, for a monatomic gas), m_H the proton mass, k_B the Boltzmann constant, and μ the mean molecular weight.

Assuming, to first order, that cooling is predominantly a process caused by collisions, we find that $\Lambda \propto \rho^2$ which leads to $\tau_{\text{netcool}} \propto 1/\rho$ showing that, in general, high density gas cools faster than low density gas.

Figure 3.7 shows the net cooling time for different densities, ρ , and pressures, P , employing the cooling functions $\Lambda(\rho, T)$ given by Sutherland & Dopita (1993) for temperatures above 10^4 K and the cooling functions by Inutsuka & Koyama (2002) for temperatures below 10^4 K. It shows that the first order assumption is valid for low pressures whereas for higher pressures it is a bit more complicated.

The net cooling time is important for a better understanding of the three regimes of gas cooling discussed in Section 3.4.1.

3.4.2 Polytropic Equation of State

The region of star formation and the impact of stellar feedback, as well as AGN depends strongly on the distribution of the gas within the interstellar medium (ISM). In particular, the multi-phase structure of the ISM represents an important ingredient that should not be neglected in numerical studies of galaxy formation. However, cosmological simulations (but partly also galaxy scale simulations) are unable to fully resolve the true spatial structure of the ISM and, and are missing various phenomena, such as thermal instabilities, and turbulence that give rise to the formation of the complex multi-phase structure of the ISM. Since an exhaustive numerical description of the ISM is not feasible in a galaxy context, there have been several attempts to include some of the relevant physics as a sub-grid model that mimics detailed ISM simulations and observations.

The idea for this sub-grid multi-phase ISM model is that thermal energy injected by randomly exploding supernovae acts as an ‘effective’ pressure, approximated by a polytropic equation of state:

$$T = T_0 \left(\frac{\rho}{\rho_0} \right)^{\kappa - 1} \quad , \quad (3.36)$$

where ρ_0 is the star formation threshold density, T_0 is the thermal equilibrium temperature threshold, and κ is the polytropic index. Note that this index is not the same as the adiabatic index γ of the underlying perfect gas (usually chosen to be equal to $5/3$). The effect of the effective pressure provided in the multiphase model is to stabilise the ISM against gravitational collapse. Springel & Hernquist (2003) note that for $\kappa > 4/3$ the effective pressure provides enough vertical thickening to stabilise gaseous discs against rapid break up into clumps as a result of dynamical instabilities. In cases where the local polytropic index would fall below $4/3$ the gas would be unstable. This can be seen when looking at the effect of the polytropic equation of state on the Jeans length and mass,

that describe the equilibrium where the hydrostatic pressure sufficiently counteracts the collapse under its own weight:

$$\lambda_J = c_s \sqrt{\frac{\pi}{G\rho}} \propto \frac{c_s}{\sqrt{\rho}} \propto \sqrt{\frac{\rho}{T}} \propto \rho^{\kappa/2-1} \quad , \quad (3.37)$$

$$M_J = \rho \lambda_J^3 = c_s^3 \sqrt{\frac{\pi^3}{G^3 \rho}} \propto \frac{c_s^3}{\sqrt{\rho}} \propto \sqrt{\frac{T^3}{\rho}} \propto \rho^{3\kappa/2-2} \quad , \quad (3.38)$$

with

$$c_s = \sqrt{\gamma \frac{k_B T}{\mu m_H}} \quad . \quad (3.39)$$

For $\kappa = 4/3$ the Jeans mass becomes independent of the gas density meaning that the gas is unstable and collapses (constant Jeans mass). For $\kappa = 2$ the Jeans length becomes independent of the density (constant Jeans length). Hence, κ is usually chosen between $4/3$ and 2 , where in the simulations presented later on a value of $\kappa = 5/3$ is chosen.

3.4.3 Star Formation

Galaxies contain stars and, hence, the creation and destruction of stars are a critical ingredient if we want to understand the Universe around us. Stars form in the very dense environment of molecular clouds in regions where the temperature is favourable for the dense structures to be gravitationally bound. Generally, simulations of galaxies are unable to capture the spatial, and density scales required to simulate star formation (SF) directly. Instead *sub-grid* models for SF must be adopted that are constructed with the help of observational constraints. It requires an analytic expression that converts a certain portion of the gas in a grid cell into stars when certain criteria are met.

Indeed, such an expression is given by the Kennicutt relation (Eq. 2.18) that connects the amount of newly formed stars to the amount of local gas. To find a local SF relation, the surface densities in the Kennicutt relation are divided by its volume to get a *Schmidt*-relation, where stars form at a rate proportional to some power of the density scaled by an efficiency:

$$\dot{\rho}_* = \begin{cases} \epsilon \rho_g / t_{\text{ff}} & \text{if } \rho > \rho_0 \\ 0 & \text{otherwise} \end{cases} \quad , \quad (3.40)$$

with ϵ being a measure of the SF efficiency and usually of order of a few percent ($\epsilon \sim 0.01 - 0.02$; Krumholz & Tan, 2007). Additionally, $t_{\text{ff}} \propto 1/\sqrt{G\rho}$ is the local free-fall time and, hence, $\dot{\rho} \propto \rho/t_{\text{ff}} \propto \rho^{1.5}$.

The density threshold ρ_0 is, thus, used to constrain the places in which stars are able to form. Applying such a criteria is absolutely necessary. SF is observed to be highly clustered under essentially all conditions (Lada & Lada, 2003, and references therein) and without a criteria such as the density threshold (for others see below), this is not captured in simulations. Not only would the stars without a proper criteria form in the wrong places, but it has also been shown that this would suppress the effects of stellar feedback (Governato et al., 2010). Generally stars form in massive star clusters that allow for overlapping SNe ‘bubbles’ that expand more efficiently than individual SNe remnants (e.g., Keller et al., 2015). Additionally, the formation of stars within the massive stellar clusters also concentrates feedback to act preferentially in the dense, star-forming gas, and, hence, where it is needed to regulate SF.

For simulations, the density threshold is typically set to be the Jeans mass M_J at the highest level of refinement (with spatial resolution Δx):

$$\lambda_J = c_s \sqrt{\frac{\pi}{G\rho_0}}, \quad (3.41)$$

$$M_J = \rho_0 \lambda_J^3 = c_s^3 \sqrt{\frac{\pi^3}{G^3 \rho_0}}, \quad (3.42)$$

where λ_J is the Jeans length, G is the gravitational constant, ρ_0 is the star formation threshold, and c_s is the sound speed given by

$$c_s = \sqrt{\gamma \frac{k_B T}{\mu m_H}}. \quad (3.43)$$

To choose an appropriate star formation threshold given by equation (3.41) the Jeans length has to be determined. Truelove et al. (1997a) showed that because of the discretisation to solve the HD equations the gas can artificially fragment due to numerical uncertainties. They showed that this artificial fragmentation can be avoided by ensuring that $\Delta x \leq \lambda_J/4$ and hence

$$\lambda_J = N_{\text{cell}} \Delta x, \quad (3.44)$$

with $N_{\text{cell}} \geq 4$. Secondly, the temperature in equation (3.41) is usually chosen to be the temperature floor in equation (3.36).

With a resolution of $\Delta x = 40$ pc, $N_{\text{cell}} = 4$, and a temperature floor of $T = 600$ K, the appropriate star formation threshold is $\rho_0 \sim 10 \text{ H cm}^{-3}$.

To reproduce the Schmidt-law in the simulation, the probability to form a star with a stellar mass of $m_* = \rho_0 \Delta x^3$ with the average density of stars formed per unit time is related to by equation (3.40) (see Rasera & Teyssier, 2006 for more detail). Once the star is formed, it is decoupled from the gas as a star particle, which behaves as an N -body particle tracing a continuous mass distribution of stars with a given initial mass function. In Section 3.4.4 stellar feedback will be considered, and how supernovae events return mass, momentum, and/or energy to the gas, and hence introduce complex feedback cycles in the SF rate.

For completeness, note that the simple density threshold, although most often used, is not the only possibility for a threshold to form stars. Other common requirements include restricting star formation to gas that is below some temperature, or is Jeans unstable, or is in convergent flows, or which has a short cooling time. Other studies have also considered a molecular criterium, where they used some combination of density and metallicity to estimate a sub-grid molecular gas fraction and restricted star formation to the ‘molecular’ gas (Robertson & Kravtsov, 2008; Kuhlen et al., 2012). And finally, Hopkins et al. (2013) include a self-gravity criterion based on the local virial parameter, and the assumption that self-gravitating gas collapses to high density in a single free-fall time.

In practice, the physical interpretation of these criteria depend both on the resolved dynamical range of the simulation and on the mean properties of the galaxies being simulated. A deeper discussion of the different SF criteria is however not the topic of this thesis.

3.4.4 Supernova Feedback

Both observations and simulations of galaxies show that galaxy evolution is highly affected by how stars form, evolve, and die within the galaxy. The latter likely being the most

important in this cycle, as an exploding supernova (SN) can have a significant influence on the gas distribution within the galaxy and, thus, on how and where further star formation occurs. Hence, SNe can influence the global properties of galaxies. The impact of SNe (and other processes like AGN, see below) on galaxies is called feedback, and is believed to be a very important driver of low-mass, dwarf galaxies (Dekel & Silk, 1986).

While the topic of this thesis did not focus on the impact of SN feedback, this Section still gives a short summary about how SN feedback is implemented in simulations and explains how it is modeled in RAMSES. This Section will mostly focus on the method used for the results presented later on.

In order to create any model of SN feedback it is first necessary to understand the population of SNe that exist in the Universe as well as the progenitor stars of these events. Minkowski (1940) created the label ‘Type I’ and ‘Type II’ to refer to SN without and with hydrogen Balmer-lines in their light curves. Since then these classifications have been further refined to create a different classes of SNe with different spectral features in their light curves. For example, Wheeler & Harkness (1990) note that SN without hydrogen lines but with strong silicon features are fairly common, and hence defined another class (‘Type Ia’), that are believed to be the result of thermonuclear explosions of white dwarf stars. ‘Type II’, on the other hand, are largely thought to be the result of core-collapse, an event where the core of a massive star collapses into a neutron star or black hole releasing a large quantity of gravitational energy into the rest of the star resulting in a SN explosion (Woosley & Janka, 2005). While the internal mechanisms governing the conversion of gravitational potential energy from a core collapse event in a massive star to a SN blastwave is still subject to research it is clear that a massive star undergoing core collapse will eject part of their envelope as stellar winds and is able to alter the shape of the ISM. This is in contrast to Type Ia SNe, whose progenitors are typically low-mass stars that do not produce strong winds. The SN feedback recipes presented in this Section will primarily focus on the modeling of Type II SNe and is based on the assumption that a star particle contains on average one Type II SN with a lifetime of ~ 10 Myr.

Once the supernova has escaped the stellar envelope, it evolves into a strong shock that can be modelled simply as a Taylor-Sedov blastwave (Sedov, 1946, Taylor, 1950). One method implemented in RAMSES, also referred to as *kinetic* feedback, deposits mass, momentum, and energy of a pre-evolved Sedov-Taylor blast wave, onto the grid over 2-3 grid cells (Dubois & Teyssier, 2008b). The reason for such an approach is that, due to limited resolution, the initial blast-wave-phase is poorly resolved. Hence, by pre-computing the Sedov blast-wave in the given density field and placing it onto the grid around the star, one successfully attains an accurate picture of the early SN evolution. It has, however, been shown, that this SN feedback implementation is not able to destroy large molecular clouds, and is not efficient at regulating the remaining cold gas reservoirs (see Dubois et al., 2015b for more detail).

An alternative method of SN feedback implemented in RAMSES, also called *delayed-cooling*, is described in Teyssier et al. (2013) and corresponds to a maximally efficient model for which 10^{51} erg per $10 M_{\odot}$ massive star is injected into non-thermal energy. To prevent the supernova-heated gas from catastrophically cooling, and losing most of its energy before it can expand into the ISM, cooling is locally turned off. They proposed a simple formalism that is thought to capture the various non-thermal processes (i.e., radiative pressure, X-ray heating, turbulent and magnetic heating, cosmic ray heating etc.). These non-thermal processes dissipate on a much longer time scale than that of the thermal component, hence, energy is stored longer before being radiated away. To mimic this process, the energy from the SN is released both into the thermal energy component,

as well as into a passive scalar ($p\Delta v = 0$), that is passively advected with the flow. This non-thermal energy decays on a timescale of t_{diss} , typically of order of ~ 1 Myr depending on the resolution (see below), and the gas cooling is locally turned off until the velocity dispersion associated with the non-thermal energy component is larger than σ_{NT} , typically $\sim 50 \text{ km s}^{-1}$ but also dependent on the resolution (see below). This approach is along similar lines to Gerritsen & Icke (1997) as well as Stinson et al. (2006); Governato et al. (2010); Agertz et al. (2011).

In the following, the choice of t_{diss} and σ_{NT} depending on resolution (following Appendix A of Dubois et al., 2015b) is now discussed in more detail.

The time evolution of the non-thermal energy (e_{NT}) is modelled using

$$\rho \frac{De_{\text{NT}}}{Dt} = \dot{E}_{\text{inj}} - \rho \frac{e_{\text{NT}}}{t_{\text{diss}}} \quad , \quad (3.45)$$

where the first term on the right-hand side is the energy injection rate by SN explosions given by

$$\dot{E}_{\text{inj}} = \dot{\rho}_* \eta_{\text{SN}} 10^{51} \text{erg}/10M_{\odot} \quad , \quad (3.46)$$

where massive stars release $10^{51} \text{ erg}/10 M_{\odot}$ in typeII SNe, and where the mass fraction of massive stars is η_{SN} . The value for a Salpeter IMF is $\eta_{\text{SN}} \approx 0.1$.

The second term on the right hand side of equation (3.45) is the decay rate due to the dissipation of the energy by processes not captured within the simulation (due to resolution or physics not included) such as turbulence, radiative pressure, cosmic rays, to name a few.

At equilibrium and, by imposing a Schmidt law (i.e., Eq. 3.40), one gets

$$\frac{e_{\text{NT}}}{\rho} = \eta_{\text{SN}} \epsilon_* \frac{10^{51} \text{erg}}{10M_{\odot}} \cdot \frac{t_{\text{diss}}}{t_{\text{ff}}} \quad , \quad (3.47)$$

and with the corresponding non-thermal velocity dispersion defined as $e_{\text{NT}} = 1/2\rho\sigma_{\text{NT}}^2$ we finally arrive at

$$\sigma_{\text{NT}}^2 = 2\eta_{\text{NT}}\epsilon_* \frac{10^{51} \text{erg}}{10M_{\odot}} \cdot \frac{t_{\text{diss}}}{t_{\text{ff}}} \quad . \quad (3.48)$$

Note that the above is a sub-grid model, and, hence, this model mimics the transfer of injected energy from unresolved small scales, with high gas densities, to resolved large-scales, with lower densities. If the non-thermal energy injection were explicitly resolved, it would dissipate on its own timescale, that depends on the underlying dissipation mechanism, such as radiative losses for cosmic rays (Enßlin et al., 2007) or turbulent dissipation.

Assuming, now, a model for unresolved turbulence, the dissipation timescale is the turbulent crossing-time over a few resolution elements:

$$t_{\text{diss}} \approx \lambda_{\text{J}}/\sigma_{\text{NT}} \quad (3.49)$$

where the length of the blast wave that can travel without any radiative losses is the Jeans length $\lambda_{\text{J}} = N_{\text{cell}}\Delta x$ with $N_{\text{cell}} \geq 4$ (see also Section 3.4.3). Equation (3.48) becomes

$$\sigma_{\text{NT}} = \left(2\eta_{\text{NT}}\epsilon_* \frac{10^{51} \text{erg}}{10M_{\odot}} \cdot \frac{\lambda_{\text{J}}}{t_{\text{ff}}} \right)^{1/3} \quad . \quad (3.50)$$

Imposing that the gas free-fall time is that at the threshold of star formation (i.e., $t_{\text{ff}} = \sqrt{3\pi/32G\rho_0}$) one finds

$$\sigma_{\text{NT}} = \left(2\eta_{\text{NT}}\epsilon_* \frac{10^{51}\text{erg}}{10M_{\odot}} N_{\text{cell}}\Delta x \right)^{1/3} \left(\frac{32G\rho_0}{3\pi} \right)^{1/6}, \quad (3.51)$$

$$\approx 48 \left(\frac{\eta_{\text{NT}}}{0.1} \right)^{1/3} \times \left(\frac{\epsilon_*}{0.01} \right)^{1/3} \times \left(\frac{N_{\text{cell}}\Delta x}{4 \times 10 \text{ pc}} \right)^{1/3} \quad (3.52)$$

$$\times \left(\frac{n_0}{200 \text{ cm}^{-3}} \right)^{1/6} \text{ km s}^{-1}, \quad (3.53)$$

with n_0 being the number density threshold for SF ($\rho_0 = n_0 m_H$, and $n_0 = n_{H,0}/X_H$, with $m_H = 1.6733 \times 10^{-24}$ g and $X_H = 0.76$).

The dissipation time-scale is also fully determined by the choice of η_{SN} , ϵ_* , Δx , and n_0 :

$$t_{\text{diss}} \approx 0.82 \left(\frac{\eta_{\text{NT}}}{0.1} \right)^{-1/3} \times \left(\frac{\epsilon_*}{0.01} \right)^{-1/3} \times \left(\frac{N_{\text{cell}}\Delta x}{4 \times 10 \text{ pc}} \right)^{2/3} \quad (3.54)$$

$$\left(\frac{n_0}{200 \text{ cm}^{-3}} \right)^{-1/6} \text{ Myr}. \quad (3.55)$$

Therefore, depending on the resolution of the simulation and the chosen parameters η_{SN} , ϵ_* , Δx , and n_0 , one ensures that the energy deposited by the SN propagates without any radiative loss up to a chosen number of cells ($N_{\text{cell}}\Delta x$) since the cooling is turned off up to that distance.

These SN feedback models are, however, still very crude. Various improvements with more physically motivated assumptions have been made over the past few years. For instance, Agertz et al. (2013) and Kimm et al. (2015) propose an approach that imparts the correct amount of momentum by the explosions. Hopkins et al. (2011) additionally include the steady input of energy from stellar winds and radiation from bright stars and find that their simulated global star formation efficiencies are consistent with the observed Kennicutt-Schmidt relation. Note that, it is still unclear which feedback process dominates the evolution of galaxies, and how they interact with the gas content and influence star formation.

3.4.5 Black Hole Feedback

None of the simulations presented in this thesis have been performed using a sub-grid model for black-hole (BH) feedback. Since a motivation for the studies in this thesis is to improve our understanding of how quasar-driven winds are powered by the complex coupling of photons with the gas in order to improve current sub-grid models for large-scale (cosmological) simulations it is of benefit to know in more detail what exactly one wants to improve. Therefore, I will revise in this Section how BH feedback is implemented in RAMSES and briefly compare it to other implementations in order to better understand the weakness' of the models. More detailed discussion can be found in Dubois et al. (2012a, 2015b)

Once the BH formation site is identified the BH is placed close to the center of the galaxy with an initial seed mass of $\sim 10^4$ - $10^5 M_{\odot}$.

The BH in the center of the galaxy then evolves with the galaxy and accretes mass at a rate estimated with a modified Bondi formula (Hoyle & Lyttleton, 1939; Bondi & Hoyle, 1944; Bondi, 1952), which takes into account the self-gravity of the gas, and limited by

the Eddington accretion rate. The motion of the BH is calculated with a direct N -body solver.

In RAMSES, AGN feedback can be modelled as a combination of two different modes, the so-called *radio* mode operating at low accretion rate (i.e., when $\chi \equiv \dot{M}_{\text{BH}}/\dot{M}_{\text{Edd}} < 0.01$) and the *quasar* mode operating otherwise at high accretion rate (i.e., when $\chi > 0.01$); see Section 2.4 for a theoretical motivation.

The quasar mode is modeled with an isotropic injection of thermal energy into the gas within a sphere of radius Δx , and an energy deposition rate of

$$\dot{E}_{\text{AGN}} = \epsilon_c \epsilon_r \dot{M}_{\text{acc}} c^2 \quad , \quad (3.56)$$

where $\epsilon_r \sim 0.1$ is the mass-to-radiation conversion efficiency, ϵ_c is a free parameter accounting for the HD coupling efficiency with a value between 0.05 (e.g., Springel et al., 2005b; Wurster & Thacker, 2013) and 0.15 (e.g., Booth & Schaye, 2009; Teyssier et al., 2011; Dubois et al., 2012a), and \dot{M}_{acc} is the mass accreted since the last feedback event, and c is the speed of light. Typically the free parameter ϵ_c is tuned by hand to reproduce global observations, for instance the BH-mass to Bulge-mass relation, BH mass to galaxy velocity dispersion relation, and BH density in our local Universe (see Dubois et al., 2012a for a detailed discussion).

At low accretion rates onto the BH the radio mode is modelled to deposit the AGN feedback energy given in equation (3.56) into a bipolar outflow with a jet velocity of around 10^4 km s^{-1} into a cylinder with a cross-section of radius Δx and height $2\Delta x$ following the implementation by Omma et al. (2004).

As already alluded at the beginning of this Section the implementation does not come without caveats that I attempted to understand better during my thesis.

Firstly, with the radio mode implementation above the jet has the same density as the ambient gas within the disc and is over-dense with respect to the gaseous halo gas (thus is also called a *heavy jet*). Such a jet generally propagates ballistically because of momentum balance, and creates almost no cocoon, hence misses backflows, and thermalises only a small part of its kinetic power. A *light jet* (under-dense with respect to the ambient gas), in contrast propagates much more slowly according to the momentum balance at the jet head and generates a prominent backflow with a wide and low-density cocoon (e.g., Sutherland & Bicknell, 2007). Most of the radio sources observed at a redshift $z \sim 1$ correspond to light-jets (see Section 2.4 for detailed discussion) that the implementation discussed above most likely fails to reproduce. The biggest difference between the heavy and light jet models is on the interaction between the jet and the galaxy that cosmological simulations are not able to resolve anyways. A more detailed discussion of a possible effect of such an interaction is given in Chapter 4.

Secondly, the free parameter used to tune global observations and used to model the quasar mode feedback hides in reality complex physics about how radiation emitted from a thin accretion disc surrounding the BH effectively couples to the surrounding ISM and eventually drives a large-scale wind. The efficiency of the coupling on the other hand depends on various physical properties e.g., optical depth around the black hole, porosity of the multiphase gas, luminosity of the black hole to name a few. A deeper investigation about the coupling between the radiation and the gas using radiation-hydrodynamical (RHD) simulations will be presented in Chapter 5. In such RHD simulations, the emission, absorption, as well as propagation of photons and their interaction with the gas is self-consistently followed. Such detailed RHD simulations in turn should help to improve our understanding of how the quasar radiation effectively couples to the gas, in particular via

the coupling of infrared (IR) radiation to dust, how powerful quasar winds are eventually driven, and how the subgrid model presented above can be improved.

Furthermore, the implementations discussed are not only implemented into RAMSES but also in other codes, albeit the implementations vary slightly between the different codes. They have been tested in cosmological simulations (e.g., Di Matteo et al., 2005; Sijacki et al., 2007; Di Matteo et al., 2008; Booth & Schaye, 2009) as well as on smaller galaxy scales (e.g., Proga et al., 2000; Nayakshin & Zubovas, 2012; Novak et al., 2012b; Wagner et al., 2012; Gabor & Bournaud, 2014). These simulations showed the importance of a strong feedback suppressing star formation in order to match the observed high-mass tail of the galaxy mass function (see Section 2.3.3 for a detailed discussion).

However, while the use of a strong feedback model is very attractive, it still has to be investigated whether the efficiencies used as well as implementations are really a good representation of what is happening in the Universe.

In order to investigate the coupling of photon energy to the gas, radiation has to be modelled with the radiation-hydrodynamical (RHD) equations (described in Section 3.5). The emission of photons from the AGN is modelled using a spectrum of radiation from the central SMBH where for each photon band modelled the corresponding photon energies are injected into the grid cells.

Knowing the frequency distribution of energy $J(\nu)$ for the radiative black hole the average photon energies within each band are evaluated by

$$\bar{\epsilon}_i = \frac{\int_{\nu_{i0}}^{\nu_{i1}} J(\nu) d\nu}{\int_{\nu_{i0}}^{\nu_{i1}} J(\nu)/h\nu d\nu} \quad (3.57)$$

where h is the Planck constant, and (ν_{i0}, ν_{i1}) the frequency interval for the photon band i .

The frequency distribution of an average quasar in the Universe is given by Sazonov et al. (2004), calculated using published AGN composite spectra in the optical, and X-rays, while also considering the cosmic X-ray background and the contribution of AGN to infrared wavelengths, and the estimated local mass density of SMBHs. Figure 3.8 shows the broad-band spectrum of the average quasar adopted by Sazonov et al. (2004) for an obscured quasar. Once the emission from the quasar is known the propagation of photons and their interaction with the gas via the dust is self-consistently modelled with the RHD equations. How the propagation of photons can be simulated is described in the next Section.

3.5 Radiation-Hydrodynamics (RHD)

To simulate how radiation couples to the gas, in particular how the IR radiation couples with the dust, radiative hydrodynamical (RHD) simulations are used where the emission, absorption, and propagation of photons and their interaction with the gas is self-consistently followed (see Chapter 5). The following Section will revise how the propagation of photons can be simulated while the methods used for the simulations presented later on. The Chapter will summarise the methods explained in detail in Rosdahl et al. (2013); Rosdahl & Teyssier (2015a).

3.5.1 The Radiation-Hydrodynamics equations

With the specific intensity of the radiation, $I_\nu(\mathbf{x}, \mathbf{n}, t)$, at the location \mathbf{x} and time t one can write the energy of photons with frequency over the range $d\nu$ around ν propagating

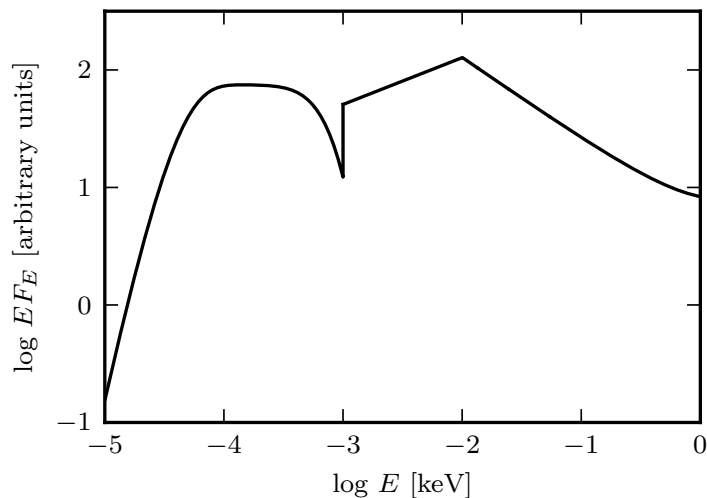


Figure 3.8: Energy spectrum of an average quasar adopted by Sazonov et al. (2004) for an obscured quasar used to calculate the effect of quasar feedback on their surrounding.

through the area dA in a solid angle $d\Omega$ around the direction \mathbf{n} as

$$\int I_\nu d\nu d\Omega dA dt \quad . \quad (3.58)$$

The equation of radiative transfer (RT) that describes the change in I_ν as a function of propagation, absorption, and emission can then be written as

$$\frac{1}{c} \frac{\partial I_\nu}{\partial t} + \mathbf{n} \cdot \nabla I_\nu = -\kappa_\nu I_\nu + \eta_\nu \quad , \quad (3.59)$$

(e.g., Mihalas & Weibel Mihalas, 1984), where c is the speed of light, κ_ν is the gas absorption, and η_ν is the source function.

There are two main challenges involved in implementing radiative transfer and coupling it to hydrodynamics. The first is the number of dimensions: Three spatial, two angular, frequency, and time. In comparison, the Euler equations of hydrodynamics involve ‘only’ four dimensions, space and time. The second challenge is the time-stepping scale which is, because of the Courant condition, inversely proportional to the speed of propagation, that is typically a thousand times shorter for RT than for HD. Because of these challenges approximations have to be made.

The different approaches to solve the RT (and also RHD) equations can be placed in two general categories, *ray-based schemes* and *moment methods*:

- **Ray-based schemes:** Make the assumption that the radiation field is dominated by sources. This leads to the local intensity of radiation I_ν to only be a function of the optical depth τ along *rays* from each source. Hence, once the radiation intensity at each point is known, the rates of photoionisation, heating, and cooling can be calculated and then the transport of photons through the gas can be determined.

Typically, ray-based schemes assume infinite light speed meaning that the rays are cast from the source and arrive at their destination instantaneously although some codes (e.g., Pawlik & Schaye, 2008; Petkova & Springel, 2011; Wise & Abel, 2011)

also allow for finite light speed, that adds to the complexity, memory requirement, and computational load. The problem with the infinite light speed is that it might overestimate the ionisation fronts speed in under-dense regions (see Rosdahl et al., 2013 first for more detail).

Another disadvantage of ray-traced methods is that they suffer from an increased computational load with the number of sources. Additionally, they also fail to model correctly the multi-scattering of IR photons, something that was of particular interest when looking at how efficiently radiation couples to the gas (see Chapter 5).

- **Moment-based methods:** The basic idea is to reduce the angular dimensions by taking angular moments of the RT equation (Eq. 3.59). This can be thought of as changing from a beam description to that of a field or a fluid, where the individual beams are now replaced at a given volume in space with a collective ‘bulk’ direction that represents an average of all the photons crossing this space. The simplifications of this approach is that the angular dimensions are now eliminated from the problem, and the equations take a form of conservation laws, like the Euler equations of HD. Because of this the radiative transfer equations can be naturally coupled to the HD equations and can be solved with the same numerical methods as described in Section 3.2.3.

However, the simplification of reducing the angular dimensions also leads to the main drawback of the approach, which is that the directionality of the propagation of the photons is largely lost and the radiation becomes diffusive. This is generally a good description of the optically thick limit, where the radiation scatters a lot anyways, but not in the optically thin regime where the radiation is free-streaming.

Futhermore, the difference between the characteristic timescale of HD and the photons pose another challenge. As described in Section 3.3.2 moments methods based on an time-centred marching scheme have to follow a Courant stability condition that basically limits the radiation (or gas) from crossing more than one volume element in one time-step. But whereas the sound speed of the gas is of order $\sim 10\text{-}1000 \text{ km s}^{-1}$, the speed-of-light is larger by at least two orders of magnitude. This either requires performing many sub-timesteps to simulate a light crossing time, or, as discusses later, artificially reducing the speed of light.

Additionally to reducing the angular dimensions, the frequency range is also reduced. With the multigroup approximation, the frequency range is split into a handful of bins (i.e., five photon groups) and the moment equations of radiative transfer are then solved separately for each group.

3.5.2 Moments of the RT equation

The zeroth and first angular moment of the RT equation (Eq. 3.59) are

$$\frac{1}{c} \frac{\partial}{\partial t} \oint I_\nu d\Omega + \nabla \cdot \oint \mathbf{n} I_\nu d\Omega = -\kappa_\nu \oint I_\nu d\Omega + \eta_\nu \oint d\Omega \quad , \quad (3.60)$$

$$\frac{1}{c} \frac{\partial}{\partial t} \oint \mathbf{n} I_\nu d\Omega + \nabla \cdot \oint \mathbf{n} \otimes \mathbf{n} I_\nu d\Omega = -\kappa_\nu \oint \mathbf{n} I_\nu d\Omega \quad , \quad (3.61)$$

where \otimes denotes the outer product and where isotropic absorption and emission is assumed.

These moments equations contain the first three moments of the specific intensity, corresponding to the radiation energy density E (erg cm^{-3}), the radiation flux \mathbf{F} ($\text{erg cm}^{-2} \text{s}^{-1}$), and the radiation pressure tensor³ \mathbb{P} (erg cm^{-3}):

$$E_\nu(\mathbf{x}, t) = \frac{1}{c} \int_{4\pi} I_\nu(\mathbf{x}, \mathbf{n}, t) d\Omega \quad , \quad (3.62)$$

$$\mathbf{F}_\nu(\mathbf{x}, t) = \int_{4\pi} I_\nu(\mathbf{x}, \mathbf{n}, t) \mathbf{n} d\Omega \quad , \quad (3.63)$$

$$\mathbb{P}_\nu(\mathbf{x}, t) = \frac{1}{c} \int_{4\pi} I_\nu(\mathbf{x}, \mathbf{n}, t) \mathbf{n} \otimes \mathbf{n} d\Omega \quad . \quad (3.64)$$

Substituting these definitions (Eq. 3.62-3.64) into equation 3.60 and equation 3.61 yields the moment equations of radiation energy and flux (see Mihalas & Weibel Mihalas, 1984 for more information)

$$\frac{\partial E_\nu}{\partial t} + \nabla \cdot \mathbf{F}_\nu = S_\nu - \kappa_\nu c E_\nu \quad , \quad (3.65)$$

$$\frac{1}{c} \frac{\partial \mathbf{F}_\nu}{\partial t} + c \nabla \cdot \mathbb{P}_\nu = -\kappa_\nu \mathbf{F}_\nu \quad . \quad (3.66)$$

Here, S_ν is a scalar, isotropic, source function and an integral of the emissivity over all solid angles. With this the angular dimensions have been suppressed from the RT equations and now instead describe an average directionality of flow.

One can now make a *multigroup approximation* where the frequency range is split into a handful of bins, or photon groups, and the equation (3.65) and equation (3.66) are solved separately for each group, that should be in principle be denoted by photon group subscripts, i.e. $E_i, \mathbf{F}_i, \mathbb{P}_i, S_i$. Additionally the gas opacity κ_ν becomes for equation (3.65) the radiation energy mean opacity $\kappa_{E,i}$, and for equation (3.66) the flux weighted mean opacity $\kappa_{F,i}$. For the sake of clarity, those subscripts are omitted unless required.

Similar to the Euler equations in HD the moment equation (3.65) and equation (3.66) need some meaningful and physical closure for the pressure tensor to solve the equations (see Section 3.5.4 for more detail). But first the RT equations have to be connected with the HD equations.

3.5.3 The RHD equations

The system of RHD equations consists of the Euler equations (Eq. 3.20), the equation of state for the gas (Eq. 3.19) that closes the HD equations, and the RT equations (Eq. 3.59) where the hydrodynamics and radiative transfer couples through the thermochemistry, Λ , and the internal energy and momentum exchange between the gas and the radiation field. Therefore the solving of thermochemistry involves not only updating the temperature but also the local radiation field via emission and absorption and preferably also the non-equilibrium ionisation state of the gas; something that has been neglected so far.

To account for the transfer of energy and momentum between radiation and gas the HD equations have additionally to be modified. In HD the fluid energy equation describes the evolution of the gas energy density (see Eq. 3.18):

$$E_{\text{gas}} = \frac{1}{2} \rho \mathbf{u} \cdot \mathbf{u} + e \quad , \quad (3.67)$$

³Not be confused with the actual radiation pressure on gas.

where here the label *gas* is added to the energy density for clarification. The fluid energy equation can be written as

$$\frac{\partial E_{\text{gas}}}{\partial t} + \nabla \cdot (\mathbf{u}(E_{\text{gas}} + P)) = \rho \mathbf{g} \cdot \mathbf{v} + \Lambda \quad , \quad (3.68)$$

where \mathbf{u} and P are the gas velocity and pressure, \mathbf{g} is the local gravitational acceleration, and Λ is the radiative cooling/heating term via thermochemical processes.

The fluid momentum equation can be written as

$$\frac{\partial}{\partial t} (\rho \mathbf{u}) + \nabla \cdot (\rho \mathbf{u} \otimes \mathbf{u}) + \nabla P = \rho \mathbf{g} + \frac{\kappa_R \rho}{c} \mathbf{F} \quad . \quad (3.69)$$

The last term on the RHS is a new term to the source term that describes the radiation momentum absorbed by the gas. Note that here one assumes $\kappa_F \approx \kappa_R$, where the latter is the *Rosseland mean*. This is a valid approximation when the fluid-radiation system is close to local thermal equilibrium and the optical depth is large.

For completeness, note that the opacities are computed in the *co-moving* frame whereas the fluid equations are defined in the laboratory frame. The equations above therefore ignore Doppler effects of these relative motions. The appropriate inclusion of these terms are described in Rosdahl & Teyssier 2015.

3.5.4 Closing the Moment Equations

If one uses both moments equation (Eq. 3.65) and equation (Eq. 3.66) to describe the propagation of the photons, a closure must be provided in the form of the radiative pressure tensor \mathbb{P} , that can be expressed in terms of the Eddington tensor \mathbb{D} , defined by

$$\mathbb{P} = \mathbb{D}E \quad , \quad (3.70)$$

where \mathbb{P} is symmetric by definition.

Note, that if only the zeroth order moment (Eq. 3.65) is taken there is no pressure tensor term in the equations. The closure is then performed on the radiation flux, \mathbf{F} .

There have been three different closure methods proposed in the literature. The first method only takes the zeroth order of the moment equations into account whereas the two other use different approaches in expressing the Eddington tensor:

- **Flux limited diffusion (FLD)**: is the simplest form of moment-based RT implementation as it only takes the zeroth order moment radiative energy conservation equation (3.65) that build an elliptic set of conservation laws. The closure is provided in the form of a local diffusion relation, where the photons essentially just follow the energy gradient, i.e. the radiation flux \mathbf{F} is set equal to the gradient of E .

With the FLD method the photons are very diffusive, which is an appropriate approximation in the optically thick limit (see Krumholz et al., 2007; Commerçon et al., 2011).

- **Optically thin variable tensor formalism (OTVET)**: Composes the radiative field, and hence the Eddington tensor \mathbb{D} , on-the-fly at every point in space from all the radiative sources in the simulation. It assumes that the medium between source and destination is transparent, thus optically thin. By using the radiation sources to close the moment equations and compute flux direction, the computational load scales with the number of sources, which basically negates the main advantage of

moment-based RT. However, given a reasonable number of sources and by neglecting the in-between gas cells (by assuming optically thin gas in-between) this calculation is computationally feasible (see Gnedin & Abel, 2001 and Petkova & Springel, 2011 for more detail). Finlator et al. (2009) take this approach further and include in the calculation the optical thickness between the source and the destination, which makes, however, the implementation additionally slow, albeit accurate.

- **M1 Eddington closure:** takes the ansatz that the specific intensity is composed of an isotropic and a highly directed term (Levermore, 1984a) where the Eddington tensor can be written as

$$\mathbb{D} = \underbrace{\frac{1-\chi}{2}\mathbf{I}}_{\text{isotropic term}} + \underbrace{\frac{3\chi-1}{2}\mathbf{n}\otimes\mathbf{n}}_{\text{directional term}}, \quad (3.71)$$

where χ is the Eddington factor that is left to be determined. Note, that χ has to be between $1/3$ and 1 , where the lower limit corresponds to completely diffusive radiation and the upper limit to completely directional radiation. The M1 model (see also Dubroca & Feugeas, 1999) proposes

$$\chi = \frac{3+4f^2}{5+2\sqrt{4-3f^2}}, \quad (3.72)$$

where f is the reduced flux, defined by

$$f = \frac{|\mathbf{f}|}{cE}, \quad (3.73)$$

which recovers the proper asymptotic limits of the purely directional and purely diffusion regime. Intermediate values of f represent a linear combination of directional and diffusive local radiation.

Because of this linear combination, the M1 closure can establish and retain general directionality of photon flows, and additionally can (unlike the FLD method) to some degree model shadows behind opaque obstacles. The big advantage of the M1 closure is that it is purely local and thus requires no information that lies outside the cell⁴ (unlike the OTVET approximation). Additionally, it makes the system of RT equations locally form a hyperbolic system of conservation laws (ignoring source terms) that are mathematically well understood and for which various numerical methods, also employed to solve HD, exist (see for instance Toro et al., 1994 for detailed discussion).

Improvements to the above M1 model have been proposed where the specific intensity is not only composed into one isotropic and one directional term but also into one additional, mildly anisotropic, term (e.g., Novak et al., 2012a) This allows for an even smoother interpolation between the optically thick and thin limit.

3.6 RAMSES-RT: An RHD extension to RAMSES to model propagation of photons

RAMSES-RT is a radiation-hydrodynamical (RHD) extension to RAMSES that self-consistently adds the propagation of photons and their on-the-fly interaction with hydrogen and helium

⁴This is because we expressed the Eddington tensor only in terms of the variables E and \mathbf{F} .

via photoionisation, heating, and momentum transfer, as well as their interaction with dust particles via momentum transfer. The implementation is fully described in Rosdahl et al. (2013) and Rosdahl & Teyssier (2015a). Because I have used this extension to study the coupling between the photons emitted from an AGN with the gas I will summarise it in this Subsection.

RAMSES-RT solves the radiation advection equations (Eq. 3.65 and Eq. 3.66) using the M1 closure for the Eddington tensor, first introduced by Levermore (1984a). It additionally makes the distinction between the IR photon groups and all other, higher-energy, groups. The IR photons cover the energy range of dust emission and are assumed to be in LTE with the dust particles and exchange energy (or momentum) via absorption and re-emission. The other groups that span energies above the dust emission can be absorbed by the dust, as well as by hydrogen and helium via photoionisation, where the dust-absorbed energy is re-emitted at lower (IR) energies. Because of their behaviour the IR radiation can also be seen as ‘multi-scattering’ whereas the other photons are ‘single-scattered’.

For the non-IR photons, the moment RT equations, following from the radiation advection equations (Eq. 3.65 and Eq. 3.66) can be written as

$$\frac{\partial E_i}{\partial t} + \nabla \cdot \mathbf{F}_i = - \sum_j^{\text{HI, HeI, HeII}} n_j \sigma_{ij} c E_i + \dot{E}_i - \kappa_i \rho c E_i \quad , \quad (3.74)$$

$$\frac{\partial \mathbf{F}_i}{\partial t} + c^2 \nabla \cdot \mathbb{P}_i = - \sum_j^{\text{HI HeI, HeII}} n_j \sigma_{ij} c \mathbf{F}_i - \kappa_i \rho c \mathbf{F}_i \quad , \quad (3.75)$$

$$\mathbb{P}_i = \mathbb{D}_i E_i \quad . \quad (3.76)$$

We sum over the photo-absorbing hydrogen and helium species (HI, HeI, HeII) and E_i is the photon energy density, \mathbf{F}_i the radiation flux, \mathbb{P} is a photon pressure tensor, and \mathbb{D} is the Eddington tensor, given by the M1 closure. Additionally, the absorption coefficients, κ_i have been broken into the corresponding terms, $n_j \sigma_{ij}$, where σ_{ij} is the ionisation cross section (cm^2) between photon group i and ion species j , and which is zero for non-ionising photons (i.e., optical photons). \dot{E} is the rate of emission from point sources (AGN, stars) and hydrogen/helium recombinations.

The dust-absorbed energy is re-emitted into the IR photon-group, for which the RT equations are

$$\frac{\partial E_{\text{IR}}}{\partial t} + \nabla \cdot \mathbf{F}_{\text{IR}} = \dot{E}_{\text{IR}} + \sum_i^{\text{other groups}} \kappa_i \rho c E_i \quad , \quad (3.77)$$

$$\frac{\partial \mathbf{F}_{\text{IR}}}{\partial t} + c^2 \nabla \cdot \mathbb{P}_{\text{IR}} = -\kappa_R \rho c \mathbf{F}_{\text{IR}} \quad , \quad (3.78)$$

$$\mathbb{P}_i = \mathbb{D}_i E_i \quad . \quad (3.79)$$

The difference to the previous equations (Eq. 3.74 - Eq. 3.76) is that firstly there are no photoionisation/recombination terms, as these photons are below the ionising energies and secondly the dust absorption terms that were negative in the previous equations now become positive because of the dust re-emission into the IR group.

In fact there is a lot of complex (dust) physics involved within the calculation of the opacities, which broadly speaking depend on temperature, the dust content and composition, and the shape of the radiation spectrum. The general implementation into RAMSES-RT considers *constant* values for the photon opacities. I have however implemented a slightly

improved version where dust sublimation above a cutoff temperature is included. Updating the opacities to more complex forms is left to future work.

The RT moment equations (Eq. 3.74 - Eq. 3.76 and Eq. 3.77 - Eq. 3.78) are solved after the HD step with an operator splitting approach that involves decomposing the equations into four steps that are executed in sequence over the same time-step Δt :

1. **Photon transport step:** propagates the photons in space. This corresponds to solving the conservative equations (Eq. 3.74 - Eq. 3.76 and Eq. 3.77 - Eq. 3.78) by setting the right hand side to zero. With the M1 closure the resulting system of RT form locally a hyperbolic system of conservative laws and can therefore be integrated using a classical Godunov scheme. For the simulations involving radiation trapping the GLF Riemann solver is used⁵. For more information about the procedure see Section 3.2.3 where a similar approach for solving the HD equations is used.
2. **Photon injection step:** injects radiation from stellar, AGN, or other radiative sources into the grid. This corresponds to the \dot{E}_i term in equation (3.74) and equation (3.77).
3. **Thermochemistry step:** updates the radiation energy density and gas temperature via other terms of absorption, emission, heating and cooling. This is where the photons and the gas couple. In this step not only the photon densities and fluxes evolve but also the ionisation state and temperature of the gas.

After the update of temperature in Step (3) and IR energy in Step (4), the 10% thermochemistry rule is applied where if either T or E_{IR} (or both) are changed by more than 10% from the original value, the entire thermochemistry plus IR-dust temperature coupling sub-step is repeated with half the time-step length. For more information about the full implementation see Rosdahl & Teyssier (2015a).

Additionally, a sub-grid scheme to account for the trapping of IR photons in regions where the mean free path is smaller than the grid spacing is implemented in RAMSES-RT. This scheme recovers the proper asymptotic limit in the radiation diffusion regime (see Rosdahl et al. 2015 for a detailed discussion).

Although all seems to be solved, there is one additional challenge regarding the coupling of the RT and HD equations. First note, that with the chosen approach the fluxes and energy densities are updated *explicitly*. On a similar note the gas properties are also updated by an *explicit* step. An explicit advection solver is constrained by the Courant condition, that states that no information should move further than the length of one cell in a single time-step. This leads to a severe problem as the radiation fluid travels at the speed of light whereas the relativistic gas travels at least two if not three orders of magnitude slower. The significantly different timescales in HD and RT lead to the fact that for every hydrodynamical time-step, one would need to perform 100 - 1000 RT time-steps, which makes it computationally very challenging to couple the RT with the HD. For the moment equations of RT, there are two known solutions to this problem: (i) The use of an implicit method and (ii) use the reduced speed of light approximation (RSLA) used in RAMSES-RT (see also Gnedin & Abel, 2001; Rosdahl et al., 2013). This approach relaxes the Courant condition by changing the speed of light to a *reduced light speed* $\tilde{c} \ll c$ which leads to the RT timestep being much longer and more comparable with the HD timestep. The rationale for the RSLA is that as long as the radiation travels faster than the ionisation fronts, the

⁵A HLL Riemann solver is also implemented in RAMSES-RT but this one is not compatible with the radiation trapping scheme.

results of RHD simulations are more or less converged with respect to the (reduced) speed of light.

However, there is another problem with using the reduced speed of light approximation that starts to become apparent when one is interested in the amount of momentum transferred from the radiation to the gas which is, in case of high luminosity and opacity, mainly driven by the IR radiation. IR radiation is not photo-ionising, and hence it is not a priori obvious whether a reduced speed of light produces converging results, especially when IR trapping becomes important. In fact, our simulations suggest that the reduced speed of light indeed does influence the amount of momentum transferred to the gas and hence an additional criteria has to be applied when using IR radiation in combination with the RSLA (see Section 5.2).

The implementation of the RSLA consist of simply exchanging the true speed of light c with the reduced speed of light \tilde{c} , in *all*, the discretised RT equations and expressions introduced in this Chapter, except equation 3.69.

External pressure-triggering of star formation

Feedback from active galactic nuclei (AGN) has become a generally invoked process in galaxy formation and evolution. It can act on different scales ranging from feedback on the interstellar medium (ISM) of the galaxy to feedback on the circumgalactic gas and (for clusters of galaxies) the intra-cluster medium.

Especially for the large scales, there are observations of cavities in the hot X-ray gas (e.g., McNamara & Nulsen, 2007, 2012) that can be used as a proxy to the jet power by linking their volume to the environmental pressure. Since these cavities are found to be filled with radio-emitting jet plasma, this is a robust approach that probably presents the strongest evidence showing that, on these scales, feedback may be sufficient to offset the gas cooling and explain the lack of strong cooling flows in clusters of galaxies.

On galactic scales, however, the role of AGN feedback is still not fully understood. While there are detailed observations available showing interaction of the AGN with interstellar gas, both for jets and winds, it is unclear what their actual importance on the evolution of the host galaxy is and how they affect the star formation within the galaxy. The wealth of different conflicting observations (see Section 2.4.5) illustrates how complex the picture is and how it possibly depends on the underlying structure of the ISM.

From a theoretical point of view, AGN feedback is thought to be responsible for a number of observations, the most prominent being the possible ability of AGN feedback to suppress or quench star formation in massive galaxies, and, thus, helping to shape the evolution of these galaxies. AGN also provide a possible explanation between the correlation of the central black hole masses with the bulge mass or velocity dispersion.

Semi-analytic models (e.g., Bower et al., 2006; Croton et al., 2006) showed that introducing AGN feedback can bring massive galaxies in agreement with observations. This is also found in cosmological hydrodynamical simulations that include AGN feedback (e.g., Di Matteo et al., 2005; Dubois et al., 2012a; Vogelsberger et al., 2014; Dubois et al., 2014; Khandai et al., 2015a; Schaye et al., 2015). Hence, negative AGN feedback has, over the past few years, grown into a widely accepted mechanism that influences the evolutionary history of massive, luminous galaxies.

It should be noted that these simulations do not make a distinction between the interaction with the gas and feedback at galaxy or intracluster scales. Feedback at large scales is not necessarily the same as on galaxy scales as it involves almost exclusively the interaction of the AGN with a hot and low density gas. On galaxy scales, on the other hand, feedback occurs in the ISM that has densities that vary over several orders of magnitudes, as well as a fractal, cloudy, and turbulent structure. For most simulations, these dense structures are well below the resolution limit, and, hence, the multi-phase structure of the ISM can only be treated with simple sub-grid prescriptions.

Hence, even though the model of AGN feedback exerting negative feedback on its surrounding is largely successful and attractive, it is important to recall that the underlying feedback process is, not yet, well understood.

High resolution, galaxy scale hydrodynamical simulations of jet-driven feedback (e.g., Wagner et al., 2012; Gaibler et al., 2012), but also radiative feedback using radiation hydrodynamics including a clumpy interstellar medium (e.g., Ciotti & Ostriker, 2007, 2012; Novak et al., 2012a; Bieri et al., 2016a), have only recently become feasible. These studies include an adequate treatment of the ISM necessary to investigate the dependence of AGN feedback on jet/radiation power and the properties of the ISM. They have shown that the multi-phase ISM is a crucial ingredient to study the effect of AGN feedback as it determines whether AGN feedback is negative and positive. Generally, negative feedback from AGN

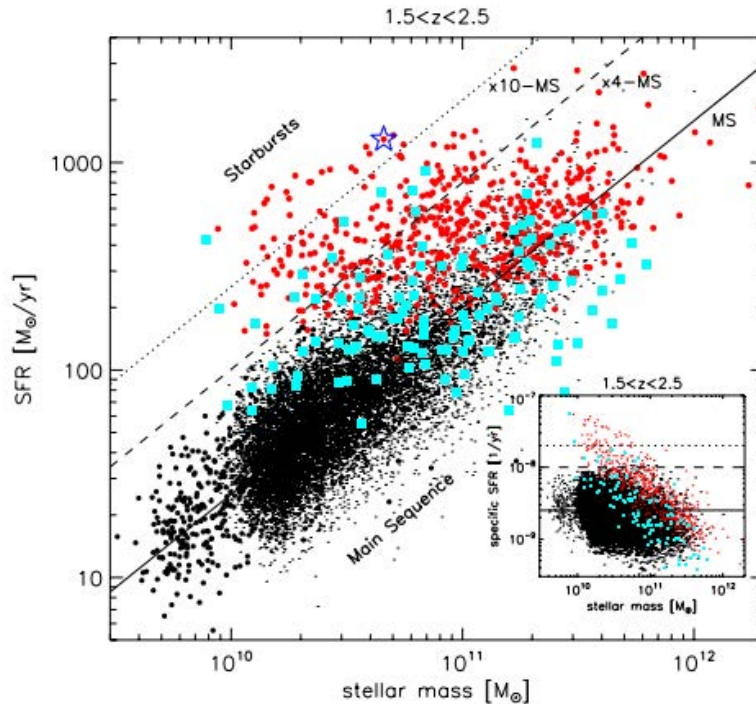


Figure 4.1: Stellar massstar formation rate relation at $1.5 < z < 2.5$. The solid black line indicates the main sequence (MS) for star-forming galaxies at $z \sim 2$ defined by Daddi et al. (2007), while the dotted and dashed lines mark the location 10 and 4 times above the MS (along the SFR axis), respectively. Figure is taken from Rodighiero et al. (2011).

jets is more efficient with small cloud sizes (Wagner et al., 2012, 2016). On the other hand, conditions for AGN jet-triggered positive feedback may be optimal in galaxies with larger clouds, e.g. high-redshift and gas-rich galaxies (Gaibler et al., 2012). Gaibler et al. (2012) simulated a powerful AGN jet within a massive gaseous, clumpy disc and showed that the jet activity causes a significant enhancement of star formation rate (SFR) that is due to the formation of a bow shock and compression of the galactic disc.

While these simulations resolved the jet interaction with the ISM, and the expansion of the blast wave realistically, they were unable to examine long-term effects since they were lacking necessary physics for these time-scales, most notably gravity. Since it is computationally time-consuming to run three-dimensional jet simulations, with the necessary physics, to study the efficiency of positive feedback over at least one dynamical time of the galaxy, it is instructive to investigate the isolated effect of over-pressurisation of a disc on its own. For this, Bieri et al. (2015) (see Section 4.2) and Bieri et al. (2016b) (see Section 4.3) performed three dimensional hydrodynamical simulations of gas-rich and gas-poor discs embedded in a hot, over-pressurised halo and followed the evolution of the disc up to ~ 400 Myr. The simulations include self-gravity of the gas and model the evolution of the SFR. Due to the over-pressure, the disc fragments faster, leading to a larger number of clumps compared to control runs in which the disc is in pressure equilibrium with the halo.

Moreover, pressure-regulated star formation has been argued (e.g., Silk, 2013; Silk & Norman, 2009) to be able to control the global star formation rate as a function of the cold gas content in the star-forming galaxies. It has been shown that it naturally accounts for the Kennicutt-Schmidt relation in both nearby and distant galaxies. Simulations by

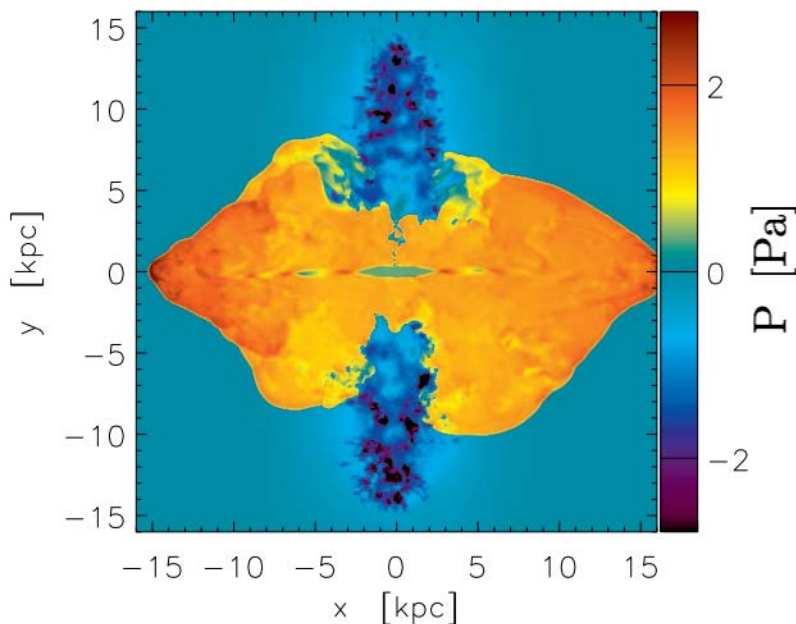


Figure 4.2: Pressure slices through $z = 0$ at $t = 13$ Myr, showing $\log p$ normalised to the ambient pressure. One can see that the bow shock starts to enclose the entire galaxy, and pressurises the ISM of the galaxy from the outside. Figure is taken from Gaibler et al. (2012).

Benincasa et al. (2016) confirm this picture. The inclusion of AGN-induced pressure, by jets and/or winds, has been proposed by Silk (2013), Bieri et al. (2015), and Bieri et al. (2016b) as a possible explanation of the remarkably high star formation rates recently found in the high redshift Universe (e.g., Drouart et al., 2014; Piconcelli et al., 2015; Rodighiero et al., 2015) (see Figure 4.1).

This Chapter will focus on the investigation of AGN-induced, pressure triggered, star formation and examine under which conditions it induces star formation. Because it relies on the pressurisation of the galaxy, Section 4.1 will first summarise why an AGN jet is thought to pressurise the galaxy. Section 4.2 (extracted from Bieri et al., 2015), and Section 4.3 (extracted from Bieri et al., 2016b) will examine possible consequences of the pressure-triggered star formation.

4.1 Jet Propagation

Launched from the accretion disc around the BH a jet propagates through an ISM that is generally much denser than the jet plasma (for an explanation see Section 2.4). Because the jet is underdense with respect to the ambient gas, its forward thrust is too low for ballistic motion and it propagates much more slowly according to the momentum balance. The propagation speed of the jet termination point, the hotspot, becomes much smaller than the bulk speed of the jet beam and a prominent backflow with a wide and low-density cocoon develops (Sutherland & Bicknell, 2007). Since the jet plasma is shocked at the hotspot, the jet thermalises its kinetic energy (e.g., Zanni et al., 2005; O’Neill et al., 2005).

The thermalisation is more efficient with stronger density contrast, and, thus, its exact location depends on the ISM density structure in the nuclear region. These sources have overpressured cocoons (Begelman & Cioffi, 1989), that can compress clouds surrounded by the cocoon. The slow propagation of the terminal shock but high cocoon sound speed allows the high pressure to spread and roughly equalise throughout the cocoon. The efficient thermalisation produces a blastwave originating from this region. Only once the blastwaves created at the two thermalisation points break out of the ISM (vertically for a disc shaped ISM), the driving cocoon pressure vents out to the circumgalactic medium causing the blastwave to weaken and the radio source can propagate to larger scales. Since the jet outside the disc is still much more underdense compared to the circumgalactic medium the bow shock expands laterally and eventually encloses the entire galaxy, and pressurised the ISM of the galaxy from the outside (see Figure 4.2). If the X-ray emission of the ambient gas is strong enough, such as in groups or clusters at low redshift, the low density cocoon causes a deficit (i.e., wide cavity) in the X-rays (Zanni et al., 2003).

There are two crucial ingredients in the jet propagation: the multi-phase ISM, and the underdense nature of the jet:

1. A clumpy and fractal structure of ISM is found in observations and is also generally expected within a supernova-regulated multi-phase medium (McKee & Ostriker, 1977). The densities of the ISM span over many orders of magnitude, although the filling factors of dense gas are usually considerably below unity. Studies of the jet interacting with a multi-phase ISM started with Sutherland & Bicknell (2007) and continued with subsequent studies (Gaibler et al., 2011; Wagner & Bicknell, 2011; Wagner et al., 2012) that found a qualitatively different evolution (as described above) from jets in a smooth ambient medium.
2. The studies cited above focus on the effect of powerful jets which generally fall into the FR II class (Fanaroff & Riley, 1974). A complete sample of these sources ($z < 1$) by Mullin et al. (2008) shows them to have wide cocoons (low lobe axial ratios R_{ax} in their paper) and hence they would correspond to underdense jets. The complementary X-ray view of galaxies with jet feedback shows wide X-ray cavities filled with radio cocoon plasma (e.g., McNamara & Nulsen, 2007; Rafferty et al., 2006), emphasising again the underdense nature of jets with respect to the ambient gas.

An additional consideration regarding the jet density, albeit more indirect, is that the jet powers for FR II radio sources require low jet densities (Saxton et al., 2002) because their jet beam speeds are mildly relativistic even on the kpc scale (Mullin & Hardcastle, 2009).

The low densities with respect to the ambient gas is a critical point, because the important mechanism of feedback is the thermalisation of the mechanical jet power, which transforms a highly anisotropic property (momentum of the bi-polar, collimated jet) into an isotropic one (thermal pressure).

4.2 Playing with Positive Feedback: External Pressure-triggering of a Star-forming Disk Galaxy

REBEKKA BIERI^{1*}, YOHAN DUBOIS¹, JOSEPH SILK^{1,2,3,4}, AND GARY A. MAMON¹

¹Institut d'Astrophysique de Paris (UMR 7095: CNRS & UPMC – Sorbonne Universités), 98 bis bd Arago, F-75014 Paris, France

²Laboratoire AIM-Paris-Saclay, CEA/DSM/IRFU, CNRS, Univ. Paris VII, F-91191 Gif-sur-Yvette, France

³Department of Physics and Astronomy, The Johns Hopkins University Homewood Campus, Baltimore, MD 21218, USA

⁴BIPAC, Department of Physics, University of Oxford, Keble Road, Oxford OX1 3RH

* bieri@iap.fr

Abstract

In massive galaxies, the currently favored method for quenching star formation is via Active Galactic Nuclei (AGN) feedback, which ejects gas from the galaxy using a central supermassive black hole. At high redshifts however, explanation of the huge rates of star formation often found in galaxies containing AGN may require a more vigorous mode of star formation than attainable by simply enriching the gas content of galaxies in the usual gravitationally-driven mode that is associated with the nearby Universe. Using idealized hydrodynamical simulations, we show that AGN-pressure-driven star formation potentially provides the positive feedback that may be required to generate the accelerated star formation rates observed in the distant Universe.

galaxies: formation — galaxies: active — methods: numerical

4.2.1 Introduction

The remarkable universality of the Schmidt-Kennicutt star formation relation, ranging from global fits to star-forming galaxies in the nearby Universe (Kennicutt, 1998b), local fits to star-forming complexes within galaxies (Kennicutt et al., 2007), and to star-forming galaxies to $z \sim 2$, (Genzel et al., 2010b) inspires considerable confidence in the theory of gravitational instability-driven star formation in galactic disks (Krumholz et al., 2012). There are exceptions, most notably in molecular complexes with anomalously low star formation rates (Rathborne et al., 2014), but simple and plausible additions to the usual density threshold criterion for star formation, most notably by incorporating turbulence, may go far towards resolving these issues, as demonstrated both theoretically (for a review see Kritsuk et al., 2011) and phenomenologically in well resolved examples such as NGC 253 (Leroy et al., 2015).

In the high redshift Universe, the accumulation of recent data on remarkably high star formation rates poses a fascinating challenge, (e.g. Drouart et al., 2014; Piconcelli et al., 2015; Rodighiero et al., 2015). Is it simply a question of turning up the gas fraction or is a new mechanism at work for inducing more efficient star formation?

In this Letter, we reinforce the case for the latter, more radical view by simulating the evolution of a fully self-consistent, gas-rich star-forming disk galaxy that is subject to the overpressuring influence of a vigorous outburst from its central Active Galactic Nuclei (AGN). Star formation is a complex interplay between gas supply, multiphase interstellar medium (ISM), cloud collapse, and gas ejection from the disk. We will consider two cases, corresponding to gas-poor (gas fraction 10%) and gas-rich (gas fraction 50%) systems at $z \sim 2$.

The case for inducing star formation via AGN activity has been made analytically (Silk & Norman, 2009) and in simulations (Gaibler et al., 2012; Ishibashi & Fabian, 2012; Wagner

et al., 2012; Zubovas et al., 2013a) with varying degrees of astrophysical reality. The densities in the ISM of high redshift clumpy galaxies are high compared to the densities of the jet. The important mechanism of jet feedback is thus the thermalization of the mechanical jet power, which transforms the highly anisotropic momentum of the bi-polar, collimated jet into a nearly isotropic thermal pressure. As shown in simulations by Sutherland & Bicknell (2007), the jet initially pressurises the disc through a central high pressure bubble; later, the entire galaxy is surrounded by a medium with enhanced pressure. Gaibler et al. (2012) simulated a powerful AGN jet within a massive gaseous, clumpy disc and showed that the jet activity causes a significant enhancement of star formation rate (SFR) that is due to the formation of a bow shock resulting in the compression of the galactic disc. Generally, the simulations demonstrate that whether the AGN activity is jet or wind-induced is irrelevant: after a few kpc, both inputs are indistinguishable.

Furthermore, negative and positive feedback are not necessarily contradictory (Silk, 2013; Zubovas et al., 2013a,b; Zinn et al., 2013) and AGN activity may both quench and induce star formation in different parts of the host galaxy and on different time-scales. A possible observational evidence of both positive and negative feedback is discussed in Cresci et al. (2015b). The outflow observed removes gas from the host galaxy (negative feedback) but also triggers star formation by outflow-induced pressure (positive feedback).

Hitherto, however, star formation in the multiphase ISM has not been followed in adequate detail because of the lack of numerical resolution. For the first time, we study the effects of pressurization of the disc by performing simulations in which we fully include self-gravity of the multiphase ISM and thereby trace the evolution of the star formation rate (SFR) as well as that of the gas content of the system. Because the effects of feedback on a clumpy media by a wind and by a jet are indistinguishable, pressurization of the disk in the simulation is induced in a general way.

4.2.2 Simulation Set-up

To study the effect of an external pressure on a galaxy, we have performed four isolated disc galaxy simulations with two different initial gas fractions of 10% (hereafter, *gasLow*) and 50% (hereafter, *gasHigh*). We allow the galaxies, of one-tenth the total mass of the Milky Way, to initially adiabatically relax to an equilibrium configuration (with a reasonable disc thickness) over the rotation time of the disc at its half-mass radius. After this first relaxation phase, we turn on the external pressure, gas cooling, star formation, and also feedback from supernovae (SNe), as will be described below.

In the initial conditions, the dark matter (DM) particles are sampled with an NFW (Navarro et al., 1997) density profile and a concentration parameter of $c = 10$ using the method introduced by Springel & Hernquist (2005). For the DM particles, the virial velocity is set to be $v_{200} = 70 \text{ km s}^{-1}$, which corresponds to a virial radius of $R_{200} \approx 96 \text{ kpc}$ and a virial mass of $M_{200} \approx 1.1 \times 10^{11} M_{\odot}$. We use 10^6 DM particles with a mass resolution of $1.21 \times 10^5 M_{\odot}$ to sample the DM halo. The stellar disc with total stellar mass of $M_{*} \approx 8.1 \times 10^9 M_{\odot}$ for the *gasLow* simulation and $M_{*} \approx 4.6 \times 10^9 M_{\odot}$ for the *gasHigh* simulation was initially sampled with 5.625×10^5 particles of which 6.25×10^4 were used to sample the bulge. The stellar particles are distributed in an exponential disc with a scale length of 3.44 kpc and scale height 0.2 kpc, and a spherical, non rotating bulge with a Hernquist (1990) profile of scale radius 0.2 kpc. The scale length of the disc explores the two regimes of star formation in a Toomre stable and Toomre unstable disc, respectively, in order to show that extra pressure boosts the star formation not only in already star forming galaxies, but can also

4.2. PLAYING WITH POSITIVE FEEDBACK: EXTERNAL PRESSURE-TRIGGERING OF A STAR-FORMING DISK GALAXY

trigger the star formation in discs that are initially stable against gravitational collapse (Martig et al., 2009).

The simulations are run with the RAMSES adaptive mesh refinement code (Teyssier, 2002). The box size is 655 kpc with a coarse level of 7, and a maximum level of 14 corresponding to a maximum resolution of $\Delta x = 40$ pc. The refinement is triggered with a quasi-Lagrangian criterion: if the gas mass within a cell is larger than $8 \times 10^7 M_\odot$ or if more than 8 dark matter particles are within the cell a new refinement level is triggered.

After relaxation, the origin of time was reset to zero and the base simulations were run further in time with an enhanced and uniform pressure outside the disc (*pressure simulations*) for another ≈ 0.42 Gyr. As mentioned in Sect. 4.2.1 above, the important mechanism of the feedback is the thermalization of the mechanical jet power transforming a highly anisotropic property (momentum of the collimated jet) into a nearly isotropic one (thermal pressure). Additionally, the bow shock in the simulation of Gaibler et al. (2012) pressurizes the outer disc only a few Myr after pressurizing the inner disc. We therefore consider the academic case of a disc galaxy on which external pressure is applied continuously (starting at a reference time), throughout the galaxy, in a spherical geometry. The effects of isotropy and the geometry of the enhancement is deferred to a future work (Bieri et al., 2016b). The assumption of a uniform positive pressure outside the galaxy is an approximation to the pressurisation seen in Gaibler et al. (2012). However, it allows us to study the effect of an enhanced pressure outside the galaxy in an isolated and controlled way.

To mimic a large-scale AGN jet that carries mass down to the disc, a pressure enhancement is applied starting at $t = 0$ for a value of $3P_{\max}$ (hereafter *pa3*) outside the sphere of radius $r_1 = 12$ kpc, where the transition between the two regimes is smoothed. P_{\max} is the maximum radially averaged pressure in the disk at $t = 0$ (reached in the central few cells), with $P_{\max} \simeq 9.8 \times 10^{-13}$ Pa for the *gasLow* simulation and $\simeq 4.7 \times 10^{-12}$ Pa for the *gasHigh* simulation set. The pressures expected can be estimated with some back-of-the-envelope calculations and relations derived by Krause (2003). Given that the jet density is low compared to the high density ISM, we can assume, to first order, a constant background density. Assuming further that the jet delivers a constant amount of energy to their cocoons, the expansion of the cocoon goes as

$$r = (15\mathcal{P}_{\text{jet}}/12\pi\rho_0) t^{3/5}, \quad (4.1)$$

where \mathcal{P}_{jet} is the jet power, r the radius at which one measures the pressure and t the time of measurement. By assuming that the injected jet power ($E = \mathcal{P}_{\text{jet}}t$) is injected over the volume of a spherical blast wave, we get a rough estimate of the pressure. With $\mathcal{P}_{\text{jet}} = 10^{44}$ erg s $^{-1}$ and $\rho_0 = 1$ H cm $^{-3}$ we get an estimate of $P \simeq 5 * 10^{-11}$ Pa. This is in agreement with the simulation by Gaibler et al. (2012), which shows that the bow shock that pressurizes the gaseous disc has a pressure of $P \simeq 8 \times 10^{-11}$ Pa.

Sub-grid models for cooling Sutherland & Dopita (1993) and star formation, as well as SN feedback, were used in the simulations. Gas is turned into star particles in dense cold regions of gas density $n_{\text{gas}} > n_0 = 14$ H cm $^{-3}$ by drawing a probability from the Schmidt law $\dot{\rho}_* = 0.01\rho_{\text{gas}}/t_{\text{ff}}$ to form a star with a stellar mass of $m_* = n_0\Delta x^3 \simeq 2 \times 10^4 M_\odot$ (Rasera & Teyssier, 2006). The gas pressure and density are evolved using the Euler equations, with an equation of state for a mono-atomic gas with $\gamma = 5/3$. In order to prevent catastrophic and artificial collapse of the self-gravitating gas, we use a polytropic equation of state $T = T_0(n_{\text{gas}}/n_0)^{\kappa-1}$ to artificially enhance the gas temperature in high gas density regions ($n_{\text{gas}} > n_0$). Here $\kappa = 2$ is the polytropic index, and $T_0 = 270$ K, chosen to resolve the Jeans length with minimum 4 cells (Dubois & Teyssier, 2008a). We

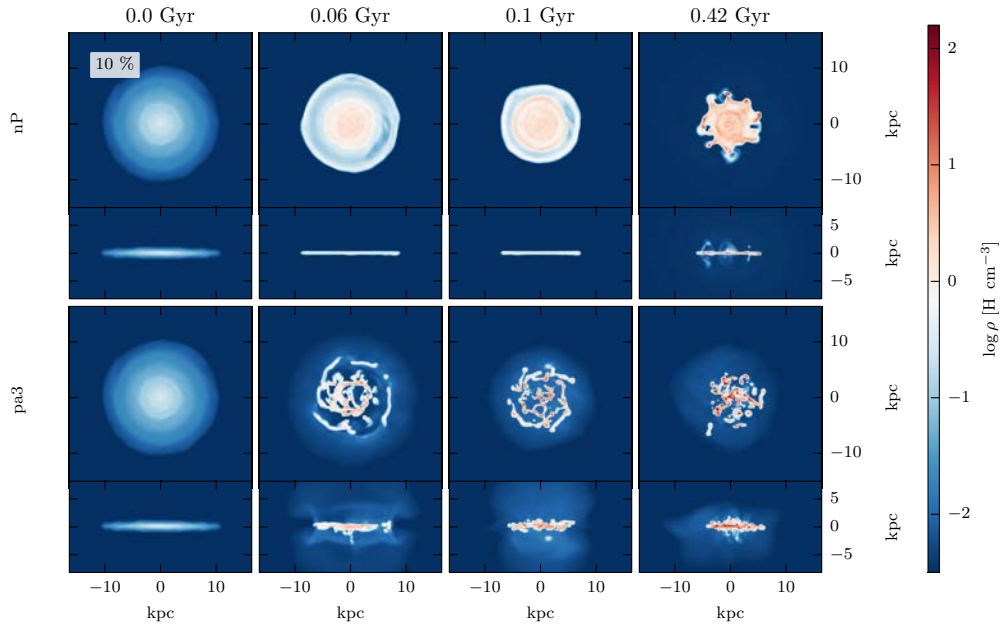


Figure 4.3: Gas density maps (mass-weighted) for the *gasLow* simulations, for no pressure enhancement (top), and for a pressure enhancement of a factor 3 (bottom), with time evolving from left to right. The galaxies are shown both face-on (upper portion of panels) and edge-on (bottom portion of panels).

account for the mass and energy release from type II SNe. The energy injection, which is purely thermal, corresponds to $E_{\text{SN}} = \eta_{\text{SN}} (m_*/M_\odot) 10^{50}$ erg, where $\eta_{\text{SN}} = 0.2$ is the mass fraction of stars going into SNe. We also return an amount $\eta_{\text{SN}} m_*$ back into the gas for each SN explosion which occurs 10 Myr after the birth of the star particle. To avoid excessive cooling of the gas due to our inability to capture the different phases of the SN bubble expansion, we used the delayed cooling approach introduced by Teyssier et al. (2013).

4.2.3 Results

4.2.3.1 Disc fragmentation and star formation history

The application of external pressure at $t = 0$ leads to fragmentation of the gaseous galaxy discs, i.e. accelerated clump formation. This can be seen in Fig. 4.3 for the *gasLow* and in Fig. 4.4 for the *gasHigh* simulations. However, the *gasHigh* case shows more gas between clumps in the enhanced pressure run, as well as more gas ejection from the disk.

Since the star formation recipe depends on the local gas density, we expect an enhanced star formation when more clumps are formed (gas gets more concentrated), assuming that the clumps have sufficient mass. Therefore, if external pressure leads to increased fragmentation and hence increased clump formation, we expect the star formation to be positively enhanced when external pressure is applied on the galaxy.

Fig. 4.13 shows the SFR as a function of time. One can see that generally the SFR is larger when external pressure is applied. In the *gasLow* simulations, the SFR starts rising almost immediately and gradually after the pressure is applied. In the absence of external pressure, the star formation is at a modest rate ($\sim 0.1 M_\odot \text{ yr}^{-1}$). This value is

4.2. PLAYING WITH POSITIVE FEEDBACK: EXTERNAL PRESSURE-TRIGGERING OF A STAR-FORMING DISK GALAXY

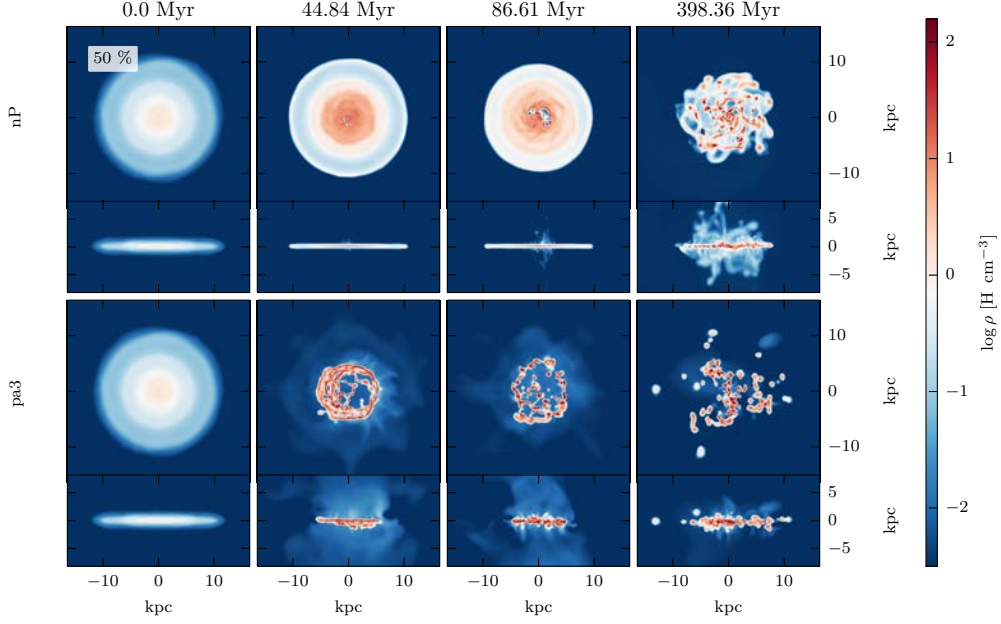


Figure 4.4: Same as in Fig. 4.3 for the *gasHigh* simulations.

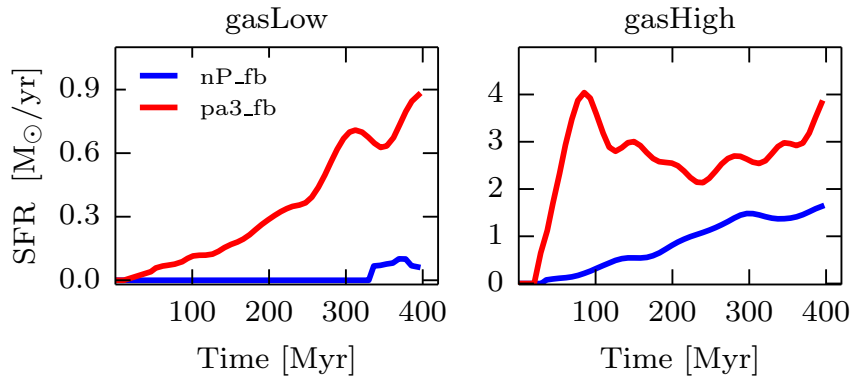


Figure 4.5: SFR as a function of time. The left panel shows the *gasLow* simulation set and the right panel shows the *gasHigh* simulation set. Here blue denotes simulations with and red simulations without external pressure applied at $t = 0$.

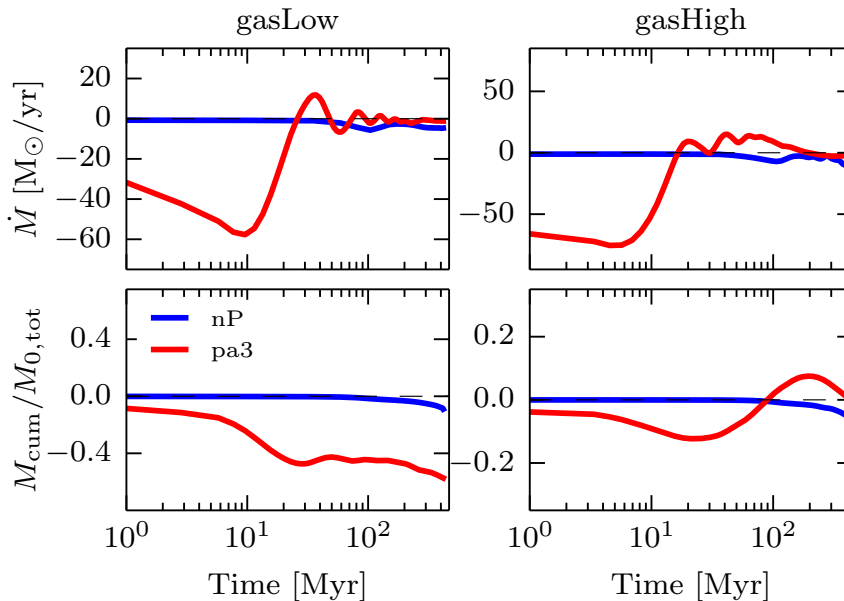


Figure 4.6: Time evolution of the net mass flow rate (top) and cumulative net mass flow relative to the initial mass $M_{0,\text{init}}$ measured within a galaxy radius of 12 kpc and a disc height of 1.5 kpc before enhancing the pressure (bottom), both at 16 kpc from the galaxy center for the *gasLow* (left), and *gasHigh* (right) simulations.

only reached at late times (after 300 Myr) once the gas has sufficiently collapsed to reach the star formation gas density threshold.

On the other hand, in the *gasHigh* simulations, star formation sets in at earlier times, even without any forcing by external pressure. This different behavior is related to differences in the Toomre (1964) Q parameter in the galaxies of the two simulations, such that the gaseous disc is stable in the *gasLow* case ($\langle Q \rangle = 3.29 > 1$ measured at $t = 0$), but unstable in the *gasHigh* case ($\langle Q \rangle = 0.72 < 1$). This demonstrates that the fragmentation of the disc can be driven by the forcing of an external pressure, even though the disc is initially Toomre stable. As we will see later, this is due to the pressure-driven mass inflow which acts as an enhancement of the disc self-gravity and makes the disc more unstable. For the *gasHigh* simulations, the rise in SFR is, however, significantly faster when external pressure is applied. At later times, the SFR flattens after ~ 80 Myr maintaining this rate for the remainder of the simulation. In contrast, for the no pressure simulation the SFR keeps rising with time.

This picture is confirmed when looking at the density probability function (PDF) of the gas, which we defer to a future article (Bieri et al., 2016b). In summary, one can see that increasing the external pressure allows one to reach higher gas densities faster. For the *gasHigh* galaxy, the non-pressure simulation catches up with the over-pressure simulations after a time delay, similar to the SFR behaviour. For the *gasLow* galaxy, the non-pressure simulation never attains the densities reached by the pressure enhancement simulations.

4.2.3.2 Mass Flow Rate

The star formation rate is sensitive to both the mass flux and to the clump mass distribution. We measure the gas mass flux through a sphere of radius 16 kpc as

$$\dot{M} = \oint \rho \mathbf{v} \cdot \hat{\mathbf{r}} dS = \sum_{i \in \text{shell}} m_i \mathbf{v}_i \cdot \hat{\mathbf{r}}_i \frac{S}{V}, \quad (4.2)$$

where i denotes the index of a cell within a shell of surface S and volume V . In all simulations with enhanced pressure, an incoming pressure-driven mass inflow is created at the beginning of the simulation and is followed by a short mass outflow (seen in the edge-on view of the galaxies in Figs. 4.3 and 4.4), after which it oscillates around zero for the remaining of the simulation (top panels of Fig. 4.16). In the early adjustment phase, the external pressure drives the ambient gas towards the disc, compressing the clouds, and eventually expelling the gas. This is to be expected from the way we set up the pressure, as the pressure wave coming into the galaxy carries momentum causing the galaxy to expel more gas when compared with the non-pressurized case where the mass outflow rate is close to zero.

The bottom panels of Fig. 4.16 shows that the cumulative mass flow remains negative for the *gasLow* pressurized simulation, indicating a greater mass inflow than outflow for this simulation, while the cumulative mass flow is close to zero for the non-pressurized simulations. The mass inflow in the pressurized simulation enhances the mass of the galaxy and makes the disc more unstable leading to more clump formation and, hence, to an enhanced SFR. For the *gasHigh* simulations, the difference in the cumulative mass flow is small over the whole simulation time, demonstrating that the two galaxies have the same amount of gas to form stars. However, the greater initial gas inflow in the *gasHigh* pressure simulation causes more instability at the beginning. This instability allows the galaxy to reach higher gas densities faster, leading to an enhanced SFR.

4.2.4 Conclusions

We show that a toy model for AGN-induced overpressurization leads to enhanced star formation in disk galaxies. The effects are dramatic at early times, regardless of the initial gas fraction of the galaxy, although the high gas fraction galaxy, which is Toomre unstable, experiences a very early rapid burst of star formation, followed by more moderate SFR that remains above the SFR in the non-pressurized case. However, even in the Toomre stable low gas fraction galaxy, external pressure can enforce fragmentation and star formation, albeit on a longer time scale.

One reason for the increased star formation in pressurized galaxies is early pressure-driven mass inflow from the halo and outer disc, on a 10 Myr time-scale (Fig. 4.16), especially on the low gas fraction galaxy. This gas inflow feeds cloud/clump growth in the inner parts of the galaxy and eventually leads to enhanced star formation (Fig. 4.13). This can also be seen in the gas density PDF of the simulations: higher gas densities are reached faster, generating a larger star formation rate. The effects of infall are more dramatic for the high gas fraction galaxy, where the disc is more unstable. (Fig. 4.4). The mass inflow due to the pressurization of the disc acts as an effective enhancement of the disc self-gravity, which in turn makes the disc more unstable. We have confirmed this with a detailed analysis of the Toomre parameter, gas density PDF, and clump properties, which we defer to a more future study (Bieri et al., 2016b).

One expects that gas-rich star-forming galaxies should have gravitationally-driven star formation rates of the order of $100 M_{\odot} \text{yr}^{-1}$, simply by scaling the gas surface density, and

maintaining a similar efficiency. Indeed, observations at $z \sim 2$ confirm this trend. The more exotic cases of very high ($\sim 1000 M_{\odot}\text{yr}^{-1}$) star formation rates are more typically found at higher redshift and almost invariably have associated luminous AGN. While any connection is speculative, and indeed the very direction of possible causality is vigorously debated, our simple tests of the effects of AGN-induced pressure, due to wind-driven or jet-initiated bow shocks that overpressurize the entire inner gaseous disk, suggest that strongly enhanced star formation rates are readily achievable.

Similar SFR enhancements are found from increased pressure in the initial stages of ram pressure harassment, although gas loss dominates the long term behavior (Fujita & Nagashima, 1999; Abadi et al., 1999; Bekki, 2014). Here, however, the gas is retained, and the star formation rate enhancement is far more pronounced.

The assumptions made in setting up our simulations will have to be checked in future studies. First of all, we are examining different geometries for the external pressure (Bieri et al., 2016b). Also, the assumption of a uniform pressure outside the disc applied in an isotropic way should be tested in a future study. The resulting evolution of the galaxy will certainly also depend on the mass and type of galaxy simulated. Nevertheless, we believe that the idea of external pressure triggering star formation within the galaxy should be robust to these details.

Acknowledgments

This work has been done within the Labex ILP (reference ANR-10-LABX-63) part of the Idex SUPER, and received financial state aid managed by the Agence Nationale de la Recherche, as part of the programme Investissements d’avenir under the reference ANR-11-IDEX-0004-02. It also has been partially supported by grant Spin(e) ANR-13-BS05- 0005 of the French ANR. YD and JS acknowledge support from ERC project 267117 (DARK) hosted by UPMC – Sorbonne Universités and JS for support at JHU by National Science Foundation grant OIA-1124403 and by the Templeton Foundation. RB has been supported in part by the Balzan foundation. The simulations have made use of the Horizon cluster, for which we specially thank Stephane Rouberol for technical support. We also thank M. D. Lehnert, V. Gaibler, A. Wagner, and J. Coles for valuable discussions.

4.3 External pressure-triggering of star formation in a disc galaxy: a template for positive feedback

REBEKKA BIERI¹ YOHAN DUBOIS¹, JOSEPH SILK^{1,2,3,4}, GARY A. MAMON¹
AND VOLKER GAIBLER⁵

¹ Institut d’Astrophysique de Paris (UMR 7095: CNRS & UPMC – Sorbonne Universités), 98 bis bd Arago, F-75014 Paris, France

² Laboratoire AIM-Paris-Saclay, CEA/DSM/IRFU, CNRS, Univ. Paris VII, F-91191 Gif-sur-Yvette, France

³ Department of Physics and Astronomy, The Johns Hopkins University Homewood Campus, Baltimore, MD 21218, USA

⁴ BIPAC, Department of Physics, University of Oxford, Keble Road, Oxford OX1 3RH

⁵ Institut für Theoretische Astrophysik, Universität Heidelberg, Albert-Ueberle-Str 2, D-69120 Heidelberg, Germany

* bieri@iap.fr

Abstract

Feedback from active galactic nuclei (AGN) has often been invoked both in simulations and in interpreting observations for regulating star formation and quenching cooling flows in massive galaxies. AGN activity can, however, also over-pressurise the dense star-forming regions of galaxies and thus enhance star formation, leading to a positive feedback effect. To understand this pressurisation better, we investigate the effect of an ambient external pressure on gas fragmentation and triggering of starburst activity by means of hydrodynamical simulations. We find that moderate levels of over-pressurisation of the galaxy boost the global star formation rate of the galaxy by an order of magnitude, turn stable discs unstable, and lead to significant fragmentation of the gas content of the galaxy, similar to what is observed in high redshift galaxies.

galaxies: formation — galaxies: active — methods: numerical

4.3.1 Introduction

Supermassive black holes are found at the centers of most, if not all, massive galaxies (e.g., Magorrian et al., 1998; Hu, 2008; Kormendy et al., 2011). Throughout cosmic history, they are thought to play an important role in regulating the baryonic mass content of massive galaxies through *feedback* from Active Galactic Nuclei (AGN) by releasing a fraction of the rest-mass accreted energy back into the galactic gas and altering the star formation rate (SFR) in the galaxy.

AGN can exert either *negative* or *positive* feedback on their surroundings. The former describes cases where the AGN inhibits star formation by heating and dispersing the gas in the galaxy, while the latter describes the possibility that an AGN may trigger star formation. Negative AGN feedback can operate in *quasar-mode* from radiation at high accretion rates, or *radio-mode* from AGN jets at predominantly low accretion rates (Churazov et al., 2005; Russell et al., 2013a). It is still unclear how efficiently AGN feedback delivers energy (through heating, e.g., Silk & Rees, 1998) and momentum (through physical pushing, King, 2003) to the galaxy’s gas and what mode of feedback dominates. Both semi-analytical (e.g., Croton et al., 2006; Bower et al., 2006) and hydrodynamical cosmological simulations (e.g., Di Matteo et al., 2005, 2008; Sijacki et al., 2007; Booth & Schaye, 2009; Dubois et al., 2010a) have shown that negative AGN feedback is an important ingredient in the formation and evolution of massive galaxies, in particular in shaping the observed high-end tail of the galaxy mass function, and the low SFRs in massive galaxies.

Moreover, observations show that cooling flows in the hot circumgalactic and intracluster media can be suppressed by the energy transferred by AGN jets (Bîrzan et al., 2004; Dunn et al., 2005), again negatively impacting star formation.

Although AGN feedback has been extensively studied in observations and through cosmological simulations, the impact on the host galaxy and the precise mechanism of the communication of the AGN with the galaxy’s interstellar medium (ISM) is far from being understood. It is not clear why jet feedback, which is thought to heat cold gas, should have a similar effect on the multi-phase ISM. It has been argued that a jet that propagates through an inhomogeneous ISM may also trigger or enhance star formation in a galaxy (i.e., positive feedback). Begelman & Cioffi (1989) and Rees (1989) proposed that the radio jet activity triggers star formation and might serve as an explanation for the alignment of radio and optical structures in high redshift radio galaxies. Radio jet-induced star formation has also been considered as a source powering luminous starbursts (Silk, 2005). Ishibashi & Fabian (2012) provide a theoretical framework linking AGN feedback triggering of star formation in the host galaxy to the oversized evolution of massive galaxies over cosmic time. Furthermore, negative and positive feedback are not necessarily contradictory (Silk, 2013; Zubovas et al., 2013a,b; Zinn et al., 2013; Cresci et al., 2015b): AGN activity may both quench and induce star formation in different parts of the host galaxy and on different time-scales.

Observationally, this positive feedback scenario is directly supported by only a few local (Croft et al., 2006; Inskip et al., 2008; Salomé et al., 2015) and high redshift (Dey et al., 1997; Bicknell et al., 2000; Rauch et al., 2013) observations. There are, however, also indirect links between jets and star formation which suggest possible positive feedback from AGN (Klamer et al., 2004; McCarthy et al., 1991; McCarthy, 1993; Balmaverde et al., 2008; Podigachoski et al., 2015; Swinbank et al., 2015).

More recently, high resolution hydrodynamical simulations of a jet including a multi-phase ISM have become feasible (Sutherland & Bicknell, 2007; Antonuccio-Delogu & Silk, 2008, 2010; Wagner & Bicknell, 2011; Gaibler et al., 2011, 2012). These studies have shown that a clumpy interstellar structure results in a different interaction between the jet and the gas than was assumed from simulations with a homogeneous ISM. It can be generally noted that an inhomogeneous ISM affects not only the jet evolution, but also the morphology of the host galaxy itself. Simulations by Tortora et al. (2009) extended the studies and generalised the simulations of Antonuccio-Delogu & Silk (2008) studying the interaction of a powerful jet in 2D, two-phase ISM. Tortora et al. (2009) have shown that star formation can initially be slightly increased (10–20 per cent) followed by a much stronger quenching (more than 50 per cent) within a time-scale of a few million years. They argue that the rapid decrease of the SFR after its initial enhancement is a consequence of both the high temperatures as well as the reduced cloud mass once the jet cocoon has propagated within the medium. Kelvin-Helmholtz instabilities reduce the mass of the clouds and, assuming a Kennicutt-Schmidt law, thereby reduce the SFR. It should, however, be noted that the 2D approach results in a very different temperature and pressure evolution as compared to a 3D simulation. Wagner & Bicknell (2011) studied the interaction of a relativistic jet interacting with a two-phase ISM at the galaxy’s center with a resolution of one kiloparsec. They found that the transfer of energy and momentum to the ISM may inhibit star formation through the dispersal of gas, but their simulations do not contain a star-formation model. It could be argued, though, that because of the short (≤ 1 Myr) simulation timescale, the impact of cooling is very weak and they therefore might underestimate the SFR.

Gaibler et al. (2012) simulated a powerful AGN jet within a massive gaseous, clumpy disc (however they neglected gravity). Their simulations show the formation of a blast

4.3. EXTERNAL PRESSURE-TRIGGERING OF STAR FORMATION IN A DISC GALAXY: A TEMPLATE FOR POSITIVE FEEDBACK

wave in the central region of the disc because the densities in the ISM are high compared to the densities of the simulated jet. The blast wave results in the formation of a cavity in the disc center pushing the gas outwards and compressing the gas within the disc at the cavity boundary, generating rings of compressed gas within the disc. The blast wave is unable to propagate further outwards in the galactic plane due to the large obstructing mass in the disc. However, it can propagate vertically out of the disc, where the bow shock reaches out to lower gas densities of the circumgalactic gas, after ~ 4 Myr, and where the propagation is thus much easier. The out-of-plane laterally-expanding cocoon further expands right along the galaxy boundary and results in the entire galaxy being surrounded by enhanced thermal pressure compacting the whole galactic disc from the outside. The expansion within the galaxy eventually stalls due to the high column density. Additionally, the disc is also pressurised by the ram pressure of the backflow that is created when the shocked plasma streams out of the high-pressure hotspot at the end of the jet (see Fig. 4.8). This backflow has a strong turbulent component in addition to an ordered motion towards the disc plane. Nevertheless, the vortices still move around and drive pressure towards the disc. Hence, the pressurisation originates both from the thermal pressure of the cocoon and the backflow originating from the jet's high-pressure hotspot region. The thermal pressure should somewhat dominate, as the turbulence is measured to be in the subsonic or transonic regime. Dugan et al. (2014) also showed that the jet activity causes a significant change of the SFR by enhancing star formation, with inside-out propagation in the galaxy.

Although the physical understanding of star formation is still limited and debated (Padoan & Nordlund, 2011), it can be assumed that a pressurised disc can trigger gravitational instabilities, compress the galaxy's clouds, and push the densities within the disc above the critical density for star formation, thus resulting in an increased SFR. This picture is further supported by a few observations of well-resolved star-forming molecular clouds (Keto et al., 2005; Rosolowsky & Blitz, 2005) and by detailed simulation of the ISM (e.g. Slyz et al., 2005; Zubovas et al., 2014).

While the simulations of Gaibler et al. (2012) resolved the jet interaction and the expansion of the blast wave more realistically, they were unable to examine the long-term effects of this pressurisation and were lacking the necessary physics for these time scales, most importantly gravity. Motivated by the observed pressurisation of the disc from the outside found in their hydrodynamical simulations of AGN jet feedback, we have investigated the isolated effects of this extra pressure on a galaxy disc in an academic model, but on a much longer timescale, by running hydrodynamical simulations with self-gravity, without AGN jets, but with simple prescriptions for external pressure such as that which may be caused by the jet cocoon. In a first study (Bieri et al., 2015), we simulated disc galaxies of one-tenth the total mass of the Milky Way, varying their initial gas fraction. We found that with a given level of external pressure, the disk fragments into numerous clumps, causing enhanced star formation. In the present article, we study the effects of external pressure in more detail, by considering different geometries and levels of external pressure, as well as studying the effects of supernova feedback and mass resolution.

In Section 4.3.2, we describe our suite of hydrodynamical simulations. Our results are presented in Section 4.3.3 and summarised in Section 4.3.4.

4.3.2 Simulation Set-up

4.3.2.1 Basic simulation scheme

Our simulations begin with a galaxy made of a disc of gas and stars, a stellar bulge and a dark matter (DM) halo. We allow this galaxy to relax to an equilibrium configuration

Table 4.1: Galaxy parameters: scale radius (r_s), gas fraction (f_g), total stellar mass (M_*), and total gas mass in the disc (M_{gas})

Identifier	r_s [kpc]	f_g [%]	M_* [$10^9 M_\odot$]	M_{gas} [$10^9 M_\odot$]
gasLow	3.4	10	8.1	0.9
gasHigh	3.4	50	4.6	4.4

(with a reasonable disc thickness) over the rotation time of the disc at its half-mass radius. This first phase is performed without gas cooling, or star formation or feedback, in order to evacuate spurious waves emitted from the imperfect equilibrium of the initial conditions. After this first relaxation phase, we turn on the external pressure, gas cooling, star formation, and also feedback from supernovae (SNe), as described below.

The initial condition method introduced by Springel & Hernquist (2005) is used to generate the DM particles with an NFW (Navarro et al., 1997) density profile and a concentration parameter of $c = 10$. The virial velocity of the DM particles is set to be $v_{200} = 70 \text{ km s}^{-1}$, which corresponds to a virial radius of $R_{200} \approx 96 \text{ kpc}$ and a virial mass of $M_{200} \approx 1.1 \times 10^{11} M_\odot$. A Hubble constant of $H_0 = 73 \text{ km s}^{-1} \text{ Mpc}^{-1}$ is assumed. The star particles as well as the gas are distributed in a rotationally supported exponential disc with a scale length of 3.44 kpc and scale height 0.2 kpc, and a spherical, non rotating bulge with a Hernquist profile (Hernquist, 1990) of scale radius 0.2 kpc. We use 10^6 DM particles with a mass resolution of $1.23 \times 10^5 M_\odot$ to sample the dark matter halo, and 5.625×10^5 star particles sampling the disc of which 6.25×10^4 star particles are used to sample the bulge. The stellar mass resolution is $1.57 \times 10^4 M_\odot$ for the 10% gas fraction simulation (hereafter, *gasLow*) whereas for the 50% gas fraction simulation (hereafter, *gasHigh*) the mass resolution is $8.73 \times 10^3 M_\odot$. The relevant galaxy parameters are shown in Table 4.1.

The gas density is truncated in the surface of a cylinder of radius $r_{\text{cut}} = 12 \text{ kpc}$ (from the disc axis) and of height $h_{\text{cut}} = 2.5 \text{ kpc}$ (above and below the disc). Beyond this cylinder, the density is set to be that of the circumgalactic medium (CGM), which is modelled with a constant hydrogen number density of $n_{\text{CGM}} = 10^{-3} \text{ H cm}^{-3}$. The pressure and temperature profiles outside the disc are calculated assuming spherical hydrostatic equilibrium. For the relaxation phase, the simulations are run for one rotation period of the half-baryonic mass radius (5 kpc) of the galaxy, i.e. $\approx 0.5 \text{ Gyr}$.

The simulations are run with the RAMSES adaptive mesh refinement code (Teyssier, 2002). Particles motions are evolved through the gravitational force with an adaptive particle mesh solver using a cloud-in-cell interpolation, together with the mass contribution of the gas component. The evolution of the gas is followed with a second-order unsplit Godunov scheme. We use the HLLC Riemann solver (Toro et al., 1994) with MinMod total variation diminishing scheme to reconstruct the interpolated variables from their cell-centred values. The box size is 655 kpc with a coarse level of 7, and a maximum refinement level of 14 corresponding to a $\Delta x = 40 \text{ pc}$ minimum cell size for most of the simulations. We used isolated boundary conditions for the Poisson solver and zero-gradient boundary conditions for the hydro solver. Given that the box size is ~ 50 times larger than the galaxy radius, the galaxy is not affected by possible effects at the boundaries of the simulation box. For convergence studies, we perform a higher resolution run with a spatial resolution of $\Delta x = 10 \text{ pc}$ (maximum level of refinement 16). The refinement is triggered with a quasi-Lagrangian criterion: if the gas mass within a cell is larger than $8 \times 10^7 M_\odot$

4.3. EXTERNAL PRESSURE-TRIGGERING OF STAR FORMATION IN A DISC GALAXY: A TEMPLATE FOR POSITIVE FEEDBACK

or if more than 8 DM particles are within the cell a new refinement level is triggered.

The simulations include sub-grid models for cooling, star formation, as well as SN feedback in a subset of runs. The cooling mechanism is that described by Sutherland & Dopita (1993), which accounts for H, He, and metal contributions to gas cooling (assuming a solar chemical composition of the various metal elements, but with a varying metallicity of the gas). The disc is initialised with a uniform solar metallicity. No metals are initially placed outside the disc. The boundary of the disc is defined using a geometrical criteria with cylindrical symmetry using the initial disc radius and disc height. Metals are passively advected with gas in the simulation and are modified by individual SNe events with a yield of 0.1, which also distribute the metals throughout and outside the galaxy. In dense and cold regions, gas is turned into star particles following a Kennicutt-Schmidt law (Kennicutt, 1998b):

$$\dot{\rho}_* = \epsilon_* \frac{\rho_{\text{gas}}}{t_{\text{ff}}} \quad \text{if } n_{\text{gas}} > n_0, \quad (4.3)$$

where $\dot{\rho}_*$ is the star formation rate density, ρ_{gas} is the gas mass density, $\epsilon_* = 0.01$ is the star formation efficiency, t_{ff} is the local gas free-fall time, and n_{gas} and $n_0 = 14 \text{ H cm}^{-3}$ for $\Delta x = 40 \text{ pc}$ ($n_0 = 224 \text{ H cm}^{-3}$ for $\Delta x = 10 \text{ pc}$) are the local H number density and H number density threshold for star formation respectively. The Schmidt law is used to draw a probability to form a star with a stellar mass of $m_* = \rho_0 \Delta x^3 \simeq 3 \times 10^4 M_\odot$ for the low resolution (*lowRes*) runs and a stellar mass of $m_* \simeq 7 \times 10^3 M_\odot$ for the high resolution (*highRes*) runs (Rasera & Teyssier, 2006). The gas temperature in high gas density regions ($n_{\text{gas}} > n_0$) is artificially enhanced by a polytropic equation of state to a temperature floor of $T_{\text{floor}} = T_0 (n_{\text{gas}}/n_0)^{\kappa-1}$, where $\kappa = 2$ is the polytropic index, and $T_0 = 270 \text{ K}$ for the low and high resolution runs. It is chosen in order to get a constant Jeans length resolved with at least 4 cells. This artificial polytropic equation of state is used to prevent the catastrophic and artificial collapse of the self-gravitating gas (Truelove et al., 1997b).

We account for the mass and energy release from type II SNe. The energy injection, which is purely thermal, corresponds to

$$E_{\text{SN}} = \eta_{\text{SN}} \frac{m_*}{M_\odot} 10^{50} \text{ erg}, \quad (4.4)$$

where $\eta_{\text{SN}} = 0.2$ is the mass fraction of stars going SNe and m_* is the mass of the star particle. We also return an amount of mass $\eta_{\text{SN}} m_*$ back into the gas for each SN explosion which occurs 10 Myr after the birth of the star particle. To avoid excessive cooling of the gas due to our inability to capture the different phases of the SN bubble expansion, we use the delayed cooling approach introduced in Teyssier et al. (2013) (in the same spirit as Stinson et al., 2006). The energy of the SN explosion is injected into a passive scalar variable and blocks the cooling of the gas if the corresponding velocity dispersion is larger than $\sigma_{\text{thres}} = 60 \text{ km s}^{-1}$. The energy within that passive scalar decays with a characteristic time-scale of $t_{\text{diss}} = 2 \text{ Myr}$ ($t_{\text{diss}} = 0.5 \text{ Myr}$) for $\Delta x = 40 \text{ pc}$ resolution ($\Delta x = 10 \text{ pc}$ respectively), long enough to block the cooling over a few cell sound crossing times (see Appendix of Dubois et al., 2015b).

4.3.2.2 Application of external pressure

After adiabatic relaxation (no gas cooling), the origin of time is reset to 0 and the base simulations are run further in time with the subgrid modeling of gas cooling, star formation and feedback, and with an enhanced and uniform pressure outside the disc (*pressure simulations*) for another $\approx 420 \text{ Myr}$. The pressure enhancement is applied at an instant

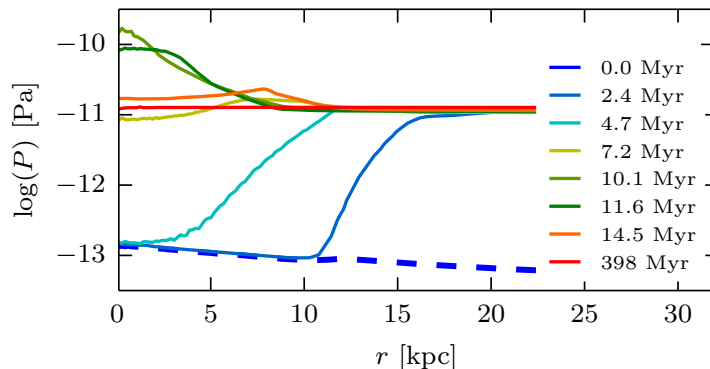


Figure 4.7: Mean pressure versus radius at different times (see legend) for the *pa3* run of the *gasHigh_fb* set. The dashed line shows the pressure profile before the onset of external pressure. The pressures are averaged within spherical shells.

starting at $t = 0$. This instant pressure increase is justified since the bow shock observed in the simulations of Gaibler et al. (2012) manages to pressurise the entire gaseous disc within a time-frame of only a few Myr. The pressure is enhanced by increasing the internal energy of gas cells according to two different criteria (i.e. two different configurations): either outside the sphere of radius $r_1 = 12$ kpc (hereafter, p_spher), or else where the gas number density is lower than 0.014 H cm^{-3} (i.e. right outside the disc component, hereafter, p_dens or equivalently *gasHigh_d*). The radius r_1 is chosen to be the cutoff radius from the initial condition setup whereas the densities for the p_dens simulations are chosen to be the radially averaged density at r_1 .

Primarily, the p_spher and p_dens models represent different numerical implementations and give an idea of the range of possible outcomes. However, the two different models also mimic the two different possible pressurisations of the disc due to the ram pressure (p_spher) from the backflow from the jet’s high-pressure hotspot and the thermal pressure (p_dens) of the cocoon. This is illustrated in Fig. 4.8. In the p_spher simulation, the bow shock pressurising the disc is assumed to be quasi-isotropic. The effect of isotropy of external pressure is compared with a simulation of a non-isotropic bipolar pressure increase in Appendix 4.3.5.1.

In the case of spherical geometry (p_spher), this pressure enhancement is calculated by

$$P(r, t) = \begin{cases} P(r, 0) & r < r_1, \\ \text{pa} f\left(\frac{r - r_1}{r_2 - r_1}\right) P_{\text{max}} & r_1 \leq r < r_2, \\ \text{pa} P_{\text{max}} & r \geq r_2, \end{cases} \quad (4.5)$$

where time $t = 0$ is just before the pressure enhancement, *pa* is the *pressure amplification*, $f(x) = 6x^5 - 15x^4 + 10x^3$ is an increasing function of x starting very gradually at $x = 0$ and smoothly reaching a plateau of unity at $x = 1$, and finally P_{max} is the maximum pressure in the disc at $t = 0$ (reached in the central few cells), with $P_{\text{max}} \simeq 9.8 \times 10^{-13}$ Pa for the *gasLow* simulation set and $P_{\text{max}} \simeq 4.7 \times 10^{-12}$ Pa for the *gasHigh* and *gasHigh_d* simulation sets. Here, we adopt $r_2 = r_1 + 3$ kpc. This gradual pressure amplification with radius is used to smoothly connect the two pressure regimes, where we choose a transition length of 3 kpc. We want to stress that, in principle, the external pressure is independent of the disc pressure. For sake of clarity, we chose to refer to the outside pressure relative to the maximum pressure inside the disc and will call *paX* a simulation run

4.3. EXTERNAL PRESSURE-TRIGGERING OF STAR FORMATION IN A DISC GALAXY: A TEMPLATE FOR POSITIVE FEEDBACK

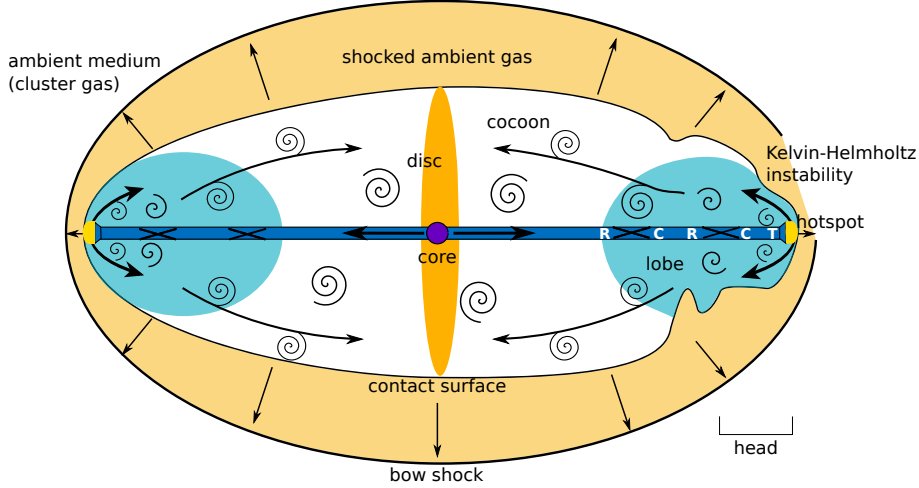


Figure 4.8: Schematic representation of the hydrodynamics of a disc galaxy with AGN jets. The beam (blue) emerges from the core containing the AGN. The jet plasma passes through regions of rarefaction (R) and compression (C) at internal shocks until it strongly decelerates at the terminal shock (T). The shocked plasma streams out of the hotspot high-pressure region (yellow) and forms a backflow. Vortices are generated and advected with the flow, inflating the cocoon (white inner region and light blue region). The outer parts of the cocoon, where radio-emitting electrons did not yet cool down, are visible as “lobes”. The overpressured cocoon drives a bow shock outwards into the ambient medium, forming a thick shell of shocked ambient gas. At this evolutionary stage, the bow shock has already overrun disc of the host galaxy. The picture is 90 degrees rotated to the setup in the simulations.

where the pressure amplification is $pa = X$. This pressure bath is maintained throughout the simulation evolution and is a minimum to the pressure evolved in that region. If the pressure within that bath becomes larger than paP_{\max} (due to SNe winds for instance) we take the new value of pressure provided by the Riemann solver. For this p_spher case (but also for the p_dens case), the simulation of no pressure amplification corresponds to $pa = P(r_1, 0)/P_{\max} \simeq 0.1$, and we will hereafter denote it as nP (for no pressure enhancement).

For the case of external pressure in disc geometry (p_dens), we increase the pressure, only at time $t = 0$, at a value of paP_{\max} wherever the gas density is below 0.014 H cm^{-3} . This gas density corresponds to a height of 1.1 kpc above and below the plane along the minor axis of the disc ($R = 0$).

In the simulations of Gaibler et al. (2012), the bow shock that pressurises the disc reaches a maximum pressure of $P \simeq 8 \times 10^{-11} \text{ Pa}$. This justifies our chosen pressure enhancement where the maximum pressure increase for the *gasHigh* (pa10) and *gasLow* (pa7) simulation corresponds to $P \simeq 9.8 \times 10^{-12} \text{ Pa}$ and $P \simeq 3.2 \times 10^{-11} \text{ Pa}$, respectively.

The pressure profiles for one of the p_spher simulations (run pa3) before and after the pressure enhancement as well as its evolution over the simulation time are shown in Fig. 4.7. We can see that at 2.4 Myr, right after the restart of the simulation, the pressure smoothly rises from $\sim 10^{-13} \text{ Pa}$ at the centre up to 10^{-11} Pa at a distance $r = 13.5 \text{ kpc}$. At later times, this pressure enhancement propagates within the central region of the halo and connects to the galaxy. The relevant physical parameters for the pressure simulations are summarised in Table 4.2.

Table 4.2: Physical parameters of runs: gas fraction (0.1 for *gasLow* and 0.5 for *gasHigh*), pressure amplification (pa), run with no feedback (nf), run with feedback (fb), spatial resolution (Δx), and pressure geometry

Identifier	gas fraction	pa	nf/fb	Δx [pc]	geometry
pa01 \equiv nP		0.1	✓/✓	40	
pa04		0.4	✓/✓	40	
pa08		0.8	✓/✓	40	
pa1.2		1.2	✓/✓	40	
pa1.5	<i>gasLow</i>	1.5	✓/✓	40	<i>p_spher</i>
pa3		3	✓/✓	40	
pa5		5	✓/✓	40	
pa7		7	✓/✓	40	
pa01 \equiv nP		0.1	✓/✓	40	
pa01_hR \equiv nP_hR		0.1	x/✓	10	
pa02		0.2	✓/✓	40	
pa04		0.4	✓/✓	40	
pa08		0.8	✓/✓	40	
pa1.2		1.2	✓/✓	40	
pa1.5	<i>gasHigh</i>	1.5	✓/✓	40	<i>p_spher</i>
pa2		2	✓/✓	40	
pa3		3	✓/✓	40	
pa3_hR		3	x/✓	10	
pa5		5	✓/✓	40	
pa7		7	✓/✓	40	
pa8		7	✓/✓	40	
pa10		10	✓/✓	40	
pa01_d \equiv nP		0.1	✓/✓	40	
pa02_d		0.2	✓/✓	40	
pa03_d		0.3	✓/✓	40	
pa04_d		0.4	✓/✓	40	
pa08_d		0.8	✓/✓	40	
pa1.2_d		1.2	✓/✓	40	
pa1.5_d	<i>gasHigh</i>	1.5	✓/✓	40	<i>p_dens</i>
pa2_d		2	✓/✓	40	
pa3_d		3	✓/✓	40	
pa5_d		5	✓/✓	40	
pa7_d		7	✓/✓	40	
pa10_d		10	✓/✓	40	

4.3. EXTERNAL PRESSURE-TRIGGERING OF STAR FORMATION IN A DISC GALAXY: A TEMPLATE FOR POSITIVE FEEDBACK

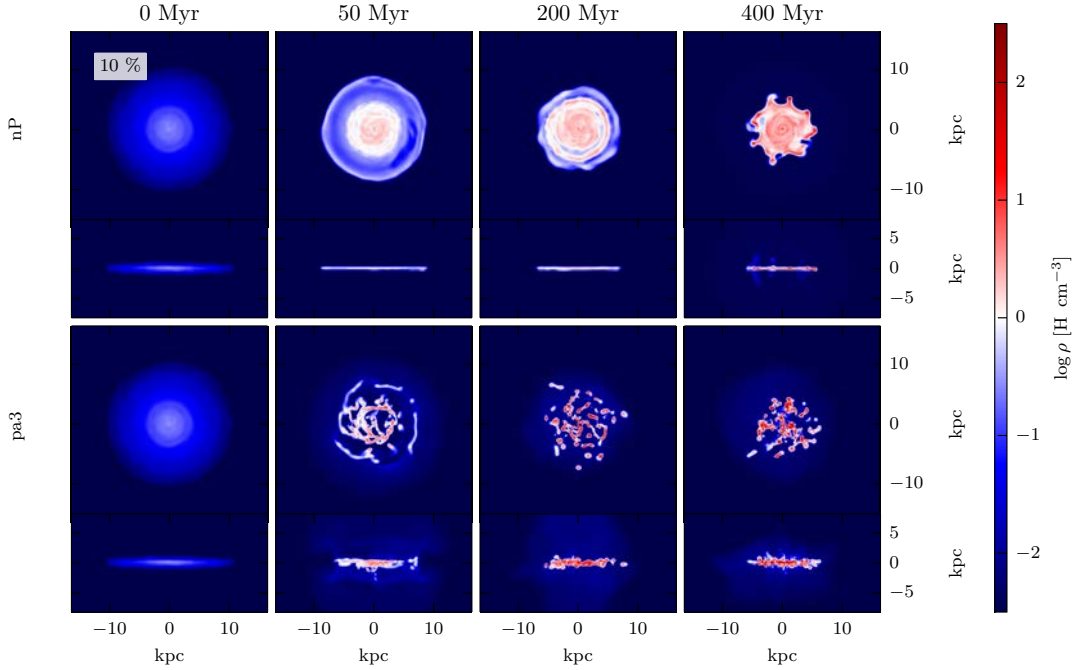


Figure 4.9: Gas density maps (mass-weighted) of two of the *gasLow_fb* simulations without enhancement of the external pressure nP (top row), and with enhancement of the external pressure pa3 (bottom row). The different columns show different times as labelled. Each panel shows both face-on (40×40 kpc, upper part) and edge-on (40×20 kpc, lower part) views. One can see that an increased pressure outside the galaxy leads to accelerated clump formation and less gas between the clumps.

4.3.3 Results

In this section, we present our simulation results considering different isolated disc simulations with various pressure boosts outside the disc. We analyse our simulations regarding disc fragmentation, star formation, clump properties, and the galaxy’s mass budget. We then compare our simulations with a simple theoretical implementation regarding the growth of the star formation rate and show that it scales approximately as a power just below unity of the external pressure. Finally, we calculate the Kennicutt-Schmidt (KS) relation and find that our toy model for AGN-induced over-pressurisation leads to the galaxies lying higher in the starburst region of the KS relation.

The effects of external pressure turn out to be similar whether or not SN feedback is included in the simulations. We will therefore only present, in this section, the results of the stellar feedback simulations. A comparison between the non-feedback and feedback simulations is provided in Appendix 4.3.5.2.

4.3.3.1 Qualitative differences

Figs. 4.9 and 4.10 show maps of the gas density for selected runs at different times, for the *gasLow_fb* and *gasHigh_fb* as well as *gasHigh_d_fb* runs respectively, and for two cases without external pressure boost nP and with extra pressure pa3. Comparing the nP runs, we observe that the gas is clumpier in the *gasHigh_fb* simulation than in the *gasLow_fb*

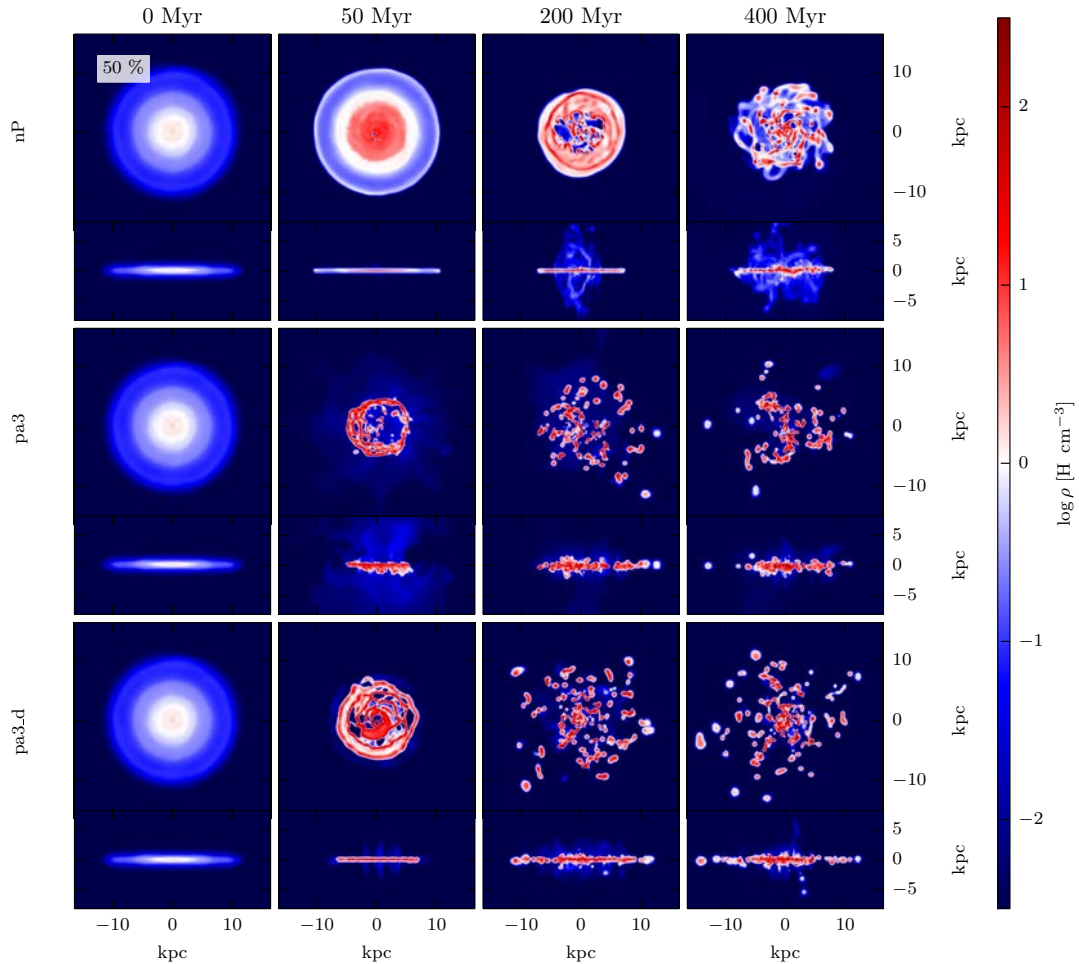


Figure 4.10: Gas density map (mass-weighted) for a selection of the *gasHigh_fb* and *gasHigh_d_fb* simulations, for no pressure enhancement (top), and for a pressure enhancement of pa3 (middle for *gasHigh_fb* and bottom for *gasHigh_d_fb*). The density scale is as in Figs. 4.9. An increased pressure outside the galaxy leads to accelerated clump formation and less gas between the clumps. The morphological structure of the two simulations with two different ways to increase the pressure (*gasHigh_fb*, and *gasHigh_d_fb*) is slightly different, but only in the outskirts of the galaxy. The edge-on view shows a mass outflow for all the simulations.

4.3. EXTERNAL PRESSURE-TRIGGERING OF STAR FORMATION IN A DISC GALAXY: A TEMPLATE FOR POSITIVE FEEDBACK

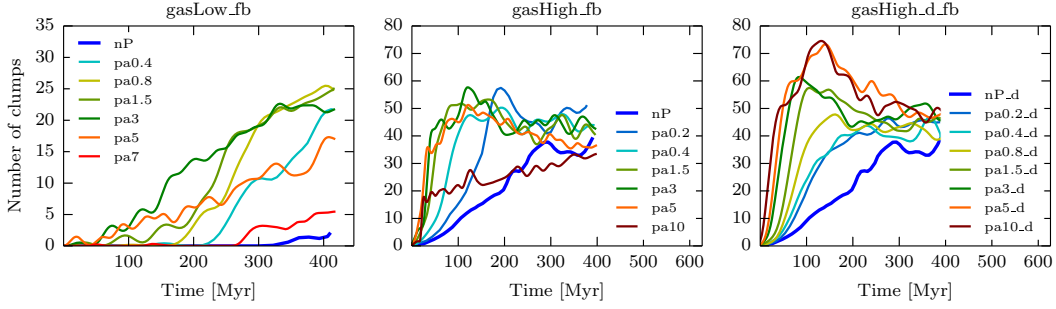


Figure 4.11: Time evolution of the number of clumps for a selection of simulations with supernova feedback: *gasLow_fb* (left), *gasHigh_fb* (middle), and *gasHigh_d_fb* (right) simulations. The lines are smoothed with a Blackman-Harris window with a width of $2\sqrt{\text{len}(\text{array})}$, where $\text{len}(\text{array})$ is the number of points. The clumps were extracted with the Bleuler & Teyssier (2014) algorithm, with a density threshold of 21 H cm^{-3} and a peak-to-saddle threshold of 1.5. The maps show that an increased pressure leads to increased clump formation and the increase in clump number is dependent on the pressure applied onto the galaxy. Beyond a certain pressure enhancement, the number of clumps decreases or remains very similar for higher pressure runs.

run. We will show in Sect. 4.3.3.2 that this is a simple consequence of the Toomre instability. The increased pressure leads to accelerated clump formation for the *gasLow_fb*, *gasHigh_fb*, *gasHigh_d_fb* simulations, and a clumpier ISM in all cases. Generally less gas between clumps in the enhanced pressure runs, in all the *gasLow_fb*, *gasHigh_fb*, and *gasHigh_d_fb* cases can be seen.

In Fig. 4.10, one can compare the two different ways to increase the pressure (p_{spher} , p_{dens}). The morphological structure of the two simulations *gasHigh_fb* and *gasHigh_d_fb* is slightly different. Fewer clumps are seen in the *gasHigh_fb* run than in the *gasHigh_d_fb* run. It seems, however, that the clumps are only missing in the outskirts of the *gasHigh_fb* galaxy, whereas a similar amount of clumps can be detected in the centre. The edge-on views indicate that in the *gasHigh_fb* simulations, a large amount of mass flows out of the galaxy due to the pressure increase, while in the *gasHigh_d_fb* simulations the mass outflow seems to be less extended. We will quantify the mass outflows in the different runs in Sect. 4.3.3.5.

4.3.3.2 Disc fragmentation

Since the star formation recipe depends on the local gas density (see eq. 4.3), we expect enhanced star formation when more clumps are formed (as the gas gets more concentrated), assuming that the clumps have sufficient mass. Therefore, if an increased pressure leads to increased fragmentation and hence increased clump formation, we expect star formation to be positively enhanced when external pressure is applied to the galaxy. We first consider the fragmentation by counting the high-density clumps. We detect the clumps in the simulation by running the clump finder described by Bleuler & Teyssier (2014). This method identifies all peaks and their highest saddle points above a given threshold (21 H cm^{-3}). A clump is recognised as an individual entity when the peak-to-saddle ratio is greater than 1.5; otherwise the density peak is merged with the neighbor peak with which it shares the highest saddle point.

The visual impression of increased clump formation when external pressure is applied on the galaxy (Figs. 4.9 and 4.10), is confirmed when looking at the number of clumps as a function of time. Fig. 4.11 shows the number of clumps as a function of time for the *gasLow_fb* (left panel), *gasHigh_fb* (middle panel), and *gasHigh_d_fb* (right panel) simulations, respectively.

In the *gasLow_fb* run, the number of clumps is constantly increasing with time, regardless of the amount of external pressure. Clump formation starts earlier in the runs with external pressure. However, the number of clumps at a given time is not a monotonic function of external pressure: at low external pressure (up to pa3), the number of clumps at given time increases with increasing pressure, while the reverse trend occurs for external pressures above $3 P_{\max}$.

The general effect that more clumps are formed in the simulations with external pressure is similar for the *gasHigh_fb* and *gasHigh_d_fb* runs. Similar to the *gasLow_fb* simulation, the number of clumps increases with increasing pressure up to a certain pressure (pa5) and then decreases again for the *gasHigh_fb* simulation and stays at the same level for the *gasHigh_d_fb* simulation. For the lower pressure as well as the non-pressure simulations, the number of clumps increases with time. However, for higher pressure simulations, the number of clumps reaches a plateau at late times. For the *gasHigh_fb* runs, the initial rise in the number of clumps is fastest for the pa3, pa5 and pa7 cases, but in the pa3 case the number of clumps reaches its plateau at a later time, hence at a higher level.

The time evolution of the number of clumps for the *gasHigh_d_fb* simulation is roughly similar to the *gasHigh_fb* simulation. At early times, the rise in number of clumps is fastest for the high pressure runs. The number of clumps keep rising with time for the lower pressure enhancements, while it reaches a maximum for the higher pressure enhancements. The time when the number of clumps reaches its plateau is also shortest for higher external pressures. After 300 Myr, there is no clear trend in number of clumps versus external pressure for the higher pressure runs. The increase of clump number is therefore highly dependent on the pressure applied on the galaxy. However, beyond a certain pressure enhancement (pa5_d), the number of clumps remains very similar for higher pressure runs. After ≈ 300 Myr the number of clumps is roughly independent of external pressure for the *gasHigh_fb* and *gasHigh_d_fb* simulations.

In the *gasLow_fb* run with no external pressure, only a single clump in the entire disc is formed, at late times (350 Myr), when the gas has sufficiently collapsed to reach the clump gas density threshold. On the contrary, in the *gasHigh_fb* run, the number of clumps increases up to $\simeq 35$, even without any forcing by the external pressure.

The difference between the gas-poor and gas-rich galaxies, before the external pressure is applied, is that the gaseous disc is Toomre-stable against small-scale fragmentation in the gas-poor case: the mean Toomre parameter $\langle Q \rangle = \langle c_s \kappa / (\pi G \Sigma_{\text{gas}}) \rangle = 3.29 > 1$; on the other hand, the gas-rich disc is Toomre-unstable ($\langle Q \rangle = 0.72 < 1$). Here, Σ_{gas} is the surface density, c_s is the sound speed, and κ is the epicyclic frequency (measuring the shear of the rotating disc). Therefore the *gasLow_fb* simulations demonstrate that fragmentation of the galactic disc can be driven by the forcing of an external pressure, even though the disc is initially Toomre-stable.

4.3.3.3 Star formation history

In Sect. 4.3.3.2, we have seen that an increased pressure enhancement leads to an increased number of clumps up to a certain value of pressure and then a typically lower number of clumps thereafter. Since the gas density threshold of clump detection is set to be above

4.3. EXTERNAL PRESSURE-TRIGGERING OF STAR FORMATION IN A DISC GALAXY: A TEMPLATE FOR POSITIVE FEEDBACK

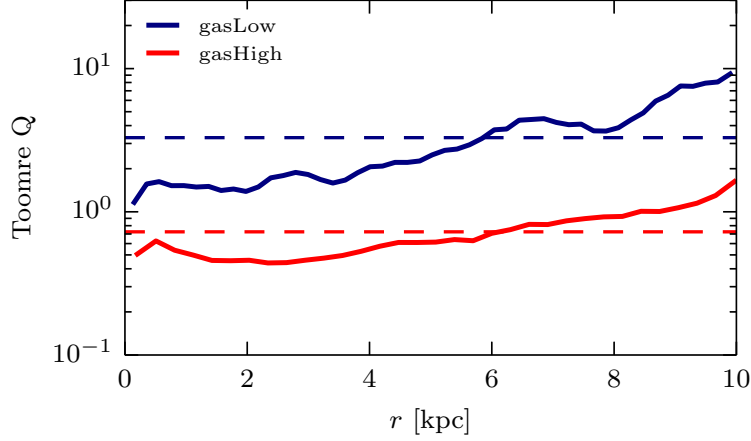


Figure 4.12: Local Toomre parameter for the relaxed disc at $t = 0$ for the *gasLow* and *gasHigh* simulations. The dashed line shows the mean Toomre parameter of the disc for the *gasLow* simulation $\langle Q \rangle = 3.29 > 1$ and for the *gasHigh* simulation $\langle Q \rangle = 0.72 < 1$. One therefore expects the *gasHigh* simulation to fragment independently of external pressure enhancement whereas the *gasLow* simulations are not expected to fragment into many clumps. The fact that the pressur-enhanced simulations of the *gasLow* galaxies shows a significant increase in the number of clumps compared to no-pressure enhancement demonstrates that external pressure can stimulate the fragmentation of a disc even if it is Toomre-stable.

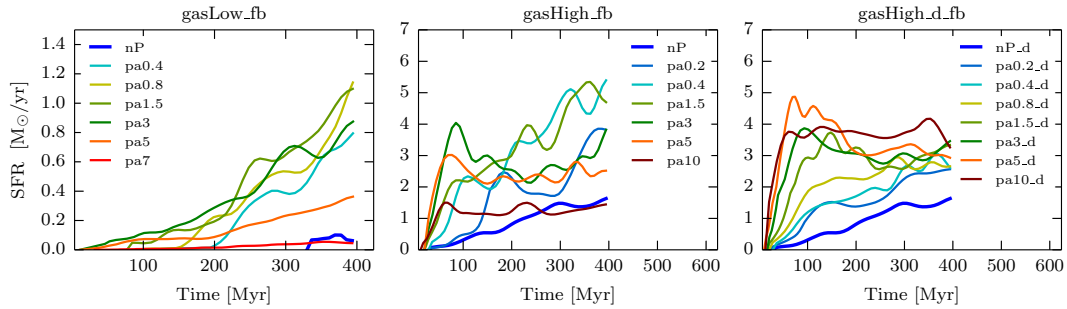


Figure 4.13: SFR for a selection of the simulations with supernova feedback: *gasLow_fb* (left), *gasHigh_fb* (middle), and *gasHigh_d_fb* (right) simulations. The lines are smoothed as in Figure 4.11. This figure shows that higher pressures lead to higher SFRs. For the higher pressure enhancement simulations, the SFR reaches a maximum or plateau at later times for the *gasHigh_fb*, and *gasHigh_d_fb* simulations. After a certain pressure increase, the SFR decreases or stays at the same level for all the simulations and hence the runs with intermediate pressure generally produce the highest SFR at all times.

that for star formation, one expects that the star formation history should evolve in a similar fashion to the evolution of the number of clumps.

Fig. 4.13 shows that the star formation histories of the different runs indeed resemble the time evolution of the number of clumps previously shown in Fig. 4.11. In particular, at early times in the runs with *gasHigh* higher pressures lead to higher SFRs. But with high pressures, the SFR saturates earlier. In the *gasHigh_fb* runs, the maximum SFRs in the high pressure runs are lower than in the other runs, while in the *gasHigh_d_fb* runs, the maximum level of SFR is reached for the three highest pressures, while the SFRs at later times (300 Myr) are roughly independent of the external pressure.

In the *gasLow_fb* runs, while the nP case leads to star formation only after a long time delay (330 Myr), the highest pressures, although leading to immediate but small levels of star formation, are unable to generate substantial star formation from the earliest times. The runs with intermediate pressures produce the highest SFR at all times. We will show in the next sections that this is due to the low mass-outflow of the intermediate pressure simulations that allows the clumps to increase in density. Conversely, larger external pressures lead to such strong pressure waves that the gas is removed from the galaxy. This prevents the formation of large clumps and tends to suppress the star formation.

The effect of the external pressure on the SFR is even more significant when looking at the *gasHigh_fb* simulations (middle panel of Fig. 4.13). The SFR of the no-pressure simulation slowly increases after a certain time, whereas the SFR increases faster when pressure is applied: it reaches a maximum at a certain rate and more or less maintains this rate for the remaining of the simulation. Towards the end of the simulation, the SFR of the no-pressure simulation catches up, again similarly to the clump number behaviour. The SFR for the *gasHigh_d_fb* simulation (right panel of Fig. 4.13) behaves quantitatively similar to the *gasHigh_fb* simulation. One can see that the SFR in these simulations reaches the maximum or plateau at later times than in the corresponding *gasHigh_fb* simulations. The rapid rise of the SFR reaches increasingly higher levels of peak SFR with higher external pressure up to pa5_d, while pa10_d reaches a slightly lower maximum SFR.

The left panels of Fig. 4.13 show that the SFRs of the *gasLow* simulations start with a significant time delay, and the maximum enhancement of the SFR relative to the nP run is highest (~ 12) at the end of the simulation (after 400 Myr). On the other hand, the corresponding SFR enhancements for the higher gas fraction simulations (middle and right panels of Fig. 4.13) are lower (~ 3.5 for *gasHigh* and ~ 1.5 for *gasHigh_d*) at the end of the simulation (after 400 Myr) than at the beginning (~ 40 for *gasHigh* and ~ 70 for *gasHigh_d* at ~ 80 Myr) of the simulation. External pressure thus first produces a significantly higher SFR in comparison to the simulation with no external pressure. But the duration of this large SFR enhancement for the *gasHigh* and *gasHigh_d* simulations is shorter than that of the *gasLow* simulation. The free fall time of the higher density gas is shorter than the free fall time of the low density gas which leads to the gas collapsing early on, whereas a delay is expected for the lower gas fraction disc.

4.3.3.4 Clump properties

Star formation requires a significant supply of cold gas as well as the fragmentation of the disc into clumps that carry a sufficient amount of gas to form stars. On the other hand, one can argue with the Jeans and Toomre instability arguments if indeed an increased pressure outside the galaxy that later increases the pressure inside the galaxy leads to higher densities, as well as a possible expulsion of disc gas depending on the momentum carried

4.3. EXTERNAL PRESSURE-TRIGGERING OF STAR FORMATION IN A DIS GALAXY: A TEMPLATE FOR POSITIVE FEEDBACK

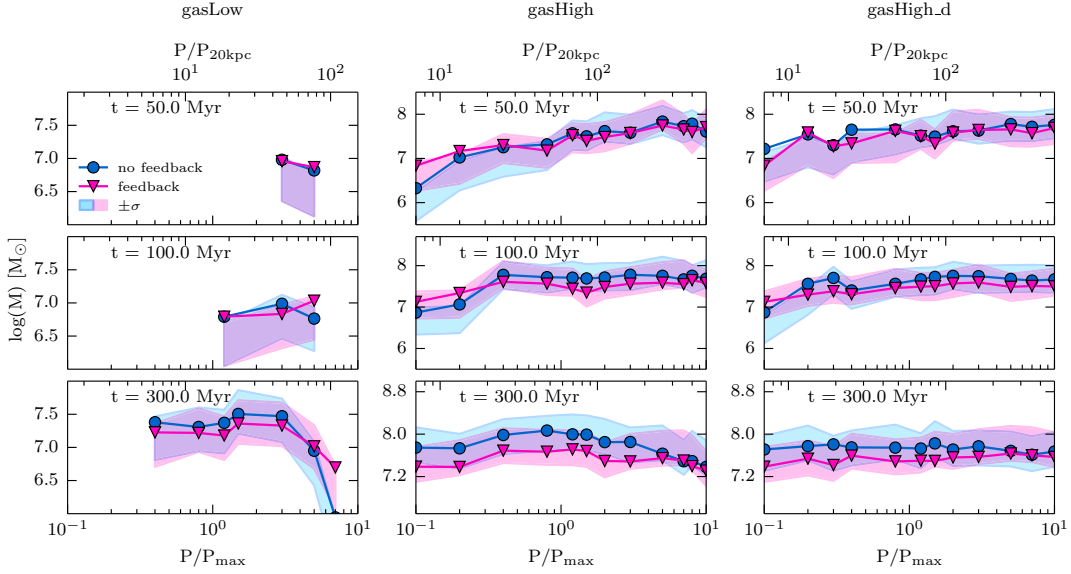


Figure 4.14: Average clump mass for the *gasLow_fb* (left), *gasHigh_fb* (middle), and *gasHigh_d_fb* (right) simulations. The blue line with round markers correspond to the non-feedback simulations whereas the pink line with triangles corresponds to the feedback simulations. The shaded green/blue area shows the area of mass containing $\pm\sigma$ of the density PDF for the no-feedback/feedback simulations. In the bottom and top of each subfigure, the x-axis shows the P/P_{\max} and $P/P_{20\text{kpc}}$ values respectively, where P_{\max} is the maximum pressure inside the disk and $P_{20\text{kpc}}$ is the averaged pressure at 20 kpc. At the beginning of the simulation, the clump masses for the *gasHigh* simulations are higher the greater the pressure for the *gasHigh* simulations. At later times, the clump masses are roughly independent of the external pressure. For the *gasLow* simulation, the clump mass does not increase with higher external pressure but rather decreases or stays at approximately the same level.

by the pressure wave coming into the disc. The competition between higher densities and mass outflow will influence the amount of gas within the clumps.

For the gas-rich disc simulations, we saw (Fig. 4.11) that, at the very beginning, when the pressure wave comes into the galaxy, the number of clumps is highest for the highest pressure. While the clumps are more numerous with the highest pressures, it is worthwhile knowing whether their masses are affected by the external pressure.

Fig. 4.14 shows the modulation of the average clump mass rises with external pressure at three times of the simulations. At early times (top panel), the clump masses for the *gasHigh* simulations (*gasHigh*, center panel, and *gasHigh_d*, right panel) are higher the greater the external pressure. At later times (middle and bottom panel), the clump masses are roughly independent of the external pressure applied, probably because the disc gas has been either already accreted onto the clumps or expelled out of the galaxy (see discussion below), leaving no more diffuse gas available for accretion onto the clumps. The time at which the diffuse gas is either consumed onto the clumps or expelled must happen earlier for the higher external pressure simulations as the fragmentation happened earlier for these simulations. This explains the different times when the SFR reaches a plateau, occurring earlier the higher the pressure. In the *gasHigh_fb* runs at high external pressures, fragmentation is not the only cause of SFR (since there is a maximum pressure enhancement

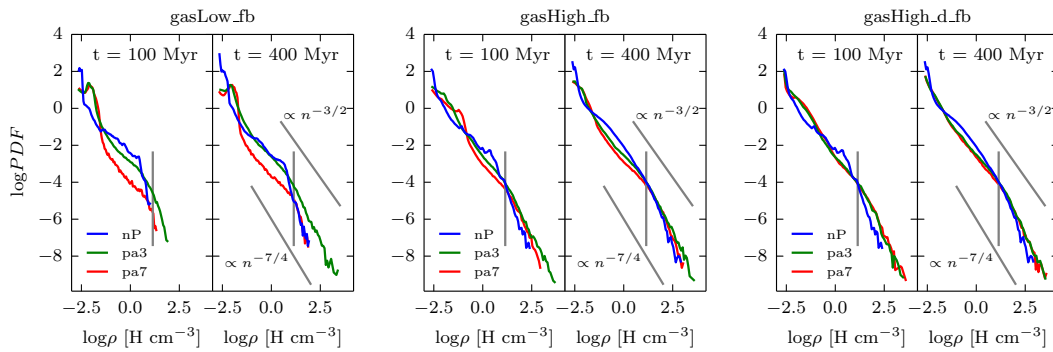


Figure 4.15: Density PDF at different times for a selection of the *gasLow_fb* (left), *gasHigh_fb* (middle) and *gasHigh_d_fb* (right) simulations. The threshold (14 H cm^{-3}) for star formation is plotted as a grey vertical line. One can see that greater external pressure allows the galaxy to reach higher densities on a faster time-scale. The nP simulation slowly catches up with the over-pressure simulations for the *gasHigh* whereas this is not the case for the *gasLow* simulation. For the *gasLow* simulation, the high pressure simulation (pa7) never reaches the high densities. As indicated with the grey power law lines one can see that over the course of the simulation a slope between $-3/2$ and $-7/4$ (or even steeper) develops at high densities. This is in agreement with simulations including gravity and turbulence done for instance by Kritsuk et al. (2011).

beyond which the SFR is lower), meaning that the gas supply is more critical, and not always available despite the high gas fraction. This suggests that the mass flow out of the galaxy also plays an important role. And indeed, the mass outflow is very efficient for pa7 and pa10 after 30 Myr. We will discuss this in detail in Sect. 4.3.3.5, below.

In the *p_dens* simulations, there is a maximum pressure enhancement (pa5_d) beyond which the SFR remains at approximately the same level without decreasing. As we will see in Sect. 4.3.3.5, mass outflows are also absent. The high gas fraction leads therefore to higher density enhancement by external pressure, hence both number of clumps and SFR are highest when the external pressure are high. However, there only is a limited amount of gas available in the galaxy. One can assume that the limited gas supply is insufficient for more star formation, so the SFR remains at the same level independently of the pressure enhancement.

Fig. 4.14 shows that, for the *gasLow* simulations (*gasLow*, left panel), the clump mass does not increase with greater external pressure, but rather decreases at early times (top panel). At later times, the clump mass is roughly independent of the pressure up to pa3, beyond which the clump mass decreases. This is the same pressure enhancement which leads to the highest SFR. As we will see in Sect. 4.3.3.5, the *gasLow* galaxies suffer from strong gas outflows that reduce the supply of gas available for clump buildup, leading in turn to smaller clump masses within the galaxy.

In Fig. 4.14, the difference in clump masses for the feedback and non-feedback simulations can also be seen for all the simulations. At early times, there is no significant difference between the no-feedback and feedback simulations. At later times, the difference in clump masses becomes more apparent for both the high gas fraction and *gasLow* simulations. One can see that the clump masses for the feedback simulations are lower at the end of the simulation than for the no-feedback simulations, independent of the pressure increase. Because the feedback increases the porosity of the interstellar medium that in

4.3. EXTERNAL PRESSURE-TRIGGERING OF STAR FORMATION IN A DISC GALAXY: A TEMPLATE FOR POSITIVE FEEDBACK

turn counteracts the formation of clumps (Silk, 2001), the observed smaller clump masses for the feedback simulations are expected. This difference is more dominant in the *gasHigh* simulation as can be seen in the left panel of Fig. 4.14. The similar mean clump masses in the feedback and non-feedback runs at the beginning of the simulation appears to be a consequence of the implementation of the SNe in the simulation. As discussed above, a SN explosion occurs 10 Myr after the birth of the star particle. The first stars form shortly before 50 Myr and one would therefore not expect to see a large difference between the feedback and no-feedback simulations. At 100 Myr, some stars exploded into SNe, but only constitute a small fraction of all stars, hence the small difference between the feedback and no-feedback simulations at this stage.

It is interesting to look at the density probability function (PDF) at different times of the simulations in order to better understand the observed SFR behaviour. The PDF can be seen in Fig. 4.15 for two different times for a selection of the *gasLow* (left), *gasHigh* (middle), and *gasHigh_d* (right) simulations. Increasing external pressure allows one to reach higher gas densities faster, which is in agreement with the SFR behaviour we have seen previously. For the *gasHigh* simulations, the nP simulation slowly catches up with the over-pressure simulations similar to the SFR behaviour. For the *gasLow* simulation, the no-pressure simulations never attain the densities reached by the moderate pressure enhancement simulations. The high pressure simulation (pa7) also never reaches high gas densities, which is due to the removal of gas within the galaxy, as we will discuss in Sect. 4.3.3.5, below. It can be seen in Fig. 4.15 that over the course of the simulation a high density power law with a slope between $-7/4$ (or even steeper) and $-3/2$ develops, especially for the high gas fraction simulations. A comparable power law range has been found in observations (e.g., Kainulainen et al., 2009, Lombardi et al., 2010) and simulations including gravity and turbulence (e.g, Kritsuk et al., 2011) where they argue that the origin of the power law tail is due to self-similar collapse solutions.

4.3.3.5 The galaxy's mass budget

The mass flow rate (MFR) as well as the total amount of newly formed stars plus dense gas should provide us a better understanding of the star formation history described above. In particular, one would like to understand why there seems to be an optimal external pressure enhancement for star formation, beyond which the SFR ends up at lower values.

We measure the gas mass flux through a sphere of radius 16 kpc as

$$\dot{M}_{\text{gas}} = \oint \rho \mathbf{v} \cdot \hat{\mathbf{r}} dS = \sum_{i \in \text{shell}} m_i \mathbf{v}_i \cdot \hat{\mathbf{r}}_i \frac{S}{V}, \quad (4.6)$$

where i denotes the index of a cell within a spherical shell of surface S and volume V . Here, we adopt a shell of thickness 4 kpc. The MFR is shown in Fig. 4.16 for the *gasLow_fb* (left), *gasHigh_fb* (middle), and *gasHigh_d_fb* (right) simulations, again only for the simulations with SN feedback.

In all three sets of simulations, external pressure leads to mass inflow at early times. This early mass inflow is large but different for the different ways pressure is applied onto the galaxy. In the *p_spher* simulations, the pressure is applied outside the galaxy in a low density medium leading the pressure to have a larger negative pressure gradient than in the *p_dens* simulations where the pressure is applied close to the galaxy and therefore in a higher density environment. The pressure gradient leads to a force acting inwards that leads to the force sweeping the gas inside the yet unaffected low density regions of the circumgalactic medium. This allows the pressure wave of the *p_spher* simulations to carry

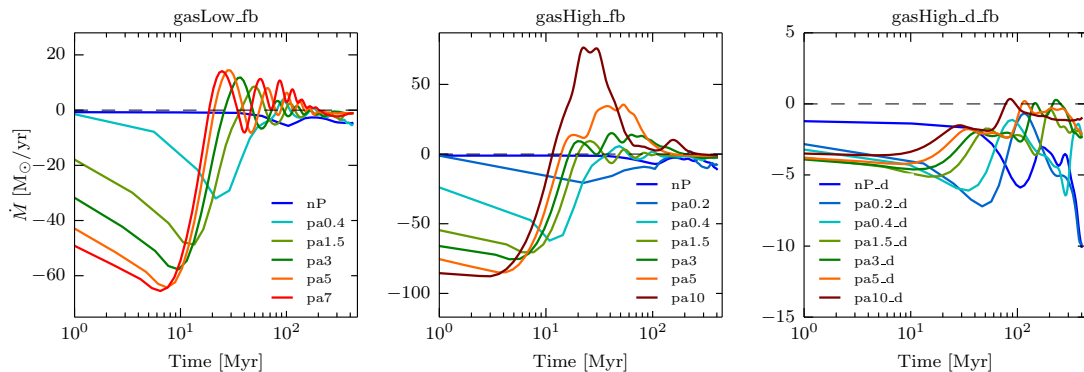


Figure 4.16: Time evolution of the mass flow rate for selected runs from the *gasLow_fb* (left), *gasHigh_fb* (middle) and *gasHigh_d_fb* (right) simulations. Negative (positive) values of the mass outflow rate denote a net mass inflow (outflow). One can see a difference in the mass flow rate (MFR) between the different ways pressure is put on the galaxy (*gasHigh_fb*, *gasHigh_d_fb*). Due to the pressure gradient in the *p_spher* simulations, the pressure wave coming into the galaxy carries a lot of momentum that leads to a mass inflow followed by a mass outflow for the higher pressure simulations. This mass outflow is negligible for the *p_dens* simulations due to the pressure wave carrying very little momentum. For the most extreme case, the expelled mass reaches 80% of the initial gas mass for the highest external pressure simulation of *gasHigh_fb*.

more mass and momentum from the ambient hot medium in comparison to the pressure wave of the *p_dens* simulations.

This explains the larger mass inflow observed in the *p_spher* simulations (left and middle panels of Fig. 4.16) compared to that at the start of the *p_dens* simulation. With its larger momentum, the mass inflow of the *p_spher* pressure wave is followed by a short period of mass outflow (for both low and high gas fractions). This reflecting wave is the analogy of a 1D experiment of a shocked wind (the inflowing gas swept by the extra-pressure wave) onto a reflective boundary (the high-density gas of the galaxy). This mass outflow is negligible for the *gasHigh_d_fb* simulations, since the pressure wave carries very little momentum.

For the *p_spher* simulation sets, higher external pressures lead to stronger maximum inflows at early times and to stronger maximum outflows at later times. In addition, in the simulations with high external pressures (pa7 and pa10), the mass outflow that follows the mass inflow occurs very rapidly (in less than 20 Myr). After these two phases of important mass inflow/outflow, the MFR oscillates around zero for both the *gasLow_fb* and *gasHigh_fb* simulations with $pa < 5$. In contrast, in the *gasHigh_d_fb* simulations, the MFR depends little on the external pressure.

We stress, however, that the pressure and no-pressure *p_dens* simulations do not differ significantly and that, overall, there is little net mass flow. This most likely explains why the SFR of the *p_dens* simulations is smoother and less noisy when compared to the *p_spher* simulations of the same gas fraction (*gasHigh*).

In order to understand the galaxy’s mass budget better, we look at the time evolution of the total mass of newly formed stars plus dense ($n > 0.1 \text{ H cm}^{-3}$) gas. $M_{\text{tot}} = M_{\text{tot,starsN}} + M_{\text{tot,gasD}}$ is shown relative to the initial galaxy gas mass (total not just dense), $M_{\text{tot,gas0}}$ (see Table 4.1) shown in the top panel of Fig. 4.17. $M_{\text{tot,starsN}}$ and $M_{\text{tot,gasD}}$ are shown in the middle and bottom panels, respectively. The initial value of $M_{\text{tot}}/M_{\text{tot,gas0}}$ is below

4.3. EXTERNAL PRESSURE-TRIGGERING OF STAR FORMATION IN A DIS GALAXY: A TEMPLATE FOR POSITIVE FEEDBACK

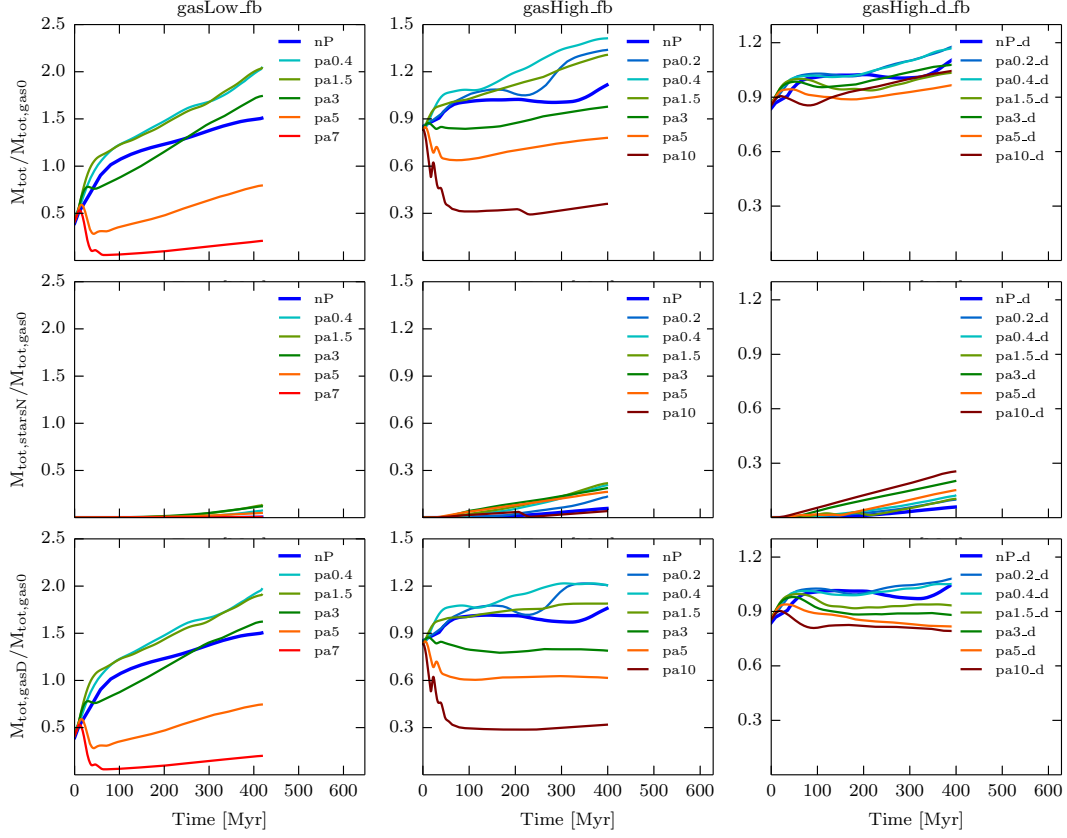


Figure 4.17: Time evolution of the mass in newly formed stars plus dense gas ($n > 0.1 \text{ H cm}^{-3}$) (top), newly formed stars (middle), and dense gas (bottom) relative to the initial gas mass for a selection of the simulations with SN feedback: *gasLow_fb* (left), *gasHigh_fb* (middle), and *gasHigh_d_fb* (right) simulations. The lines are smoothed as in Figure 4.11. Due to the mass inflow shown in Fig. 4.16, at the beginning of the simulation more mass can end up in the galaxy. This extra mass of gas is more significant for the *gasLow* galaxy for both the no-pressure and low-pressure enhancement simulations. For high pressure enhancement in the *gasLow* simulation, the incoming pressure wave significantly disperses the galactic gas. The evolution of M_{tot} is similar for the *gasHigh_fb* simulation albeit with less mass variation. For the *gasHigh_d_fb* simulations, no significant mass variation within the galaxy due to pressurisation is observed. Comparing the top, middle and bottom panels, one sees that for the low-gas fraction simulations, gas dominates the total mass budget of the galaxy. For the higher-gas fraction simulations, the mass of the stars plays a role for the low-pressure enhancement simulations.

unity at $t = 0$ since the gas density in the galaxy is not everywhere above $n > 0.1 \text{ H cm}^{-3}$, especially in the outskirts of the disc and for the *gasLow* galaxy. In the absence of extra external pressure (nP runs), the ratio $M_{\text{tot}}/M_{\text{tot,gas0}}$ quickly moves significantly beyond unity as the gas cooling allows the gas to reach densities above $n > 0.1 \text{ H cm}^{-3}$. The gas cooling also takes place in the circumgalactic medium that feeds the galaxy with some extra gas. The extra mass of gas from the mass inflow and from the gas cooling adds more significantly to the low-gas fraction galaxy because of its lower initial gas mass, which explains why the increase in SFR is more significant in the *gasLow* runs than in the *gasHigh* runs. Comparing the top panel with the middle and bottom panels, one sees that dominates the total mass budget of the disc for the low-gas fraction simulations. For the higher-gas fraction simulations, the mass of stars plays a role for the low external pressure simulations. For the *p_dens* simulations the fraction of stars affects the SFR at late times in the simulation.

For the *gasLow* simulations, intermediate regimes of forced external pressure (from pa0.4 to pa3) also show values of $M_{\text{tot}}/M_{\text{tot,gas0}}$ above 1 with values comparable to the nP run. Therefore, the increase in SFR (an order of magnitude above nP) is to be attributed to the extra compression of the ISM and exploration of larger gas densities with shorter collapsing time-scales (see Fig. 4.15). In contrast, higher pressurisation values of the ISM (pa5 and pa7) lead to strong gas removal due to the incoming pressure wave that manages to significantly disperse the galactic gas. Since the gas reservoir is reduced, the SFR is also suppressed compared to more intermediate regimes of pressurisation, but the overall SFR is still larger than in the nP case, where gas fragmentation is not reached.

The evolution of $M_{\text{tot}}/M_{\text{tot,gas0}}$ in the *p_spher gasHigh* galaxy behaves similarly to that for the *gasLow* galaxy, although with lower mass variation. It starts below unity for all pressures, and decreases even more for the high pressure increases (pa5 and pa10), because of the large mass outflows observed for those runs. This shows that the large mass outflows associated with high pressures prevent star formation. On the other hand, $M_{\text{tot}}/M_{\text{tot,gas0}}$ keeps rising for the lower pressure enhancements, showing that because no large mass outflow is observed, more stars can be formed. The $M_{\text{tot}}/M_{\text{tot,gas0}}$ curve is higher when a small pressure is applied outside the galaxy compared with the no-pressure simulation. In the case of *p_dens* over-pressurisation, there is no significant (< 20 percent relative) mass variation in the galaxy. Thus, the early fragmentation due to the increased pressure drives the different SFR levels for the different pressure simulations.

4.3.3.6 The star formation rate

Fig. 4.18 illustrates how the SFRs of different pressure simulations compare with one another at different times. For the *gasLow*, *gasHigh*, and *gasHigh_d* simulation sets, the SFR increases with increasing external pressure until a maximum is reached and then decreases again or stays at a similar level as for the *gasHigh_d* simulations. Also, no significant difference in the SFR can be seen between the feedback and non-feedback simulations, indicating that the external pressure increase is the dominant effect driving the increased SFR.

In order to compare with the prediction explained below, a dark red dashed curve is plotted to guide the eye in Fig. 4.18 representing a power 9/10 fit of the SFR as a function of the external pressure applied on the galaxy. One sees that, for the gas-rich *gasHigh* and *gasHigh_d* simulations, the SFR follows a power 9/10 of the external pressure very well. At later times, the 9/10-th power law is only fulfilled until the optimal pressure is reached. For the *gasLow* simulations, the SFR does not scale well with the 9/10th power of the

4.3. EXTERNAL PRESSURE-TRIGGERING OF STAR FORMATION IN A DISC GALAXY: A TEMPLATE FOR POSITIVE FEEDBACK

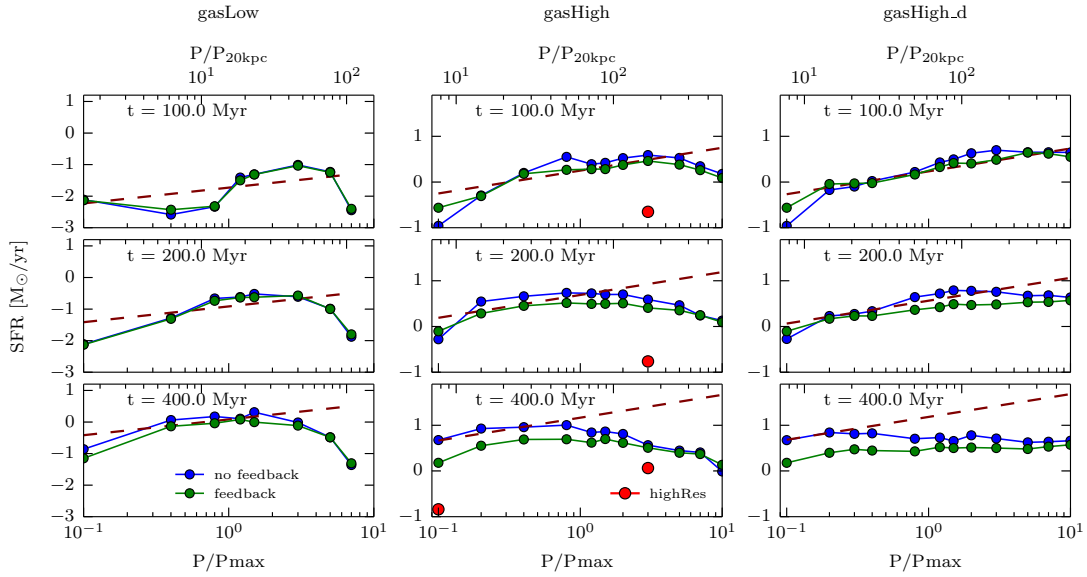


Figure 4.18: Time evolution of the star formation rate for all the *gasLow_fb* (left), *gasHigh_fb* (middle), and *gasHigh_d_fb* (right) simulations. Here, the no-feedback simulations are shown in blue and the feedback simulations are shown in green. The red points are the corresponding points from the *highRes* runs. The calculation of the SFR at a given time has been performed on the smoothed data. The SFR data are smoothed as in Figure 4.11. The dark red-dashed straight lines correspond to visual fits with a slope 9/10th to guide the eye. One can see that for higher gas fraction simulations, the SFR increases with external pressure and follows a power 9/10th of the external pressure. At later times, this is only true up until a certain external pressure. For the low gas fraction simulation, the SFR growth rate does not scale with power 9/10 of the external pressure.

external pressure. But as explained below, this was not unexpected.

The bright red points in Fig. 4.18 are the corresponding points from the *highRes* run. As can be seen in Appendix 4.3.5.3 the formation of stars in the *highRes* run shows a delay compared to the *lowRes* run. This is due to the increase in star formation threshold for the higher resolution run. Because of this delay, one can also see a delayed behaviour of the SFR of the *highRes* run in Fig. 4.18. However, at later times, the *highRes* simulation shows a similar behaviour to the *lowRes* simulation.

We expect the SFR to scale as the power 9/10th of the external pressure, at least in the *gasHigh* and *gasHigh_d* cases (where the discs are initially Toomre unstable and the clumps are formed before the arrival of the pressure wave), for the following reason. According to the Schmidt law of equation (4.3), the star formation rate $\dot{\rho}_*$ in a clump of density ρ_g in a galactic disc is

$$\dot{\rho}_* = \epsilon \frac{\rho_g}{t_{\text{dyn}}} \propto \rho_g^{3/2}, \quad (4.7)$$

where ϵ is a dimensionless constant of order 0.02 and $t_{\text{dyn}} \propto \sqrt{G \rho_g}$ is the dynamical time in the clump.

The clumps, which have started forming at $t = 0$ because the disc is initially Toomre unstable (Fig. 4.12), are compressed when they are hit by the pressure wave. Since the disc gas does not cool significantly when the pressure wave hits the disc (the ratio of clump size to external sound speed is shorter than the clump cooling time), it is reasonable to assume

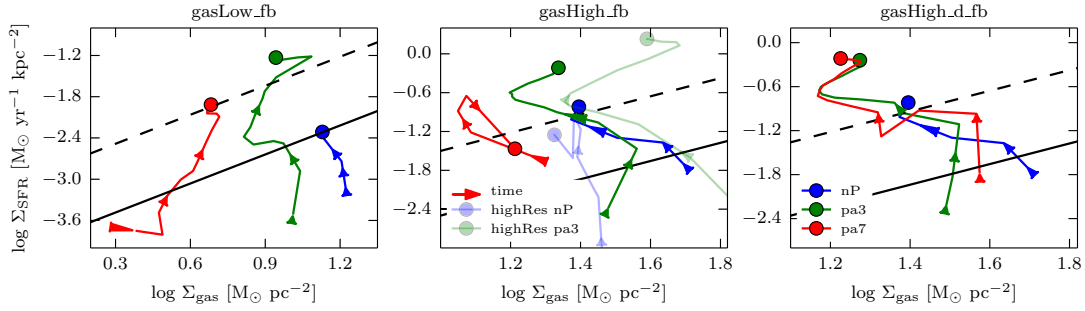


Figure 4.19: Kennicutt-Schmidt (KS) relation for selected runs (nP, pa3, pa7 with blue, green and red curves, respectively, with lighter colours for the runs with 4 times higher spatial resolution) from the *gasLow_fb* (left), *gasHigh_fb* (middle) and *gasHigh_d_fb* (right) simulations at 16 different times in color. The evolution in time is shown with arrows. The 16 different times are equally spaced between $t_{\text{start}} = 25$ Myr and $t_{\text{end}} = 400$ Myr. The circle shown corresponds to t_{end} of the simulation with the corresponding color. Data from Daddi et al. (2010) for the starburst (dashed line) and quiescent (solid line) sequences are over-plotted for reference. For all the simulations, independently of the gas fraction, the simulations with external pressure lie closer to the starburst sequence than the no-pressure simulations. This shows that our toy model for AGN-induced star-formation might be a possible explanation for explaining the increased number of starburst galaxies observed in the distant Universe.

adiabatic clump evolution. One then expects that density will rise as the power $1/\gamma$ of the pressure, hence, according to equation (4.7), $\dot{\rho}_* \propto P_{\text{ext}}^{3/(2\gamma)}$. Therefore, for $\gamma = 5/3$, one finds $\dot{\rho}_* \propto P_{\text{ext}}^{9/10}$ for a given clump.

Finally, since most of the star formation happens within the dense regions it is safe to assume that most of the star formation happens within the clumps. We hence expect the total SFR of the disc to vary as $P_{\text{ext}}^{9/10}$ which matches the modulation of the SFR measured in our simulations with external pressure. After around 100/200 Myr, the assumption of adiabatic evolution is no longer valid, especially for the high density clumps for which the temperature cools down faster and reaches the temperature floor T_{floor} .

Admittedly, this approximation is crude because the clumps are still forming when the pressure wave hits the *gasHigh* and *gasHigh_d* discs. Also, our adiabatic approximation neglects the possible role of turbulence, for example induced by supernova explosions (Silk, 2001; Silk & Norman, 2009; Silk, 2013), in modulating the SFR in clumps. But we notice that, in our simulations, the relation between the disc SFR and the external pressure is only weakly affected by the presence of supernovae (compare the no feedback and feedback points in Figure 4.18), which explains why the adiabatic evolution of clump densities appears to explain the modulation of disc SFR with external pressure of Figure 4.18.

Hence, we expect that AGN-induced pressure should provide a boost of the star formation rate, independently of any possible increase in star formation efficiency, and initially roughly vary as the power 0.9 of the external pressure.

4.3.3.7 The Kennicutt-Schmidt relation

The Kennicutt-Schmidt (KS) law (Kennicutt, 1998b) law relates the SFR per unit area as a power of the surface density of gas. This relation holds over several orders of magnitude

4.3. EXTERNAL PRESSURE-TRIGGERING OF STAR FORMATION IN A DISC GALAXY: A TEMPLATE FOR POSITIVE FEEDBACK

in both quantities (Krumholz, Dekel, & McKee, 2012, and references therein), with the same normalisation for global galaxies (including high redshift ones, Genzel et al., 2010b) and giant molecular clouds in the Milky Way (Heiderman et al., 2010; Lada, Lombardi, & Alves, 2010) and in the nearby M51 galaxy (Kennicutt et al., 2007). This demonstrates the remarkable universality of the SFR. At high redshift, starburst galaxies lie above the KS law for normal galaxies (Genzel et al., 2010b). While the cause of this observed offset is not known, one may speculate that this increased SFR may be caused by positive AGN feedback.

To investigate this in further detail, we check whether our pressurised galactic discs follow the KS relation for normal galaxies, or are above it as starbursts are observed to be, or below it. We adapt here an equivalent technique to Powell et al. (2013) and calculate the half-light radius by assigning a luminosity to each star particle dependent on their age and proportional to their mass (Weidner et al., 2004),

$$L(\text{age} < 10 \text{ Myr}) \propto M_{\text{stars}} \quad (4.8)$$

$$L(\text{age} > 10 \text{ Myr}) \propto M_{\text{stars}} \left(\frac{\text{age}}{10 \text{ Myr}} \right)^{-0.7} \quad (4.9)$$

We randomly assign an age in the range 0–5 Gyr for stars that are specified in the initial conditions and therefore have an age equal to zero when the simulation starts. For a given output, Σ_{SFR} is calculated within the half-light radius using the SFR averaged over the previous 10 Myr. The KS relation is calculated by finding the 3D half-light-radius. Within this volume, all the gas above a threshold of 0.1 H cm^{-3} is used to calculate Σ_{gas} and all the new stars are used to calculate Σ_{SFR} , however the quantities are divided by the area $\pi r_{3\text{D}}^2$.

Fig. 4.19 shows the KS relation at different times for several simulations for the three cases of *gasLow_fb*, *gasHigh_fb*, and *gasHigh_d_fb* with the observed relation from Daddi et al. (2010) overplotted. One can see that, over the course of 400 Myr, all runs lead to an increase in Σ_{SFR} , by one to two dex, with much smaller variations (less than 0.3 dex) in Σ_{gas} . In particular, the runs with high gas fraction (with or without external pressure) show a decrease in Σ_{gas} . This decrease in gas surface density is related to the gas mass outflow at late times (Fig. 4.16) and to the consumption of gas by star formation. For the *gasLow* simulation, the evolution of Σ_{gas} is tied to the evolution of the total baryonic mass within the galaxy shown in Fig. 4.17. The light blue and green lines in Fig. 4.19 show the *highRes* simulations for the nP and pa3 set, respectively. One can see that the trends of the *highRes* simulation are very similar to the trends of the *lowRes* simulations, specifically at late times. Especially for the pa3 *highRes* simulation, one can see that higher gas densities are reached due to the higher resolution which allows the gas to collapse even further.

For all the simulations independently of the gas fraction, the simulations with external pressure end up being pushed closer to or further beyond the starburst sequence than the corresponding simulations without external pressure. This trend is not changed for the *highRes* runs. Runs with external pressures leading to higher SFR also have a higher Σ_{SFR} and therefore end up even closer to the starburst sequence. For instance, for the *p_spher* simulations, the pa7 run does not extend as far beyond the observed starburst sequence as the pa3 run, which reaches higher SFR for both the *gasLow_fb* and *gasHigh_fb* simulations (Figs. 4.13 and 4.18). This is not as significant for the *gasHigh_d_fb* simulations as they do not experience a decrease of SFR but rather that the SFR stays at a certain level after a certain pressure increase ($\sim \text{pa5}$). We therefore see for this simulation set that the KS relations end in a very similar parameter space.

We conclude that this toy model for AGN-induced over-pressurisation plausibly leads to AGN-associated star-forming galaxies having enhanced specific star formation rates, for example as suggested by recent observations, cf. (Zinn et al., 2013; Drouart et al., 2014).

4.3.4 Conclusions

It is a fascinating challenge to understand the extreme star formation rates observed for some high-redshift galaxies, typically with luminous AGN and massive outflows: are these caused by higher contents of molecular gas or by a greater efficiency of star formation relative to this molecular gas content? Is turbulence sufficient to explain the high SFR values, or do we need recourse to a more exotic pathway that enhances star formation rates even more? The latter option is motivated by the increasing evidence for the role of AGN in star formation, and in particular their role in a putative phase of positive feedback that accompanies or even precedes the commonly observed massive, star formation-quenching, outflows stimulated by AGN activity.

Using hydrodynamical simulations of isolated disc galaxies embedded in a hot over-pressurised halo, we have been able to study the response of the galaxy SFR to the forcing exerted by this external gas pressure onto the disc. The pressure enhancement triggers instabilities leading to more fragmentation when compared to the no-pressure simulations (Figs. 4.9 and 4.10). The enhanced fragmentation leads to the formation of more clumps (Fig. 4.11) as well as larger values of SFR (Fig. 4.13). This hints at a positive effect of the pressurisation of the disc and therefore to positive feedback.

We observe a difference in the behaviour for the different ways in which the pressure is applied. In the simulations where external pressure is continuously applied beyond a certain radius (*p_spher* simulations), we observe an optimal pressure beyond which the number of clumps as well as the SFR is decreased. For the simulations where the pressure is instantaneously applied using a density threshold (over-pressure applied closer to the galaxy disc), such an optimal pressure is not observed.

We have seen that the mass outflow plays a role in explaining this optimal pressure. In particular, for the *gasHigh_fb* simulations, a significant amount of gas gets expelled out of the galaxy, leaving little gas left to form stars and thereby lowering the SFR. The difference in SFR between the high and low external pressures for the *gasLow_fb* simulations is explained by the stagnation of the accumulation of mass in the clumps, which is again related to the large amount of gas that is removed by the incoming pressure wave. Our simulations have been tested with respect to the resolution and local presence or absence of SN explosions: the over-pressurisation of the disc still leads to a positive feedback effect (enhanced SFR).

We found that at given times of the *p_spher* simulations, the SFR (and its mean growth rate) vary as the power 9/10th of the applied pressure. We explain this by adapting the Schmidt law for the SFR as a function of 3D gas density for the inclusion of extra pressure caused by the AGN bow shock-driven radio lobe or wind, leading to compression times typically an order of magnitude shorter than the dynamical time, as argued by Silk & Norman (2009).

Though our setup of the extra pressure exerted by circumgalactic gas onto the galaxy is crudely modeled to mimic the pressure confinement by AGN activity, we are confident that such a mechanism could operate in more realistic configurations (see the jet simulations of Gaibler et al., 2012). We have demonstrated that such pressure confinement of the ISM drives the galaxy into an intense star formation regime, and could explain observations of star formation-enhanced galaxies in the presence of jet activity (Zinn et al., 2013).

Cosmological simulations of pure AGN jet feedback in galaxy clusters (Dubois et al., 2010a) have shown that it has a negative impact on the galaxy SFR on the long-term, though these simulations were lacking spatial resolution in order to properly capture the small-scale fragmentation of the ISM. Our more global picture could suggest a two-stage mechanism for AGN feedback: a compression phase leading to a short burst of star formation, together with the expulsion or heating of the circumgalactic gas leading to a suppression of the gas accretion onto the galaxy and its star formation on longer time-scales. This remains to be verified with simulations of galaxies embedded in a cosmological environment with high spatial resolution and a self-consistent treatment of AGN feedback. We defer this study to future work.

Acknowledgments

YD and JS acknowledge support hosted by UPMC – Sorbonne Universités and JS for support at JHU by National Science Foundation grant OIA-1124403 and by the Templeton Foundation. RB has been supported in part by the Balzan foundation and the Institute Lagrange de Paris. This work has been partially supported by grant Spin(e) ANR-13-BS05- 0005 of the French ANR. The simulations have made use of the Horizon cluster. We specially thank S. Rouberol for technical support with the horizon cluster at IAP. We also thank M. D. Lehnert, M. Volonteri, A. Wagner, J. Coles and A. Cattaneo for valuable discussions. We finally thank the anonymous referee for his/her constructive comments that definitely improved this article.

4.3.5 Appendix

4.3.5.1 Bipolar pressure increase

To study the assumption of a isotropic pressure increase, we have performed a simulation of a non-isotropic bipolar pressure increase. For this the pressure has only been increased after a certain height (1.5 kpc) in the vertical direction of the galaxy, where the pressure has been kept at the normal value in the radial direction. The SFR of the *bipolar* and *isotropic* simulations are shown in Fig. 4.20. One can see that while the *bipolar* SFR oscillates more the general behaviour is not changed by the way pressure is applied on the galaxy.

4.3.5.2 Effects of supernova feedback

Here, we compare the feedback run with the no-feedback run. In Fig. 4.21 the gas density maps of the no-pressure enhancement simulations are shown for the non-feedback (nf, left panel) and feedback (fb, right panel) simulations. In Fig. 4.22 the comparison between fb and nf is shown for the pa3 simulations. We see that for the no-pressure simulations, the effect of SN explosions is to disrupt the interstellar medium into smaller but more numerous clumps. In the edge-on-view, we can also see that the feedback simulation thickens the disc and enhances the mass outflow close to the galaxy. For the pressure simulation, no significant difference can be observed. It shows that the effect of external pressure is stronger than the effect of SN explosions.

In Fig. 4.23, we show the number of clumps as a function of time for a selection of the *gasLow* (left), *gasHigh* (middle), and *gasHigh_d* (right) simulations with (fb) or without (nf) SN feedback. In Fig. 4.24, we show the time evolution of the SFR for the same selection of runs. We see that the number of clumps is enhanced by the presence of SN explosions in all cases since the clumps are regularly destroyed by the SN activity (Dubois et al., 2015b). SNe regulate the mass growth of the gas clumps, and since the most massive clumps are

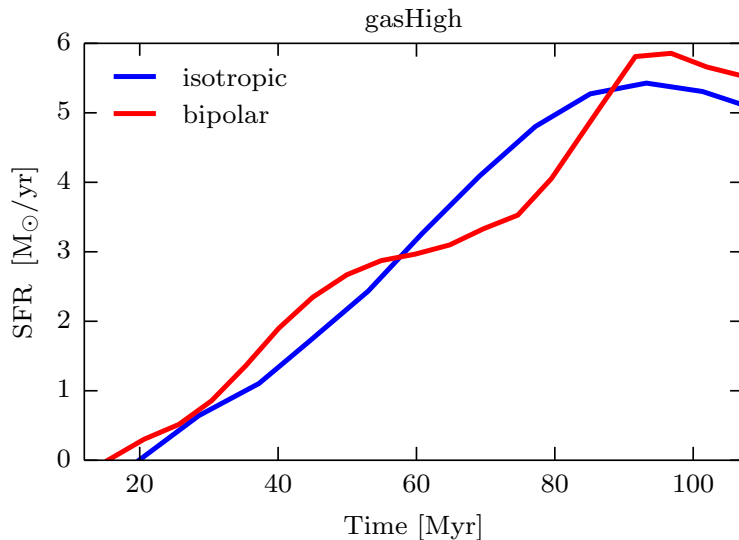


Figure 4.20: Star formation rate (SFR) as a function of time: In blue for the case where the pressure is applied isotropically (*isotropic*) and in red when the pressure is applied to the galaxy in a bipolar geometry. (*bipolar*).

expected to capture the smaller clumps, SNe allow for the increase in the number of clumps, thereby reducing their average cross section and mass (see Fig. 4.14). We also see that the SFR is higher for the non-feedback simulation compared to the feedback simulations as a consequence of the absence of a local regulating process within gas clumps.

Reassuringly, the effect of over-pressurisation of the disc onto the SFR enhancement is independent of the presence of SN explosions: it still leads to a positive feedback effect that SNe only marginally modulate.

4.3.5.3 Convergence Studies

In this section, we test how the results depend on the resolution of the simulation. We performed two high resolution (*highRes*) simulations for the *gasHigh* case, one with no external pressure (nP_hR) and the other with external pressure (pa3_hR). The higher resolution runs have been performed with a resolution of $\Delta x = 10$ kpc (compared to 40 kpc for the standard runs). We changed the density threshold for star formation ($n_0 = 224 \text{ H cm}^{-3}$) in the polytropic EoS as well as the dissipation time-scale of the non-thermal component for the SN feedback ($\Delta x = 10$ pc) with the resolution. The simulations were run for a similar timescale (~ 400 Myr) as the lower resolution (*lowRes*) simulations.

In Fig. 4.25, we show the comparison between the *highRes* and *lowRes* simulations. In the upper panel, the number of clumps is shown for the high and low resolution runs where for both simulations the same clump detection density threshold of 21 H cm^{-3} and a peak-to-saddle threshold of 1.5 was chosen.

Fig. 4.25 shows that, in both *highRes* and *lowRes* runs, clumps are formed at a faster rate when over-pressure is applied on the galaxy. Comparing the two resolution runs, we see that the rates of clump formation for both resolutions are comparable at the start of the simulations, for both the pressure and no-pressure runs. While the *lowRes* run with external pressure (pa3) sees a sharp rise in its clump number at 25 Myr, the number of

4.3. EXTERNAL PRESSURE-TRIGGERING OF STAR FORMATION IN A DIS GALAXY: A TEMPLATE FOR POSITIVE FEEDBACK

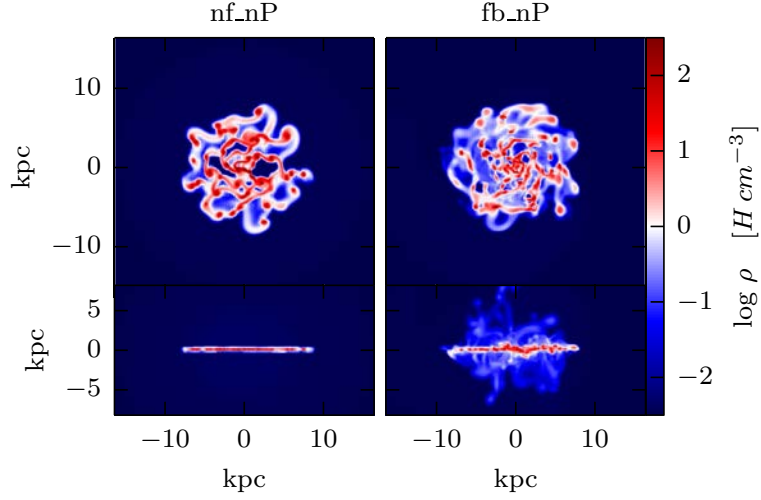


Figure 4.21: Gas density maps (mass-weighted) of the *gasHigh* non-feedback (left) and feedback (right) simulations without enhancement of the external pressure (nP). The maps are taken at the end of the simulation (~ 400 Myr). Each panel shows both face-on (40×40 kpc, upper part) and edge-on (40×20 kpc, lower part) views.

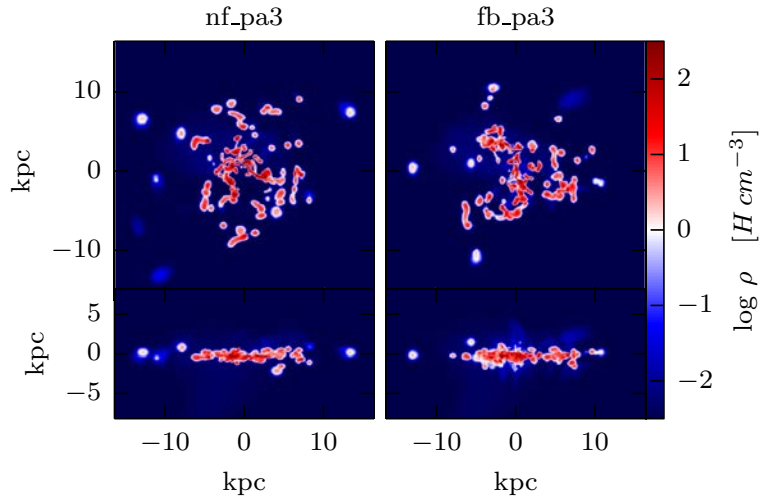


Figure 4.22: Similar as Fig. 4.21 but for the simulations with pressure enhancement pa3.

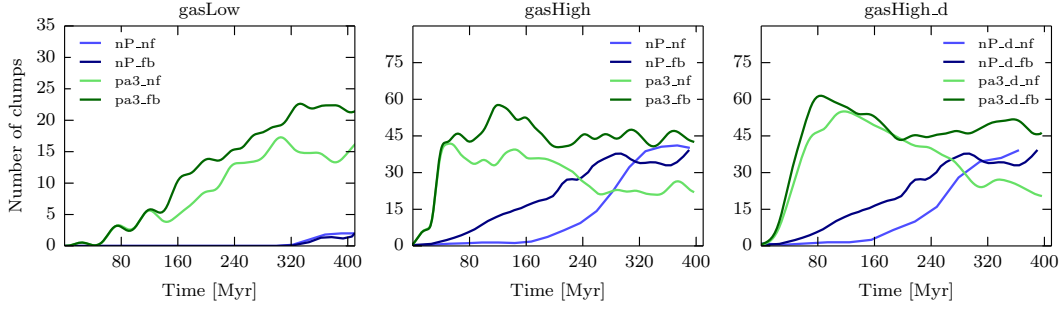


Figure 4.23: Time evolution of the number of clumps for a selection of the *gasLow* (left), *gasHigh* (middle), and *gasHigh_d* (right) simulations. For each simulation set the feedback (fb) and non-feedback (nf) runs are shown for comparison. They are indicated by the suffixes in the legend. The lines are smoothed as in Figure 4.11.

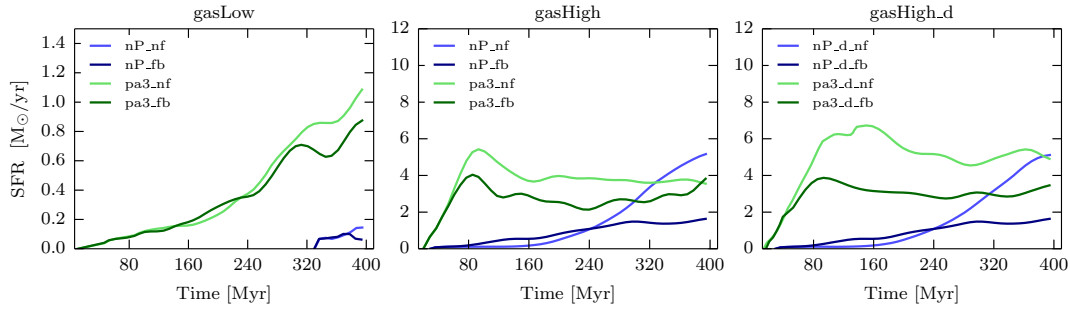


Figure 4.24: Time evolution of SFR for a selection of the *gasLow* (left), *gasHigh* (middle), and *gasHigh_d* (right) simulations. For each simulation set the feedback (fb) and non-feedback (nf) runs are shown for comparison. They are indicated by suffixes in the legend. The lines are smoothed as in Figure 4.11.

clumps in the *highRes* run with external pressure (pa3_hR) starts catching up after 50 Myr and soon (at 70 Myr) overtakes that of the pa3 run, to end up with nearly double the number of clumps. A similar effect is seen in the no-pressure runs: the number of clumps in the *highRes* simulation starts slowly, but overtakes that of the *lowRes* run (at 230 Myr) to also end up with nearly double the number of clumps.

Similar trends are seen in the star formation histories (lower panel of Fig. 4.25). For the no-pressure runs, the *highRes* one overtakes the other one in SFR at 280 Myr to end up with twice the SFR, while in the corresponding runs with external pressure, the *highRes* one has its SFR overtake that of the *lowRes* analog at 150 Myr, end the *highRes* run ends up with over double the SFR of the *lowRes* one. The very slow rise of the SFRs in the *highRes* runs is the consequence of our choice of a higher density threshold for the *highRes* simulations, which is reached at later times. Once stars start to form, the SFR is greater in the pressure simulation than in the no-pressure simulation. The general effect that the pressurisation leads to more star formation is therefore still the same.

4.3. EXTERNAL PRESSURE-TRIGGERING OF STAR FORMATION IN A DIS GALAXY: A TEMPLATE FOR POSITIVE FEEDBACK

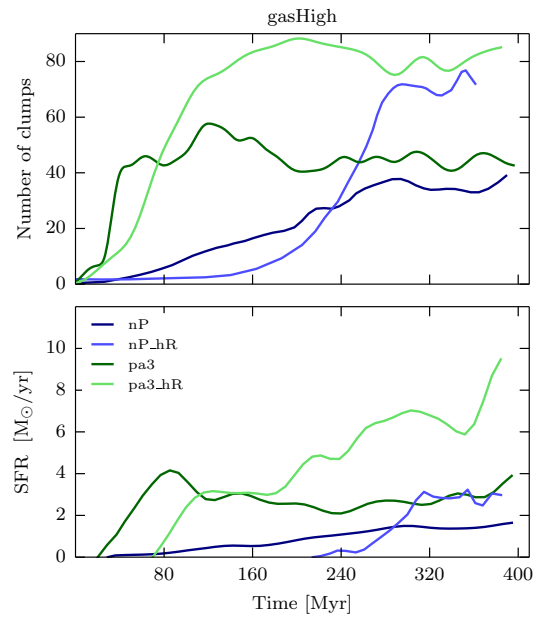


Figure 4.25: Time evolution of the number of clumps (upper panel) and SFR (lower panel) for the low resolution and high resolution *gasHigh_fb* simulations. The clumps were extracted using a gas density threshold of 21 H cm^{-3} .

Feedback from Radiatively-driven AGN Winds

Extreme episodes of gas accretion onto supermassive black holes (SMBHs), in particular in high-redshift galaxies, are followed by quasar activity. The photons emitted by a quasar eventually couple to the gas and drive large-scale winds. In most hydrodynamical simulations, quasar feedback is approximated as a local thermal energy deposit within a few resolution elements, where the efficiency of the coupling between radiation of the gas is represented by a single parameter tuned to match global observations, typically, the correlation between SMBH mass and the galaxy velocity dispersion (e.g., Ferrarese & Merritt, 2000). In reality, the efficiency of the coupling between the radiation field and the dusty gas conceals complex physics and is not yet fully understood as they rely on a number of assumptions about, for instance, the absorption of photons, mean free paths, optical depths, and shielding. Our limited understanding of how the radiation-gas interaction eventually leads to large-scale outflows and effects the ISM, has hence made the assessing of the claims of these studies difficult.

A more accurate description is to self-consistently model the radiation from a SMBH via radiation-hydrodynamics (RHD). Photons moving through gas and dust grains can be scattered or absorbed and transfer some of their momentum, which eventually results in a powerful quasar wind. If the gas around the quasar is optically thick, the infrared (IR) radiation, partly coming from the quasar spectrum and partly from the re-emitted dust-absorbed energy from ultra-violet (UV) photons, can be trapped. The radiation pressure from these IR photons depends on the optical depth around the source, which complicates the determination of the efficiency of the radiation-gas coupling. The difficulties arise because the distribution of gas around the black hole is often unknown, and, hence, it is unclear whether the IR photons manage to scatter a sufficient number of times to boost the momentum transfer onto the gas. In general, the (IR) photons tend to escape through the path of least resistance along optically thin sightlines before they are able to impart a large momentum boost onto the gas. Additionally, the gas is also capable of reshaping the radiation field leading to complex phenomena such as Rayleigh-Taylor instabilities (see for instance Krumholz & Thompson, 2012, 2013; Davis et al., 2014) that again can help the formation of low density tunnels through which the (IR) radiation can escape, and in turn lower the efficiency of the radiation-gas coupling.

There is little consensus whether the radiatively-driven winds are momentum-conserving ($\dot{p} \simeq L/c$; as proposed by King, 2003) or energy-conserving ($\dot{p} \gg L/c$; as proposed by Silk & Rees, 1998; Faucher-Giguère & Quataert, 2012; Zubovas & King, 2012). However, evidence for energy conservation in quasar-mode feedback is growing. There is recent observational evidence, in two low redshift ultra-luminous infrared galaxies, for AGN accretion disc winds at $\sim 0.2 c$, which drive large-scale massive molecular outflows (Tombesi et al., 2015; Feruglio et al., 2015). Momentum-driven flows fail to drive the observed fast ($\sim 1000 \text{ km s}^{-1}$) molecular outflows detected on kpc scales, whereas energy-conserving outflows are found to provide the observed mechanical energy (Faucher-Giguère & Quataert, 2012; Wagner et al., 2013).

In order to investigate the dependence of radiation feedback efficiency on the properties of the ISM, Bieri et al. (2016a) used a series of galaxies initialised with a two-phase ISM consisting of a warm and tenuous hot phase that simultaneously satisfies single-point log-normal statistics and two-point fractal statistics. The coupling between the injected photons and the ISM is simulated using the RHD equations, describing the emission, absorption, and propagation of photons with the gas and dust.

The simulations show that radiation from a quasar is capable of driving large-scale

high-velocity wind with mass outflow rates comparable to observations. The models favour winds that are energy-driven via extremely fast outflows, interpreted as being IR-radiatively-driven winds. IR radiation is necessary to efficiently transfer momentum to the gas via multi-scattering on dust in dense clouds. Albeit IR multi-scattering is extremely important, especially at early times, the amount of momentum quickly declines as the central gas cloud expands and breaks up, allowing the radiation to escape through low density channels. The typical number of multi-scattering events from an IR photons is only about a quarter of the mean optical depth from the center of the cloud.

This Chapter is mainly extracted from the paper Bieri et al. (2016a) describing in more detail the investigation of how the radiation emitted from the thin accretion disc surrounding the SMBH effectively couples to the ISM by means of RHD.

5.1 Setting up the initial two-phase density distribution

Turbulence naturally gives rise to a non-uniform structure in the velocity and density field. For a detailed review on the topic of turbulence see Elmegreen & Scalo 2004, and Scalo & Elmegreen 2004. To setup a non-uniform medium we make the analogy with a turbulent medium. The approach used does however not model actual turbulence in a genuine causally generated ISM (see Kritsuk et al. 2011 and references therein). It rather parametrises the non-uniform properties of generic turbulent medium and focuses on characteristics such as the variance σ^2 , the intermittency, and two-point self-similar structures, and relies on a range of previous experimental and theoretical results from the field of turbulence. The initial distribution of the ISM that is adopted should therefore be regarded as a physically motivated generalisation of an inhomogeneous ISM, but may not necessarily represent an accurate model of a turbulent ISM.

The setup of the inhomogeneous interstellar medium density field is on average isotropic, meaning that there is no dependence on location. The density distribution is setup via an iterative process described first in Lewis & Austin (2002) such that it simultaneously follows log-normal single-point statistics (see Eq. 5.1) and a power-law self-similar structure. Section 5.2.2.1 discusses in more detail the different parameters chosen. We have used the PYFC package introduced in Wagner & Bicknell (2011) and adapted it to our needs (mainly paralised part of the code in order to have a smaller minimum sampling wave-number). The code PYFC first constructs a cube in which each n cells follows a Gaussian distribution with mean m and standard deviation s (see Eq. 5.1). This cube is then Fourier transformed and apodised by a Kolmogorov power-law in wave-number with index $-5/3$ and minimum sampling wave-number k_{\min} . In real space the minimum sampling wave-number determines the scale of the largest fractal structure in the cube relative to the size of the cube. Effectively, it is the average number of clouds per dimension divided by two. For example, in one setup of our simulation we used $k_{\min} = 5$ for a cube mapped to a galaxy with a radius of $r = 3$ kpc. Then the largest structures (clouds) extend to $R_{c,\max} = 3\text{kpc}/(2k_{\min}) = 300$ pc. In the next step of the iterative process the cube is Fourier transformed back to the spatial domain and exponentiated. The last step alters the power-law structure in Fourier space. The cube is iteratively transformed between Fourier space and real space until a satisfactory convergence to the power-law within 1% is obtained.

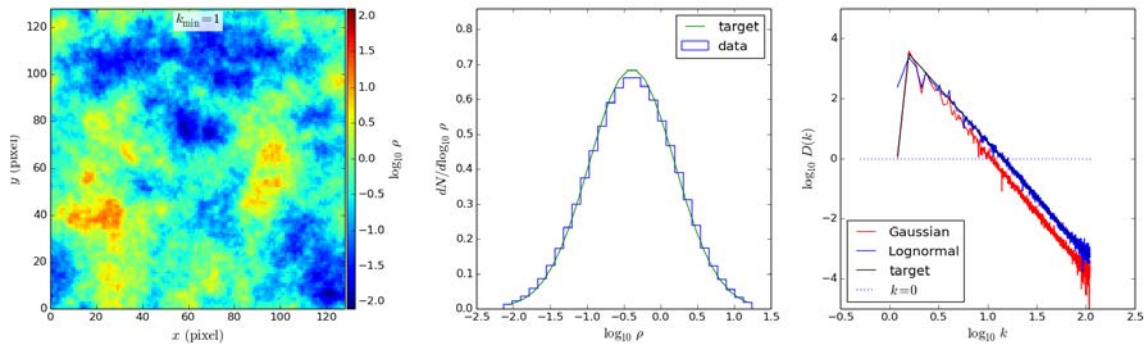


Figure 5.1: Visualisation of density scalar field and statistical distribution of the fractal cube. *Left*: Slice through the density scalar field, *Middle* log-normal probability density function of the density scalar, and *Right* power-law power spectrum in Fourier space. The minimum sampling wavenumber in this example is chosen to be $k_{\min} = 1$.

The density cube is placed into the RAMSES simulation domain by reading each density value within the cube and placing it into a cell of the RAMSES grid. Note that the resolution of the produced cube does not necessarily need to be the resolution of the smallest cell within the simulation box.

Additionally, the density cube can be moved such that the densest cell within the cube is placed in the center of the simulation box. The changing of the density structure is done by moving around the grid of the initial density cube. Since the fractal cubes are generated purely by manipulations in the fourier space of the scalar field, the cube read into RAMSES is by construction periodic and hence can be tessellated or shifted. By leaving the source of the BH at the center of the disc structure this thus changes the environment around the black hole. Note, however, that the statistical properties are still the same.

5.2 Outflows Driven by Quasars in High-Redshift Galaxies with Radiation Hydrodynamics

REBEKKA BIERI¹, YOHAN DUBOIS¹, JOAKIM ROSDAHL², ALEXANDER WAGNER³,
JOSEPH SILK^{1,4,5,6}, AND GARY A. MAMON¹

¹ Institut d’Astrophysique de Paris (UMR 7095: CNRS & UPMC – Sorbonne Universités), 98 bis bd Arago, F-75014 Paris, France

² Leiden Observatory, Leiden University, P.O. Box 9513, 2300 RA, Leiden, The Netherlands

³ Center for Computational Sciences, University of Tsukuba, 1-1-1 Tennodai, Tsukuba, Ibaraki, 305-8577, Japan

⁴ Laboratoire AIM-Paris-Saclay, CEA/DSM/IRFU, CNRS, Univ. Paris VII, F-91191 Gif-sur-Yvette, France

⁵ Department of Physics and Astronomy, The Johns Hopkins University Homewood Campus, Baltimore, MD 21218, USA

⁶ BIPAC, Department of Physics, University of Oxford, Keble Road, Oxford OX1 3RH

* bieri@iap.fr

Abstract

The quasar mode of Active Galactic Nuclei (AGN) in the high-redshift Universe is routinely observed in gas-rich galaxies together with large-scale AGN-driven winds. It is crucial to understand how photons emitted by the central AGN source couple to the ambient interstellar-medium to trigger large-scale outflows. By means of radiation-hydrodynamical simulations of idealised galactic discs, we study the coupling of photons with the multiphase galactic gas, and how it varies with gas cloud sizes, and the radiation bands included in the simulations, which are ultraviolet (UV), optical, and infrared (IR). We show how a quasar with a luminosity of 10^{46} erg s⁻¹ can drive large-scale winds with velocities of $10^2 - 10^3$ km s⁻¹ and mass outflow rates around $10^3 M_{\odot}$ yr⁻¹ for times of order a few million years. Infrared radiation is necessary to efficiently transfer momentum to the gas via multi-scattering on dust in dense clouds. However, IR multi-scattering, despite being extremely important at early times, quickly declines as the central gas cloud expands and breaks up, allowing the radiation to escape through low gas density channels. The typical number of multi-scattering events for an IR photon is only about a quarter of the mean optical depth from the center of the cloud. Our models account for the observed outflow rates of ~ 500 - $1000 M_{\odot}$ yr⁻¹ and high velocities of $\sim 10^3$ km s⁻¹, favouring winds that are energy-driven via extremely fast nuclear outflows, interpreted here as being IR-radiatively-driven winds.

galaxies: active — galaxies: high-redshift — galaxies: ISM — methods: numerical

5.2.1 Introduction

Galaxy formation and evolution is highly non-linear and poses significant challenges to our current understanding of the Universe. One particular issue is the relation between the mass function of dark matter halos, provided by theoretical models, and the luminosity function of galaxies, given by observations and usually fit by a Schechter (1976) function. By assuming that stellar mass follows halo mass, we are left with a theoretical prediction that leads to excessive numbers of galaxies at both the low-mass and the high-mass ends. Thus, some mechanisms have been advocated to regulate the baryon budget in galaxies. Feedback is likely an important mechanism, operating within galaxies and driving large-scale outflows, removing the star-forming gas and/or preventing further infall. In high-mass galaxies, efficient feedback is thought to be provided by active galactic nuclei (AGN) hosting supermassive black holes (SMBHs) (e.g. Magorrian et al., 1998; Hu, 2008; Kormendy et al.,

5.2. OUTFLOWS DRIVEN BY QUASARS IN HIGH-REDSHIFT GALAXIES WITH RADIATION HYDRODYNAMICS

2011). Gas accretion onto a black hole (BH) leads to energy release capable of driving outflows that regulate star formation and the local baryonic content (Silk & Rees, 1998), hence regulating the BH growth and that of the surrounding galaxy (Kormendy & Ho, 2013).

The two main modes of AGN feedback identified so far are the so-called *radio*-mode (radiatively-inefficient) powered by mechanical jets, and the radiatively-efficient *quasar*-mode powered by photons that couple to the gas and transfer their momentum to it. Several studies have examined the effects of these different modes in cosmological hydrodynamical simulations (e.g. Di Matteo et al., 2005, 2008; Sijacki et al., 2007; Booth & Schaye, 2009; Dubois et al., 2012b) and also on smaller galaxy scales (e.g. Proga et al., 2000; Wagner & Bicknell, 2011; Novak et al., 2012a; Nayakshin & Zubovas, 2012; Gabor & Bournaud, 2014), and have highlighted the capacity of regulating the baryon content of galaxies with AGN feedback. The general findings of these hydrodynamical simulations and also of semi-analytical models (e.g. Croton et al., 2006; Bower et al., 2006) is that AGN feedback suppresses star formation in massive galaxies, reproduces the observed high-end tail of the galaxy mass function, and is largely responsible for the morphological transformation of massive galaxies into ellipticals.

Although the picture of supermassive black holes exerting strong feedback on their host galaxies is very attractive, the details of the mechanism remain vague, primarily because the implementation of the black hole feedback in these studies relies on subgrid recipes in pure hydrodynamical (HD) simulations. The implementations in these studies vary slightly, but in most cases, quasar feedback is approximated by depositing thermal energy within the resolution element, with the efficiency of the radiation-gas coupling represented by a single parameter chosen to match global observations of SMBH mass-bulge velocity dispersion (Ferrarese & Merritt, 2000). This is the quasar mode of AGN feedback implemented in recent ~ 100 Mpc state-of-the-art hydrodynamical cosmological simulations such as Horizon-AGN (Dubois et al., 2014), Illustris (Vogelsberger et al., 2014), MassiveBlack-II (Khandai et al., 2015a), or Eagle (Schaye et al., 2015).

In reality, this sub-grid model of quasar feedback hides complex physics. There is a general consensus that photons emitted from a thin accretion disc surrounding the SMBH (Shakura & Sunyaev, 1973) will effectively couple to the surrounding interstellar medium (ISM) and eventually drive a large-scale wind. These radiatively-driven winds are not necessarily simply momentum-conserving with $\dot{p} \simeq L/c$ (as proposed by King, 2003), where \dot{p} is the momentum input rate, L is the bolometric luminosity of the source, and c is the speed of light, as opposed to energy-conserving, where the momentum of the gas builds up from the pressure work of the gas, hence, $\dot{p} \gg L/c$ (Silk & Rees, 1998; Faucher-Giguère & Quataert, 2012; Zubovas & King, 2012). For example, observations by Cicone et al. (2014) show outflows with mechanical advantages of a few tens, where the mechanical advantage is defined as the ratio between \dot{p} and L/c . Recent observations of fast ($> 10^3 \text{ km s}^{-1}$) molecular outflows from AGN favour energy-conserving winds from the nuclear accretion disc (Tombesi et al., 2015; Feruglio et al., 2015) as do recent multiphase simulations discussed below, (e.g. Costa et al., 2014).

Alternate approaches to simple internal energy input have been implemented, where the gas close to the BH is explicitly given a momentum input rate of L/c multiplied by a factor of a few (Debuhr et al., 2010, 2011; Choi et al., 2012, 2014; Barai et al., 2014; Zubovas & Nayakshin, 2014; Costa et al., 2014; Hopkins et al., 2016). However, simulations show contradictory results regarding the plausibility of regulating the BH growth and impact on the baryon content of the galaxy using momentum-driven winds. While Costa et al. (2014, see also Barai et al., 2014) advocate an energy-conserving wind to significantly affect the

galaxy and its surroundings, Choi et al. (2012) show that their momentum feedback drives faster winds than their energy feedback model. Since quasar-driven winds are powered by the complex coupling of photons with the gas, it becomes timely to improve our current understanding of the transfer of momentum and energy from AGN-emitted radiation to the ISM by means of radiation-hydrodynamical (RHD) simulations. In such RHD simulations, the emission, absorption, and propagation of photons and their interaction with the gas is self-consistently followed. Detailed RHD simulations should help to improve our understanding in how the quasar radiation couples to the gas, in particular via the coupling of infrared (IR) radiation to dust, and how powerful quasar winds are eventually driven. Therefore, RHD simulations can provide better sub-grid models for large-scale cosmological simulations.

RHD simulations of quasar feedback on galactic scales have become feasible (e.g., Ciotti & Ostriker, 2007, 2012; Kim et al., 2011; Novak et al., 2012b) and allow us to measure how much of the radiation momentum is transferred to the gas. These studies manage to resolve important physics involving the variability of the AGN (the *duty cycle*). RHD simulations also show how a strong radiation source at the centre of a galaxy affects the surrounding ISM. Ciotti & Ostriker (2007, 2012); Novak et al. (2012b) show that, for elliptical gas-poor galaxies, the momentum input rate very rarely exceeds L/c due to the low opacity of dust to the re-radiated IR and the destruction of dust in high temperature environments, which in turn limits the amount of momentum the radiation can transfer to the gas. Kim et al. (2011) simulate the evolution of a high-redshift galaxy with radiation from the SMBH, however, the IR radiation has not been considered in this work, and, hence, the impact of radiation into the gas is probably underestimated. Similarly in Roos et al. (2015), the effect of the UV photo-heating only from a central quasar (treated in post-processing) has very little impact on the evolution of a gas-rich isolated disc galaxy. The IR radiation is potentially important because in optically-thick gas it is constantly absorbed by dust and re-emitted, and hence can give several times its momentum L_{IR}/c to the dust up to the dust optical depth $\tau_{\text{IR}} = \Sigma_{\text{g}}\kappa_{\text{IR}}$, where Σ_{g} is the gas surface density and κ_{IR} is the dust opacity. It can create radiation pressure-driven winds where the momentum input rate exceeds the momentum flux of the source by one or two orders of magnitude, mimicking the effect of an energy-driven wind. Star clusters in starburst galaxies can easily reach values of $\tau_{\text{IR}} = 10 - 100$ (see Fig. 3 of Agertz et al., 2013), possibly explaining the observed energy-conserving winds in high-redshift quasars.

High-resolution hydrodynamical simulations of AGN jet feedback (e.g., Bicknell et al., 2000; Sutherland & Bicknell, 2007; Antonuccio-Delogu & Silk, 2010; Wagner & Bicknell, 2011; Gaibler et al., 2012) have shown that a clumpy interstellar structure results in interactions between the jet and the gas that differ from those in simulations with a homogeneous ISM. It is hence expected that multiphase ISM properties also affect the momentum transfer from the radiation to the gas. Modelling a clumpy interstellar structure might be even more important when considering photons, as low density gas can trace escape paths in which the radiation-matter interaction is reduced because the radiation field is not fully trapped. Also, it is expected that as the radiation is sweeping up the dense gas, low-density channels form and photons start to escape along these preferred directions, lowering the mechanical advantage (Krumholz & Thompson, 2012, 2013; Davis et al., 2014; Rosdahl & Teyssier, 2015b).

The aim of this paper is to quantify the coupling of quasar radiation with a clumpy ISM and to study how photons (UV, optical and IR) can drive powerful winds using RHD simulations. Since radiation-gas coupling depends on the clumpiness of the gas, we consider a two-phase (see McKee & Ostriker, 2007) fractal interstellar medium at pc-scale

5.2. OUTFLOWS DRIVEN BY QUASARS IN HIGH-REDSHIFT GALAXIES WITH RADIATION HYDRODYNAMICS

resolution. We investigate the momentum budget associated with the dispersion of the clouds in the galaxy and its dependence on different cloud sizes, filling factors, quasar luminosities, and energy bands of the quasar spectrum.

In Section 5.2.2, we describe our suite of RHD simulations. Our results are presented in Section 5.2.4. Section 5.2.6 is a discussion of the caveats of our methods and setup. Section 5.2.7 provides the final conclusions.

5.2.2 Methods

We perform a suite of simulations using RAMSES-RT, an RHD extension of the adaptive mesh refinement (AMR) code RAMSES (Teyssier, 2002). We model quasar-emitted radiation interacting with a surrounding multiphase ISM, in order to study how efficiently radiation couples to the gas within the galaxy.

5.2.2.1 Initial Gas Density Distribution

We set up a gaseous disc with a two-phase ISM in pressure equilibrium, with a uniform hot phase with temperature $T \sim 10^6$ K, and a cold $T \sim 1 - 10^4$ K phase that is uniform on large scales, but very clumpy on small scales. Our ISM setup is described in detail in Wagner et al. (2013), which followed work done by Sutherland & Bicknell (2007) investigating the interaction of an AGN jet with a non-uniform ISM.

The density field for the cold phase is homogeneous on large scales, i.e. there is no radial density gradient, but it is very clumpy on small scales: it follows a single-point log-normal distribution and two-point fractal statistics. In a log-normal distribution, the logarithm of the ISM density is a Gaussian, with mean m and variance s^2 . With $P(\rho)$ being the log-normal probability distribution of the mass density ρ , one can write

$$P(\rho) = \frac{1}{\sqrt{2\pi} s \rho} \exp \left[-\frac{(\ln \rho - m)^2}{2s^2} \right], \quad (5.1)$$

with

$$m = \ln \left(\frac{\mu^2}{\sqrt{\sigma^2 + \mu^2}} \right), \quad s = \sqrt{\ln \left(\frac{\sigma^2}{\mu^2} + 1 \right)}, \quad (5.2)$$

where μ and σ^2 are the mean and the variance of the linear density field. In the simulations presented here, we adopt $\mu = 1$ and $\sigma^2 = 5$, identically to what has been used by Wagner & Bicknell (2011). These values are in agreement with ranges found by Fischera et al. (2003) and Fischera & Dopita (2004), observing the column density distribution in a turbulent ISM. The variance in Eq. (5.2) gives a measure of how concentrated the mass is within the density cores, or, conversely, the fraction of the volume within the low density regions. With these values, gas densities below the mean μ encompass one-quarter of the mass and occupy three-quarters of the volume of the simulated disc. For further discussion of the adopted values, we refer to Bicknell et al. (2000).

We define $F(\mathbf{k})$ to be the Fourier transform of the density $\rho(\mathbf{r})$, where \mathbf{k} and \mathbf{r} are the wave-number and position vectors, respectively. The two-point structure of a homogeneous turbulent medium is characterised in Fourier space by an isotropic power spectrum $D(k)$ defined as

$$D(k) = \int k^2 F(\mathbf{k}) F^*(\mathbf{k}) d\Omega. \quad (5.3)$$

The power-spectrum is proportional to a power-law with index $-5/3$ in order to reproduce the spectrum driven by Kolmogorov turbulence. The Fourier transform of the density ρ is

proportional to the turbulent field usually described by the velocity vector (Warhaft, 2000). We follow Wagner & Bicknell (2011) and adopt a standard Kolmogorov power spectrum for our non-uniformly distributed gas within the disc.

We want to stress that our initial setup is stationary and hence does not capture the actual ISM turbulence (see Kritsuk et al., 2011 and references therein). We rather parametrise the non-uniform properties of a generic turbulent medium and focus on characteristics such as the variance of the gas density σ^2 and the two-point self-similar power-law structures, and hence rely on a range of previous experimental and theoretical results from the field of turbulence. The initial distribution of the ISM that we adopt should therefore be regarded as a physically motivated generalisation of an inhomogeneous ISM, while it may not necessarily represent an accurate model of a turbulent ISM.

The density distribution is set up via an iterative process, described first by Lewis & Austin (2002), where we have adapted the PYFC package (Wagner & Bicknell, 2011) to our needs (mainly parallelised part of the code in order to have a smaller minimum sampling wave-number). Our density field simultaneously follows log-normal single-point statistics (see Eq. [5.1]) and a Kolmogorov power-law self-similar structure in wave-number with index $-5/3$ and minimum sampling wave-number k_{\min} . In real space, the minimum sampling wave-number determines the scale of the largest fractal structure in the cube relative to the size of the cube. Effectively, it is the average number of clouds per dimension divided by two. For example, in one setup of our simulation, we used $k_{\min} = 5 \text{ kpc}^{-1}$ for a cube mapped to a disc with a diameter of $d = 3 \text{ kpc}$. Then the largest structures (clouds) extend to $R_{\text{c,max}} = 3/(2 k_{\min}) = 300 \text{ pc}$.

Finally, we place the cube into the RAMSES simulation domain by reading each density value within the cube and placing it into a cell of the RAMSES grid. Here the resolution of the generated cube does not necessarily need to be the resolution of the smallest cell within the RAMSES simulation box. In order to obtain a cylindrical shape resembling a galaxy, the density cube is filtered, in the xy -plane, by a symmetric flat mean density profile with mean cold phase density $\langle n_w \rangle$ and radius $r = 1.5 \text{ kpc}$, and in the z -plane the density cube is filtered by a step function with height $h = 0.3 \text{ kpc}$. The porosity of the ISM arises by imposing a temperature roof T_{roof} above which the gas is defined to be in the hot phase. The mean density of the cold ISM phase is chosen such that the total mass of the cold phase is $\sim 2 \times 10^{10} M_{\odot}$ and is around 500 H cm^{-3} . The roof temperature is around 50 K for the different simulations.

In our simulations, clouds are initially in pressure equilibrium with the surrounding hot phase, where the pressure is set to be $P \sim 7 \times 10^{-12} \text{ Pa}$. For the hot phase, whose temperature is fixed at $T_{\text{h}} \sim 10^7 \text{ K}$, the density is constant and set as $n_{\text{H,h}} = 0.01 \text{ H cm}^{-3}$ for all the simulations, while the initial metallicity is set to zero. The cold gas is initialised with solar metallicity. With these values and with a disc radius of 1.5 kpc and thickness of 0.15 kpc , we simulate a typical compact, gas-rich, high-redshift galaxy (e.g. Tacconi et al., 2010; Daddi et al., 2010; Genzel et al., 2010a).

The density and pressure profiles of the hydrostatic environment in a massive gas-rich proto-galaxy are fairly flat under the gravitational influence of the bulge and dark matter halo (assuming a Navarro et al., 1996 profile; e.g., Capelo et al., 2010). Hence this justifies the uniform hot phase distribution adopted in our simulation.

The filling factor of cold phase within the disc is given by

$$f_V = \frac{V_{\text{cold}}}{V_{\text{tot}}}, \quad (5.4)$$

where V_{cold} is the volume of the cold phase and V_{tot} the total cylindrical volume of the

5.2. OUTFLOWS DRIVEN BY QUASARS IN HIGH-REDSHIFT GALAXIES WITH RADIATION HYDRODYNAMICS

region in which the density is distributed.

Since the minimum sampling wave-number relates to the largest fractal structure in the cube, we will hereafter respectively refer to the simulations with $k_{\min} = 30 \text{ kpc}^{-1}$, 5 kpc^{-1} , and 1 kpc^{-1} as *smallC* (smallest clouds), *medC* (medium clouds), and *bigC* (biggest clouds). For our simulations we chose a mean cold phase density $\langle n_w \rangle$ of 508 H cm^{-3} , 503 H cm^{-3} , and 435 H cm^{-3} for the *smallC*, *medC*, and *bigC* simulations, respectively. Additionally, we chose roof temperatures of 43 K, 70 K, and 70 K for the *smallC*, *medC*, and *bigC* simulations, respectively.

5.2.3 Radiation Hydrodynamics

Among the possible RHD implementations that are both helpful for cosmological and galaxy-scale simulations (e.g., Petkova & Springel, 2009; Krumholz et al., 2011; Pawlik & Schaye, 2011; Wise & Abel, 2011; Jiang et al., 2012; Skinner & Ostriker, 2013), we chose RAMSES-RT (Rosdahl et al., 2013, 2015), implemented in the RAMSES (Teyssier, 2002) AMR HD code, to model the interaction of radiation from the central black hole with the galaxy’s interstellar gas. The evolution of the gas is computed using a second-order unsplit Godunov scheme for the Euler equations. We use the HLLC Riemann solver (Toro et al., 1994) with the MinMod total variation diminishing scheme to reconstruct the interpolated variables from their cell-centered values. The RAMSES-RT RHD extension to RAMSES self-consistently adds the propagation of photons and their on-the-fly interaction with hydrogen and helium via photoionisation, heating, and momentum transfer, as well as their interaction with dust particles via momentum transfer. The advection of photons between grid cells is implemented with a first-order moment method, whereas the set of radiation transport equations is closed with the M1 relation for the Eddington tensor (Rosdahl et al., 2013). The M1 closure relation (Levermore, 1984b) can establish and retain bulk directionality of photon flows, and can to some degree model shadows behind opaque obstacles.

The radiation is split into different photon groups, defined by frequency bands. For each photon group, the radiation is described, in each grid cell, by the radiation energy density (energy per unit volume) and the bulk radiation flux (energy per unit area per unit time), which corresponds to the radiation intensity integrated over all solid angles. RAMSES-RT solves the non-equilibrium evolution of the ionization fractions of hydrogen and helium, along with photon fluxes and the gas temperature in each grid cell. For the lowest-energy IR group, the photons can give momentum to the gas multiple times via absorption and re-emission. Higher-energy radiation groups are absorbed by dust and re-emitted (conserving energy) into the IR group, but they can also interact with hydrogen and helium via photoionisation. We use a subgrid scheme to account for the trapping of IR photons in regions where the mean free path is smaller than the grid spacing. This scheme recovers the proper asymptotic limit in the radiation diffusion regime (see Rosdahl et al., 2015 for a detailed discussion).

Since the Courant condition imposes that the time-step duration (and therefore the computational load) scales inversely with the speed of light c , we apply the so-called reduced speed of light approximation (RSLA; see also Gnedin & Abel, 2001; Rosdahl et al., 2013). The rationale for the RSLA is that as long as the radiation travels faster than ionisation fronts, the results of RHD simulations are more or less converged with respect to the (reduced) speed of light.

However, IR radiation is not photo-ionising, so it is not obvious whether a reduced speed of light produces converging results, especially when IR trapping becomes important. For our simulations, we chose a reduced speed of light fraction $c_{\text{red}}/c = 0.2$, leading to

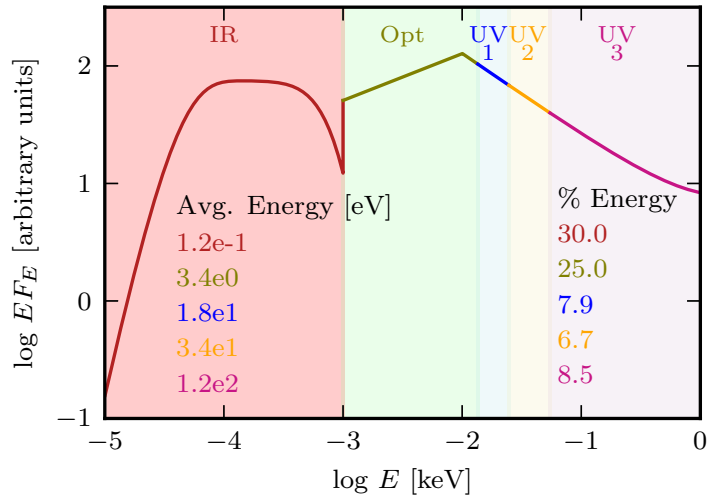


Figure 5.2: Broad-band spectrum of a typical quasar (adopted from Sazonov et al., 2004). The shaded areas show the energy range of each photon group: IR (red), optical (green), UV1 (blue), UV2 (yellow), UV3 (pink). In the plot we show the fraction of the total energy going into each photon group (% Energy) as well as the energy per photon (Avg. Energy) within the groups. Note that we do not model the hard X-ray energy band, which contributes 22% to the total energy of the quasar.

$c_{\text{red}} \sim 6 \times 10^4 \text{ km s}^{-1}$. We test our chosen reduced speed of light by performing convergence tests in Appendix 5.2.8 but leave a detailed discussion to a forthcoming paper.

We implement outflow boundary conditions, such that any matter that leaves the simulation volume is lost to the system. We however choose a sufficiently large simulation box size $L_{\text{box}} = 96 \text{ kpc}$ to ensure negligible mass loss. The simulation employs a coarse grid of cell size $L_{\text{box}}/2^9 = 187 \text{ pc}$ and allows up to 5 additional levels of refinement, so that the smallest cell size is $L_{\text{box}}/2^{14} = 5.9 \text{ pc}$. The refinement is triggered with a quasi-Lagrangian criterion ensuring that if the gas mass within a cell is larger than $80 M_{\odot}$ a new refinement level is triggered. We ensure that all of the disc is maximally refined at the beginning of the simulation, leading to $\sim 10^7$ cells initially at the maximum level of refinement. For convergence studies, we have performed lower resolution runs with a spatial resolution of $\Delta x = 11.6 \text{ pc}$ using a maximum of 6 levels of additional refinement.

The gas in our simulations follows the equation of state for an ideal monoatomic gas with an adiabatic index of $\gamma = 5/3$. To keep our setup as simple as possible and only probe the effect of radiation-matter coupling, we neglect gas cooling¹, star formation, feedback from stars, and gravitational forces, but these effects will be studied in future work. We discuss those caveats in Section 5.2.6.

5.2.3.1 Modeling the Quasar

The spectrum of radiation from the central quasar is modelled using a maximum of five photon groups, defined by the photon energy bands listed in Table 5.1. The photons

¹Hence the only role of metals in our simulations is to set the dust opacities, as shown by Eq. (5.5)

5.2. OUTFLOWS DRIVEN BY QUASARS IN HIGH-REDSHIFT GALAXIES WITH RADIATION HYDRODYNAMICS

Table 5.1: Properties of the photon groups used in the simulations. Columns are name; minimum and maximum energies; cross sections to ionisation by H I, He I, and He II; dust opacity; luminosity fraction (from quasar spectrum of Sazonov et al., 2004). The dust opacity $\tilde{\kappa}$ for each group scales with the gas metallicity $\kappa_i = \tilde{\kappa}_i Z/Z_\odot$. The luminosity fraction per photon group is used to calculate the designated energy from the quasar that goes into each corresponding photo group.

Photon group	E_{\min} (eV)	E_{\max} (eV)	$\sigma_{\text{H I}}$ (cm ²)	$\sigma_{\text{He I}}$ (cm ²)	$\sigma_{\text{He II}}$ (cm ²)	$\tilde{\kappa}$ (cm ² g ⁻¹)	Energy fraction
IR	0.01	1.	0	0	0	10	0.300
Opt	1.	13.5	0	0	0	10 ³	0.250
UV1	13.5	24.6	3.1×10^{-18}	0	0	10 ³	0.079
UV2	24.6	54.4	4.7×10^{-19}	4.2×10^{-18}	0	10 ³	0.067
UV3	54.4	10 ³	1.1×10^{-20}	2.3×10^{-19}	1.7×10^{-19}	10 ³	0.085

groups consist of one infrared (IR) group (0.01 - 1 eV), one optical group ('Opt' from 1 - 13.5 eV), and three groups of ionising ultraviolet (UV) photons, the first two (UV1 and UV2) bracketed by the ionisation energies of H I, He I and He II, and the third (UV3) extending from He II ionisation to soft X-rays (1 keV). For a given quasar luminosity, we split the spectral energy distribution (SED) of a typical quasar, as calculated by Sazonov et al. (2004) and shown in Fig. 5.2, into these 5 photon groups, and the corresponding fractions of the quasar luminosity are given in Table 5.1. Sazonov et al. calculated the typical quasar SED using published AGN composite spectra in the optical, UV, and X-rays, also considering the cosmic X-ray background and the contribution of AGN to infrared wavelengths, and the estimated local mass density of SMBHs. Note that we do not model the hard X-ray energy band ($E > 1$ keV), where photons can heat (or cool) the gas to an equilibrium temperature of $\sim 2 \times 10^7$ K through Compton (or inverse Compton) scattering of electrons, but this happens at a very small distance from the source, and hence, these photons have little overall impact on the ISM (e.g., Ciotti & Ostriker, 2012; Hopkins et al., 2016). The ionization cross-sections $\sigma(E)$ are taken from Verner et al. (1996). For each photon group, the cross-sections are luminosity-weighted averages over the energy interval, as described in Rosdahl et al. (2013).

Dust opacities are important for calculating the momentum transfer between the photons and the gas as it happens via scattering on dust. Interstellar dust grains are destroyed, mostly by sputtering, by shock-heated gas above temperatures of $T \geq 10^5$ K (Draine & Salpeter, 1979) (albeit the exact temperature and destruction time scale depend on the dust grain size). For this work, we modified the calculation of the dust opacity in RAMSES-RT to include dust destruction by thermal sputtering when the gas temperature is above a cutoff temperature $T_{\text{cut}} = 10^5$ K. This is necessary when the source luminosity is sufficiently high to heat up the gas to very high temperatures. The cut-off temperature for sputtering is weakly dependent on density, an effect we ignore here. We did not include dust sublimation since RAMSES-RT does not follow the dust temperature (which sublimates above 10^3 K) and leave this for future work.

In our simulations the opacities for the different photon groups are given by

$$\kappa_i = \tilde{\kappa}_i \frac{Z}{Z_\odot} \exp\left(-\frac{T}{T_{\text{cut}}}\right). \quad (5.5)$$

We thus assume that the dust content simply scales with the metallicity of the gas below

the cutoff temperature.

For the IR, we assume an opacity of $\kappa_i = \kappa_{\text{IR}} = 10 (Z/Z_{\odot}) \text{ cm}^2 \text{ g}^{-1}$, whereas for the higher energy photons (optical and UV) we assume $\kappa_i = 1000 (Z/Z_{\odot}) \text{ cm}^2 \text{ g}^{-1}$, i.e., one hundred times higher than of the IR. The chosen opacities are physically motivated by a combination of observations and dust-formation theory of the ISM and stellar nurseries (Semenov et al., 2003 for the IR photons, and Li & Draine, 2001 for higher energy radiation). They are however uncertain by a factor of a few, due to model uncertainties as well as the temperature dependence on the opacity, which is ignored in our simulations. Past studies have used similar values (e.g. Hopkins et al., 2011; Agertz et al., 2013; Roškar et al., 2014). The usual IR opacities are in the range of $\kappa_{\text{IR}} = 5 - 10 \text{ cm}^2 \text{ g}^{-1}$ and hence our assumed IR opacity is at the high-end of what is usually considered.

Table 5.1 lists the values for the photon group energies, where for each photon group, the energy intervals are between the lower bound E_{min} and upper bound E_{max} . Also shown are the photoionisation cross-sections (σ_{HI} , σ_{HeI} , and σ_{HeII}) for hydrogen and helium, calculated as described above, the dust-interaction opacities ($\tilde{\kappa}_i$), and fractions of total quasar luminosity emitted into each photon group.

We have chosen two different quasar luminosities $10^{43} \text{ erg s}^{-1}$ and $10^{46} \text{ erg s}^{-1}$ for our simulations. The bolometric quasar luminosity function (QLF) at redshift $z = 3$, compiled by Hopkins et al. (2007), shows that the chosen quasar luminosities are very common and nicely bracket the QLF.

In the present work, we explore the effect of an AGN radiation source that is steady, isotropic, and located at the centre of the galaxy. In reality, the quasar luminosity is proportional to its accretion rate, which varies in time. Additionally, the black hole can move around the potential well of the dark matter halo and galaxy and hence is not always exactly located at the centre of the galaxy. Usually, a lower (higher) density environment around the black hole results in a lower (higher) luminosity of the quasar. Moreover, changing the location of the black hole changes the optical depth around the source, as the encompassing density changes, which should alter the level of coupling between the radiation and matter. For this reason, we have ensured that the initial conditions for the density field are such that the black hole for the $10^{46} \text{ erg s}^{-1}$ simulations is in the densest region of the entire density distribution, while the initial conditions place the lower luminosity source at an intermediate density. Aside from this, the statistical properties (as discussed above) of the simulations with both quasar luminosities are exactly the same. We have also performed a simulation with a $10^{46} \text{ erg s}^{-1}$ quasar surrounded by the exact same density distribution as for the $10^{43} \text{ erg s}^{-1}$ simulations to assess the role of quasar luminosity independently of the density around the quasar.

In summary, the key model parameters used in the different simulations are the quasar luminosity, the radius of the largest fractal structure, and the location of the quasar. Table 5.2 summarises the assigned and derived parameters that we used for our simulations and Fig. 5.3 shows an example of the *smallC*, *medC*, and *bigC* cloud distributions, where the volume filling factor is kept at 50%. We have also performed simulations with a filling factor of 100%, but the results do not significantly change from those shown in the paper.

5.2.4 Results

We now present our simulation results and examine the interplay of the BH-emitted radiation with the surrounding gas, focusing on the momentum transferred from the radiation onto the gas. We start with a comparison of the effects of radiation on the galaxy for

5.2. OUTFLOWS DRIVEN BY QUASARS IN HIGH-REDSHIFT GALAXIES WITH RADIATION HYDRODYNAMICS

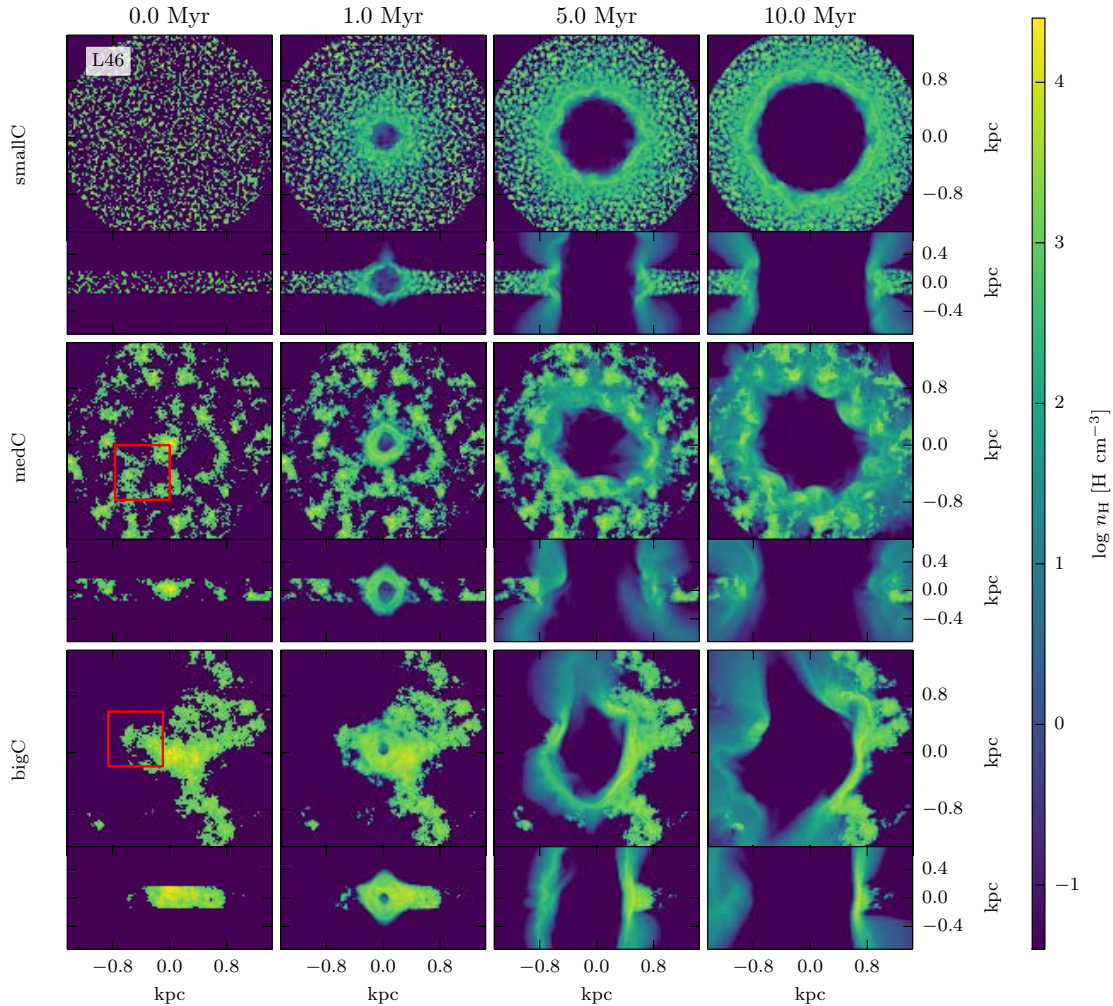


Figure 5.3: Slices of the gas density for the *L46_smallC* simulations (top row), *L46_medC* simulations (middle row), and for the *L46_bigC* simulations (bottom row). The different columns show different times as labeled. The galaxies are shown both face-on (upper portion of rows) and edge-on (bottom portion of rows). The galaxy is destroyed by radiation, and a large-scale radiatively-driven wind is generated. While in the *smallC* simulation the wave induced by the radiation expands almost uniformly in the xy -plane, this is not the case for the *medC* and *bigC* simulations where the outflow escapes via tunnels of low density. The red square over-plotted at the 0 Myr plot for the *bigC* simulation corresponds to the zoomed-in region of Figs. 5.5 and 5.6, whereas the red square in the *medC* simulation corresponds to the zoomed-in region in Fig. 5.9.

Table 5.2: Simulation parameters: quasar luminosity (L), largest possible cloud size ($R_{c,\max}$), and the gas density (‘environment’) around the quasar. If, for instance, the quasar environment is denoted with *max* the quasar is placed into the cell within a maximum density. Additionally, no suffix about the quasar position is used if the position of the quasar is in a maximum density environment for the *L46* simulation, or in a medium density environment for the *L43* simulation, respectively.

Simulation name	$\log L$ (erg s^{-1})	$R_{c,\max}$ (kpc)	Quasar environment
<i>L46_smallC</i>	46	0.05	<i>max</i>
<i>L46_medC</i>	46	0.3	<i>max</i>
<i>L46_bigC</i>	46	1.5	<i>max</i>
<i>L46_bigC_med</i> ρ_Q	46	1.5	<i>med</i>
<i>L46_bigC_min</i> ρ_Q	46	1.5	<i>min</i>
<i>L43_smallC</i>	43	0.05	<i>med</i>
<i>L43_medC</i>	43	0.3	<i>med</i>
<i>L43_bigC</i>	43	1.5	<i>med</i>
<i>L43_bigC_max</i> ρ_Q	43	1.5	<i>max</i>

different cloud sizes for the more luminous $L = 10^{46} \text{ erg s}^{-1}$ source. Then we investigate how the wind becomes radiatively-driven. We next compare the effects of different quasar positions relative to the clouds, and end with a comparison of different quasar luminosities. Additionally, we include in Appendix 5.2.8 a study of how the transferred momentum depends on the speed of light and conclude that this approximation is a crucial component in recovering the correct mechanical advantage from the radiation onto the gas for the first few Myr.

5.2.4.1 Effects of Different Cloud Sizes

We explore the impact of radiation on the gas clouds and velocity evolution for galaxy discs with different cloud sizes. We focus here on the *L46* simulations, where the source is embedded into the high density environment of the clouds.

5.2.4.2 Qualitative Effects of Cloud Sizes

In Fig. 5.3, we show maps of the gas density in the disc at different times for the *L46_smallC*, *L46_medC*, and *L46_bigC* simulations. Comparing the three different cloud sizes, we observe that the outflow is less symmetric for less uniform initial conditions, i.e. larger clouds. For all the simulations, the radiation from the central source destroys the encompassing high density cloud hosting the source before reaching a lower density environment. The ionised outflow generated by the radiation pushes the gas out into the circum-galactic medium through the lower density channels, which are more prominent with larger clouds.

Until the cloud is destroyed, the source is surrounded by a high density environment where the optical depth is sufficiently high for the IR radiation to boost the momentum transfer to the gas. Once the radiation manages to destroy the central cloud, the optical depth drops to lower values, reducing the effect of momentum-boost from IR multi-scattering. The time it takes for the radiation to break from the central source through the cloud is hence crucial and is much shorter for the *L46_smallC* simulation than for

5.2. OUTFLOWS DRIVEN BY QUASARS IN HIGH-REDSHIFT GALAXIES WITH RADIATION HYDRODYNAMICS

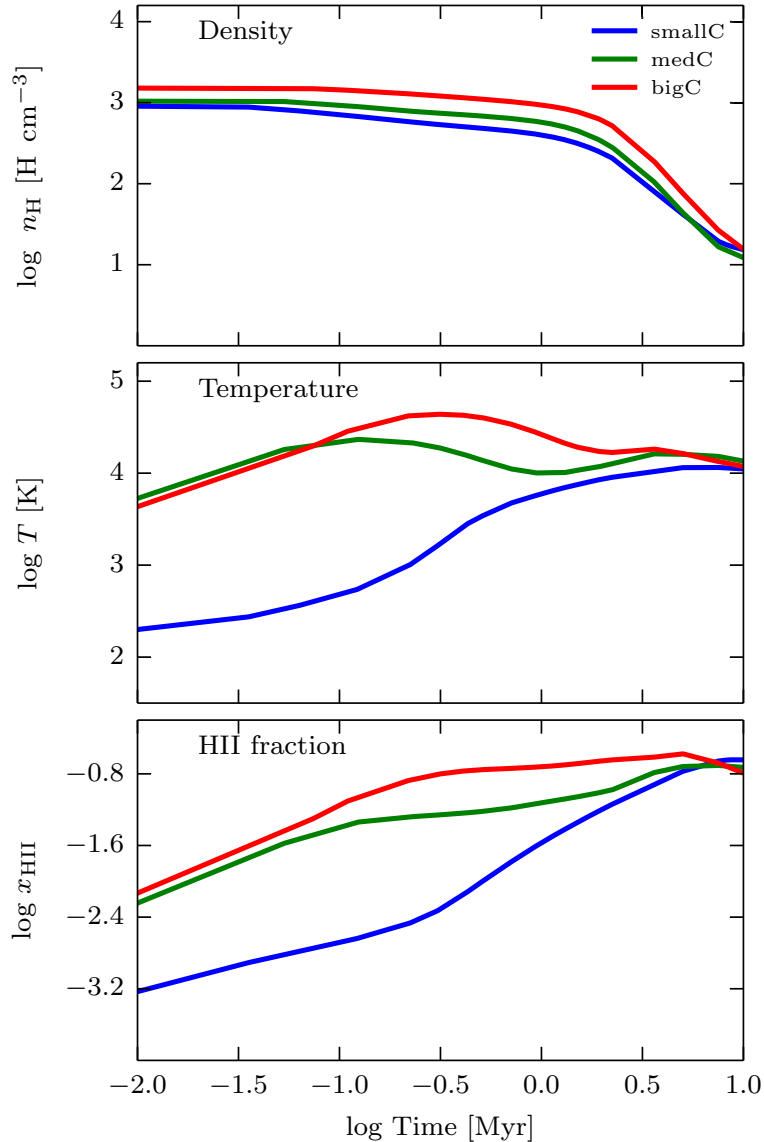


Figure 5.4: Evolution of the mean density (top), temperature (middle), and H II fraction (bottom) of the clouds as a function of time for the *L46_smallC* (blue), *L46_medC* (green), and *L46_bigC* (red) simulations. The lines show the mass-weighted mean value for the clouds, using only the cells with a metallicity above a cutoff value of 0.5 Solar (where the maximum and minimum metallicities are Solar and zero). The radiation manages to disperse the clouds, as can be seen by the decreasing mean densities. The mean temperature as well as ionisation fraction increase with time. This lowers the influence of the radiation as time passes due to the gas being either transparent and/or ionised.

the larger-cloud *L46_medC* or *L46_bigC* simulations. This gives the photons in the *L46_medC* and *L46_bigC* simulations more time to transfer momentum to the gas via the trapped photons in the optically-thick gas.

After the radiation has destroyed the encompassing cloud, the gas from the cloud continues to expand until it reaches the neighbouring over-densities. Since the clouds distributed within the *L46_smallC* simulation are all relatively small, they are rapidly destroyed by the radiation, and the cloud gas efficiently mixes with the background gas and fills up tunnels of lower density, quickly creating smooth isotropic shells of outflowing gas. Clouds in the *L46_medC*, and *L46_bigC* simulations are much bigger, and, at $t = 1$ Myr, the shell evolution is less spherically-symmetric compared to the *L46_smallC* simulation. Additionally, the outflow generated by the radiation creates a shell of swept-up gas, which is most apparent in the *L46_bigC* and also at early times of the *L46_medC* simulation, while less dominant for the *L46_smallC* simulation. Indeed, the larger the clouds, the more gas mass they contain and the greater (and hence more apparent) the overdensity of the shell can become.

Cloud Evolution

Fig. 5.4 illustrates the evolution of the mass-weighted cloud mean density, temperature, and H II fraction for the different *L46* simulations. The lines show the mean values of all gas with metallicity larger than 0.5 Solar. This picks out the gas originally belonging to dense clouds, since the gas within clouds is initialised with Solar metallicity, while the diffuse gas outside them is initially metal-free.

Looking at the mean density evolution for the three simulations, we see that the clouds start to disperse right from the beginning, causing the mean density of the clouds to drop. The decrease in mean density is similar for the different simulations. With the mean density of the clouds declining with time, the mean free path of the IR photons also increases and one therefore expects the IR photons to scatter less within the gas.

For the *L46_medC* and *L46_bigC* simulations the mean temperature rises within a very short amount of time (~ 0.1 Myr) to $10^{4.3-4.5}$ K, whereas it takes ~ 10 Myr for the *L46_smallC* simulation to reach similar values. Additionally, the H II fraction of the clouds also increases with time, with a roughly 30% ionisation fraction for the gas within the clouds at the end of the simulation. Photoionisation proceeds much more slowly for the small cloud than for the more massive clouds.

As seen in Fig. 5.3 the early evolution of the density evolution is sensitive to small-scale inhomogeneities. In the *L46_smallC* simulation the photons manage to quickly destroy the encompassing cloud and then escape through lower density channels without efficiently heating, ionising, and pushing the higher density gas. For the bigger cloud simulations, on the other hand, the radiation is trapped for longer within the encompassing cloud, leading to the photons to interact with the higher density gas. On long timescales, the radiation has smoothed out the inhomogeneities, and hence the evolution of the mean temperature and ionisation fraction is similar for all the cloud masses, and converges to the same values since the total masses are the same.

Fig. 5.5 shows a close-up of a slice of the gas density, gas temperature, H II fraction, and velocity from the *L46_bigC* simulation as indicated by the red square in Fig. 5.3. The position of the quasar is just outside the zoomed-in slice, on the right-hand side. Fig. 5.6 displays the time evolution of the radiation fluxes in two wavebands: IR and optical + UV, for the *L46_bigC* simulation in the same zoomed-in region as in Fig. 5.5.

At the start of the simulation (left panels of Fig. 5.5 and Fig. 5.6), the gas is in a fractal two-phase medium, with a cold, fully neutral, high-density component and a hot, fully

5.2. OUTFLOWS DRIVEN BY QUASARS IN HIGH-REDSHIFT GALAXIES WITH RADIATION HYDRODYNAMICS

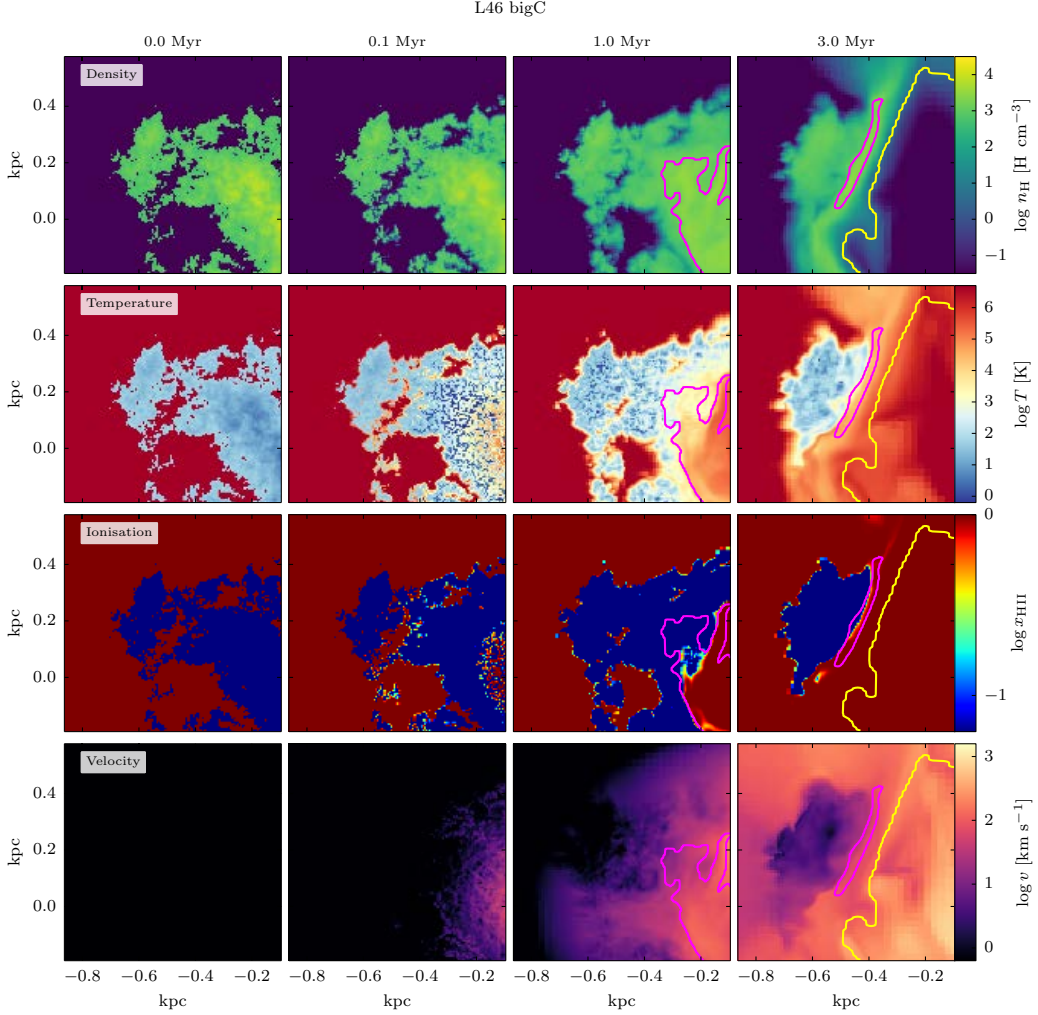


Figure 5.5: Slices of the gas density (top row), temperature (second to top row), ionisation fraction (second to bottom row), and velocity field (bottom row) for a slice of a zoomed region in the *L46_bigC* simulation. The position of the zoomed-in region is marked by a red square in Fig. 5.3. To guide the eye, selected density contours are overlotted at 1 Myr and 3 Myr. At 1 Myr, the magenta contour denotes a density of 4000 H cm^{-3} . At 3 Myr, the magenta and yellow contours show densities of $4 \times 10^3 \text{ H cm}^{-3}$ and 2.5 H cm^{-3} , respectively. The radiation pushes the gas from the outside and disperses the outer region of the cloud. The dispersed gas moves at a speed of $\sim 100 \text{ km s}^{-1}$ and is heated to a temperature of 10^{4-5} K .

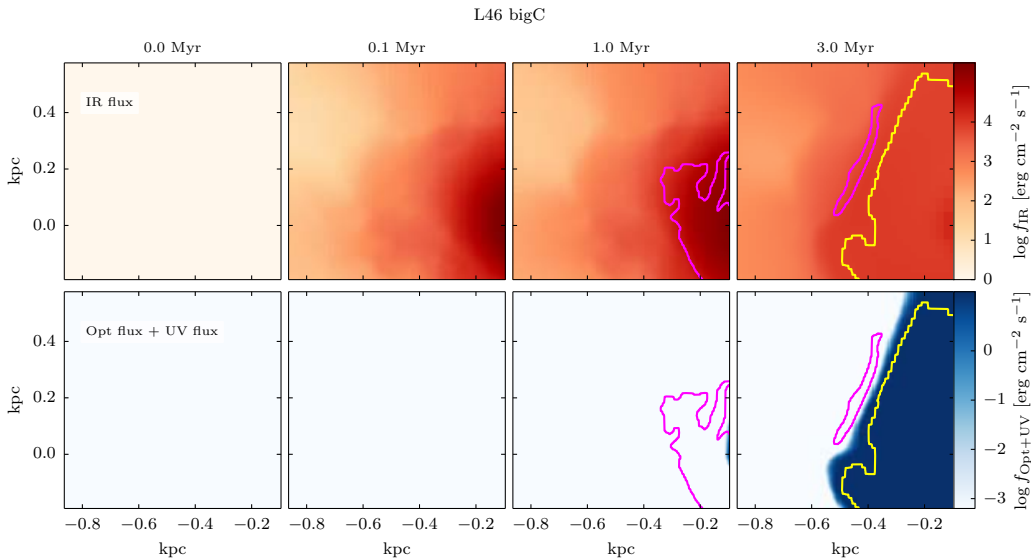


Figure 5.6: Slices of the IR (top row) and optical + UV (bottom row) radiation flux (over all directions) as a function of time for the same zoomed region as in Fig. 5.5 for the same (*L46_bigC*) simulation. Here the UV flux is the sum of the flux from the individual photon groups UV1, UV2, and UV3. The IR flux is computed by considering both the streaming and trapped contributions to the IR energy density. The same density contours as in Fig. 5.5 are over-plotted to guide the eye. While the IR radiation is completely penetrating the cloud after ≤ 0.1 Myr, the column density of the cloud is too high for the optical and UV radiation to penetrate the overdensity of the cloud.

ionised low density component, with both components at rest.

At 0.1 Myr, the IR photons have already penetrated the whole cloud. Where the IR photon flux is high, the dense gas has already started moving outwards as indicated by the moderate velocities ($10\text{--}50 \text{ km s}^{-1}$) on the right edge of the zoomed-in region. During this early stage, the gas in the high IR flux region is already at higher temperatures than the rest of the gas within the cloud (second panel of the second row of Fig. 5.6) but has not yet shock-heated to very high temperatures. Given the moderate temperatures well below dust destruction the cloud is not yet transparent and the IR photons multi-scatter within it, giving a boosted push from the inside-out. At 0.1 Myr, the cloud is still fully neutral as the UV photons do not penetrate into the cloud (shown in Fig. 5.6) because the gas is too dense and UV-shielded.

At 1 Myr, the gas has begun to move away from the radiation source. To guide the eye, we have marked the outflowing gas at 3 Myr with selected contours. The magenta contours at density 4000 H cm^{-3} mark the shock front. At 1 Myr, the shock front is still neutral with a temperature of roughly 10^3 K and is traveling at a velocity of $\sim 50 \text{ km s}^{-1}$. Given the mean density of the front at 1 Myr of $\sim 4 \times 10^3 \text{ H cm}^{-3}$, the mean free path, $1/(\kappa \rho)$, of IR photons is only $\sim 1.8 \text{ pc}$, which indicates the IR radiation is trapped and multi-scattering in this region allowing the IR radiation to efficiently transfer momentum onto the gas. In the regions where the gas is dense and the IR flux is high, the temperature of the gas is also higher compared to the rest of the cloud indicating a shock. Additionally, in the regions of high IR flux, the IR radiation is mixing the multiphase gas and creating a more uniform structure.

At the right edge of the cloud, i.e. in the direction of the source, the diffuse gas is heated

5.2. OUTFLOWS DRIVEN BY QUASARS IN HIGH-REDSHIFT GALAXIES WITH RADIATION HYDRODYNAMICS

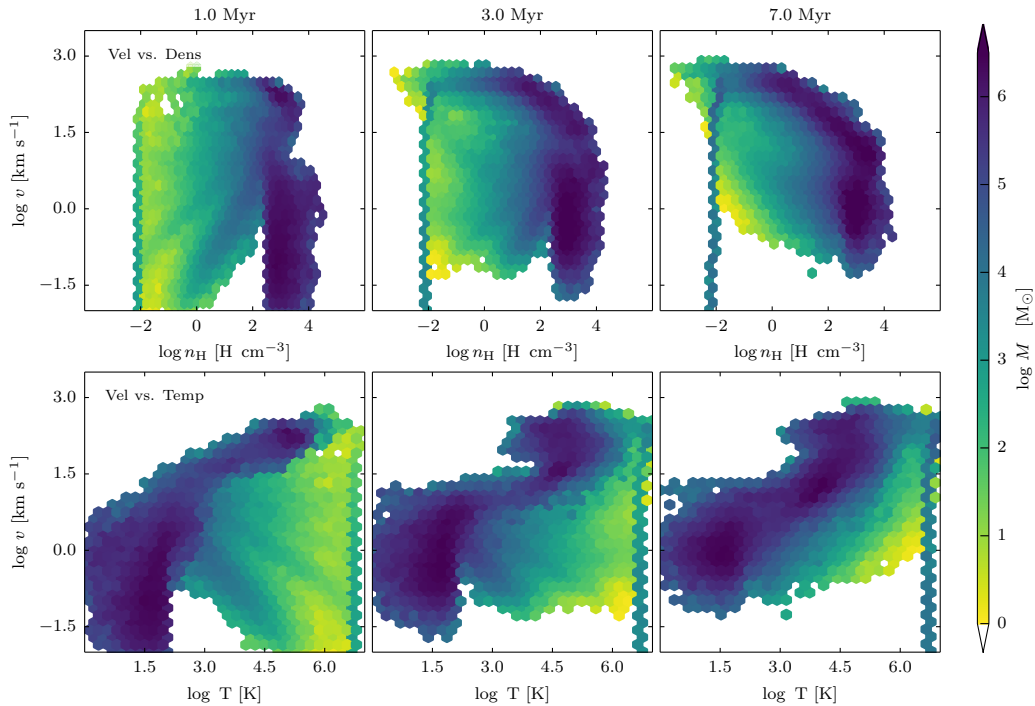


Figure 5.7: *Top*: Mass-weighted velocity versus density for the *L46_medC* simulation. *Bottom*: Mass-weighted velocity versus temperature for the *L46_medC* simulation. The points are coloured by the total mass within each 2D-histogram cell. The different columns show different times as labeled. The dense cold gas is accelerated by the radiation, expands and results in a broad, diffuse, and fast wind. The highest velocities for the dense gas is lower at late times, since it corresponds to more distant clouds receiving a lower photon flux. The fastest velocities are reached for gas with temperature below dust destruction.

up to high temperatures ($\sim 10^6$ K), is fully ionised, and has a velocity of $\sim 10^3$ km s⁻¹. When looking at the photon flux of the different radiation groups (see Fig. 5.6), we see that, unlike the IR photons, the UV and optical radiation still does not deeply penetrate the dense cloud. We will later see in more detail that the early evolution of dense clouds is clearly dominated by the IR radiation, whereas the UV radiation plays a more important role at later times.

When the radiation illuminates dense clouds, the gas is dispersed starting from the illuminated side, as seen in the density slice at 3 Myr. To guide the eye, we have again marked the outflowing gas with two selected contours. The magenta contour at density 4×10^3 H cm⁻³ marks the shock front, while the yellow contour at density 2.5 H cm⁻³ marks the outflow tail before the density drops to the background density. The dispersed gas moves away from the source at a velocity of $\sim 50 - 150$ km s⁻¹ and has a temperature of around $\sim 10^5$ K. The gas flowing away from the dispersed cloud still has only a marginally smaller density than the cloud, but is smoothed out by the IR radiation. A large portion of the outflow behind the density ridge (magenta contour) is fully ionised whereas the cold cloud preceding the outflow is still neutral (see also Fig. 5.4). As seen in Fig. 5.6, the UV radiation has only just reached into the tail edge of the outflowing gas (yellow contour), started to ionise the gas from the outside and heat it via photoionisation, and hence push it further from the back end. The rest of the gas is thus ionised via collisional

ionisation. We will see below that gas is accelerated by the radiation pressure from the UV photons and by photoionisation heating, but UV photons contribute mostly to the overall radiatively-driven wind once they are reprocessed in the IR. The gas reaches temperatures of around $\sim 10^5$ K and velocities up to 500 km s^{-1} beside the neutral gas, but still within the smooth outflowing gas from the clouds (left from the yellow contour in Fig. 5.5). In the regions where the gas mixed with the background gas (right from the yellow contour), the gas reaches temperatures up to $10^{6.5}$ K and velocities of up to 1000 km s^{-1} . At $t = 3 \text{ Myr}$, the cloud size with a mean density of $\sim 10^3 \text{ H cm}^{-3}$ is now comparable to the mean free path of the IR radiation, $\sim 30 \text{ pc}$, causing the IR flux, and thus the influence of the IR photons, to decrease.

In summary, we find that for smaller, more fragmented clouds encompassing the radiation source, the radiation has a tendency to escape, and hence it is less efficient at heating and ionising the gas compared to larger and more coherent surrounding structures which efficiently trap the radiation. Focusing on a single cloud close to (but separated from) the source of radiation, we see that the IR efficiently penetrates the cloud and pushes from the inside out, smoothing out inhomogeneities, while the UV (and optical) radiation cannot penetrate and acts more by pushing on and heating into the side of the cloud.

Velocity Evolution

Fig. 5.7 shows mass-weighted velocity-density diagrams and velocity-temperature diagrams for the *L46_medC* simulation at different times (1 Myr, 3 Myr, and 7 Myr from left to right). Three regions can be highlighted in the velocity-density diagram. At low densities, there is a range of velocities in distinct intervals. In light of Fig. 5.5, we see that the low density gas far from the source is not accelerated while that closer to the source is already accelerated close to 10^3 km s^{-1} . At the highest densities, some of the gas has low to moderate velocities up to 100 km s^{-1} . Again, comparing to Fig. 5.5, the almost zero velocity gas is on the far side of the source and has not yet been accelerated. And finally, in the mid density range (between 6 and 150 H cm^{-3}) diagonal stripes of mass of $\sim 10^4 M_{\odot}$ arise due to the dispersion of the fast-moving high density gas to lower densities. Because of the dispersion and mixing with the background at rest, the dispersed gas also slows down building the diagonal stripes observed.

The highest velocity gas (tip of the velocity-density diagram) shows an anti-correlation with density. This corresponds to gas near the source, where the radiation from the source disperses the clouds to lower densities, which reach the highest velocities. Lower density gas is moved earlier by the outflow created by the photon-gas interaction whereas it takes longer for high-density gas to reach the same velocities. The high-density gas eventually also reaches high velocities resulting in the whole cloud to move, which leads to the destruction of the whole disc. Comparing the velocity-density diagrams at different times, we see that at earlier times, gas at high densities has faster velocities than at later times, which is caused by several factors. First, the outflow front reaching an overdensity must decelerate while interacting with the gas from the cloud. Secondly, as we already have seen above, the high density regions are dispersed, leading to lower densities and higher velocities as seen at 7 Myr. Finally, the flux of photons decreases with distance from the source, and late times correspond to clouds farther away from the central source, which receive a smaller flux of photons.

The mass-weighted temperature versus velocity evolution shows that the radiation accelerates the cold and dense gas which expands further into a more diffuse and broader wind. Then, an increasing amount of gas reaches higher temperatures, resulting in a high mass fraction of high-speed hot gas at the end of the simulation. At later times, the dense

5.2. OUTFLOWS DRIVEN BY QUASARS IN HIGH-REDSHIFT GALAXIES WITH RADIATION HYDRODYNAMICS

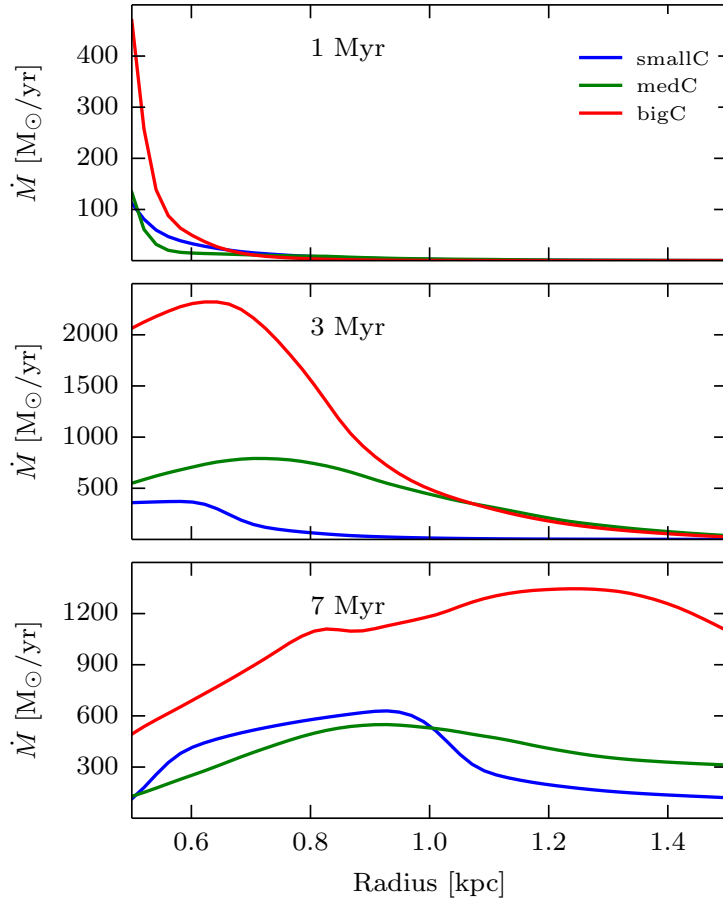


Figure 5.8: Mass outflow rate as a function of radius for three different times 1, 3 and 7 Myr from top to bottom (same time as those used in Fig. 5.7) for the $L46$ simulations. The radiation causes the gas to move out of the galaxy, reaching mass outflow rates of up to $500 - 1200 M_{\odot} \text{ yr}^{-1}$ after 7 Myr depending on the cloud encompassing the source. The outflow rate is larger the bigger the encompassing cloud because the radiation is trapped for longer within the big clouds and hence has longer time to impart momentum onto the gas.

and cold gas has lower velocities than at earlier times, as it corresponds to more distant clouds receiving a lower photon flux. The hot ($T > 10^5$ K) gas is optically thin because it is fully ionised and the dust is destroyed in it. Therefore, the bulk of the high velocity gas ($v > 100 \text{ km s}^{-1}$) corresponds to intermediate values of temperature of a few 10^4 K.

We have measured the velocities of the gas for the two other simulations (not shown here), and they have a very similar evolution. The main difference is in the intermediate density ($1\text{-}100 \text{ H cm}^{-3}$) and temperature ($10^3\text{-}10^5$ K) range, where the gas velocity is higher with increasing cloud size around the source: $100 - 500 \text{ km s}^{-1}$, $100 - 600 \text{ km s}^{-1}$, and $200 - 1000 \text{ km s}^{-1}$ for the *smallC*, *medC*, and *bigC* simulations, respectively.

We now measure the mass outflow rate with

$$\dot{M}_{\text{gas}} = \oint \rho \mathbf{v} \cdot \hat{\mathbf{r}} \, dS = \sum_{i \in \text{shell}} m_i \mathbf{v}_i \cdot \hat{\mathbf{r}}_i \frac{S}{V}, \quad (5.6)$$

by considering only the outward flow (cells with $\mathbf{v}_i \cdot \hat{\mathbf{r}}_i > 0$) across a spherical shell of radius r , where i denotes the index of a cell within the spherical shell of surface S and volume V . Finally, $\hat{\mathbf{r}}_i$ is the unit vector of the cell with velocity \mathbf{v}_i . Here, we adopt a shell of thickness 0.25 kpc . Fig. 5.8 shows the mass outflow rate as a function of radius for the *L46* simulations measured at different times. The radiation pressure causes the gas to move out, reaching outflow rates of up to 500 to $2400 \text{ M}_{\odot} \text{ yr}^{-1}$ depending on the initial cloud setup. The mass outflow rate is always larger the bigger the encompassing cloud around the source, due to the radiation being trapped for longer within the large clouds. The values of the mass outflow rates of $1000 - 2000 \text{ M}_{\odot} \text{ yr}^{-1}$ measured in the largest cloud simulation at $t \geq 3 \text{ Myr}$ as well as the high velocities of $\sim 1000 \text{ km s}^{-1}$ are close to those measured by Tombesi et al. (2015). As already stated above, the collapse time of the cloud encompassing the source is $\sim 4 \text{ Myr}$, which hence dynamically influences the mass outflow of the galaxy, at least towards the end of the simulation. Thus, our predictions of the mass outflow rates are optimistic and have to be tested with simulations including gravity. We leave this to future work.

5.2.4.3 Effects of Different Photon Groups on the Cloud Evolution

To better determine the specific contribution of each photon group, we have performed simulations of the same density distribution and quasar luminosity for the medium cloud size simulation (*L46_medC*) where we excluded certain photon groups. The density, temperature, H II fraction, and velocity maps of these simulations at 5 Myr can be seen in Fig. 5.9. The position of the quasar source, at the coordinate origin, is at the top right corner of the images. In the top row, all the photon groups are included. In the middle row, the IR radiation is excluded, and in the bottom row only the IR radiation is included (i.e. the UV groups and optical are excluded).

Comparing the different rows in Fig. 5.9, we see that each photon group contributes to dispersing the dense gas, but the IR contribution dominates as the outflow is clearly more advanced in the IR-only run than in the run with only UV and optical. However, even if the IR photons are most important in the gas dispersion, the effect of the UV radiation is non-negligible.

Comparing the middle row with the bottom row of Fig. 5.9, we see that the main difference between the effects of IR and UV + optical photons is that the IR radiation plays the role of smoothing out the dense gas, especially the regions which the UV and optical radiation cannot reach. When not including the IR photons, the cloud structure is maintained with a similar multiphase state to that of the initial conditions. Generally, the

5.2. OUTFLOWS DRIVEN BY QUASARS IN HIGH-REDSHIFT GALAXIES WITH RADIATION HYDRODYNAMICS

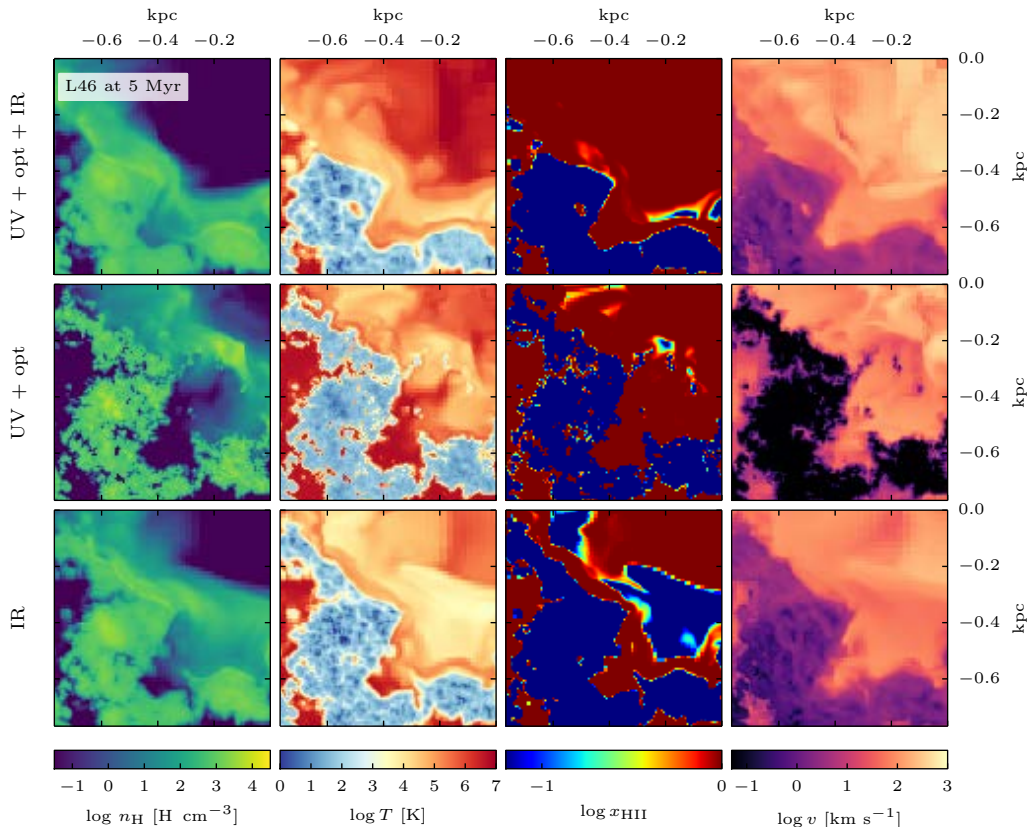


Figure 5.9: Zoomed-in slices of a cloud region in the *L46_medC* simulation (red square of the middle row in Fig. 5.3) at 5 Myr, showing, from left to right, maps of density, temperature, H II fraction, and velocity. The source is at the coordinate origin at the top right corner each image. The different rows show the same simulation with different photon groups included, with, from top to bottom: all photon groups (UV + Opt + IR), excluding the IR photons (UV + Opt), and finally including only the IR photons (IR). The dispersion of the cloud is driven by a complicated interplay between the IR and UV radiation. At early times, the dominant contribution is however the IR radiation.

UV photons only manage to disperse and ionise the gas at the shock front and do not as efficiently mix and disperse the gas of the cloud with that of the background, but instead push the over-dense gas by direct radiation pressure and photoionisation. The inability of UV photons in efficiently mixing the multiphase gas is most apparent when looking at the temperature (and velocity) structure.

With only the IR radiation included, the gas of the cloud is much more mixed with the background gas creating a more uniform density structure at the shock front. This arises because the IR photons are isotropically pushing the gas from the inside of the clouds and are, thus, responsible for the smoothing of the multiphase density distribution and the puffing-up of the clouds.

Comparing the temperature slices of the rows, we observe that when the UV photons are included, the temperature of the smoothed gas with densities of $\sim 100 \text{ H cm}^{-3}$ and fully ionised is higher, due to the photoionisation heating and extra momentum input. We also see that the increased velocity in the simulation incorporating all photon groups is due to the combined contribution of all these photon groups. As expected, the ionization front is

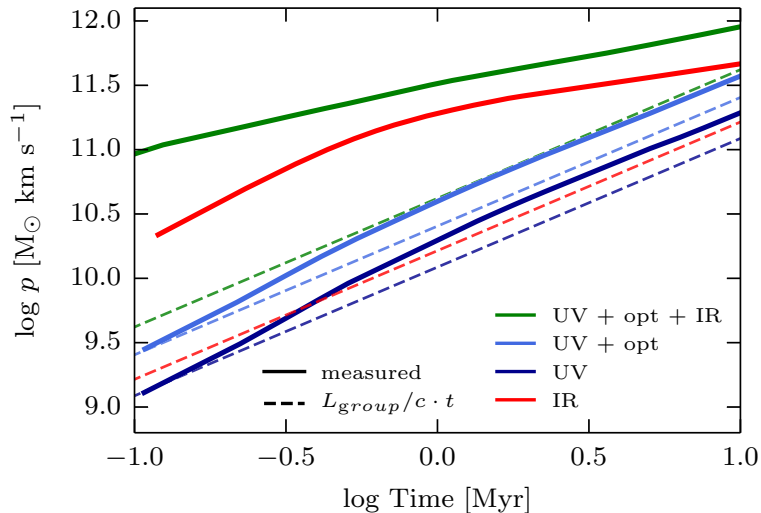


Figure 5.10: Evolution of the total momentum for simulations where the contribution of different photon groups are included: IR only (red lines), UV only (dark blue lines), UV and optical (light blue lines), and all groups (green lines). For the simulations, the exact same initial conditions as for the *L46_medC* simulation, with all the photon groups included (solid green line), are used. The dashed lines show $(L_{group}/c)t$, where t is the time elapsed since the start of the simulations and L_{group} is the luminosity in the photon group bands used in the simulation with the same colour. Through multiple scatterings on the dust, the IR radiation imparts many times a momentum L_{group}/c onto the gas, thus greatly boosting the total momentum transferred to the gas. The main contribution to the total momentum from the UV and optical photons comes from the reprocessed UV photons into IR photons that then multi-scatter and impart a momentum boost onto the gas. Photoionisation heating has a small but non-negligible effect. Finally, the optical photons give a small contribution to the momentum.

more advanced when both the UV (+ optical) and IR photons are included compared to when only the IR radiation is included in the simulation.

Looking at the velocity maps from the different simulations at 5 Myr, we see that when the IR radiation is excluded, only the ionised hot gas ($10^4 - 10^{6.5}$ K) moves with large velocities ranging from 100 to 1000 km s^{-1} . However, with the IR photons, the neutral gas is also moving with a velocity of up to 100 km s^{-1} where the gas is warm (10^4 K), and $\simeq 10 \text{ km s}^{-1}$ where the gas is cold ($< 10^2$ K). The IR photons are, hence, capable of moving the dense, neutral gas, which the UV and optical radiation cannot reach due to the high optical depth of the cloud. We see that when all photon groups are included, the wind, driven from the central region, collides with the external parts due to the UV photon heating and contributes to driving the wind on large-scales.

Fig. 5.10 shows the evolution of the total momentum for the same simulations (*L46_medC*) as shown in Fig. 5.9: including all photon groups (solid green line), excluding contribution from IR photons (solid light blue line). Additionally shown, is a simulation only including the UV photons (solid dark blue line). The dashed lines show L_{group}/ct , where t is measured as the time passed since the beginning of the simulation and L_{group} is the luminosity in the used photon group bands used in the corresponding simulation (indicated with the same color). The ratio between the solid and dashed lines shows how much the correspond-

5.2. OUTFLOWS DRIVEN BY QUASARS IN HIGH-REDSHIFT GALAXIES WITH RADIATION HYDRODYNAMICS

ing photon groups boost the amount of momentum transferred to the gas. Hence, the IR photons are capable of strongly boosting the momentum transfer due to multi-scattering. The UV photons indirectly transfer momentum to the gas via photoionisation heating and with this additionally boost the momentum transfer, however not as strongly as the IR photons. Comparing the simulations that use the different photon groups shows that the inclusion of the IR photons to the optical and UV photons produces a greater momentum boost than in the simulation with only the UV and optical groups, especially at early times. This shows that the main effect of the UV and optical photons on the momentum comes from the dust-absorbed photons that are reprocessed into IR radiation and then additionally boost the momentum transfer onto the gas via multi-scattering.

The small difference between the total momentum of the simulation including only the UV photons and the simulation including the optical as well as UV photons confirms that the optical photons have a non negligible impact on the evolution of the gas, since it doubles its total momentum (the fraction of energy in the optical band is the same than in the UV). Obviously, the contribution of all the photon groups is required to achieve the full momentum (solid green line).

5.2.4.4 Efficiency of the Photon-Gas Coupling

In order to quantify the efficiency with which the radiation couples to the gas and transfers momentum to it, we define the mechanical advantage as the ratio between the momentum input rate \dot{p} and the instantaneous momentum from the radiation source given by L/c , where L is the bolometric luminosity of the source. We calculate the instantaneous momentum injection to the gas as $\dot{p} = (p_N - p_{N-1})/\Delta t_N$, with p_N the total gas momentum at one given snapshot of the simulation, and Δt_N the time interval between two snapshots. As shown in Fig. 5.2, $\sim 80\%$ of the total bolometric luminosity is covered by the photon groups used in the simulations (recall that we do not cover the hard X-ray band). A mechanical advantage above unity occurs when the photons boost the momentum transfer between the radiation and the gas. This can happen when, the IR photons are multiply scattered, as well as by photoionisation heating and subsequent shock formation. The reason we used the bolometric momentum in this calculation is because it is consistent with subgrid models of BH feedback in the literature (e.g. Debuhr et al., 2011; Choi et al., 2014; Barai et al., 2014; Zubovas & Nayakshin, 2014; Costa et al., 2014; Hopkins et al., 2016).

Fig. 5.11 displays the evolution of the mechanical advantage for the *L46_smallC*, *L46_medC*, and *L46_bigC* simulations. For all the simulations, the mechanical advantage decreases with time. However, the magnitude of the mechanical advantage is not the same for the three different cloud size simulations, in particular in the early stages. The efficiency of the momentum transfer for the *L46_smallC*, *L46_medC*, and *L46_bigC* simulations is bigger, the larger the cloud encompassing the source of radiation. Because it takes more time to destroy larger clouds, the photons are trapped and scatter for a longer time. Indeed, a bigger encompassing region around the quasar results in larger the momentum boost from the radiation. For all the simulations, the radiation carves, right from the beginning, a hole into the center of the galaxy, through which the radiation can escape (Fig. 5.3). This causes the mechanical advantage to decrease with time as the photons injected by the source are more likely to escape the system without scattering.

We see that the optical depth (or cloud size) plays a very important factor in the evolution of the mechanical advantage. In addition, dust destruction in hot gas can play a role in suppressing the amount of momentum passed from radiation to gas. We have seen in Section 5.2.4.2, and especially in Fig. 5.4, that the gas is quickly heated to high

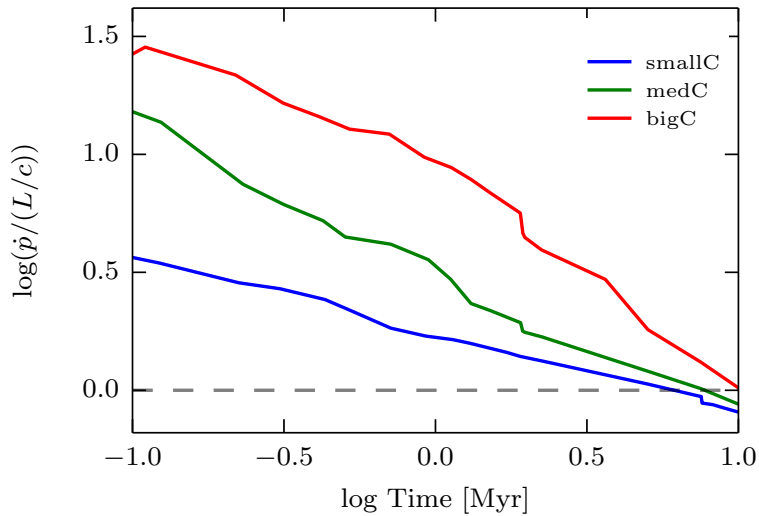


Figure 5.11: Evolution of the mechanical advantage (momentum input rate \dot{p} over L/c , where L is bolometric luminosity) as a function of time for the $L46$ simulations. The mechanical advantage is above unity until 10 Myr, it is larger the bigger the encompassing cloud, and it decreases with time. For the *medC* and *bigC* simulations the mechanical advantage starts decreasing before the central cloud is fully destroyed as the efficiency of the momentum transfer is already less efficient once the radiation manages to carve a hole into the center of the galaxy.

temperatures for the $L46_medC$ and $L46_bigC$ simulations whereas it takes longer for the $L46_smallC$ gas to reach similarly high temperatures. It leads us to the conclusion that dust destruction has more influence for the bigger cloud simulations compared to the $L46_smallC$ simulation. However, as we will see in Section 5.2.5, this effect is not as important as the effect of the cloud size and gas density surrounding the source.

5.2.5 Evolution of the Optical Depth

For a better understanding of the mechanical advantage from the radiation and the efficiency of photon-gas coupling, we measure the optical depth through the disc for the quasar IR radiation as a function of time for the $L46_smallC$, $L46_medC$, and $L46_bigC$ simulations. The IR optical depth is defined as

$$\tau_{\text{IR}} = \int \rho \kappa_{\text{IR}} dl = \sum_{i \in \text{LOS}} \rho_i \kappa_{\text{IR}}(T_i, Z_i) \Delta l_i \quad (5.7)$$

where the opacity κ_{IR} , function of temperature and metallicity, is given in Eq. (5.5), l is the line-of-sight (LOS) coordinate, and where ρ_i , T_i and Z_i are respectively the density, temperature and metallicity of the cell of index i along the LOS, while Δl_i is the length of the LOS through the i th cell.

Fig. 5.12 shows the evolution of the mean optical depth calculated over 500 randomly selected LOS, uniformly sampling a sphere from the centre of the disc, where the quasar source is located, up to a distance of 1.5 kpc.

At the beginning of the simulation, the optical depth calculated over the central cloud is ~ 0.8 times that of the optical depth calculated over the whole disc for $L46_medC$

5.2. OUTFLOWS DRIVEN BY QUASARS IN HIGH-REDSHIFT GALAXIES WITH RADIATION HYDRODYNAMICS

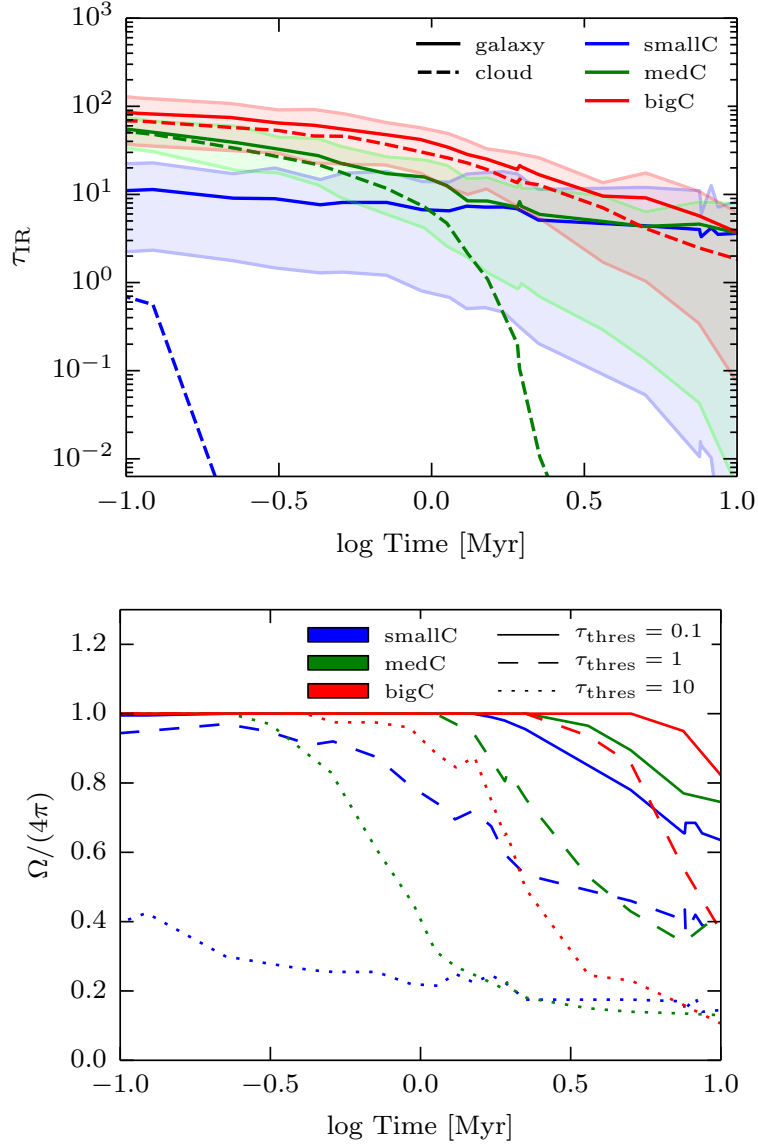


Figure 5.12: *Left:* Evolution of the optical depth τ_{IR} as a function of time for the *L46_smallC*, *L46_medC*, and *L46_bigC* simulations. The lines show the mean values of the optical depth calculated by sampling the sphere along 500 different lines of sight, over the galaxy disc (up to 1.5 kpc, solid lines) or over the central cloud using a radius corresponding to the largest fractal structure within the respective simulation box (see Tab. 5.2, dashed lines). The shaded areas show the $\pm 1\sigma$ distribution of the optical depth over the galaxy. The mean optical depth of the three simulations depends on the cloud size and is larger the bigger the clouds within the disc. *Right:* Fraction of solid angle over the sphere covered by an optical depth greater than a threshold optical depth τ_{thres} of 0.1 (solid), 1 (dashed), or 10 (dotted). The optical depth is calculated over the whole sphere. The figure shows that with increasingly bigger clouds, the covering fraction of $\tau_{\text{IR}} > 1$ is enhanced at given times and decreases at later times.

and *L46_bigC*, while it is 0.1 that of the disc for *L46_smallC*. Once the radiation carves a hole into the central cloud, the optical depth calculated over the cloud drops to zero. This happens later for bigger encompassing clouds. Note that at 10 Myr, the mean optical depths from the source for the three simulations converge to the same value of $\tau_{\text{IR}} \simeq 4$.

As discussed above, there are two important phases for the IR radiation. First, the radiation is trapped within an optically-thick region of the central cloud and imparts momentum onto the gas, which dominates the evolution of the outflow. Once the radiation has destroyed the central cloud, the IR radiation is only trapped within the densest regions of the gas. We have seen that the mean density of the cloud decreases with time, which, in turn, reduces the optical depth of the gas and hence reduces the influence of the trapped photons at later stages. Therefore, in this second phase, the IR radiation plays a less dominant role in pushing the gas out of the disc. These two phases are clear in Fig. 5.12: the cloud starts at high optical depth with little decrease, and then there is a rapid drop.

The optical depths displayed in the left panel of Fig. 5.12 show considerable scatter, so that much radiation can escape even when the mean optical depth is high. The right panel of Fig. 5.12, the fraction of the solid angle covered with τ_{IR} larger than a threshold optical depth τ_{thres} is shown. The fraction of the solid angle covered with $\tau_{\text{IR}} > 1$ gives an indication of the trapping of the IR photons, i.e. their multiple scattering, which in turn gives an indication of the efficiency of photon to gas coupling.

The general evolution of the optical depth distribution for the *L46_smallC*, *L46_medC*, and *L46_bigC* simulation helps to understand the evolution of the mechanical advantage. At the start of the simulations, before the central cloud is destroyed, the optical depth distributions calculated over the cloud for the *L46_medC* and *L46_bigC* simulations overlap, with mean optical depths of $\langle \tau_{\text{IR}} \rangle = 75$ and 56 for the *L46_bigC* and *L46_medC* simulations, respectively (left panel). However, the *L46_bigC* simulation has more scatter in the optical depth distribution compared to that of the *L46_medC* simulation. Additionally, the two simulations have the same unity fraction of solid angle over the sphere covered by τ_{IR} larger than unity for the first ~ 1 Myr (right panel). The larger optical depth for the *L46_bigC* simulation compared with the *L46_medC* simulation leads to a larger mechanical advantage at the start of the simulation. The mean optical depth of the two simulations decreases with time and they converge after ~ 10 Myr. The mean optical depth at the beginning of the *L46_smallC* simulation, on the other hand, is much smaller ($\langle \tau_{\text{IR}} \rangle \sim 11$). Moreover, the fraction of solid angle around the quasar with $\tau_{\text{IR}} > 1$ is at 80 % from the start for *L46_smallC*. Thus, it explains the small mechanical advantage for the small cloud simulation when compared to the larger cloud simulations since a significant fraction (20 %) of all possible lines of sight are optically thin.

Indeed, the optical depth around the source is the important factor in understanding how much momentum from the photons can be transferred to the gas. However, as we have seen, channels of optically-thin gas can form within the optically-thick layers of gas, reducing the expected amount of momentum that is effectively transferred to the gas. Following Hopkins et al. (2011), we write the expected momentum boost as

$$\dot{p} = (1 + \eta \tau_{\text{IR}}) \frac{L}{c} \quad , \quad (5.8)$$

where the factor of $\eta \tau_{\text{IR}} L/c$ accounts for the momentum boost passed onto the gas by the total number of IR scattering events. Eq. (5.8) includes a dimensionless ad hoc *reduction factor* η that accounts for extra sources of momentum (e.g. UV photo-heating, X-ray Compton scattering off the electrons, dust photo-electric heating increasing η above unity) and inhomogeneities in the gas (decreasing η below unity). Hence, the reduction factor

5.2. OUTFLOWS DRIVEN BY QUASARS IN HIGH-REDSHIFT GALAXIES WITH RADIATION HYDRODYNAMICS

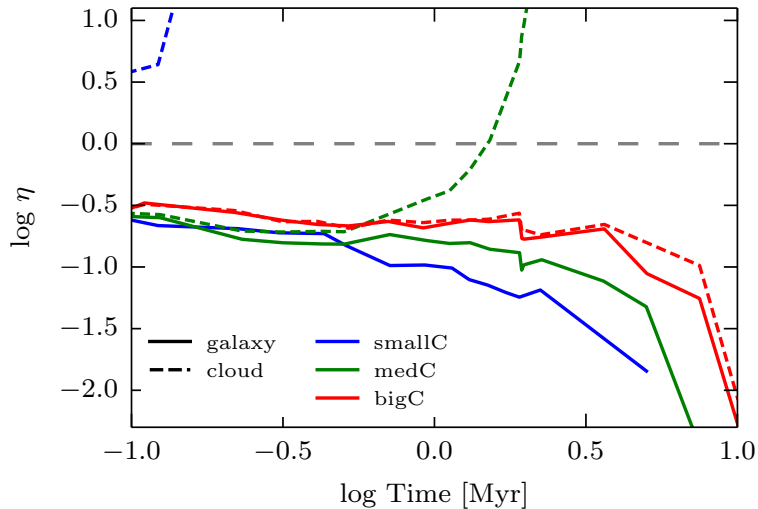


Figure 5.13: Evolution of the reduction factor η , providing a measure of the coupling efficiency of IR photons (see eq. [5.8]) as a function of time for the $L46$ simulations. The solid and dashed lines show the reduction factor calculated with the mean optical depth within the galaxy (η_{gal}) and within the central cloud (η_{cloud}). The values of the reduction factor become unphysical when τ_{IR} falls below values around unity (cloud destruction).

accounts for the fraction of expected multiple scattering that effectively happen. Note that Hopkins et al. (2011) (and others) also use the mean optical depth when defining η .

Given the change in momentum estimated from the simulation, we can determine the reduction factor η from Eq. (5.8), and this is shown in Fig. 5.13. The solid lines show the reduction factor calculated with the mean optical depth within the galaxy (η_{gal}), whereas the dashed line show the reduction factor calculated using the mean optical depth over the central cloud (η_{cloud}).

For all the three simulations, η_{gal} starts below unity starting at ~ 0.2 for the $L46_smallC$ and $L46_medC$ simulation and ~ 0.3 for the $L46_bigC$ simulation and then decreases slowly with time. On the other hand, η_{cloud} starts with a similar value as that of η_{galaxy} for the $L46_medC$ and $L46_bigC$ simulations, whereas η_{cloud} for the $L46_smallC$ simulation already starts at a higher value due to the reduced optical depth over the cloud for this simulation. After ~ 1 Myr, η_{cloud} rises steeply in the $L46_medC$ simulation due to the optical depth dropping to zero around that time. The two reduction factors for the $L46_bigC$ simulation evolve very similarly, again due to the similar behaviour of the optical depth calculated either over the whole galaxy or the encompassing cloud.

It is important to keep in mind that Eq. (5.8) does not hold when the IR radiation is not trapped anymore and escapes without multi-scattering i.e., when $\langle\tau_{\text{IR}}\rangle < 1$, which explains why the value of η diverges in this regime. This is mostly the case for η_{cloud} when the central cloud is destroyed. Our measurements show that, for the cases where $\langle\tau_{\text{IR}}\rangle \geq 1$, the measured mechanical advantage is well below unity even when the source is placed in a region surrounded by a large optical depth. It shows that the non-uniform structure of the ISM and the subsequent building of low density channels as well as the building of a hole in the center of the galaxy has a great influence in setting the reduction factor.

This is in line with the argumentation by Krumholz & Matzner (2009) and Krumholz & Thompson (2012, 2013), who use analytical arguments to show that the effective optical

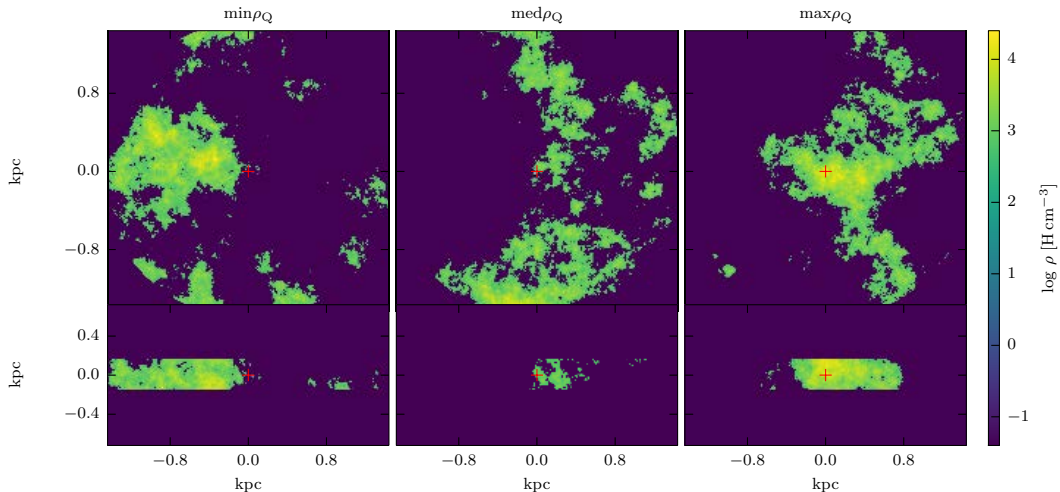


Figure 5.14: Initial density distribution of the different environments for the quasar with $L46_bigC_min\rho_Q$ (left panel), $L46_bigC_med\rho_Q$ (middle panel), $L46_bigC_max\rho_Q$ (right panel). The quasar position is marked by a red cross at the center of each image.

depth can never be larger than a few, due to the tendency of photons to escape through lower density channels, even though if the average optical depth is much larger than unity. Their findings have been challenged by Davis et al. (2014), who showed that the results highly depend on the solver used for the radiative transfer. The flux-limited diffusion (FLD) method used in Krumholz & Thompson (2012) and Krumholz & Thompson (2013) leads to a significantly lower efficiency in accelerating the gas via radiation pressure than in the more accurate method (variable Eddington tensor; VET) used by Davis et al. that showed a stronger acceleration of the gas. Rosdahl & Teyssier (2015b) showed that the M1 method used in our simulations lies somewhat between those of FLD and VET. Using an Implicit Monte Carlo radiation transfer scheme, Tsang & Milosavljević (2015) find results consistent with Davis et al., demonstrating again the importance of accurate radiative transfer in simulations of radiative feedback.

We have already seen that the initial stage, when the radiation is trapped within the central cloud, plays a crucial role in the early acceleration of the gas. We thus expect the IR radiation to be an important driver of the outflow at early times. However, the large IR luminosity rapidly destroys the cloud encompassing the source, which leads to a decrease in the optical depth. This, in turn, shortens the time the radiation is trapped within the central cloud, where it can scatter sufficiently to impart a larger momentum boost onto the gas.

5.2.5.1 Effects of the Quasar Position

As radiatively-driven AGN winds are stronger when the source is embedded within more massive clouds, we expect that the location of the source relative to the cloud should also influence the momentum given to the gas. We have re-simulated the $L46_bigC$ simulation, changing the underlying density at the position of the quasar from a high-density environment ($L46_bigC$ simulation shown before, hereby referred to as $max\rho_Q$ simulation) to a medium-density region ($med\rho_Q$) and to a low-density environment ($min\rho_Q$). The regions are chosen such that the average density, calculated over a region including the direct neighbouring cells, is maximum ($\sim 8000 \text{ H cm}^{-3}$), around the mean ($\sim 320 \text{ H cm}^{-3}$),

5.2. OUTFLOWS DRIVEN BY QUASARS IN HIGH-REDSHIFT GALAXIES WITH RADIATION HYDRODYNAMICS

and minimum ($\sim 0.7 \text{ H cm}^{-3}$), respectively. The initial density distribution of the three different simulations is shown in Fig. 5.14.

The top panel of Fig. 5.15 displays the evolution of the mechanical advantage for the three different quasar positions. This figure indicates that the maximum mechanical advantage reached in the simulation increases by up to a factor 10 when the gas density at the position of the quasar is increased from $\sim 0.7 \text{ H cm}^{-3}$ to $\sim 8000 \text{ H cm}^{-3}$.

The middle panel of Fig. 5.15 shows that the quasar position has an important effect on the mean IR optical depth, which increases by a factor of ~ 30 with increasing density at the quasar location. According to the lower panel of Fig. 5.15, at the start of the simulation, the fractions of solid angle covered with $\tau_{\text{IR}} > 1$ increases from 40% for the low gas density around the source to 100% for the run with the high gas density at the source location.

When the quasar is placed within the minimum density environment, the mean optical depth is initially at $\langle \tau_{\text{IR}} \rangle \sim 3$, but the solid angle covered by an optical depth larger than $\tau_{\text{IR}} = 1$ is only $\sim 30\%$, and $\sim 60\%$ of the IR photons have $\tau_{\text{IR}} < 0.1$. A significant fraction of the photons can hence free-stream out of the disc via optically-thin channels and multi-scattering is negligible. The mechanical advantage is at roughly unity for the first few 0.1 Myr before dropping off. Thus, there is no overall momentum boost in the beginning, but since a fraction of the radiation escapes freely without interactions, another fraction of the radiation must give a boosted momentum to the gas.

With the quasar placed at an intermediate density, $\sim 80\%$ of the solid angle around the source initially has $\tau_{\text{IR}} > 1$, but a non-negligible fraction of $\sim 15\%$ of lines-of-sight have $\tau_{\text{IR}} < 0.1$ and hence are more or less free-streaming channels. In this set-up, the mechanical advantage is intermediate between the two other cases, starting at ~ 3 , steadily dropping, and going below unity after about 1 Myr. Thus, the probability of the photons scattering more than once is much smaller when the local density around the quasar is intermediate compared to when it has the largest value. The environment of the source determines the optical depth around the quasar, which influences the amount of momentum the photons can impart onto the gas. If the source is already in an environment where the covering fraction for $\tau_{\text{IR}} > 1$ is small, the mechanical advantage is much smaller than when the source is in an environment with a large optical depth and the covering fraction for $\tau_{\text{IR}} > 1$ is higher.

5.2.5.2 Comparison between Different Luminosities

We now study the effect of the quasar luminosity on the mechanical advantage. We compare four simulations, using two different quasar luminosities, $L = 10^{43}$ and $10^{46} \text{ erg s}^{-1}$ (the *L43* and *L46* simulations, respectively), and two different quasar locations: intermediate and high gas density around the source, for the largest cloud size simulation.

The top panel of Fig. 5.16 shows the mechanical advantage of the four simulations as a function of time. For a given density at the quasar location, the mechanical advantage at early times (0.1 Myr) has similar values for the two different luminosities. However, in the higher luminosity case it peaks and drops sooner than in the lower luminosity case.

The reason for the higher mechanical advantage in the low luminosity simulations is that the time it takes for the *L46* source to disperse the encompassing cloud and to carve a hole into the centre of the disc is shorter than for the *L43* source. This is clear when comparing the evolution of the optical depth for low and high luminosity (middle panel of Fig. 5.16). The optical depth decreases faster with the high-luminosity quasar than with the lower luminosity one. Indeed, with the lower luminosity quasar, the radiation has thus more

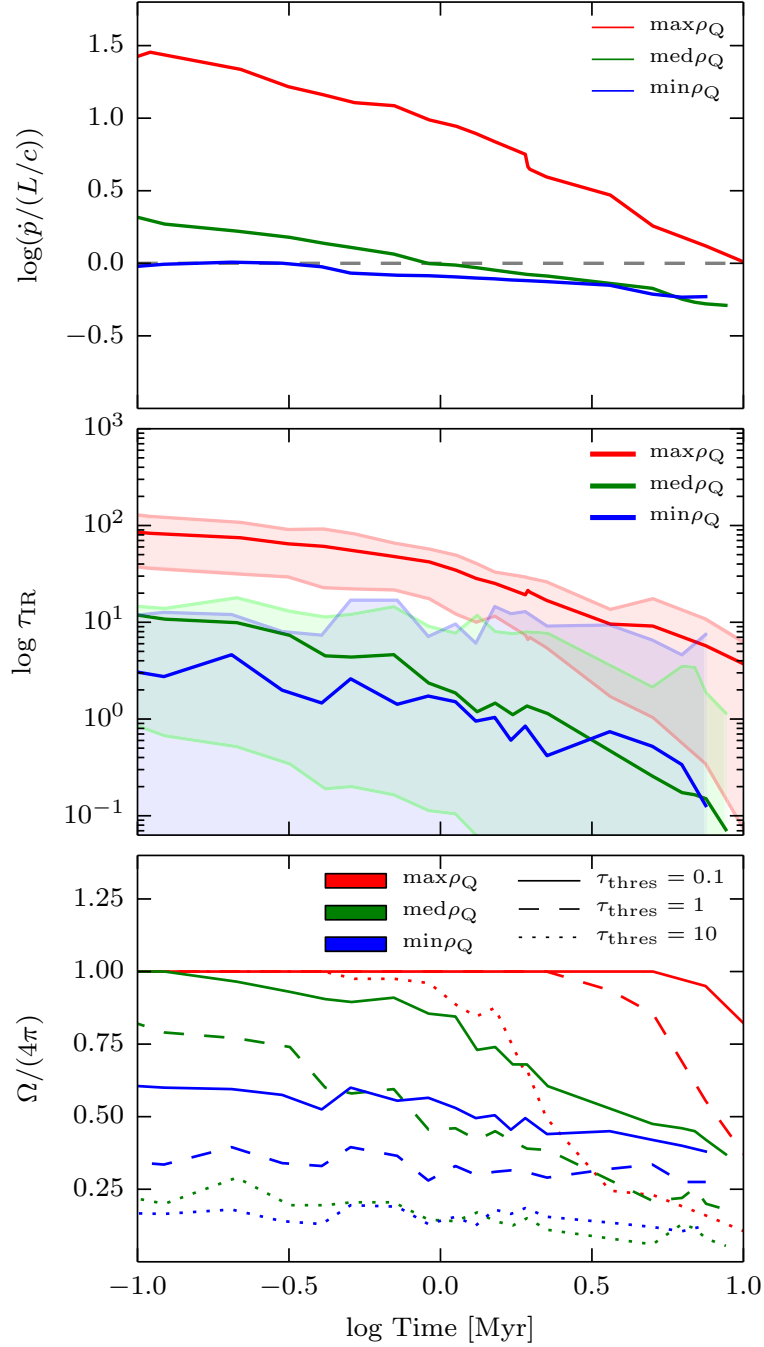


Figure 5.15: *Top*: Evolution of the mechanical advantage for the *L46_bigC* simulations, where the position of the quasar within the density field has been varied. The labels *max*, *mean*, and *min* stand for the quasar position within the environment of maximum, mean and minimum density, respectively. *Middle*: Evolution of the mean galaxy optical depth τ_{IR} with the one $\pm\sigma$ standard deviation (shaded areas). *Bottom*: Fractions of solid angle over the sphere covered with τ_{IR} larger than a threshold optical depth τ_{thres} . We see that the environment of the luminous source has a strong effect on the maximum boost gained by the photons.

5.2. OUTFLOWS DRIVEN BY QUASARS IN HIGH-REDSHIFT GALAXIES WITH RADIATION HYDRODYNAMICS

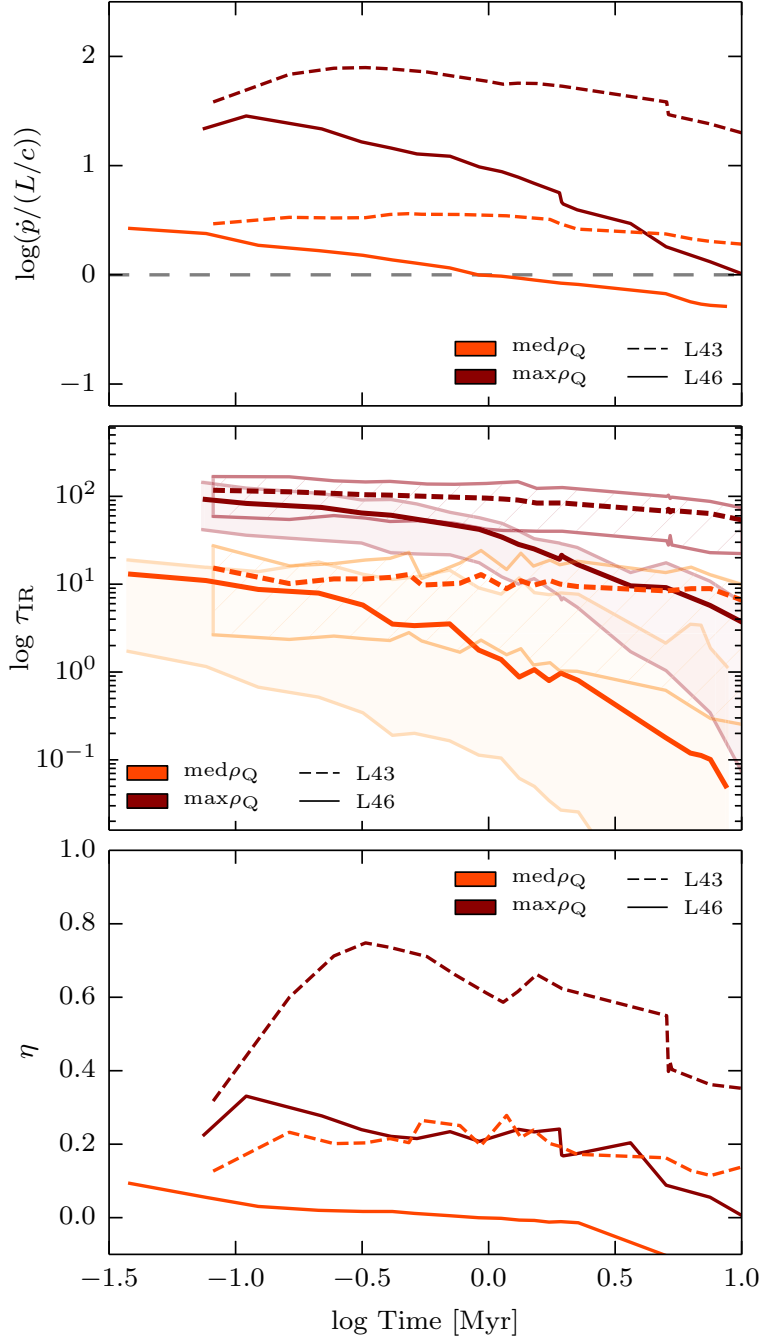


Figure 5.16: *Top*: Evolution of the mechanical advantage for low and high quasar luminosities, respectively $L = 10^{43} \text{ erg s}^{-1}$ ($L43$) and $L = 10^{46} \text{ erg s}^{-1}$ ($L46$), and two different local gas densities (see Fig. 5.14). *Middle*: Evolution of the mean IR optical depth with the $\pm 1\sigma$ standard deviation (shaded areas for $L46$ simulations, hatched areas for $L43$ simulations). *Bottom*: Evolution of the reduction factor η . The mechanical advantage for the lower luminosity simulation is higher than that of the higher luminosity simulation with a larger value of η . The higher luminosity leads to a faster destruction of the central cloud compared to the lower luminosity, leaving less time for the radiation to impart its momentum to the gas.

time during which the surrounding cloud is intact and the radiation multi-scatters inside it. On the other hand, with a more luminous source, the surrounding cloud is more quickly dispersed, allowing the photons to escape, and giving a lower mechanical advantage.

It is important to stress that the mechanical advantage is defined as the fraction of the momentum change over the total bolometric momentum, where the use of the bolometric momentum is consistent with subgrid models of black hole feedback in the literature (e.g. Zubovas & Nayakshin, 2014; Costa et al., 2014; Hopkins et al., 2016). Hence, even though the mechanical advantage is higher for the lower luminosity source, the total momentum at ~ 1 Myr for the high luminosity source is $82 M_{\odot} \text{ km s}^{-1}$ ($7.8 M_{\odot} \text{ km s}^{-1}$) and with this ~ 210 (~ 360) times higher than the total momentum in the low luminosity quasar simulation, with the quasar placed in both simulations in a maximum (medium) density environment.

The reduction factor η starts between 0.1 and 0.3 for the simulations with the bright quasar and is roughly twice as great in the simulations with the faint quasar (bottom panel Fig. 5.16). The higher reduction factor for lower luminosities is not only caused by the higher mechanical advantage for the low luminosity simulation, but is also a consequence of the different distributions of the optical depth. The mean and lower error bound of the optical depth distribution of the high quasar luminosity simulation reaches much lower values than the corresponding values in the low quasar luminosity run. Hence, while the high quasar luminosity run produces a rapidly evolving outflow, with low-density channels that arise, in the low luminosity run the gas has more time to mix with the surrounding gas, leading to a smoother outflow, with no low-density channels arising. Therefore, a larger fraction of photons manage to escape through lower density channels for the higher luminosity simulation that then in turn lowers the reduction factor.

In summary, we find that the mechanical advantage is higher for lower luminosities because the radiation manages to destroy the encompassing cloud faster if the source is more luminous. The reduction factor starts in a similar range (0.1 - 0.3) for the two different luminosities, but then reaches highest values for the simulation with low luminosity and quasar placed in a maximum density environment. The reason for the higher reduction factor for lower luminosities is that in the high luminosity run the radiation causes the formation of low-density tunnels that are not formed in the lower luminosity simulation due to the slower propagation of the wind. A larger amount of low-density tunnels lead to a smaller efficiency of the momentum transfer between the radiation and the gas and hence a smaller reduction factor for the higher luminosity simulation. However, the amount of momentum gained still scales with the luminosity of the source.

5.2.6 Discussion

While our simulations are well suited for studying the interactions between radiation and gas, they come with caveats. We now discuss the shortcomings of our simulations and possible implications and changes when taking them into account.

First of all, including gravity in our simulations could have different, possibly opposing, effects. The first effect is that gravity may slow down the propagation of the outflows, as the gravitational potential will make it harder for the gas to escape the galaxy, which in turn would decrease the mass outflow rate out of the galaxy. However, part of the outflow reaches velocities up to 1000 km s^{-1} , which is fast enough for the gas to escape the central encompassing cloud and even escape out of the massive halo. The escape velocity out of the largest encompassing cloud of mean density of $\sim 100 \text{ H cm}^{-3}$ and radius $\sim 1.5 \text{ kpc}$ is $\sim 450 \text{ km s}^{-1}$. The cloud collapse time, on the other hand, is $\sim 9 \text{ Myr}$. Since the outflow

5.2. OUTFLOWS DRIVEN BY QUASARS IN HIGH-REDSHIFT GALAXIES WITH RADIATION HYDRODYNAMICS

velocities of 1000 km s^{-1} are greater than the escape velocity out of the cloud and are reached on a faster timescale ($\leq 5 \text{ Myr}$) than the free-fall time of the central cloud, it is reasonable to assume that the central cloud indeed gets destroyed and that the outflow progresses further out of the galaxy.

Within the disc, the influence of gravity is less clear. In our simulation, radiation is capable of carving a hole in the central regions of the galaxy. In reality, part of the gas displaced by the radiation (that displaced vertically above the now rotating disc) would likely fall back to the centre, which would enhance the optical depth around the black hole and thus could help to boost the momentum transfer from the radiation for a longer time than observed in our simulations.

With the inclusion of radiative cooling, in addition to gravity, the collapse of massive clouds would be enhanced, leading to a larger cloud mass of smaller size. This would likely strengthen the matter-radiation coupling due to the larger optical depths of the clouds. However, radiative cooling (in combination with gravity) could also lead to a fragmentation of the massive clouds (by reducing the Jeans length) and thus speed up the formation of lower density channels through which the radiation would escape.

In addition, our simulations explore the effect of a steady, uniform quasar, located at the centre of the galaxy. Actual black holes radiate with a luminosity that is proportional to their accretion rate, and hence their luminosities are not steady. Once the radiation manages to carve a hole in the central regions of the galaxy, the luminosity of the quasar should drop to lower values hence decreasing the amount of momentum transferred to the gas.

The interplay between the effect of gravity and the changing luminosity of the quasar may lead to a self-regulating feedback cycle, where AGN activity pushes the gas out of the central regions of the galaxy leading to starvation of the black hole, shutdown of radiative emission and subsequent fall-back of the gas onto the black hole. Furthermore, black holes presumably accrete gas clouds of varying masses and sizes. Therefore, the amount of momentum (and feedback) transferred to the galaxy, and the galactic mass outflow rate will vary with time.

The inclusion of gravity, cooling, and the time variability of the quasar luminosity, increases the complexity of the non-linear interplay between the radiation and the gas, and we defer this study to future work.

Finally, it is still under debate whether an outflow driven by radiation from the black hole may also lead to a (local) enhancement of star-formation due to the compression of the clouds and the subsequent formation of more stars. We have neglected the formation of stars and stellar feedback in our simulations. Stars generally form in dense, cold gas regions. Removing gas mass from the galaxy is thought to negatively impact the formation of stars. As deduced in observations (e.g. Cresci et al., 2015b), it may also be plausible that the compression of the gas during a burst of quasar activity also triggers star formation. Such a positive feedback effect has been shown for the non-radiative modes of AGN feedback (Gaibler et al., 2012; Zubovas et al., 2013a; Bieri et al., 2015, 2016b). We defer to future work a deeper discussion of the possibility of triggered star formation due to quasar feedback.

5.2.7 Conclusions

Quasar-driven winds are powered by complex interactions between radiation and gas. In most recent state-of-the-art hydrodynamical cosmological simulations (but also in hydrodynamical simulations of isolated disc galaxies), quasar feedback is approximated by deposit-

ing thermal energy within the resolution element, where the efficiency of the radiation-gas coupling is represented by a single parameter chosen to match global observations such as the SMBH mass-bulge velocity dispersion (Ferrarese & Merritt, 2000). Additionally, there is no consensus from these simulations on whether these AGN winds are momentum-conserving or energy-conserving, although recent observations favour energy-conserving winds from the nuclear accretion disc (Tombesi et al., 2015; Feruglio et al., 2015). Generally we refer to the outflow as energy-conserving if the radiation is capable of efficiently boosting the momentum transfer between the photons and the gas (i.e., $\dot{p} \gg L/c$), and to momentum-conserving if the amount of momentum transferred to the gas is similar to the momentum flux of photons provided by the source (i.e., $\dot{p} \approx L/c$).

Given the likely importance of AGN feedback in the evolution of massive galaxies and the increasing amount of radio galaxy observations — e.g., from the Low-Frequency Array (LOFAR), the Australian Square Kilometer Array Pathfinder (ASKAP), as well the Atacama Large Millimeter Array (ALMA), which promise to provide us a better view of the ISM properties in these galaxies — it is time to improve our theoretical understanding of the mechanisms that drive the momentum and energy transfer from the photons to the ISM in order to properly quantify the role of AGN feedback in the evolution of galaxies.

We have performed idealised galactic disc RHD simulations to study the coupling of photons with the highly multiphase galactic gas using different cloud sizes. In the simulations, the emission, absorption, and propagation of photons and their interaction with the gas via photoionisation, momentum transfer, and absorption/scattering on dust, is followed self-consistently.

We find that radiation from a bright quasar is capable of driving a powerful wind, with multi-scattering IR photons playing the dominant role, especially at early times. The UV and optical photons never manage to reach the high density regions of clouds due to the large optical depths. Therefore, the UV and optical photons exert their direct push to the clouds from outside. Some of the UV and optical radiation is dust-absorbed and reprocessed into IR radiation that can propagate much deeper into the dense gas. This reprocessed IR radiation is the most significant contribution of the higher-energy radiation to the total momentum of the gas (see Fig. 5.10).

The mass outflow rates as well as the velocity reached by the galactic wind depend on the structure of the ISM (and luminosity of the source). Larger clouds have greater IR optical depths, hence longer time during which IR photons are trapped within and scatter multiple times. This first phase plays a crucial role in the early acceleration of the gas. Once the radiation has destroyed the central encompassing cloud, the IR radiation can stream out of the galaxy through low density regions, decreasing the efficiency of the momentum transfer from the photons to the gas.

Both the outflow rates of ~ 500 to $1000 M_{\odot} \text{ yr}^{-1}$ and high velocities of $\sim 1000 \text{ km s}^{-1}$ that we measured in our simulations with a large encompassing cloud around the quasar are close to those observed by Tombesi et al. (2015) and Feruglio et al. (2015). This agreement favours winds that appear as energy-driven, which in our case are actually radiatively-driven. But as mentioned above, our measured outflow rates are optimistic predictions as we did not include gravity in our simulations.

The mechanical advantage, defined as the ratio of the imparted momentum rate \dot{p} and L/c , decreases with time, from ~ 3 to 30 at the beginning of the simulation to unity after ~ 10 Myr, thanks to the decreasing efficiency of the photon-gas coupling. This mechanical advantage largely depends on the size of the encompassing cloud as well as the position of the quasar (and the quasar luminosity). It varies by a factor of 10, depending on the size of the encompassing cloud (50 pc to 1.5 kpc) used in our simulations, with the IR optical

5.2. OUTFLOWS DRIVEN BY QUASARS IN HIGH-REDSHIFT GALAXIES WITH RADIATION HYDRODYNAMICS

depths ranging from $\tau_{\text{IR}} = 10$ to 100. The position of the quasar plays an important role in setting the amount of momentum transferred from the photons to the gas, where the mechanical advantage changes by a factor of 50, depending on whether the source is buried within the cloud or illuminating it from the outside. Thus, the IR optical depth τ_{IR} (i.e., the cloud size and mass) around the quasar is the most important criterion in determining the momentum injection rate at a given quasar luminosity.

The reduction factor $\eta = [\dot{p}/(L/c) - 1]/\tau_{\text{IR}}$ is an empirical estimate that accounts for extra sources of momentum (e.g., UV photoionisation heating, X-ray Compton scattering off the electrons, dust photo-electric heating, etc.) and inhomogeneities in the gas. The measured reduction factor never reaches values of unity, showing that the mechanical advantage never reaches values as high as τ_{IR} . The non-uniform structure of the ISM and the formation of low density channels is responsible in setting this low value of $\eta = 0.2-0.3$, that decreases significantly once the most central cloud starts breaking up and becomes optically thin. Thus, the number of scattering events of IR photons is roughly one quarter of the IR optical depth.

The radiation emitted by the central quasar destroys the cloud encompassing the source, which leads to a rapid decrease in the optical depth and reduction factor. We demonstrated that the destruction time is shorter for larger luminosities, which leads to a smaller mechanical advantage. Additionally, the fast evolution of the wind in the high luminosity simulation leads to the formation of low density channels leading to a smaller efficiency of the radiation-gas coupling. For the low luminosity simulation, on the other hand, the evolution is slower which leaves the gas more time with to mix with the surrounding gas and thus leads to a smaller amount of optically-thin gas. This in turn leads to a higher reduction factor for the lower luminosity simulation. Nonetheless, large luminosities are required to obtain radiatively-driven quasar winds with fast velocities and high mass outflow rates.

In the future, this study will be extended to AGN radiation within self-regulated turbulent discs including gravity, gas cooling, star formation, stellar feedback and a model for dust creation and destruction.

Acknowledgments

It is our pleasure to thank Romain Teyssier, Marta Volonteri, Pierre Guillard, and Jonathan Coles for valuable discussions. This work was granted access to the HPC resources of CINES under the allocations c2015047421 made by GENCI. RB has been supported by the Institute Lagrange de Paris. JR was funded by the European Research Council under the European Union's Seventh Framework Programme (FP7/2007-2013) / ERC Grant agreement 278594-GasAroundGalaxies, and the Marie Curie Training Network CosmoComp (PITN-GA-2009-238356). JS acknowledges support from project 267117 (DARK) hosted by UPMC – Sorbonne Universités, from JHU by National Science Foundation grant OIA-1124403. This work has made use of the Horizon cluster, hosted by the Institut d'Astrophysique de Paris. We warmly thank S. Rouberol for running it smoothly.

5.2.8 Appendix

With the explicit M1 scheme that we use for the transport of radiation between grid cells, the RHD timestep is limited by the speed of light, since the solver breaks down if radiation is allowed to travel more than one cell width in one timestep. We thus use the reduced speed of light approximation (Gnedin & Abel, 2001), with a fiducial light speed of $c_{\text{red}} = 0.2c$ in this work.

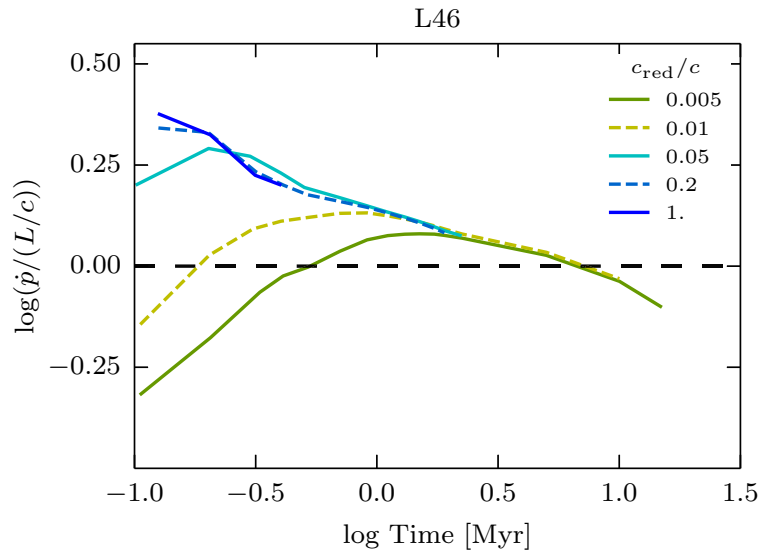


Figure 5.17: Convergence test of the mechanical advantage for the lower resolution $L46_medC_med\rho_Q$ simulation using different values for the reduced speed of light c_{red} , whose default value is $0.2c$ in our simulations. Convergence occurs for $c_{\text{red}} \geq 0.2c$.

To understand how much our reduced speed of light affects our results, we have run lower-resolution equivalents to $L46_medC_med\rho_Q$ with a spatial resolution of $\Delta x = 11.6$ pc (as opposed to fiducial resolution of $\Delta x = 5.8$ pc used in the rest of the paper), and where we adopt different values for the reduced speed of light c_{red} . The evolution of the mechanical advantage, shown in Fig. 5.17, indicates that the choice of c_{red} has a significant effect on the mechanical advantage, especially at the beginning of the simulation. In fact, the mechanical advantage can increase by an order of magnitude, at early times (0.1 Myr), if the reduced speed of light fraction is increased from $c_{\text{red}} = 0.005$ to unity. Yet, this increase is very limited when changing from $c_{\text{red}} = 0.2c$ (as in our study) to c . After ~ 2 Myr, when the radiation has managed to carve a hole through which it escapes, all runs converge towards the same momentum input rate.

We conclude that our results regarding the mechanical advantage are not significantly altered by the reduced speed of light to $0.2c$ and that our results are thus well converged. In a forthcoming paper (Bieri et al, in prep.), we will discuss in more detail the measured reduction factor and its dependence on the reduced speed of light.

Conclusions and Perspectives

In this thesis I have studied the interactions between AGN outflows and the ISM, how feedback impacts the host galaxy, and the communication mechanism of the AGN with the galaxy's gas. In particular, I have focused on two possible mechanisms of outflows, related to AGN jets and related to outflows produced by the radiation of AGN. The studies investigated

1. Under which conditions AGN jet feedback induces or suppresses star formation and whether jet-induced star-formation is a possible explanation for the starburst galaxies found at high-redshift and
2. How radiation emitted from a thin accretion disc surrounding the SMBH effectively couples to the surrounding ISM and drives a large-scale wind.

I have run idealised hydrodynamical simulations to test the effect of the different feedback mechanisms described above. To study the coupling of the radiation to the galactic gas I have also performed radiative hydrodynamics simulations.

In the following Sections I first summarise the important conclusions of these studies and then discuss possible improvements and implications.

6.1 Conclusions

External pressure-triggering of star formation

Pressure-regulated star formation may control the global star formation rate as a function of the cold gas content in the star-forming galaxies. It has been shown that it naturally accounts for the Kennicutt-Schmidt relation in both nearby and distant galaxies.

The inclusion of AGN-induced pressure, by jets and/or winds, has been proposed to explain of the remarkably high star formation rates recently found in the high redshift Universe. To study the effects of AGN-jet induced pressurisation of the disc, I performed a large number of isolated disc simulations with varying gas-richness of the galaxy (Bieri et al., 2015, 2016b) in which I fully included self-gravity of the multiphase ISM and thereby traced the evolution of the star formation rate (SFR) as well as that of the gas content of the system. The simulations have been run without AGN jets, but with simple prescriptions for external pressure such as that which may be caused by jet cocoon.

By doing so, I have been able to study the response of the galaxy SFR to the forcing exerted by the external pressure. I found that already moderate levels of over-pressurisation of the galaxy boost the global SFR of the galaxy by an order of magnitude. The over-pressurisation turns Toomre stable discs unstable, and leads to significant fragmentation of the gas content of the galaxy, leading to clump sizes and masses similar to what is observed in high redshift galaxies. Interestingly, the findings were not significantly different when stellar feedback from the formed stars was included in the simulations. By analysing the Kennicutt-Schmidt (KS) relation I found that, independently of the gas fraction, the simulations with external pressure end up being pushed closer or further beyond the starburst sequence than the corresponding simulations without external pressure.

Although the setup of the extra pressure exerted by circum-galactic gas onto the galaxy is crudely modeled to mimic the pressure confinement by AGN activity, simulations suggest

that such a mechanism could operate in more realistic configurations (see the jet simulations of Gaibler et al. 2012).

My simulations hence suggest that such jet-induced star formation is a possible explanation of the starburst galaxies found in the high-redshift Universe. The simulations, therefore, demonstrate that the over-pressurisation of the disc could explain observations of star formation-enhanced galaxies in the presence of jet activity (Zinn et al. 2013).

A possible global picture might be a two-stage mechanism for AGN feedback: a compression phase leading to a short burst of star formation, together with the expulsion or heating of the circumgalactic gas leading to a suppression of the gas accretion onto the galaxy and its star formation on longer time-scales. This remains to be verified with simulations of galaxies embedded in a cosmological environment with high spatial resolution and a self-consistent treatment of AGN feedback.

Feedback from Radiatively-driven AGN Winds

In order to assess the role of quasar feedback on the evolution of galaxies it is crucial to better understand how photons emitted by the central AGN source couple to the ambient ISM to trigger large-scale outflows by means of radiation-hydrodynamical (RHD) simulations.

To investigate the coupling between the multiphase galactic gas and the radiation, I performed idealised galactic disc RHD simulations. The radiative transfer module of RAMSES-RT (Rosdahl et al. 2013, 2014) was used to release photons at the centre of the gas distribution in several different bands: optical, UV, IR. The UV band contributes to the photo-heating of the gas and to the radiation pressure, and the IR to the radiation pressure on dust through multi-scattering. Additionally, I modified the standard dust model in RAMSES-RT in order to simulate dust destruction at high temperatures.

I found that radiation from a bright quasar is capable of driving a powerful wind, where the multi-scattering IR photons play the dominant role, especially at early times. The UV and optical photons never manage to reach the high density regions of clouds due to the large optical depths and therefore exert their direct push to the clouds from the outside. The most significant contribution of the higher-energy radiation to the total momentum of the gas comes from the dust-absorbed UV and optical photons that are then reprocessed into IR radiation.

The measured mass outflow rates, as well as the velocity reached by the galactic wind, depend on the structure of the ISM as well as luminosity of the source. Generally, larger clouds have greater IR optical depths, hence longer time during which IR photons are trapped within, scatter multiple times and impart their momentum onto the gas. The first phase plays a crucial role in the acceleration of the gas. Once the radiation has destroyed the central encompassing cloud, the IR radiation streams out of the galaxy through low density regions, decreasing the efficiency of the momentum transfer from the photons to the gas. The typical number of multi-scattering events for an IR photon is only about a quarter of the mean optical depth from the center of the cloud.

The simulations account for the observed outflow rates of $500\text{-}1000 M_{\odot} \text{ yr}^{-1}$ and high velocities of $\sim 10^3 \text{ km s}^{-1}$, favouring winds that are energy-driven via extremely fast nuclear outflows, interpreted as being IR-radiatively-driven winds.

While these simulations are well suited for studying the interactions between radiation and gas, they are, however, highly idealised. The inclusion of gravity, cooling, and the time variability of the quasar luminosity, increases complexity of the non-linear interplay between the radiation and the gas, that could possibly lead to a self-regulating feedback cycle, where AGN activity pushes the gas out of the central regions of the galaxy leading to

starvation of the BH. Furthermore, BHs presumably accrete gas clouds of varying masses and sizes, that in turn would change the optical depth around the BH. Therefore, the amount of momentum (and feedback) transferred to the galaxy, and the galactic mass outflow rate will vary with time.

In the future, this study will be extended to AGN radiation within self-regulated turbulent discs including gravity, gas cooling, star formation, stellar feedback and a model for dust creating and destruction.

Additionally, it is still under debate whether an outflow driven by radiation from the BH may also lead to a (local) enhancement of star-formation due to the compression of the clouds and the subsequent formation of more stars, as suggested by various recent observations (e.g. Rauch et al., 2013; Cresci et al., 2015b; Carniani et al., 2016). Such a positive feedback effect has been shown for the non-radiative modes of AGN feedback (Gaibler et al. 2012; Zubovas et al. 2013; Bieri et al. 2015, 2016). Future work will have to investigate in more detail the possibility of triggered star formation due to quasar feedback.

6.2 Future Prospects

One of the biggest shortcomings in numerical models of star, SMBHs, and galaxy formation is an incomplete understanding of the underlying physics and the feedback cycle.

In nearly all models of galaxy formation, strong feedback from both stars and BHs plays a critical role in regulating the ISM and with this star formation and BH growth. The goal of my thesis was the investigation of the interaction of AGN outflows and the ISM, how the feedback impacts the gas structure of the galaxy, and the communication mechanism of the AGN with the ISM. The simulations performed here include an adequate treatment of the ISM necessary to investigate the dependence of AGN feedback on jet/radiation power and the properties of the ISM. However, they have so far been restricted to idealised cases.

A first natural advancement of the simulations investigating the coupling between the radiation and the ISM is to include self-gravity, cooling and star formation. While the first simulations in this direction have already been made, the results are very preliminary and could be improved. Comparisons with observations (e.g. Cresci et al., 2015b; Carniani et al., 2016) reveal a similar picture where the radiation-triggered outflow is able to suppress star formation in the region where the outflow is expanding. As in the observations the outflow locally enhances the SFR in regions of high $H\alpha$ emission, which correspond to high density regions. The emission of $H\alpha$ appeared, similar to the observations, anti-correlated with the fast outflows.

Although the radiation-triggered outflow is capable of locally enhancing the star formation, the global star formation reveals that the simulation with a quasar in the center of the galaxy manages to suppress the global star formation compared to a control run without a quasar in the center. Hence, even though AGN feedback does enhance star formation at certain places within the galaxy, the quasar feedback still manages to suppress the global SFR.

As with jet-triggered star formation, the conditions for local, quasar-triggered positive feedback are more optimal in galaxies with larger clouds, e.g. high-redshift and gas-rich galaxies. Negative feedback, on the other hand, is more efficient with small cloud sizes.

Such triggering of star formation within dense clumps has also been revealed by recent observations of Oteo et al. (2016). They found extreme SFR densities in a pair of dusty starbursts at redshift $z = 3.442$ using ALMA 20-milliarcsec resolution imaging and argue

that their results suggest that a significant fraction of the enormous far-IR luminosity in some dusty starbursts is concentrated in very small star-forming regions. My preliminary analysis of the simulations with a radiation-triggered outflow reveal that quasar feedback may indeed be able to lead to a short burst of star formation in the high-redshift Universe.

Such star burst event could then likely be followed by the expulsion and/or heating of the circumgalactic gas due to the quasar as well as stellar feedback from the young stars. This would lead to a suppression of the gas accretion onto the galaxy and the star formation of the galaxy on a longer timescale, leading to a self-regulation of star formation and AGN feedback within the galaxy. The interplay between AGN triggering of star formation within the densest regions in the galaxy and the subsequent ejection of a large portion of the galaxy's gas could well be more effective than AGN feedback alone. Especially because the triggering of star formation happens exactly where more feedback is needed, in the densest regions of the galaxy. It is possible, that star formation triggered by AGN may lead to a self-regulation process, as has also been suggested by recent observations Pitchford et al. (2016).

It should be noted that other processes, such as mergers resulting in bursty star-formation, may also offer a valid explanation of, at least, a few of these galaxies (e.g., Emonts et al., 2015). It is traditionally assumed that galaxy mergers is the main trigger for AGN activity (e.g., Hopkins et al. 2006). This picture is supported in the low redshift Universe, where there is increasing evidence that powerful radio galaxies as well as starbursts are often associated with gas-rich galaxy mergers (e.g., Heckman et al. 1986; Ramos Almeida et al. 2012; Sanders & Mirabel 1996). However, it is not clear whether mergers fuel AGN activity that then induce star formation, or whether mergers redistribute gas on roughly the same timescale as it is depleted by star-formation which in turn results in a high star-formation rate driven by mergers alone.

While any connection is still speculative and vigorously debated, the fact that outflows, as well as AGN activity, are detected for most of these galaxies, whereas only a few undergo mergers, indicates that AGN-induced pressure-regulated star formation is a very possible explanation for the presence of the starburst galaxies.

A simple analytical model by Zubovas & King (2016) suggest that the interplay between quenching and triggering within a single disc galaxy could also likely explain the recently observed inside-out disc quenching of star formation in galaxy discs (Tacchella et al. 2015).

All these claims have to be verified with simulations of galaxies embedded in a cosmological environment with high spatial resolution and a self-consistent treatment of AGN feedback. Cosmological simulations place galaxies in a much more violent and realistic environment that affect the evolution of these galaxies, possibly in a way that is not predicted by isolated disc simulations. To make a bridge between high-resolution galaxy scale simulations and cosmological simulations, cosmological zoom simulations can be performed that allow a realistic treatment of jet and radiation feedback. Critically, these simulations simultaneously resolve the ISM and both fueling and feedback from BHs, and include fundamentally new physics on galactic scales. They allow a better understanding of the interaction of both natures of AGN feedback (radiative and mechanical) with the multi-phase ISM, its impact in high-redshift, gas-rich galaxies, and on the precise mechanism of the communication of AGN with the galaxy's gas in a cosmological context. Furthermore, this will allow for a better understanding of how the small-scale physics of AGN feedback impacts cosmological star formation and how sub-grid models for other studies can be improved.

Additionally, by performing cosmological zoom simulations one is able to investigate the

interplay between mergers, fuelling, and feedback in order to better understand under which conditions AGN feedback induces star formation and to study the possible self-regulation process of star formation triggered by AGN.

Having established a machinery to study both a realistic radiation feedback model as well as a jet-feedback model within a cosmological environment one will be able to study many other outstanding questions:

- Under which conditions does AGN feedback induce star formation? Is there a self-regulation process of star formation triggered by AGN feedback, where a phase of positive feedback precedes the commonly observed massive, star formation-quenching, outflows stimulated by AGN activity?
- Is the interplay between quenching and triggering indeed a possible explanation of the observed inside-out disc quenching of star formation in galaxy discs?
- What is the relative efficiency of these models when combined into a single AGN model where radiation or jet feedback is turned on depending on the accretion/feeding onto the black hole? This is also desirable because they may both be acting simultaneously in some cases.
- What is the interplay between AGN feedback and other physical processes such as star formation and stellar feedback? What happens to the gas that is ejected by AGN as opposed to the gas ejected (or not) by star formation? Will stellar feedback support the mass outflow induced by AGN? Will AGN induce star formation that in turn leads to more efficient mass outflow? This will of course depend on our physical understanding of star formation as well as stellar feedback which is still limited and debated (e.g., Padoan & Nordlund, 2011, Agertz & Kravtsov, 2015).
- Does mechanical/radiative feedback have the right amount of coupling to the ISM/star formation or are other feedback mechanisms such as radiative processes through cosmic rays necessary?
- How does the star formation history of the galaxies with AGN evolve with redshift compared to the galaxies without AGN? Is the galaxy main sequence evolving and bifurcating?
- Are the simulations able to give adequate predictions of emission lines, outflow rates, wind speeds, and velocity maps that might help astronomers better understand their observations and in turn improve their models?

The focus on AGN feedback interacting with a realistic ISM is additionally motivated by the increasing amount of data of radio galaxies from , e.g., LOFAR and ASKAP observations, as well as ALMA observations, that promise to give us a better view of the interstellar medium (ISM) properties in these galaxies. We are therefore in need of more rigorous theoretical work involving realistic hydrodynamical simulations of AGN feedback in order to properly quantify the role of AGN in the evolution of galaxies. Additionally, such simulations can make direct predictions for outflow properties in different ISM phases, which is especially relevant for recent multi-wavelength observations from HST COS, NuSTAR, Herschel, GALEX, XMM-Newton, and Chandra, and future observations with ALMA and JWST.

Acknowledgements

Science starts with ideas and there are surely only a handful of people that have had as many as **Joe Silk**. I want to thank Joe for sharing a few of his many thoughts with me and for giving me the opportunity to work at the Institut d'Astrophysique de Paris. My few visits to Baltimore were certainly some of the best times during the last three years. Thank you for sending me around the world and for your continuous support and encouragement.

I also would like to thank **Gary A. Mamon** for his support. Not only for enduring my dreadful English but also for his constant encouragement, enthusiasm, and belief in me. Thank you for always having an open door, cheering me on, and for never ever leaving me without new ideas for improvement ;-)

A humongous thank you goes to **Yohan Dubois**. Although he probably did not ask for his role, he, more and more, was of enormous help during the last few years. Not only did he guide me through my thesis with ideas and wisdom, was always around if I had questions, corrected and overlooked my various written texts, including this thesis, but he also shared with me his dislike of too many grandios strong adjectives, extremely long sentences and too few commas. One can see that with this thank you note alone I owe him at least two more beers, and a distillery on top. Merci Yohan.

Thank you to **Lars Hernquist** and **Tiziana di Matteo** for the reading of my thesis and agreeing to be the *rapporteurs* of my committee.

Another big thank you goes to **Joki Rosdahl**. I stopped counting the number of times I wrote him an email asking questions about RAMSES-RT. His patient and caring answers and support, his sharing in the joy when things finally worked (stupid bug we finally beat you... for now) and his moral support when it did not is deeply valued. Thank you!

I also want to thank **Alex Wagner**. Our time in Japan, albeit actually short, was just the very best. As I said, things started to go upwards afterwards and your willingness to share your knowledge, time, and energy with us certainly had a great impact on me. Vielen lieben Dank und bis auf weitere Projekte; ich freue mich!

My gratitude goes also towards **Volker Gaibler**, who very patiently explained all (jet-related) questions to me. Vielen lieben Dank für deine Behmühungen, Geduld und deine Ausdauer.

Thank you to **Christophe Pichon** for letting me be a small part of your group; for including me in meetings and workshops; for forcing me to give a talk at your conference; for constantly, but silently, supporting me in the background; for keeping an eye out; and for letting me work with Jibe. But also, merci, for letting me continue to work on HORIZON, the greatest machine ever made of course, despite the well known **Rebekka effect** that almost crashed various nodes or almost shut down Observatoire Meudon for an entire day.

Hand in hand goes a merci beaucoup to **Stephane Rouberol**, the computer whisperer, for answering all my emails, being patient with me and my simulations, for running our cluster smoothly, and for letting me test new clusters before anyone else was on it.

Thank you **Marta Volonteri** for your constant support, wisdom, help, and overlooking eye over the last few years. Thank you for always being around. I know that, some day, I will be extremely thankful for the first year of group meetings. Let's just say that Mélanie and I paved the road for everyone else (you are all welcome). Thank you for your questions



ACKNOWLEDGEMENTS

and sharing your joy of science with us. And thank you for being a great Yoga partner in crime. I will miss the BAD-Y breaks ;-)

I also want to thank **Romain Teyssier** who is always around when really needed, especially for questions related to his superb code of course. But also for his general open ear and eye. Merci.

Thank goes also to **Matthew Lehnert, Valérie de Lapparent, and Olivia Leroy** for making me feel more welcome at the IAP, for helping me with various questions, for supporting me, as well as always having an open door.

Of course I want to thank the rest of the AGN/BH group, **Mélanie Habouzit, Salvo Cielo, Tilman Hartwig, Andrea Negri, and Latif Muhammad**. Thank you to the best girl and guys. Thank you Mélanie for being such a great office partner and always being around, Salvo for being a great Proposal buddie, Andrea for being the best to ask the most stupid questions (luckily behind closed doors), Tilman for always, always, having an open ear and for being extremely thoughtful (don't ever change!), and to Latif for being around for questions and your encouragement.

A grand thank you goes to **Jibe Fouvry** for very (very) patiently guiding me through the deep pond of the Secular Diffusion equations, especially during the Roscoff retreat. I am sorry I did not let you have a free minute to yourself and for keeping you up until 3 in the morning, although part of it was also someone else's fault, we both know who. I genuinely enjoyed working with you. Merci pour tous.

Merci to the coolest girls in town, my office mates and/or coffee partners, **Alba, Julia, Mélanie, and Caterina**. I guess together we went through about every emotion possible and supported each other, especially over the last few months. You guys are the best. Thank you just for everything.

Thank you, thank you, thank you to **Pips, Brad, Sam, Andrea, Marius, Steph, Jared, and Nico**, as well as the rest of the Friday beer gang, for providing me with some distraction, for all the fun games, for the laughter and the joy, for the beer and wine, and for the love. Love you all right back. Thank you!

Ganz ganz fescht willi au minere Familie, **Barbara, Ueli, und Lisa**, danke. Danke vöu vöu mou für euri konstanti Understützig, für d'Erinnerig dassi au uf mich muess luege, fürs eifach da si und für mich gärn zha. Han eui au ganz fescht lieb. Au wänn mir mängisch alli chli chaotisch sind ;-) Wäri ja langwillig andersch ume.

I am beyond grateful to my husband **Jonathan** :-) This all would absolutely not have been possible without you. Thank you for your love, continuous support, encouragement, and help. I cannot wait for what the future holds for us. I am extremely thankful I get to spend it with you. Jau Hai Gugent Tai.

Thank you to every one of you, for helping me to see the CALM, especially at times when I could only see the CHAOS.

ACKNOWLEDGEMENTS

THE CHAOS



THE CALM



Bibliography

- Abadi M. G., Moore B., Bower R. G., 1999, MNRAS, 308, 947
- Abadi M. G., Navarro J. F., Steinmetz M., Eke V. R., 2003a, ApJ, 591, 499
- Abadi M. G., Navarro J. F., Steinmetz M., Eke V. R., 2003b, ApJ, 597, 21
- Abel T., 2011, MNRAS, 413, 271
- Abramowicz M. A., Czerny B., Lasota J. P., Szuszkiewicz E., 1988, ApJ, 332, 646
- Agertz O., Kravtsov A. V., 2015, ArXiv e-prints
- Agertz O., Kravtsov A. V., Leitner S. N., Gnedin N. Y., 2013, ApJ, 770, 25
- Agertz O., Lake G., Moore B., Mayer L., Teyssier R., Romeo A. B., 2009, in IAU Symposium, Vol. 254, The Galaxy Disk in Cosmological Context, Andersen J., Nordström A., Bland-Hawthorn J., eds., p. 1
- Agertz O. et al., 2007, MNRAS, 380, 963
- Agertz O., Teyssier R., Moore B., 2011, MNRAS, 410, 1391
- Alexander D. M., Swinbank A. M., Smail I., McDermid R., Nesvadba N. P. H., 2010, in Astronomical Society of the Pacific Conference Series, Vol. 427, Accretion and Ejection in AGN: a Global View, Maraschi L., Ghisellini G., Della Ceca R., Tavecchio F., eds., p. 74
- Alexander P., Brown M. T., Scott P. F., 1984, MNRAS, 209, 851
- Aller M. C., Richstone D. O., 2007, ApJ, 665, 120
- Ambrosiano J., Greengard L., Rokhlin V., 1988, Computer Physics Communications, 48, 117
- Anderhalden D., Schneider A., Macciò A. V., Diemand J., Bertone G., 2013, JCAP, 3, 014
- Antonucci R., 1993, ARA&A, 31, 473
- Antonucci R. R. J., Miller J. S., 1985, ApJ, 297, 621
- Antonuccio-Delogu V., Silk J., 2008, MNRAS, 389, 1750
- Antonuccio-Delogu V., Silk J., 2010, MNRAS, 405, 1303
- Arp H. C., Bolton J. G., Kinman T. D., 1967, ApJ, 147, 840
- Bañados E. et al., 2014, AJ, 148, 14
- Baade W., Minkowski R., 1954, ApJ, 119, 206
- Babul A., Balogh M. L., Lewis G. F., Poole G. B., 2002, MNRAS, 330, 329
- Balbus S. A., Hawley J. F., 1991, ApJ, 376, 214
- Baldry I. K. et al., 2012, MNRAS, 421, 621

BIBLIOGRAPHY

- Balmaverde B., Baldi R. D., Capetti A., 2008, *A&A*, 486, 119
- Barai P., Viel M., Murante G., Gaspari M., Borgani S., 2014, *MNRAS*, 437, 1456
- Barthel P., 1989, *Scientific American*, 260, 20
- Bauer A., Springel V., Vogelsberger M., Genel S., Torrey P., Sijacki D., Nelson D., Hernquist L., 2015, *MNRAS*, 453, 3593
- Baugh C. M., 2006, *Reports on Progress in Physics*, 69, 3101
- Becerra F., Greif T. H., Springel V., Hernquist L. E., 2015, *MNRAS*, 446, 2380
- Beck R., Krause M., 2005, *Astronomische Nachrichten*, 326, 414
- Begelman M. C., 1985, *ApJ*, 297, 492
- Begelman M. C., 2012, *MNRAS*, 420, 2912
- Begelman M. C., Cioffi D. F., 1989, *ApJ*, 345, L21
- Behroozi P. et al., 2015, *MNRAS*, 454, 3020
- Behroozi P. S., Wechsler R. H., Conroy C., 2013, *ApJ*, 770, 57
- Bekki K., 2014, *MNRAS*, 438, 444
- Belokurov V. et al., 2010, *ApJ*, 712, L103
- Belokurov V. et al., 2009, *MNRAS*, 397, 1748
- Benincasa S. M., Wadsley J., Couchman H. M. P., Keller B. W., 2016, *ArXiv e-prints*
- Benson A. J., 2012, *New Astronomy*, 17, 175
- Benson A. J., Frenk C. S., Baugh C. M., Cole S., Lacey C. G., 2003, *MNRAS*, 343, 679
- Benson A. J., Frenk C. S., Lacey C. G., Baugh C. M., Cole S., 2002, *MNRAS*, 333, 177
- Benson A. J., Madau P., 2003, *MNRAS*, 344, 835
- Bernardi M., Meert A., Sheth R. K., Vikram V., Huertas-Company M., Mei S., Shankar F., 2013, *MNRAS*, 436, 697
- Best P. N., Kauffmann G., Heckman T. M., Brinchmann J., Charlot S., Ivezić Ž., White S. D. M., 2005, *MNRAS*, 362, 25
- Bicknell G. V., Sutherland R. S., van Breugel W. J. M., Dopita M. A., Dey A., Miley G. K., 2000, *ApJ*, 540, 678
- Bieri R., Dubois Y., Rosdahl J., Wagner A. Y., Silk J., Mamon G. A., 2016a, *ArXiv e-prints*
- Bieri R., Dubois Y., Silk J., Mamon G. A., 2015, *ApJ*, 812, L36
- Bieri R., Dubois Y., Silk J., Mamon G. A., Gaibler V., 2016b, *MNRAS*, 455, 4166
- Binney J., 1977, *ApJ*, 215, 492

BIBLIOGRAPHY

- Binney J., Tabor G., 1995, *MNRAS*, 276, 663
- Binney J., Tremaine S., 2008, *Galactic Dynamics: Second Edition*. Princeton University Press
- Birnboim Y., Dekel A., 2003, *MNRAS*, 345, 349
- Birnboim Y., Dekel A., Neistein E., 2007, *MNRAS*, 380, 339
- Birzan L., Rafferty D. A., McNamara B. R., Wise M. W., Nulsen P. E. J., 2004, *ApJ*, 607, 800
- Blandford R. D., Begelman M. C., 1999, *MNRAS*, 303, L1
- Blandford R. D., Payne D. G., 1982, *MNRAS*, 199, 883
- Blandford R. D., Rees M. J., 1974, *MNRAS*, 169, 395
- Blandford R. D., Znajek R. L., 1977, *MNRAS*, 179, 433
- Bleuler A., Teyssier R., 2014, *MNRAS*, 445, 4015
- Blitz L., 1993, in *Protostars and Planets III*, Levy E. H., Lunine J. I., eds., pp. 125–161
- Blumenthal G. R., Faber S. M., Primack J. R., Rees M. J., 1984, *Nature*, 311, 517
- Blumenthal G. R., Mathews W. G., 1979, *ApJ*, 233, 479
- Blundell K. M., 2008, in *Astronomical Society of the Pacific Conference Series*, Vol. 386, *Extragalactic Jets: Theory and Observation from Radio to Gamma Ray*, Rector T. A., De Young D. S., eds., p. 467
- Bond J. R., Cole S., Efstathiou G., Kaiser N., 1991, *ApJ*, 379, 440
- Bondi H., 1952, *MNRAS*, 112, 195
- Bondi H., Hoyle F., 1944, *MNRAS*, 104, 273
- Booth C. M., Agertz O., Kravtsov A. V., Gnedin N. Y., 2013, *ApJ*, 777, L16
- Booth C. M., Schaye J., 2009, *MNRAS*, 398, 53
- Bower R. G., 1991, *MNRAS*, 248, 332
- Bower R. G., Benson A. J., Malbon R., Helly J. C., Frenk C. S., Baugh C. M., Cole S., Lacey C. G., 2006, *MNRAS*, 370, 645
- Breitschwerdt D., Shapiro V., Shevchenko V., 1991, *International Cosmic Ray Conference*, 2, 229
- Bridle A. H., Perley R. A., 1984, *ARA&A*, 22, 319
- Brook C. B. et al., 2011, *MNRAS*, 415, 1051
- Bunker P. R., Jensen P., eds., 1998, *Molecular symmetry and spectroscopy*
- Busha M. T., Alvarez M. A., Wechsler R. H., Abel T., Strigari L. E., 2010, *ApJ*, 710, 408

- Cano-Díaz M., Maiolino R., Marconi A., Netzer H., Shemmer O., Cresci G., 2012, *A&A*, 537, L8
- Capelo P. R., Natarajan P., Coppi P. S., 2010, *MNRAS*, 407, 1148
- Carniani S. et al., 2016, *A&A*, 591, A28
- Cen R., 1992, *ApJS*, 78, 341
- Cen R., McDonald P., Trac H., Loeb A., 2009, *ApJ*, 706, L164
- Ceverino D., Klypin A., 2009, *ApJ*, 695, 292
- Chambers K. C., Miley G. K., van Breugel W. J. M., 1990, *ApJ*, 363, 21
- Chang C. A., Schiano A. V. R., Wolfe A. M., 1987, *ApJ*, 322, 180
- Chartas G., Brandt W. N., Gallagher S. C., Proga D., 2007, *AJ*, 133, 1849
- Chisari N. et al., 2015, *MNRAS*, 454, 2736
- Chisari N. E. et al., 2016, *ArXiv e-prints*
- Choi E., Naab T., Ostriker J. P., Johansson P. H., Moster B. P., 2014, *MNRAS*, 442, 440
- Choi E., Ostriker J. P., Naab T., Johansson P. H., 2012, *ApJ*, 754, 125
- Churazov E., Sazonov S., Sunyaev R., Forman W., Jones C., Böhringer H., 2005, *MNRAS*, 363, L91
- Cicone C. et al., 2014, *A&A*, 562, A21
- Ciotti L., Ostriker J. P., 2007, *ApJ*, 665, 1038
- Ciotti L., Ostriker J. P., 2012, in *Astrophysics and Space Science Library*, Vol. 378, *Astrophysics and Space Science Library*, Kim D.-W., Pellegrini S., eds., p. 83
- Coil A. L. et al., 2011, *ApJ*, 741, 8
- Cole S., Lacey C. G., Baugh C. M., Frenk C. S., 2000a, *MNRAS*, 319, 168
- Cole S., Lacey C. G., Baugh C. M., Frenk C. S., 2000b, *MNRAS*, 319, 168
- Colín P., Avila-Reese V., Vázquez-Semadeni E., Valenzuela O., Ceverino D., 2010, *ApJ*, 713, 535
- Commerçon B., Teyssier R., Audit E., Hennebelle P., Chabrier G., 2011, *A&A*, 529, A35
- Cool R. J., Eisenstein D. J., Hogg D. W., Blanton M. R., 2005a, *GRB Coordinates Network*, 4353
- Cool R. J., Eisenstein D. J., Hogg D. W., Blanton M. R., Brinkmann J., Schneider D. P., vanden Berk D. E., 2005b, *GRB Coordinates Network*, 4399
- Cool R. J., Eisenstein D. J., Johnston D., Scranton R., Brinkmann J., Schneider D. P., Zehavi I., 2006, *AJ*, 131, 736

BIBLIOGRAPHY

- Cool R. J., Moellenbrock G. A., 2003, in *Bulletin of the American Astronomical Society*, Vol. 35, American Astronomical Society Meeting Abstracts, p. 1330
- Cool R. J. et al., 2013, *ApJ*, 767, 118
- Cool R. J., Schaefer J. J., 2002, *GRB Coordinates Network*, 1584
- Cooper A. P. et al., 2010, *MNRAS*, 406, 744
- Cooray A., Sheth R., 2002, *Phys. Rep.*, 372, 1
- Costa T., Sijacki D., Haehnelt M. G., 2014, *MNRAS*, 444, 2355
- Cresci G. et al., 2015a, *ApJ*, 799, 82
- Cresci G. et al., 2015b, *A&A*, 582, A63
- Croft S. et al., 2006, *ApJ*, 647, 1040
- Croom S. et al., 2004, in *Multiwavelength AGN Surveys*, Mújica R., Maiolino R., eds., pp. 57–62
- Croton D. J. et al., 2006, *MNRAS*, 365, 11
- Daddi E. et al., 2010, *ApJ*, 714, L118
- Daddi E. et al., 2005, *ApJ*, 626, 680
- Dalgarno A., McCray R. A., 1972, *ARA&A*, 10, 375
- Daly R. A., 1990, *ApJ*, 355, 416
- Dasyra K. M., Combes F., Novak G. S., Bremer M., Spinoglio L., Pereira Santaella M., Salomé P., Falgarone E., 2014, *A&A*, 565, A46
- Davis S. W., Jiang Y.-F., Stone J. M., Murray N., 2014, *ApJ*, 796, 107
- de Avillez M., Breitschwerdt D., 2004, *Ap&SS*, 289, 479
- de Kool M., Arav N., Becker R. H., Gregg M. D., White R. L., Laurent-Muehleisen S. A., Price T., Korista K. T., 2001, *ApJ*, 548, 609
- de Lapparent V., Geller M. J., Huchra J. P., 1986, *ApJ*, 302, L1
- De Rosa G., Decarli R., Walter F., Fan X., Jiang L., Kurk J., Pasquali A., Rix H. W., 2011, *ApJ*, 739, 56
- De Young D. S., 1981, *Nature*, 293, 43
- De Young D. S., 1989, *ApJ*, 342, L59
- Debuhr J., Quataert E., Ma C.-P., 2011, *MNRAS*, 412, 1341
- Debuhr J., Quataert E., Ma C.-P., Hopkins P., 2010, *MNRAS*, 406, L55
- DeGraf C., Di Matteo T., Khandai N., Croft R., Lopez J., Springel V., 2012, *MNRAS*, 424, 1892

- Dehnen W., 2001, MNRAS, 324, 273
- Dehnen W., Read J. I., 2011, European Physical Journal Plus, 126, 55
- Dekel A., Birnboim Y., 2006, MNRAS, 368, 2
- Dekel A. et al., 2009, Nature, 457, 451
- Dekel A., Silk J., 1986, ApJ, 303, 39
- Dey A., van Breugel W., Vacca W. D., Antonucci R., 1997, ApJ, 490, 698
- Di Matteo T., Colberg J., Springel V., Hernquist L., Sijacki D., 2008, ApJ, 676, 33
- Di Matteo T., Croft R. A. C., Feng Y., Waters D., Wilkins S., 2016, ArXiv e-prints
- Di Matteo T., Croft R. A. C., Springel V., Hernquist L., 2003, ApJ, 593, 56
- Di Matteo T., Quataert E., Allen S. W., Narayan R., Fabian A. C., 2000, MNRAS, 311, 507
- Di Matteo T., Springel V., Hernquist L., 2005, Nature, 433, 604
- Diemand J., Kuhlen M., Madau P., Zemp M., Moore B., Potter D., Stadel J., 2008, Nature, 454, 735
- Done C., Gierliński M., Kubota A., 2007, A&A Rev., 15, 1
- Draine B. T., Salpeter E. E., 1979, ApJ, 231, 77
- Draper A. R., Ballantyne D. R., 2012, ApJ, 751, 72
- Drouart G. et al., 2014, A&A, 566, A53
- Dubois Y., Devriendt J., Slyz A., Teyssier R., 2010a, MNRAS, 409, 985
- Dubois Y., Devriendt J., Slyz A., Teyssier R., 2010b, MNRAS, 409, 985
- Dubois Y., Devriendt J., Slyz A., Teyssier R., 2012a, in Astronomical Society of the Pacific Conference Series, Vol. 453, Advances in Computational Astrophysics: Methods, Tools, and Outcome, Capuzzo-Dolcetta R., Limongi M., Tornambè A., eds., p. 281
- Dubois Y., Devriendt J., Slyz A., Teyssier R., 2012b, MNRAS, 420, 2662
- Dubois Y., Gavazzi R., Peirani S., Silk J., 2013, MNRAS, 433, 3297
- Dubois Y., Peirani S., Pichon C., Devriendt J., Gavazzi R., Welker C., Volonteri M., 2016, ArXiv e-prints
- Dubois Y. et al., 2014, MNRAS, 444, 1453
- Dubois Y., Teyssier R., 2008a, A&A, 477, 79
- Dubois Y., Teyssier R., 2008b, in Astronomical Society of the Pacific Conference Series, Vol. 390, Pathways Through an Eclectic Universe, Knapen J. H., Mahoney T. J., Vazdekis A., eds., p. 388

BIBLIOGRAPHY

- Dubois Y., Volonteri M., Silk J., Devriendt J., Slyz A., Teyssier R., 2015a, MNRAS, 452, 1502
- Dubois Y., Volonteri M., Silk J., Devriendt J., Slyz A., Teyssier R., 2015b, ArXiv e-prints, mNRAS, submitted, arXiv:1504.00018
- Dubroca B., Feugeas J., 1999, CRAS, 329, 915
- Dugan Z., Bryan S., Gaibler V., Silk J., Haas M., 2014, ApJ, 796, 113
- Dunn R. J. H., Fabian A. C., Taylor G. B., 2005, MNRAS, 364, 1343
- Dyson F. W., Eddington A. S., Davidson C., 1920, Philosophical Transactions of the Royal Society of London Series A, 220, 291
- Eddington A. S., 1919, The Observatory, 42, 119
- Efstathiou G., 2000, MNRAS, 317, 697
- Einstein A., 1916, Annalen der Physik, 354, 769
- Elmegreen B. G., 1997, in Revista Mexicana de Astronomia y Astrofisica, vol. 27, Vol. 6, Revista Mexicana de Astronomia y Astrofisica Conference Series, Franco J., Terlevich R., Serrano A., eds., p. 165
- Enßlin T. A., Pfrommer C., Springel V., Jubelgas M., 2007, A&A, 473, 41
- Everett J. E., Zweibel E. G., Benjamin R. A., McCammon D., Rocks L., Gallagher, III J. S., 2008, ApJ, 674, 258
- Fabian A. C., 2012, ARA&A, 50, 455
- Fabian A. C., Iwasawa K., 1999, MNRAS, 303, L34
- Fabjan D., Borgani S., Tornatore L., Saro A., Murante G., Dolag K., 2010, MNRAS, 401, 1670
- Fall S. M., Efstathiou G., 1980, MNRAS, 193, 189
- Fan X., Carilli C. L., Keating B., 2006, ARA&A, 44, 415
- Fan X. et al., 2000, AJ, 120, 1167
- Fanaroff B. L., Riley J. M., 1974, MNRAS, 167, 31P
- Fattahi A., Navarro J. F., Sawala T., Frenk C. S., Sales L. V., Oman K., Schaller M., Wang J., 2016, ArXiv e-prints
- Faucher-Giguère C.-A., Quataert E., 2012, MNRAS, 425, 605
- Fender R. P., Belloni T. M., Gallo E., 2004, MNRAS, 355, 1105
- Feoli A., Mancini L., 2009, ApJ, 703, 1502
- Ferrarese L., Merritt D., 2000, ApJ, 539, L9
- Feruglio C. et al., 2015, A&A, 583, A99

- Finlator K., Özel F., Davé R., 2009, MNRAS, 393, 1090
- Fischera J., Dopita M. A., 2004, ApJ, 611, 919
- Fischera J., Dopita M. A., Sutherland R. S., 2003, ApJ, 599, L21
- Friedmann A., 1922, Zeitschrift für Physik, 10, 377
- Fromang S., Hennebelle P., Teyssier R., 2006, A&A, 457, 371
- Fryxell B. et al., 2000, ApJS, 131, 273
- Fujita Y., Nagashima M., 1999, ApJ, 516, 619
- Fukui Y. et al., 1999, PASJ, 51, 745
- Gabor J. M., Bournaud F., 2014, MNRAS, 441, 1615
- Gaibler V., Khochfar S., Krause M., 2011, MNRAS, 411, 155
- Gaibler V., Khochfar S., Krause M., Silk J., 2012, MNRAS, 425, 438
- García-Burillo S. et al., 2015, A&A, 580, A35
- Gaspari M., Brighenti F., D’Ercole A., Melioli C., 2011, MNRAS, 415, 1549
- Gebhardt K. et al., 2000, ApJ, 539, L13
- Genel S. et al., 2014, MNRAS, 445, 175
- Genzel R. et al., 2010a, MNRAS, 407, 2091
- Genzel R. et al., 2010b, MNRAS, 407, 2091
- Gerritsen J. P. E., Icke V., 1997, A&A, 325, 972
- Girichidis P., Naab T., Walch S., Hanasz M., 2014, ArXiv e-prints
- Glover S. C. O., 2015, MNRAS, 453, 2901
- Gnedin N. Y., Abel T., 2001, new Astronomy, 6, 437
- Goto T., 2006, MNRAS, 371, 769
- Governato F. et al., 2010, Nature, 463, 203
- Governato F. et al., 2004, ApJ, 607, 688
- Governato F., Willman B., Mayer L., Brooks A., Stinson G., Valenzuela O., Wadsley J., Quinn T., 2007, MNRAS, 374, 1479
- Guo Q., White S., Li C., Boylan-Kolchin M., 2010, MNRAS, 404, 1111
- Haardt F., Madau P., 1996, ApJ, 461, 20
- Habouzit M., Volonteri M., Dubois Y., 2016, ArXiv e-prints
- Haiman Z., Dijkstra M., Mesinger A., 2005, in Growing Black Holes: Accretion in a Cosmological Context, Merloni A., Nayakshin S., Sunyaev R. A., eds., pp. 30–41

- Hardcastle M. J., Alexander P., Pooley G. G., Riley J. M., 1999, MNRAS, 304, 135
- Harfst S., Gualandris A., Merritt D., Spurzem R., Portegies Zwart S., Berczik P., 2007, New Astronomy, 12, 357
- Hatton S., Devriendt J. E. G., Ninin S., Bouchet F. R., Guiderdoni B., Vibert D., 2003, MNRAS, 343, 75
- Heckman T. M., Armus L., Miley G. K., 1990, ApJS, 74, 833
- Heckman T. M., Kauffmann G., 2011, Science, 333, 182
- Heckman T. M., Lehnert M. D., 2000, ApJ, 537, 690
- Heiderman A., Evans, II N. J., Allen L. E., Huard T., Heyer M., 2010, ApJ, 723, 1019
- Hellwing W. A., Schaller M., Frenk C. S., Theuns T., Schaye J., Bower R. G., Crain R. A., 2016, MNRAS, 461, L11
- Hernquist L., 1990, ApJ, 356, 359
- Heß S., Springel V., 2010, MNRAS, 406, 2289
- Hilbert S., Xu D., Schneider P., Springel V., Vogelsberger M., Hernquist L., 2016, ArXiv e-prints
- Ho L. C., 2002, ApJ, 564, 120
- Hockney R. W., Eastwood J. W., 1981, Computer Simulation Using Particles
- Hoffmann K. et al., 2014, MNRAS, 442, 1197
- Holt J., Tadhunter C. N., Morganti R., 2008, MNRAS, 387, 639
- Hopkins P. F., Murray N., Thompson T. A., 2009, MNRAS, 398, 303
- Hopkins P. F., Narayanan D., Murray N., 2013, MNRAS, 432, 2647
- Hopkins P. F., Quataert E., Murray N., 2011, MNRAS, 417, 950
- Hopkins P. F., Richards G. T., Hernquist L., 2007, ApJ, 654, 731
- Hopkins P. F., Robertson B., Krause E., Hernquist L., Cox T. J., 2006, ApJ, 652, 107
- Hopkins P. F., Torrey P., Faucher-Giguere C.-A., Quataert E., Murray N., 2015, ArXiv e-prints
- Hopkins P. F., Torrey P., Faucher-Giguère C.-A., Quataert E., Murray N., 2016, MNRAS, 458, 816
- Hoyle F., Lyttleton R. A., 1939, Proceedings of the Cambridge Philosophical Society, 35, 405
- Hu J., 2008, MNRAS, 386, 2242
- Hu W., Kravtsov A. V., 2003, ApJ, 584, 702
- Hubble E., 1929, Proceedings of the National Academy of Science, 15, 168

BIBLIOGRAPHY

- Inskip K. J., Villar-Martín M., Tadhunter C. N., Morganti R., Holt J., Dicken D., 2008, *MNRAS*, 386, 1797
- Inutsuka S.-I., Koyama H., 2002, *Ap&SS*, 281, 67
- Ishibashi W., Fabian A. C., 2012, *MNRAS*, 427, 2998
- Jenkins A., Frenk C. S., White S. D. M., Colberg J. M., Cole S., Evrard A. E., Couchman H. M. P., Yoshida N., 2001, *MNRAS*, 321, 372
- Jiang L. et al., 2009, *AJ*, 138, 305
- Jiang L., Fan X., Vestergaard M., 2008, *ApJ*, 679, 962
- Jiang Y.-F., Stone J. M., Davis S. W., 2012, *ApJS*, 199, 14
- Joung M. K. R., Cen R., Bryan G. L., 2009, in *Bulletin of the American Astronomical Society*, Vol. 41, American Astronomical Society Meeting Abstracts #213, p. 329
- Joung M. K. R., Mac Low M.-M., 2006, *ApJ*, 653, 1266
- Jubelgas M., Springel V., Enßlin T., Pfrommer C., 2008, *A&A*, 481, 33
- Junk V., Walch S., Heitsch F., Burkert A., Wetzstein M., Schartmann M., Price D., 2010, *MNRAS*, 407, 1933
- Kainulainen J., Beuther H., Henning T., Plume R., 2009, *A&A*, 508, L35
- Kaiser C. R., Best P. N., 2008, *MNRAS*, 384, 1742
- Kalfountzou E., Jarvis M. J., Bonfield D. G., Hardcastle M. J., 2012, *MNRAS*, 427, 2401
- Kannan R., Stinson G. S., Macciò A. V., Brook C., Weinmann S. M., Wadsley J., Couchman H. M. P., 2014, *MNRAS*, 437, 3529
- Karouzos M., Woo J.-H., Bae H.-J., 2016, *ApJ*, 819, 148
- Katz N., Gunn J. E., 1991, *ApJ*, 377, 365
- Katz N., Keres D., Dave R., Weinberg D. H., 2003, in *Astrophysics and Space Science Library*, Vol. 281, *The IGM/Galaxy Connection. The Distribution of Baryons at z=0*, Rosenberg J. L., Putman M. E., eds., p. 185
- Katz N., Weinberg D. H., Hernquist L., 1996, *ApJS*, 105, 19
- Kauffmann G., White S. D. M., Guiderdoni B., 1993, *MNRAS*, 264, 201
- Kaviraj S. et al., 2016, *ArXiv e-prints*
- Keller B. W., Wadsley J., Couchman H. M. P., 2015, *MNRAS*, 453, 3499
- Kennicutt, Jr. R. C., 1998a, *ApJ*, 498, 541
- Kennicutt, Jr. R. C., 1998b, *ApJ*, 498, 541
- Kennicutt, Jr. R. C. et al., 2007, *ApJ*, 671, 333
- Kereš D., Katz N., Fardal M., Davé R., Weinberg D. H., 2009, *MNRAS*, 395, 160

BIBLIOGRAPHY

- Kereš D., Katz N., Weinberg D. H., Davé R., 2005, *MNRAS*, 363, 2
- Keto E., Ho L. C., Lo K.-Y., 2005, *ApJ*, 635, 1062
- Khandai N., Di Matteo T., Croft R., Wilkins S., Feng Y., Tucker E., DeGraf C., Liu M.-S., 2015a, *MNRAS*, 450, 1349
- Khandai N., Di Matteo T., Croft R., Wilkins S., Feng Y., Tucker E., DeGraf C., Liu M.-S., 2015b, *MNRAS*, 450, 1349
- Khokhlov A., 1998, *Journal of Computational Physics*, 143, 519
- Kim J., Balsara D., Mac Low M.-M., 2001, *Journal of Korean Astronomical Society*, 34, 333
- Kim J.-h., Wise J. H., Alvarez M. A., Abel T., 2011, *ApJ*, 738, 54
- Kimm T., Cen R., Devriendt J., Dubois Y., Slyz A., 2015, *MNRAS*, 451, 2900
- King A., 2003, *ApJ*, 596, L27
- Klamer I. J., Ekers R. D., Sadler E. M., Hunstead R. W., 2004, *ApJ*, 612, L97
- Klein R. I., 1999, *Journal of Computational and Applied Mathematics*, 109, 123
- Klimentowski J., Łokas E. L., Knebe A., Gottlöber S., Martinez-Vaquero L. A., Yepes G., Hoffman Y., 2010, *MNRAS*, 402, 1899
- Klypin A. A., Trujillo-Gomez S., Primack J., 2011, *ApJ*, 740, 102
- Kollmeier J. A. et al., 2006, *ApJ*, 648, 128
- Komatsu E. et al., 2011, *ApJS*, 192, 18
- Koposov S. et al., 2008, *ApJ*, 686, 279
- Kormendy J., Bender R., Cornell M. E., 2011, *Nature*, 469, 374
- Kormendy J., Ho L. C., 2013, *ARA&A*, 51, 511
- Krause M., 2003, *A&A*, 398, 113
- Kravtsov A. V., Gnedin O. Y., Klypin A. A., 2004, *ApJ*, 609, 482
- Kravtsov A. V., Klypin A. A., Khokhlov A. M., 1997, *ApJS*, 111, 73
- Kritsuk A. G., Norman M. L., Wagner R., 2011, *ApJ*, 727, L20
- Krumholz M. R., Dekel A., McKee C. F., 2012, *ApJ*, 745, 69
- Krumholz M. R., Klein R. I., McKee C. F., 2011, *ApJ*, 740, 74
- Krumholz M. R., Klein R. I., McKee C. F., Bolstad J., 2007, *ApJ*, 667, 626
- Krumholz M. R., Matzner C. D., 2009, *ApJ*, 703, 1352
- Krumholz M. R., Tan J. C., 2007, *ApJ*, 654, 304

- Krumholz M. R., Thompson T. A., 2012, *ApJ*, 760, 155
- Krumholz M. R., Thompson T. A., 2013, *MNRAS*, 434, 2329
- Kuhlen M., Krumholz M. R., Madau P., Smith B. D., Wise J., 2012, *ApJ*, 749, 36
- Kurk J. D., Walter F., Fan X., Jiang L., Jester S., Rix H.-W., Riechers D. A., 2009, *ApJ*, 702, 833
- Labiano A. et al., 2016, *Astronomische Nachrichten*, 337, 188
- Lacey C., Guiderdoni B., Rocca-Volmerange B., Silk J., 1993, *ApJ*, 402, 15
- Lada C. J., Lada E. A., 2003, *ARA&A*, 41, 57
- Lada C. J., Lombardi M., Alves J. F., 2010, *ApJ*, 724, 687
- Lagos C. d. P. et al., 2016, *MNRAS*, 459, 2632
- Lee J., Shandarin S. F., 1998, *ApJ*, 500, 14
- Lee J. et al., 2014, *MNRAS*, 445, 4197
- Lehnert M. D., Tasse C., Nesvadba N. P. H., Best P. N., van Driel W., 2011, *A&A*, 532, L3
- Leisawitz D., Bash F. N., Thaddeus P., 1989, *ApJS*, 70, 731
- Lemaître G., 1927, *Annales de la Société Scientifique de Bruxelles*, 47, 49
- Leroy A. K. et al., 2015, *ApJ*, 801, 25
- Levermore C. D., 1984a, *J. Quant. Spec. Radiat. Transf.*, 31, 149
- Levermore C. D., 1984b, *J. Quant. Spec. Radiat. Transf.*, 31, 149
- Lewis A., 2013, *Phys. Rev.*, D87, 103529
- Lewis A., Bridle S., 2002, *Phys. Rev.*, D66, 103511
- Lewis G. M., Austin P. H., 2002, Jp4.16 an iterative method for generating scaling log-normal simulations
- Li A., Draine B. T., 2001, *ApJ*, 554, 778
- Li C., White S. D. M., 2009, *MNRAS*, 398, 2177
- Liddle A., 2002, *The Cosmological Constant and its Interpretation*, Murdin P., ed.
- Liddle A. R., Lyth D. H., 2000, *Cosmological Inflation and Large-Scale Structure*. p. 414
- Lombardi M., Lada C. J., Alves J., 2010, *A&A*, 512, A67
- Mac Low M.-M., Klessen R. S., 2004, *Reviews of Modern Physics*, 76, 125
- Macciò A. V., Kang X., Fontanot F., Somerville R. S., Koposov S., Monaco P., 2010, *MNRAS*, 402, 1995

BIBLIOGRAPHY

- Madau P., Diemand J., Kuhlen M., 2008, *ApJ*, 679, 1260
- Magorrian J. et al., 1998, *AJ*, 115, 2285
- Mahabal A., Stern D., Bogosavljević M., Djorgovski S. G., Thompson D., 2005, *ApJ*, 634, L9
- Marconi A., Risaliti G., Gilli R., Hunt L. K., Maiolino R., Salvati M., 2004, *MNRAS*, 351, 169
- Martig M., Bournaud F., Teyssier R., Dekel A., 2009, *ApJ*, 707, 250
- Martin C. L., 1999, *ApJ*, 513, 156
- Martin C. L., 2005, *ApJ*, 621, 227
- Martizzi D., Teyssier R., Moore B., Wentz T., 2012, *MNRAS*, 422, 3081
- Mathews W. G., Brighenti F., Buote D. A., Lewis A. D., 2003, *ApJ*, 596, 159
- Mayer L., Governato F., Kaufmann T., 2008, *Advanced Science Letters*, 1, 7
- Mayer L., Mastropietro C., Wadsley J., Stadel J., Moore B., 2006, *MNRAS*, 369, 1021
- McCarthy I. G. et al., 2010, *MNRAS*, 406, 822
- McCarthy P. J., 1993, *ARA&A*, 31, 639
- McCarthy P. J., van Breugel W., Kapahi V. K., 1991, *ApJ*, 371, 478
- McConnell N. J., Ma C., Graham J. R., Gebhardt K., Lauer T. R., Wright S. A., Richstone D. O., 2011, in *Bulletin of the American Astronomical Society*, Vol. 43, American Astronomical Society Meeting Abstracts #217, p. 422.06
- McGreer I. D., Becker R. H., Helfand D. J., White R. L., 2006, *ApJ*, 652, 157
- McKee C. F., Ostriker E. C., 2007, *ARA&A*, 45, 565
- McKee C. F., Ostriker J. P., 1977, *ApJ*, 218, 148
- McKinney J. C., Tchekhovskoy A., Blandford R. D., 2012, *MNRAS*, 423, 3083
- McLure R. J., Dunlop J. S., 2004, in *Multiwavelength AGN Surveys*, Mújica R., Maiolino R., eds., pp. 389–392
- McNamara B. R., Nulsen P. E. J., 2007, *ARA&A*, 45, 117
- McNamara B. R., Nulsen P. E. J., 2012, *New Journal of Physics*, 14, 055023
- McNamara B. R., Nulsen P. E. J., Wise M. W., Rafferty D. A., Carilli C., Sarazin C. L., Blanton E. L., 2005, *Nature*, 433, 45
- Merloni A., 2004, *MNRAS*, 353, 1035
- Merloni A., Heinz S., 2008, *MNRAS*, 388, 1011
- Mesinger A., Furlanetto S., 2009, *MNRAS*, 400, 1461

BIBLIOGRAPHY

- Mihalas D., Weibel Mihalas B., 1984, *Foundations of radiation hydrodynamics*
- Minkowski R., 1940, *PASP*, 52, 206
- Mirabel I. F., Chaty S., Rodríguez L. F., Sauvage M., 2015, in *IAU Symposium*, Vol. 313, *Extragalactic Jets from Every Angle*, Massaro F., Cheung C. C., Lopez E., Siemiginowska A., eds., pp. 370–373
- Mitchell N. L., McCarthy I. G., Bower R. G., Theuns T., Crain R. A., 2009, *MNRAS*, 395, 180
- Moore B., 1994, *Nature*, 370, 629
- Moore B., Diemand J., Madau P., Zemp M., Stadel J., 2006, *MNRAS*, 368, 563
- Moore B., Ghigna S., Governato F., Lake G., Quinn T., Stadel J., Tozzi P., 1999, *ApJ*, 524, L19
- Morganson E. et al., 2012, *AJ*, 143, 142
- Morganti R., Fogasy J., Paragi Z., Oosterloo T., Orienti M., 2013, *Science*, 341, 1082
- Morganti R., Oosterloo T., Tsvetanov Z., 1998, *AJ*, 115, 915
- Morganti R., Oosterloo T. A., Oonk J. B. R., Frieswijk W., Tadhunter C. N., 2015, in *Astronomical Society of the Pacific Conference Series*, Vol. 499, *Revolution in Astronomy with ALMA: The Third Year*, Iono D., Tatematsu K., Wootten A., Testi L., eds., p. 125
- Morganti R., Tadhunter C., Oosterloo T., Holt J., Emonts B., 2007, in *Astronomical Society of the Pacific Conference Series*, Vol. 373, *The Central Engine of Active Galactic Nuclei*, Ho L. C., Wang J.-W., eds., p. 343
- Morganti R., Tadhunter C. N., Oosterloo T. A., 2005, *A&A*, 444, L9
- Mortlock D. J. et al., 2009, *A&A*, 505, 97
- Mortlock D. J. et al., 2011, *Nature*, 474, 616
- Moster B. P., Macciò A. V., Somerville R. S., Naab T., Cox T. J., 2011, *MNRAS*, 415, 3750
- Moster B. P., Macciò A. V., Somerville R. S., Naab T., Cox T. J., 2012, *MNRAS*, 423, 2045
- Moster B. P., Somerville R. S., Maulbetsch C., van den Bosch F. C., Macciò A. V., Naab T., Oser L., 2010, *ApJ*, 710, 903
- Moustakas J. et al., 2013, *ApJ*, 767, 50
- Muñoz J. A., Madau P., Loeb A., Diemand J., 2009, *MNRAS*, 400, 1593
- Mullin L. M., Hardcastle M. J., 2009, *MNRAS*, 398, 1989
- Mullin L. M., Riley J. M., Hardcastle M. J., 2008, *MNRAS*, 390, 595
- Murante G., Borgani S., Brunino R., Cha S.-H., 2011, *MNRAS*, 417, 136

BIBLIOGRAPHY

- Murray N., Chiang J., 1995, *ApJ*, 454, L105
- Murray N., Ménard B., Thompson T. A., 2011, *ApJ*, 735, 66
- Murray N., Quataert E., Thompson T. A., 2005, *ApJ*, 618, 569
- Murray N., Quataert E., Thompson T. A., 2010, *ApJ*, 709, 191
- Mushotzky R. F., Solomon P. M., Strittmatter P. A., 1972, *ApJ*, 174, 7
- Naab T., Johansson P. H., Ostriker J. P., 2009, *ApJ*, 699, L178
- Nagar N. M., Falcke H., Wilson A. S., 2005, *A&A*, 435, 521
- Narayan R., Igumenshchev I. V., Abramowicz M. A., 2003, *PASJ*, 55, L69
- Narayan R., Yi I., 1995, *ApJ*, 452, 710
- Navarro J. F., Frenk C. S., White S. D. M., 1996, *ApJ*, 462, 563
- Navarro J. F., Frenk C. S., White S. D. M., 1997, *ApJ*, 490, 493
- Nayakshin S., Zubovas K., 2012, *MNRAS*, 427, 372
- Nelson D., Genel S., Vogelsberger M., Springel V., Sijacki D., Torrey P., Hernquist L., 2015, *MNRAS*, 448, 59
- Nelson R. P., Gressel O., Umurhan O. M., 2013, *MNRAS*, 435, 2610
- Nesvadba N. P. H., Lehnert M. D., De Breuck C., Gilbert A. M., van Breugel W., 2008, *A&A*, 491, 407
- Nesvadba N. P. H., Lehnert M. D., Eisenhauer F., Gilbert A., Tecza M., Abuter R., 2006, *ApJ*, 650, 693
- Nickerson S., Stinson G., Couchman H. M. P., Bailin J., Wadsley J., 2011, *MNRAS*, 415, 257
- Norberg P. et al., 2002, *MNRAS*, 336, 907
- Novak G. S., Ostriker J. P., Ciotti L., 2012a, *MNRAS*, 427, 2734
- Novak G. S., Ostriker J. P., Ciotti L., 2012b, *MNRAS*, 427, 2734
- Nulsen P. E. J., Hambrick D. C., McNamara B. R., Rafferty D., Birzan L., Wise M. W., David L. P., 2005, *ApJ*, 625, L9
- Ocvirk P., Pichon C., Teyssier R., 2008, *MNRAS*, 390, 1326
- Omma H., Binney J., Bryan G., Slyz A., 2004, *MNRAS*, 348, 1105
- O'Neill S. M., Tregillis I. L., Jones T. W., Ryu D., 2005, *ApJ*, 633, 717
- Oppenheimer B. D., Davé R., 2006, *MNRAS*, 373, 1265
- Oppenheimer B. D., Dave R., Keres D., 2010, in *Bulletin of the American Astronomical Society*, Vol. 42, American Astronomical Society Meeting Abstracts #215, p. 584

BIBLIOGRAPHY

- Oser L., Naab T., Ostriker J. P., Johansson P. H., 2012, *ApJ*, 744, 63
- Oser L., Ostriker J. P., Naab T., Johansson P. H., Burkert A., 2010, *ApJ*, 725, 2312
- O'Shea B. W., Bryan G., Bordner J., Norman M. L., Abel T., Harkness R., Kritsuk A., 2004, *ArXiv Astrophysics e-prints*
- Osterbrock D. E., Shaw R. A., 1988, *ApJ*, 327, 89
- Oteo I., Zwaan M. A., Ivison R. J., Smail I., Biggs A. D., 2016, *ArXiv e-prints*
- Padoan P., Nordlund Å., 2011, *ApJ*, 741, L22
- Parkinson H., Cole S., Helly J., 2008, *MNRAS*, 383, 557
- Pawlik A. H., Schaye J., 2008, *MNRAS*, 389, 651
- Pawlik A. H., Schaye J., 2011, *MNRAS*, 412, 1943
- Peng X., Xiao F., Takahashi K., 2007, *Q.J.R. Meteorol. Soc.*, 132, 979
- Petkova M., Springel V., 2009, *MNRAS*, 396, 1383
- Petkova M., Springel V., 2011, *MNRAS*, 415, 3731
- Piconcelli E. et al., 2015, *A&A*, 574, L9
- Piontek F., Steinmetz M., 2011, *MNRAS*, 410, 2625
- Pitchford L. K. et al., 2016, *ArXiv e-prints*
- Planck Collaboration et al., 2014, *A&A*, 571, A16
- Planck Collaboration et al., 2015a, *ArXiv e-prints*
- Planck Collaboration et al., 2015b, *ArXiv e-prints*
- Planelles S., Borgani S., Fabjan D., Killedear M., Murante G., Granato G. L., Ragone-Figueroa C., Dolag K., 2014, *MNRAS*, 438, 195
- Podigachoski P. et al., 2015, *A&A*, 575, A80
- Powell L. C., Bournaud F., Chapon D., Teyssier R., 2013, *MNRAS*, 434, 1028
- Powell L. C., Slyz A., Devriendt J., 2011, *MNRAS*, 414, 3671
- Press W. H., Schechter P., 1974, *ApJ*, 187, 425
- Price D. J., 2008, *Journal of Computational Physics*, 227, 10040
- Privon G. C., O'Dea C. P., Baum S. A., Axon D. J., Kharb P., Buchanan C. L., Sparks W., Chiaberge M., 2008, *ApJS*, 175, 423
- Proga D., Stone J. M., Kallman T. R., 2000, *ApJ*, 543, 686
- Puchwein E., Sijacki D., Springel V., 2008, *ApJ*, 687, L53
- Puchwein E., Springel V., 2013, *MNRAS*, 428, 2966

BIBLIOGRAPHY

- Quataert E., Gruzinov A., 2000, *ApJ*, 539, 809
- Rafferty D. A., McNamara B. R., Nulsen P. E. J., Wise M. W., 2006, *ApJ*, 652, 216
- Rasera Y., Teyssier R., 2006, *A&A*, 445, 1
- Rathborne J. M. et al., 2014, *ApJ*, 795, L25
- Rauch M., Becker G. D., Haehnelt M. G., Carswell R. F., Gauthier J.-R., 2013, *MNRAS*, 431, L68
- Read J. I., Hayfield T., 2012, *MNRAS*, 422, 3037
- Rees M. J., 1989, *MNRAS*, 239, 1P
- Rees M. J., Ostriker J. P., 1977, *MNRAS*, 179, 541
- Richards G. et al., 2006, in *Astronomical Society of the Pacific Conference Series*, Vol. 357, *Astronomical Society of the Pacific Conference Series*, Armus L., Reach W. T., eds., p. 261
- Riess A. G. et al., 1998, *AJ*, 116, 1009
- Robertson B. E., Kravtsov A. V., 2008, *ApJ*, 680, 1083
- Robertson H. P., 1935, *ApJ*, 82, 284
- Robertson H. P., 1936a, *ApJ*, 83, 187
- Robertson H. P., 1936b, *ApJ*, 83, 257
- Rocca-Volmerange B. et al., 2013, *MNRAS*, 429, 2780
- Rodighiero G. et al., 2015, *ApJ*, 800, L10
- Rodighiero G. et al., 2011, *ApJ*, 739, L40
- Rodriguez-Gomez V. et al., 2016, *MNRAS*, 458, 2371
- Roos O., Juneau S., Bournaud F., Gabor J. M., 2015, *ApJ*, 800, 19
- Rosas-Guevara Y., Bower R. G., Schaye J., McAlpine S., Dalla-Vecchia C., Frenk C. S., Schaller M., Theuns T., 2016, *ArXiv e-prints*
- Rosdahl J., Blaizot J., Aubert D., Stranex T., Teyssier R., 2013, *MNRAS*, 436, 2188
- Rosdahl J., Schaye J., Teyssier R., Agertz O., 2015, *MNRAS*, 451, 34
- Rosdahl J., Teyssier R., 2015a, *MNRAS*, 449, 4380
- Rosdahl J., Teyssier R., 2015b, *MNRAS*, 449, 4380
- Rosen A., Bregman J. N., 1995, *ApJ*, 440, 634
- Rosolowsky E., Blitz L., 2005, *ApJ*, 623, 826
- Roškar R., Teyssier R., Agertz O., Wetzstein M., Moore B., 2014, *MNRAS*, 444, 2837

BIBLIOGRAPHY

- Rupke D. S. N., Veilleux S., 2011, *ApJ*, 729, L27
- Russell H. R., McNamara B. R., Edge A. C., Hogan M. T., Main R. A., Vantyghem A. N., 2013a, *MNRAS*, 432, 530
- Russell H. R., McNamara B. R., Edge A. C., Hogan M. T., Main R. A., Vantyghem A. N., 2013b, *MNRAS*, 432, 530
- Salem M., Bryan G. L., Corlies L., 2016, *MNRAS*, 456, 582
- Salem M., Bryan G. L., Hummels C., 2014, *ApJ*, 797, L18
- Sales L. V., Navarro J. F., Schaye J., Dalla Vecchia C., Springel V., Booth C. M., 2010, *MNRAS*, 409, 1541
- Salomé Q., Salomé P., Combes F., 2015, *A&A*, 574, A34
- Sandage A., 1965, *ApJ*, 141, 1560
- Saxton C. J., Bicknell G. V., Sutherland R. S., 2002, *ApJ*, 579, 176
- Sazonov S. Y., Ostriker J. P., Sunyaev R. A., 2004, *MNRAS*, 347, 144
- Scannapieco C., 2013, *Astronomische Nachrichten*, 334, 499
- Scannapieco C., Tissera P. B., White S. D. M., Springel V., 2008, *MNRAS*, 389, 1137
- Scannapieco C. et al., 2012, *MNRAS*, 423, 1726
- Scannapieco C., White S. D. M., Springel V., Tissera P. B., 2009, *MNRAS*, 396, 696
- Scannapieco C., White S. D. M., Springel V., Tissera P. B., 2011, *MNRAS*, 417, 154
- Schaye J. et al., 2015, *MNRAS*, 446, 521
- Schechter P., 1976, *ApJ*, 203, 297
- Scheuer P. A. G., 1974, *MNRAS*, 166, 513
- Scheuer P. A. G., 1995, *MNRAS*, 277, 331
- Schiano A. V. R., 1986, *ApJ*, 302, 95
- Schmidt M., 1963, *Nature*, 197, 1040
- Schmidt M., 1965, *ApJ*, 141, 1295
- Schwamb M. E., Lintott C., Smethurst R., Kruk S., Matsushita S., Wong I., Wang S.-Y., 2016, in *American Astronomical Society Meeting Abstracts*, Vol. 227, American Astronomical Society Meeting Abstracts, p. 209.03
- Semenov D., Henning T., Helling C., Ilgner M., Sedlmayr E., 2003, *A&A*, 410, 611
- Shakura N. I., Sunyaev R. A., 1973, *A&A*, 24, 337
- Shankar F., Salucci P., Granato G. L., De Zotti G., Danese L., 2004, *MNRAS*, 354, 1020

BIBLIOGRAPHY

- Sharma M., Theuns T., Frenk C., Bower R., Crain R., Schaller M., Schaye J., 2016a, MNRAS, 458, L94
- Sharma M., Theuns T., Frenk C., Bower R. G., Crain R. A., Schaller M., Schaye J., 2016b, ArXiv e-prints
- Sheth R. K., Mo H. J., Tormen G., 2001, MNRAS, 323, 1
- Sheth R. K., Tormen G., 1999, MNRAS, 308, 119
- Sijacki D., Springel V., Di Matteo T., Hernquist L., 2007, MNRAS, 380, 877
- Sijacki D., Vogelsberger M., Genel S., Springel V., Torrey P., Snyder G. F., Nelson D., Hernquist L., 2015, MNRAS, 452, 575
- Sikora M., Stawarz Ł., Lasota J.-P., 2007, ApJ, 658, 815
- Silk J., 1997, ApJ, 481, 703
- Silk J., 2001, MNRAS, 324, 313
- Silk J., 2005, MNRAS, 364, 1337
- Silk J., 2011, in IAU Symposium, Vol. 277, Tracing the Ancestry of Galaxies, Carignan C., Combes F., Freeman K. C., eds., pp. 273–281
- Silk J., 2013, ApJ, 772, 112
- Silk J., Norman C., 2009, ApJ, 700, 262
- Silk J., Rees M. J., 1998, A&A, 331, L1
- Skinner M. A., Ostriker E. C., 2013, ApJS, 206, 21
- Slyz A. D., Devriendt J. E. G., Bryan G., Silk J., 2005, MNRAS, 356, 737
- Snyder G. F. et al., 2015, MNRAS, 454, 1886
- Socrates A., Davis S. W., Ramirez-Ruiz E., 2008, ApJ, 687, 202
- Soltan A., 1982, MNRAS, 200, 115
- Somerville R. S., 2002, ApJ, 572, L23
- Somerville R. S., Gilmore R. C., Primack J. R., Domínguez A., 2012, MNRAS, 423, 1992
- Sommer-Larsen J., Dolgov A., 2001, ApJ, 551, 608
- Springel V., 2005, MNRAS, 364, 1105
- Springel V., 2010, MNRAS, 401, 791
- Springel V., 2011, ArXiv e-prints
- Springel V., Di Matteo T., Hernquist L., 2005a, MNRAS, 361, 776
- Springel V., Hernquist L., 2003, MNRAS, 339, 289

BIBLIOGRAPHY

- Springel V., Hernquist L., 2005, *ApJ*, 622, L9
- Springel V. et al., 2005b, *Nature*, 435, 629
- Stinson G., Seth A., Katz N., Wadsley J., Governato F., Quinn T., 2006, *MNRAS*, 373, 1074
- Stinson G. S., Bailin J., Couchman H., Wadsley J., Shen S., Nickerson S., Brook C., Quinn T., 2010, *MNRAS*, 408, 812
- Sutherland R. S., Bicknell G. V., 2007, *ApJS*, 173, 37
- Sutherland R. S., Dopita M. A., 1993, *ApJS*, 88, 253
- Swinbank M. et al., 2015, *ArXiv e-prints*
- Tacconi L. J. et al., 2010, *Nature*, 463, 781
- Tadhunter C. et al., 2011, *MNRAS*, 412, 960
- Tadhunter C., Morganti R., Rose M., Oonk J. B. R., Oosterloo T., 2014, *Nature*, 511, 440
- Tamburro D., Rix H.-W., Leroy A. K., Mac Low M.-M., Walter F., Kennicutt R. C., Brinks E., de Blok W. J. G., 2009, *AJ*, 137, 4424
- Tenneti A., Mandelbaum R., Di Matteo T., 2015a, *ArXiv e-prints*
- Tenneti A., Mandelbaum R., Di Matteo T., Kiessling A., Khandai N., 2015b, *MNRAS*, 453, 469
- Teyssier R., 2002, *A&A*, 385, 337
- Teyssier R., Fromang S., Dormy E., 2006, *Journal of Computational Physics*, 218, 44
- Teyssier R., Moore B., Martizzi D., Dubois Y., Mayer L., 2011, *MNRAS*, 414, 195
- Teyssier R., Pontzen A., Dubois Y., Read J. I., 2013, *MNRAS*, 429, 3068
- Tollerud E. J., Bullock J. S., Strigari L. E., Willman B., 2008, *ApJ*, 688, 277
- Tombesi F., Meléndez M., Veilleux S., Reeves J. N., González-Alfonso E., Reynolds C. S., 2015, *Nature*, 519, 436
- Toomre A., 1964, *ApJ*, 139, 1217
- Toro E. F., Spruce M., Speares W., 1993, *Shock Waves*
- Toro E. F., Spruce M., Speares W., 1994, *Shock Waves*, 4, 25
- Tortora C., Antonuccio-Delogu V., Kaviraj S., Silk J., Romeo A. D., Becciani U., 2009, *MNRAS*, 396, 61
- Tremaine S. et al., 2002, *ApJ*, 574, 740
- Tremblay G., 2016, in *American Astronomical Society Meeting Abstracts*, Vol. 227, *American Astronomical Society Meeting Abstracts*, p. 202.07

BIBLIOGRAPHY

- Truelove J. K., Klein R. I., McKee C. F., Holliman, II J. H., Howell L. H., Greenough J. A., 1997a, *ApJ*, 489, L179
- Truelove J. K., Klein R. I., McKee C. F., Holliman, II J. H., Howell L. H., Greenough J. A., 1997b, *ApJ*, 489, L179
- Trujillo I. et al., 2006, *ApJ*, 650, 18
- Tsang B. T.-H., Milosavljević M., 2015, *MNRAS*, 453, 1108
- Umemura M., 2001, *ApJ*, 560, L29
- Urry C. M., Padovani P., 1995, *PASP*, 107, 803
- van Breugel W. J. M., Dey A., 1993, *ApJ*, 414, 563
- van de Voort F., Schaye J., Booth C. M., Haas M. R., Dalla Vecchia C., 2011, *MNRAS*, 414, 2458
- Velliscig M. et al., 2015, *MNRAS*, 454, 3328
- Venemans B. P., Kurk J. D., Miley G. K., Röttgering H. J. A., 2003, *New Astronomy Reviews*, 47, 353
- Venemans B. P., McMahon R. G., Warren S. J., Gonzalez-Solares E. A., Hewett P. C., Mortlock D. J., Dye S., Sharp R. G., 2007, *MNRAS*, 376, L76
- Verner D. A., Ferland G. J., Korista K. T., Yakovlev D. G., 1996, *ApJ*, 465, 487
- Vogelsberger M. et al., 2014, *MNRAS*, 444, 1518
- Volonteri M., 2012, *Science*, 337, 544
- Volonteri M., Bellovary J., 2012, *Reports on Progress in Physics*, 75, 124901
- Volonteri M., Dubois Y., Pichon C., Devriendt J., 2016, *ArXiv e-prints*
- Wadepuhl M., Springel V., 2011, *MNRAS*, 410, 1975
- Wadsley J. W., Stadel J., Quinn T., 2004, *new Astronomy*, 9, 137
- Wagner A. Y., Bicknell G. V., 2011, *ApJ*, 728, 29
- Wagner A. Y., Bicknell G. V., Umemura M., 2012, *ApJ*, 757, 136
- Wagner A. Y., Bicknell G. V., Umemura M., Sutherland R. S., Silk J., 2016, *Astronomische Nachrichten*, 337, 167
- Wagner A. Y., Umemura M., Bicknell G. V., 2013, *ApJ*, 763, L18
- Walker A. G., 1935, *MNRAS*, 95, 263
- Walter F., Riechers D., Cox P., Neri R., Carilli C., Bertoldi F., Weiss A., Maiolino R., 2009, *Nature*, 457, 699
- Wang R. et al., 2013, *ApJ*, 773, 44
- Wardle J. F. C., Aaron S. E., 1997, *MNRAS*, 286, 425

BIBLIOGRAPHY

- Warhaft Z., 2000, *Annual Review of Fluid Mechanics*, 32, 203
- Weidner C., Kroupa P., Larsen S. S., 2004, *MNRAS*, 350, 1503
- Welker C., Dubois Y., Devriendt J., Pichon C., Kaviraj S., Peirani S., 2015, *ArXiv e-prints*
- Weymann R. J., Scott J. S., Schiano A. V. R., Christiansen W. A., 1982, *ApJ*, 262, 497
- Wheeler J. C., Harkness R. P., 1990, *Reports on Progress in Physics*, 53, 1467
- White S. D. M., Frenk C. S., 1991, *ApJ*, 379, 52
- White S. D. M., Rees M. J., 1978, *MNRAS*, 183, 341
- Williams B. F., Battinelli P., Efremov Y., Hodge P. W., Magnier E., 2000, in *Bulletin of the American Astronomical Society*, Vol. 32, American Astronomical Society Meeting Abstracts, p. 1465
- Williams R. E., 1972, *ApJ*, 178, 105
- Willott C. J. et al., 2010a, *AJ*, 140, 546
- Willott C. J. et al., 2007, *AJ*, 134, 2435
- Willott C. J. et al., 2009, *AJ*, 137, 3541
- Willott C. J. et al., 2010b, *AJ*, 139, 906
- Wise J. H., Abel T., 2011, *MNRAS*, 414, 3458
- Woosley S., Janka T., 2005, *Nature Physics*, 1, 147
- Wurster J., Thacker R. J., 2013, *MNRAS*, 431, 2513
- Yang X., Mo H. J., van den Bosch F. C., 2003, *MNRAS*, 339, 1057
- Zaldarriaga M., Seljak U., 2000, *ApJS*, 129, 431
- Zanni C., Bodo G., Rossi P., Massaglia S., Durbala A., Ferrari A., 2003, *A&A*, 402, 949
- Zanni C., Ferrari A., Massaglia S., Bodo G., Rossi P., 2005, *Mem. Soc. Astron. Italiana*, 76, 372
- Zensus J. A., 1997, *ARA&A*, 35, 607
- Zhu Q., Hernquist L., Li Y., 2015, *ApJ*, 800, 6
- Zinn P.-C., Middelberg E., Norris R. P., Dettmar R.-J., 2013, *ApJ*, 774, 66
- Zubovas K., King A., 2012, *ApJ*, 745, L34
- Zubovas K., King A., 2016, *ArXiv e-prints*
- Zubovas K., Nayakshin S., 2014, *MNRAS*, 440, 2625
- Zubovas K., Nayakshin S., Sazonov S., Sunyaev R., 2013a, *MNRAS*, 431, 793
- Zubovas K., Nayakshin S., Sazonov S., Sunyaev R., 2013b, *MNRAS*, 431, 793
- Zubovas K., Sabulis K., Naujalis R., 2014, *MNRAS*, 442, 2837